Femtosecond Pump-Probe Spectroscopy of Gas-Phase Atomic and Molecular Systems Using the Free-Electron Laser FLASH

Dissertation
zur Erlangung des Doktorgrades
an der Fakultät für Mathematik, Informatik und Naturwissenschaften

Fachbereich Physik
der Universität Hamburg

vorgelegt von

Sonu Kumar

Hamburg
2026

Gutachter/innen der Dissertation: Prof. Dr. Markus Drescher
Prof. Dr. Melanie Schnell

Zusammensetzung der Prüfungskommission: Prof. Dr. Markus Drescher
Prof. Dr. Melanie Schnell
Dr. Benjamin Erk
Prof. Dr. Markus Gühr
Prof. Dr. Ludwig Mathey

Vorsitzender des Prüfungsausschusses: Prof. Dr. Ludwig Mathey

Datum der Disputation: 13.05.2026

Vorsitzender des Fach-Promotionsausschusses PHYSIK: Prof. Dr. Johannes Haller

Leiter des Fachbereichs PHYSIK: Prof. Dr. Markus Drescher

Dekan der Fakultät MIN: Prof. Dr.-Ing. Norbert Ritter

This work is dedicated to the scientists, engineers, and researchers who built the incredible machine known as FLASH. Developing the first XUV free-electron laser was an immense scientific and technological challenge, yet their pioneering efforts transformed the vision of a free-electron laser into the world's first operational FEL user facility, opening a new era of ultrafast spectroscopy and inspiring future generations of accelerator physicists.

Abstract

This thesis explores ultrafast dynamics in atomic and molecular systems using pump–probe techniques at the free-electron laser (FLASH), with the goal of achieving the high temporal resolution required to resolve processes on the order of 100 fs and below. To address this challenge, an active feedback scheme based on a laser arrival time monitor is implemented to improve synchronization between optical laser and FEL pulses. This approach significantly enhances timing stability and is realized at the FL26 beamline of FLASH2, enabling an overall temporal resolution below 50 fs at the REMI endstation, as validated by photoionization experiments on xenon.

With this improved time resolution, the ionization and relaxation dynamics of xenon were investigated using extreme-ultraviolet (XUV) FEL pulses at photon energies near the $4d$ giant resonance (90 eV) and the Cooper minimum (160 eV). Ion time-of-flight spectroscopy reveals energy-dependent Auger–Meitner decay pathways and signatures of two-photon sequential ionization. Time-resolved XUV-pump–near-infrared-probe measurements identify transient intermediate states, yielding a characteristic lifetime of (49 ± 3) fs associated with the $4d$ double-core-hole decay at 160 eV.

The methodology is further extended to molecular systems through time-resolved Coulomb-explosion imaging experiments on CO_2 and CS_2 at the REMI endstation, triggered by 90 eV FEL pulses and probed with a near-infrared pulse. For both molecules, two-body and three-body fragmentation channels are observed, with contributions from both concerted and sequential breakup mechanisms. The intermediate dissociative cation states ($CO_2{}^{+*}$ and $CS_2{}^{+*}$) show similar lifetimes of approximately 60 fs. Comparative analysis shows that the heavier mass and distinct electronic structure of sulfur lead to enhanced bending dynamics and greater stability of highly charged states in CS_2.

Finally, UV-induced dynamics in 1-butanethiol were studied at the CAMP endstation using time-resolved ion and electron-spectroscopy. This measurement shows rapid fragmentation of the molecule, as well as hydrogen-transfer processes and charge redistribution. Photoelectron and Auger-Meitner spectra indicate excited-state lifetimes on the order of hundreds of femtoseconds, with C–S bond cleavage occurring on a 200 fs timescale. Despite spectral overlap arising from mixing of unresolved states due to finite experimental resolution, the combined results provide a picture of ultrafast relaxation followed by dissociation.

Overall, this work demonstrates how improved temporal resolution and complementary experimental techniques, i.e., multi-ion coincidence and simultaneous ion and electron spectroscopy, can enable detailed insight into the coupling between electronic and nuclear dynamics in atomic and molecular systems on femtosecond timescales.

Zusammenfassung

Diese Arbeit untersucht die ultraschnelle Dynamik in atomaren und molekularen Systemen mithilfe von Pump-Probe-Techniken am Freie-Elektronen-Laser (FLASH), um eine hohe zeitliche Auflösung zu erreichen, die erforderlich ist, um Prozesse in der Größenordnung von 100 fs und darunter aufzulösen. Um diese Herausforderung zu bewältigen, wird ein aktives Rückkopplungsschema auf Basis eines Laserankunftszeitmonitors implementiert, um die Synchronisation zwischen optischen Laser- und FEL-Pulsen zu verbessern. Dieser Ansatz verbessert die Zeitstabilität erheblich und wird an der FL26-Strahlführung von FLASH2 realisiert. Hiermit wird am REMI-Experiment eine Gesamtzeitauflösung von unter 50 fs ermöglicht, wie durch Photoionisationsversuche an Xenon bestätigt wurde.

Mit dieser verbesserten Zeitauflösung wurden die Ionisations- und Relaxationsdynamik von xenon unter Verwendung von FEL-Impulsen im extremen Ultraviolett (XUV) bei Photonenenergien nahe der $4d$-Riesenresonanz (90 eV) und des Cooper-Minimums (160 eV) untersucht. Die Ionen-Flugzeitspektroskopie zeigt energieabhängige Auger-Meitner-Zerfallswege sowie Anzeichen einer sequenziellen Zwei-Photonen-Ionisation. Zeitaufgelöste XUV-Pump-Nahinfrarot-Probe-Messungen identifizieren transiente Zwischenzustände mit einer charakteristischen Lebensdauer von (49 ± 3) fs, die mit dem $4d$-Doppelkernloch-Zerfall bei 160 eV assoziiert ist.

Die Methodik wird hin zu molekularen Systemen erweitert durch zeitaufgelöste Coulomb-Explosions-Bildgebung an CO_2 und CS_2 Molekülen mit dem an der REMI, ausgelöst durch 90 eV-FEL-Pulse, und untersucht mit einem Nahinfrarot-Puls. Für beide Moleküle werden Zwei- und Dreifach-Fragmentationskanäle beobachtet, mit Beiträgen sowohl konzertierter als auch sequenzieller Zerfallsmechanismen. Die dissoziativen kationischen Übergangszustände ($CO_2{}^{+*}$ und $CS_2{}^{+*}$) weisen ähnliche Lebensdauern von etwa 60 fs auf. Eine vergleichende Analyse zeigt, dass die höhere Masse und die unterschiedliche elektronische Struktur von Schwefel zu einer verstärkten Biegedynamik und einer größeren Stabilität hochgeladener Zustände in CS_2 führen.

Schließlich wurde die UV-induzierte Dynamik in 1-Butanthiol CAMP mittels zeitaufgelöster Ionen- und Elektronenspektroskopie untersucht. Diese Messung zeigt eine schnelle Fragmentierung des Moleküls, Wasserstofftransfer sowie eine Ladungsumverteilung. Photoelektronen- und Auger-Meitner-Spektren weisen auf Lebensdauern der angeregten Zustände in der Größenordnung von Hunderten Femtosekunden hin, wobei die Spaltung der C−S-Bindung auf einer Zeitskala von 200 fs erfolgt. Trotz spektraler Überlappungen, die durch die Vermischung nicht aufgelöster Zustände aufgrund der endlichen experimentellen Auflösung entstehen, liefern die kombinierten Ergebnisse ein Bild von ultraschneller Relaxation, gefolgt von Dissoziation.

Insgesamt zeigt diese Arbeit, wie eine verbesserte zeitliche Auflösung und komplementäre experimentelle Techniken, d.h. Multi-Ionen-Koinzidenzen und simultane Ionen- und Elektronenspektroskopie, detaillierte Einblicke in die Kopplung zwischen elektronischer und nuklearer Dynamik in atomaren und molekularen Systemen auf Femtosekunden-Zeitskalen ermöglichen.

Contents

1 Introduction **1**
- 1.1 Evolution of X-ray Sources . . . 2
- 1.2 Objectives and Structure of the Thesis . . . 4

2 Theoretical Background **5**
- 2.1 Interaction of Photons with Atoms and Molecules . . . 5
  - 2.1.1 Strong-Field Ionization . . . 5
  - 2.1.2 Core Ionization . . . 9
- 2.2 Coulomb Explosion Imaging . . . 11
  - 2.2.1 Principles of Coulomb Explosion Imaging . . . 13
- 2.3 Pump–Probe Model and Fitting Procedure . . . 14
  - 2.3.1 Pump–Probe Fitting Model . . . 15
  - 2.3.2 Numerical Fitting Strategy . . . 18

3 Experimental Techniques using Free-Electron Laser FLASH **19**
- 3.1 Introduction . . . 19
- 3.2 Free-Electron Laser . . . 20
  - 3.2.1 FEL Components . . . 21
  - 3.2.2 Microbunching and SASE . . . 24
  - 3.2.3 Free-Electron-Laser in Hamburg (FLASH) . . . 27
  - 3.2.4 Free-electron laser (FEL) Photon Beam Diagnostics . . . 27
- 3.3 The Reaction Microscope Setup . . . 29
  - 3.3.1 Vacuum Requirement for REMI Experiment . . . 29
  - 3.3.2 Gas Jet Source . . . 30
  - 3.3.3 Spectrometer and Detectors . . . 31
  - 3.3.4 Reconstruction of Ion momenta . . . 34
  - 3.3.5 Data Analysis of REMI . . . 35
- 3.4 CAMP End-Station . . . 38
  - 3.4.1 Layout of the Experimental Hall . . . 38
  - 3.4.2 FLASH1 Optical Laser System . . . 39
  - 3.4.3 Molecular Source . . . 39
  - 3.4.4 Electron and Ion Spectrometer . . . 39
  - 3.4.5 Velocity Map Imaging . . . 40
  - 3.4.6 Abel Inversion . . . 41

4 Achieving Sub-50 fs Temporal Resolution at FLASH2 **45**
- 4.1 Experimental Setup . . . 46
  - 4.1.1 FLASH Timing Infrastructure . . . 48
  - 4.1.2 Laser Arrival Monitor . . . 49
  - 4.1.3 Active Drift Compensation . . . 50
- 4.2 Results . . . 52

4.3 Summary . . . 55

5 Xenon Photoionization Dynamics in the Vicinity of the 4*d* Giant Resonance and Cooper Minimum 57
5.1 Introduction . . . 57
5.2 Experimental Methods . . . 58
5.2.1 Data Acquisition and Analysis . . . 59
5.3 Results . . . 60
5.3.1 Mass Spectra and Relative Ion Yields . . . 60
5.3.2 Intensity-Dependent Ion Yields . . . 63
5.3.3 Delay-dependent Ion Yields at 90 eV . . . 64
5.3.4 Delay-dependent Ion Yields at 160 eV . . . 66
5.4 Summary . . . 67

6 Fragmentation Dynamics of CO_2 and CS_2 using an FEL Pump–NIR Probe Technique 69
6.1 Introduction . . . 69
6.2 Experimental Setup . . . 70
6.2.1 Data Acquisition and Analysis . . . 71
6.3 Results . . . 73
6.3.1 Fragmentation Dynamics of CO_2 . . . 73
6.3.2 Fragmentation Dynamics of CS_2 . . . 83
6.4 Summary and Conclusions: Comparative Dynamics of CO_2 and CS_2 . . . 91

7 UV-Induced Dissociation of 1-Butanethiol 93
7.1 Introduction . . . 93
7.2 Experimental Method . . . 94
7.2.1 Data Analysis . . . 96
7.3 Results . . . 97
7.3.1 Time-Resolved Ion Spectroscopy . . . 97
7.3.2 Electron VMI: Probing Site-Specific Dynamics with TR-XPS and TR-AMS . . . 106
7.4 Summary . . . 113

8 Summary and Outlook 115

A Laser Pulse Characterization 119
A.1 Estimation of near-infrared (NIR) Intensity . . . 121

B Pump-probe Laser Drift Measurement 123
B.1 Two-Color Balanced Cross-Correlator . . . 123
B.2 Interferometer Measurement Data at the REMI Endstation . . . 124

C Supplementary Material: UV-Induced Dynamics of 1-Butanethiol 129
C.1 Mass Spectrum . . . 129
C.2 Ion velocity map imaging (VMI) . . . 130
C.3 Electron VMI: Helium and Krypton . . . 132
C.4 Simulation of XPS Spectra . . . 133

List of Publications 155

List of Abbreviations

ADC analog-to-digital converter. 95

AM Auger-Meitner. 2, 4, 10, 11, 52, 57, 58, 60–64, 66–68, 94, 99–101, 103, 104, 106–113, 115, 116

AMO atomic, molecular, and optical physics. 4, 20, 27

AMS Auger-Meitner spectroscopy. 106, 107

ATI above-threshold ionization. 6, 8, 9

BAM bunch arrival-time monitor. 36, 38, 46, 47, 49, 52–54, 60, 94, 96

BBO beta-barium borate. 49, 50, 94, 123

BCC balanced cross-correlators. 47, 49, 123, 124

BE binding energy. 106

BOA Born–Oppenheimer approximation. 106

CAMP CFEL-ASG Multi-Purpose instrument. 19, 38, 39, 94, 95

CCD charge-coupled device. 33, 39, 40, 43, 95, 113

CEI Coulomb explosion imaging. 4, 12–14, 69, 91, 116

CFD constant fraction discriminator. 35

CI conical intersection. 106

DAQ data acquisition. 35, 53, 59, 60

eKE electron kinetic energy. 112

EuXFEL European XFEL. 2, 3, 20, 45

FEL Free-electron laser. vii, 2–5, 7, 9, 12, 19–24, 26–32, 36, 38–41, 45–49, 52, 53, 55, 58–60, 63, 64, 67–70, 73, 86, 89–91, 93–96, 106–109, 111, 113, 115–117, 119, 120, 129, 132

FLASH Free-electron LASer in Hamburg. 2–4, 19–21, 27, 45–48, 53, 55, 58, 59, 115

FWHM full width at half maximum. 45, 46, 94

GENERiC Grand unifiEd reactioN microscopE souRce Code. 35

GMD gas monitor detector. 19, 27, 28, 38, 53, 70, 94, 120

Go4 GSI Object Oriented On-line Off-line system. 35, 59, 71

HHG high-harmonic generation. 3, 5, 7, 9, 29

HOMO highest occupied molecular orbital. 7

IP ionization potential. 97–99

KB Kirkpatrick–Baez. 38, 94

KE kinetic energy. 106

KER kinetic energy release. 13, 35, 69, 71–73, 75–78, 80, 81, 83, 85–87, 89–91

LAM Laser arrival monitor. 36, 46, 47, 49–55, 60, 115, 125

LCLS Linac Coherent Light Source. 2, 3, 20, 45

MCP Micro-channel plate. 31–33, 39, 40, 70, 95

MLO master laser oscillator. 47–50, 54, 123

MO main oscillator. 47, 48

MPI multiphoton ionization. 7

NIR near-infrared. viii, 4, 5, 7, 9, 46–50, 52–55, 58, 60–62, 64–70, 73–76, 80, 83, 84, 87, 89, 91, 94, 115, 119, 121, 122

NSI non-sequential ionization. 7

OPCPA optical parametric chirped-pulse amplification. 46, 47

PEC potential energy curve. 95, 98, 99

PES potential-energy surface. 70, 86

PImMS Pixel imaging mass spectrometry. 117

PIPICO photoion-photoion coincidence. 71, 72, 75, 76, 83, 85, 87

REMI reaction microscope. 4, 9, 19, 29–31, 35, 39, 46–49, 53, 54, 58–60, 67, 69–71, 73, 91, 115–117, 119–122, 124

RF radio frequency. 21, 46–48

SASE self-amplified spontaneous emission. 19–21, 24, 25, 27, 29, 46, 54, 55, 58, 60, 94, 114, 117

SFG sum frequency generation. 49, 50, 123, 124

SFI Strong-field ionization. 5, 7

SI sequential ionization. 7

TD-DFT time-dependent density functional theory. 95

TOF time-of-flight. 31, 32, 34–36, 57–61, 66, 67, 70, 71, 73, 75, 76, 83, 85, 95–97, 130

TOF-MS time-of-flight mass spectrometry. 19, 40, 58, 98, 106, 113, 121

TR-AMS time-resolved X-ray Auger-Meitner spectroscopy. 94, 107, 111, 112

TR-XPS time-resolved X-ray photoelectron spectroscopy. 94, 106, 107, 110

UV ultraviolet. 1, 4, 69, 93–111, 113, 129, 130

VMI velocity map imaging. viii, 4, 14, 19, 39–44, 94–97, 106, 111, 113–117, 129, 130, 132

XFEL X-ray free-electron laser. 2

XPS X-ray photoelectron spectroscopy. 106–108

XRD X-ray diffraction. 1

XUV extreme-ultraviolet. 2–4, 7, 20, 29, 45–48, 52–55, 57, 58, 60–70, 73–75, 80, 83, 84, 87, 91, 94–106, 108, 112, 113, 115, 117, 130

Chapter 1

Introduction

Direct observation of ultrafast processes in atomic and molecular systems is a central challenge in chemical physics [1, 2]. Fundamental phenomena such as electronic excitation, photoionization, charge migration, and nuclear rearrangement occur on timescales from femtoseconds ($1\,\mathrm{fs} = 10^{-15}\,\mathrm{s}$) to attoseconds ($1\,\mathrm{as} = 10^{-18}\,\mathrm{s}$) and involve structural changes [3] on the Ångström scale ($1\,\text{Å} = 10^{-10}\,\mathrm{m} = 0.1\,\mathrm{nm}$), comparable to the typical bond length of molecules. These processes govern chemical reactivity and energy flow in matter, yet many of the intermediate states that define reaction pathways are extremely short-lived and difficult to access experimentally. In atomic systems, ultrafast photoionization and electronic relaxation dominate, whereas in molecules, femtosecond dynamics are largely driven by nuclear motion on Born–Oppenheimer potential energy surfaces [4], including vibrational wave packet motion, bond dissociation, isomerization, and nonadiabatic transitions [5]. Although attosecond processes probe purely electronic motion [6] that precedes significant nuclear displacement, the present work focuses on femtosecond-scale relaxation processes in atomic xenon and on coupled electronic and nuclear dynamics in molecular systems. A detailed understanding of such processes requires experimental techniques that combine high temporal resolution with atomic-scale spatial sensitivity. Femtosecond pump–probe spectroscopy, particularly when employing short-wavelength radiation, provides both.

Traditional spectroscopic methods based on optical absorption, fluorescence, and photoemission have played a foundational role in establishing our understanding of atomic and molecular structure. However, steady-state measurements typically probe time-averaged observables and therefore offer only indirect information about the transient state [7, 8]. The development of ultrafast lasers in the 1980s gave rise to femtochemistry, a field pioneered by Ahmed Zewail, who was awarded the 1999 Nobel prize in Chemistry for demonstrating that chemical reactions can be observed in real time using femtosecond pump-probe techniques [9]. In these experiments, a short pump pulse initiates a reaction, and a delayed probe pulse tracks the evolving system, enabling direct observation of vibrational wave-packet motion and bond rearrangement.

Despite this breakthrough, optical pump–probe methods have intrinsic limitations. The duration of few-cycle ultraviolet (UV) pulses is constrained by the optical period (≈ 1 fs at 300 nm) and by the large spectral bandwidth required for ultrashort pulses, which complicates selective excitation. In addition, optical wavelengths are much larger than interatomic distances, limiting spatial resolution and element specificity. Consequently, purely optical probes are not well suited for localized, atom-specific tracking of structural dynamics, particularly in complex molecular systems.

Since the discovery of X-rays by Wilhelm Röntgen in 1895, they have served as a uniquely powerful probe of matter at the atomic scale [10]. Early applications focused on radiographic imaging, which rapidly transformed medical diagnostics [11]. A major conceptual breakthrough followed with the discovery of X-ray diffraction (XRD) by Max

von Laue et al.[12] and the subsequent development of crystallographic methods by William Lawrence Bragg and William Henry Bragg. X-ray crystallography established a direct link between diffraction patterns and atomic structure, enabling the determination of crystal lattice and, later, complex biological macromolecules such as DNA [13]. These achievements demonstrated the exceptional capability of X-rays to resolve atomic arrangements in matter.

In parallel with diffraction-based methods, X-ray spectroscopic techniques have become an indispensable tool for probing electronic structure and chemical composition. Photoelectron spectroscopy [14] and Auger-Meitner (AM) electron spectroscopy provide site-and shell-specific information about atoms in isolated systems as well as in condensed matter phases [15]. Because core-level energies are strongly element-dependent, these methods enable chemical-selective investigation of local bonding environments and charge distributions. Such capabilities make X-rays particularly attractive for time-resolved studies that require element specificity and local sensitivity.

1.1 Evolution of X-ray Sources

The impact of X-ray science has been closely tied to the development of increasingly advanced radiation sources, as illustrated in Fig. 1.1, which compares the peak spectral brilliance of storage-ring synchrotrons and X-ray free-electron lasers (XFELs). Early X-ray tubes were limited in brightness, coherence, and temporal structure, restricting the scope of possible experiments. A major advance occurred with the development of accelerator-based synchrotron radiation sources in the mid-twentieth century [16]. Originally developed for high-energy physics, synchrotrons produce intense, highly collimated, and tunable photon beams with substantial spatial coherence. These properties revolutionized X-ray science and enabled a broad spectrum of applications in physics, chemistry, biology, and materials research. Nevertheless, the pulse durations available at synchrotron facilities are typically in the 10-100 ps regime [17]. While their brightness enables high-resolution spectroscopic studies, the accessible peak intensities generally limit investigations of nonlinear ultrafast dynamics.

The demand for shorter, brighter, and more coherent X-ray pulses motivated the development of FEL. First proposed in the early 1970s [20] and initially demonstrated at infrared wavelengths, FEL concepts were progressively extended towards shorter wavelengths. The realization of XFELs in the early twenty-first century marked the emergence of a new class of light sources capable of delivering femtosecond, ultra-intense, and highly coherent X-ray pulses. Early facilities such as FLASH operated in the extreme-ultraviolet (XUV) regime, whereas subsequent XFELs, including the LCLS and EuXFEL, extended these capabilities into the soft and hard X-ray spectral ranges. Hard X-ray FELs combine the tunability characteristic of synchrotron radiation with laser-like temporal coherence and peak brilliance several orders of magnitude higher than previous light sources. These properties enable experiments that were previously inaccessible, including nonlinear X-ray interactions with atoms and molecules [21] and single-shot imaging [22].

FLASH occupies a central position in the development of ultrafast X-ray science as one of the first user facilities to provide intense femtosecond pulses in the XUV and soft X-ray range. Its radiation characteristics—high peak intensity, short pulse duration, and improved synchronization—make it well suited for pump–probe spectroscopy. In such experiments, an initial pump pulse excites or ionizes a system, while a time-delayed probe pulse records its subsequent evolution. By scanning the relative delay between these pulses, dynamical processes can be reconstructed with femtosecond resolution. When applied to gas-phase targets, where interactions with surrounding media are minimized, pump–probe techniques enable precise investigation of intrinsic atomic and molecular dynamics.

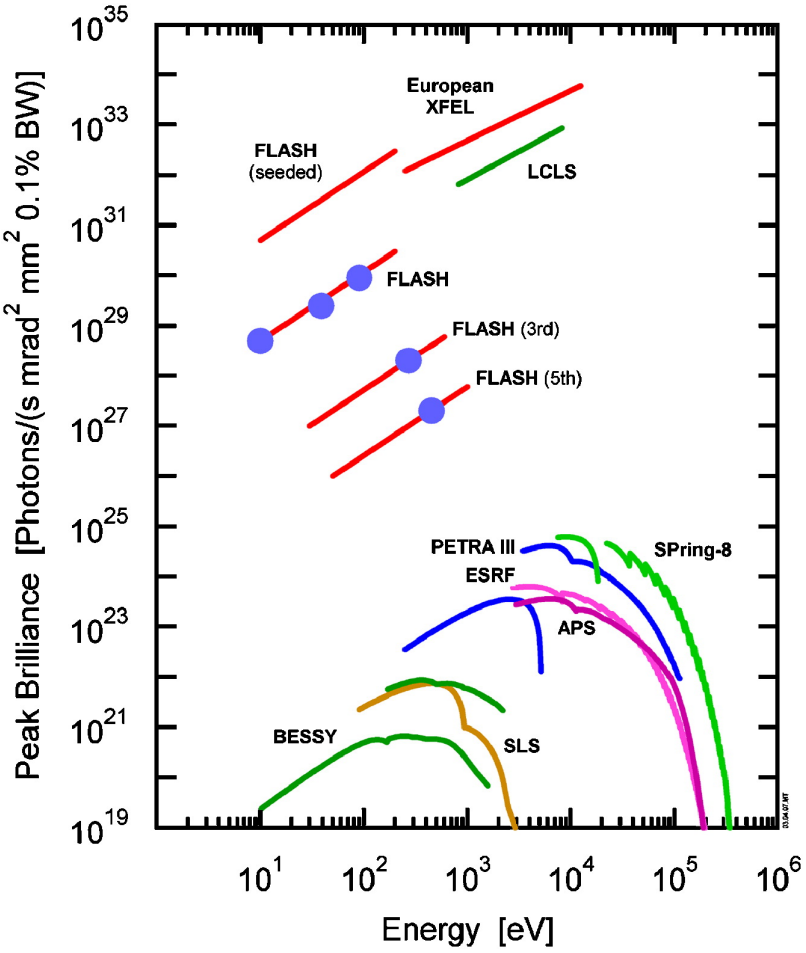

Figure 1.1: Peak spectral brilliance versus photon energy for selected synchrotron radiation sources and FELs. FEL facilities (Free-electron LASer in Hamburg (FLASH), Linac Coherent Light Source (LCLS), European XFEL (EuXFEL)) exceed storage-ring sources (BESSY, SLS, ESRF, APS, PETRA III, SPring-8) by several orders of magnitude in peak brilliance across the VUV to hard X-ray range. Red lines indicate theoretical performance prediction for FEL sources; blue dots represent experimentally measured peak brilliance values at FLASH. Adapted from Ref. [18, 19]

Although high-harmonic generation (HHG) [23] based XUV sources were established well before the first FEL facilities, the advent of FELs has positioned these two light sources as complementary tools for ultrafast science. FELs provide high-brightness, short-wavelength radiation at large-scale user facilities, whereas modern tabletop HHG sources deliver initially synchronized femtosecond-to-attosecond pulses, ideally suited to study electron dynamics. With mid-infrared driving-laser technologies and optimized phase-matching conditions, HHG photon energies now extend into the water window [24], and isolated pulses as short as 53 as [25] have been demonstrated. These capabilities enable element- and site-specific probing of electronic and nuclear motion, direct access to inner-shell excitation, and investigation of multiphoton interactions. Experimental approaches, including time-resolved photoelectron spectroscopy, single- and multiphoton ionization studies, and fragmentation measurements, provide detailed insight into excitation pathways and subsequent dynamical evolution.

Within this broader context, femtosecond pump-probe spectroscopy at FLASH offers a versatile platform for investigating fundamental processes in gas-phase atomic and molecular systems. FLASH facility has played a pioneering role in establishing ultrafast X-ray science. One of its earliest and most significant achievements was the demonstration of single-shot coherent diffractive imaging of nanoscale particles and biological samples, providing the first

proof of structure determination without crystallization [22]. In parallel, FLASH enabled studies of few-photon and multi-electron dynamics in atoms and molecules. Its intense femtosecond pulses in the XUV and soft X-ray range, combined with flexible pump–probe capabilities, make it an ideal platform for investigating ultrafast processes in isolated gas-phase systems.

1.2 Objectives and Structure of the Thesis

The objective of this thesis is to advance femtosecond pump–probe spectroscopy of gas-phase atomic and molecular systems using the FEL FLASH by achieving high temporal resolution with long-term stability and applying it to the investigation of ultrafast electronic relaxation and structural dynamics. A central goal is to improve synchronization between the FEL pulses and the external optical pump-probe laser at the FL26 beamline. Because arrival-time jitter of the external laser and long-term timing drift limit the achievable overall time resolution in pump–probe experiments, an optical arrival-time monitor is implemented to actively stabilize the timing of the NIR and to measure the jitter relative to the FEL master clock. This approach enables sub-50 fs (FWHM) temporal resolution, as demonstrated by benchmark measurements of xenon photoionization.

After improving the temporal resolution, the first scientific study investigates the relaxation processes in atomic xenon following core ionization of the $4d$ and $4p$ subshells by extreme ultraviolet pulses. Using ion time-of-flight spectroscopy and a two-color XUV pump–NIR probe scheme, the dynamics near the giant resonance and the Cooper minimum are compared. Signatures of sequential two-photon absorption followed by AM decay are identified, and the lifetimes of transient excited states are extracted.

The second part of the thesis extends these methods to small molecular systems by examining the fragmentation dynamics of CO_2 and CS_2 using time-resolved Coulomb explosion imaging (CEI) with a reaction microscope (REMI). High-energy photons at 90 eV from FEL pulses create triply charged molecular states in CO_2 and CS_2, which dissociate via multiple pathways and are probed by the NIR pulse. Coincidence measurements with three-dimensional momentum imaging allow determination of fragment charge states, kinetic energies, and emission angles, revealing how atomic substitution influences ultrafast fragmentation dynamics.

Finally, time-resolved pump–probe spectroscopy is applied to the larger molecule 1-butanethiol to elucidate UV-induced fragmentation dynamics. An UV pump pulse excites the molecule, and a time-delayed soft X-ray FEL pulse probes the excited-state evolution. Ion and electron VMI are recorded, enabling correlated analysis of fragmentation pathways. Element-specific probing of the sulfur (2p) core levels provides site-sensitive insight into electronic and nuclear dynamics and their connection to molecular fragmentation.

The thesis is organized as follows. Chapter 2 introduces the theoretical background of atom–laser and molecule–laser interactions, atomic decay processes, CEI in molecules, and the models used to analyze pump–probe data. Chapter 3 describes the principles of FEL and the two atomic, molecular, and optical physics (AMO) beamlines used in this work, including the REMI, the FL26 beamline, and the CAMP endstation at the FL11 beamline, formerly known as BL1. Chapter 4 presents the methods developed to improve the time resolution at FLASH2, including measurements and stabilization of timing jitter and drift in the pump–probe system. Chapter 5 focuses on xenon photoionization following 4d ionization and near the Cooper minimum at 160 eV. Chapter 6 discusses Coulomb explosion imaging of CO_2 and CS_2. Chapter 7 presents time-resolved UV-induced fragmentation dynamics of 1-butanethiol. Chapter 8 summarizes the thesis' main findings and offers an outlook on future experiments in ultrafast X-ray science.

Chapter 2

Theoretical Background

This chapter presents the theoretical background necessary for understanding the experimental results discussed in this thesis. It introduces the fundamental concepts of atomic and molecular photoionization and outlines the interaction of intense ultrafast laser fields with matter. The chapter begins with a discussion of photoionization theory, followed by separate treatments of valence-shell and core-shell ionization processes. The principles of Coulomb explosion imaging are then described as a structural probing technique. Finally, the chapter concludes with a detailed presentation of the fitting procedure used to analyze the pump–probe experimental data.

2.1 Interaction of Photons with Atoms and Molecules

Photoionization occurs when an atom absorbs electromagnetic radiation and an electron acquires sufficient energy to escape. This can occur via the absorption of a single high-energy photon or multiple lower-energy photons. The electron transitions from a bound state to a free (continuum) state, thereby ionizing the atom.

In molecules, removing an electron can also break chemical bonds, causing photodissociation. The ejected electron and resulting ion or fragments contain information about the system's original state.

Following the invention of the laser, multiphoton processes enabled ionization of atoms using multiple low-energy photons. Later, synchrotrons and FELs source enabled multiple ionization with X-rays. HHG sources provide an additional means of achieving ionization via high-energy photons generated by laser-driven harmonic conversion.

2.1.1 Strong-Field Ionization

Strong-field ionization (SFI) refers to the removal of valence electrons from atoms or molecules by intense ultrashort laser pulses. Typically, such laser fields have pulse durations on the order of tens of femtoseconds and intensities in the range of 10^{13}–10^{14} W/cm^2, most commonly in the NIR spectral region [26]. Under these conditions, the laser electric field becomes comparable to the Coulomb field binding the valence electron, and the pulse duration is comparable to the characteristic timescales of nuclear motion, thereby influencing strong-field ionization and molecular dissociation dynamics [27, 28].

When an external oscillating laser electric field interacts with an atomic or molecular system, the valence electron density is displaced along the field's polarization direction. This displacement leads to a time-dependent deformation of the Coulomb potential, such that the electron experiences the combined influence of the ionic core and the laser field as depicted

in Fig. 2.1 [29]. Depending on the laser intensity and pulse duration, the resulting degree of potential distortion determines which ionization pathways become accessible [30, 31].

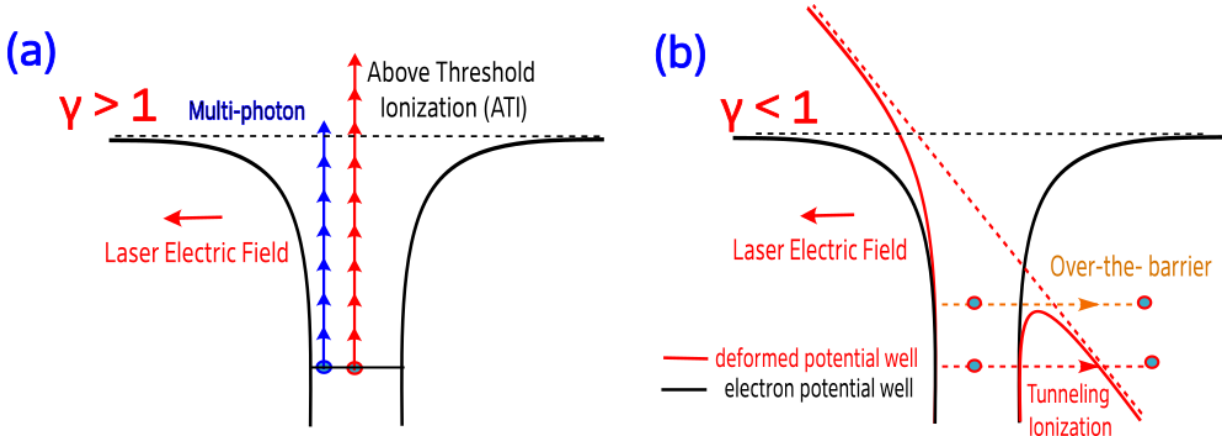

Figure 2.1: Photoionization processes in atomic and molecular systems. (a) Multiphoton ionization and above-threshold ionization (ATI) regime ($\gamma \gg 1$). (b) Schematic representation of strong-field photoionization for $\gamma \ll 1$, illustrating tunnel ionization and over-the-barrier ionization.

Fig. 2.1 shows two different ionization schemes, multiphoton ionization and tunneling ionization. The ionization regime depends on the target's ionization threshold and the laser intensity. In the multiphoton ionization regime, electrons absorb multiple photons simultaneously and acquire sufficient energy to escape into the continuum. If more photons are absorbed than the minimum number required for ionization, the process is referred to as ATI [32, 33]. In the tunneling regime, the strong laser field suppresses the Coulomb barrier to such an extent that a narrow potential barrier is formed, through which the electron can tunnel quantum mechanically into the continuum [34].

The dominant ionization regime of an atomic or molecular system is commonly characterized by the Keldysh parameter γ, which relates the ionization potential I_p of the target to the ponderomotive potential U_p of an electron oscillating in the laser field [35].

The Keldysh parameter is defined as

$$\gamma = \sqrt{\frac{I_p}{2U_p}} \tag{2.1}$$

where I_p is the ionization potential and U_p is the ponderomotive potential, i.e., the cycle-averaged quiver energy of a free electron in an oscillating electric field.

The ponderomotive potential is given by

$$U_p = \frac{e^2 E_0^2}{4 m_e \omega^2} \tag{2.2}$$

where e is the elementary charge, E_0 is the peak electric field amplitude of the laser, m_e is the electron mass, and ω is the angular frequency of the laser field. The electric field amplitude is related to the laser intensity I by

$$E_0 = \sqrt{\frac{2I}{c\epsilon_0}} \tag{2.3}$$

with c denoting the speed of light and ϵ_0 the vacuum permittivity. Substituting this relation into the expression for U_p yields

$$U_p = \frac{e^2}{4m_e\omega^2}\frac{2I}{c\epsilon_0}. \tag{2.4}$$

Expressed in practical units, the ponderomotive potential can be written as

$$U_p\,[\mathrm{eV}] = 9.338 \times 10^{-20}\, I\,[\mathrm{W/cm^2}]\,\lambda^2\,[\mathrm{nm}] \tag{2.5}$$

Considering xenon ($I_p = 12.13$ eV) interacting with NIR radiation ($\lambda = 800$ nm) and XUV radiation ($\lambda = 13.7$ nm, $h\nu = 90$ eV) at an intensity of 10^{14} W/cm^2, the ponderomotive energy is $U_p^{\mathrm{IR}} \approx 6$ eV in the NIR, but only $U_p^{\mathrm{XUV}} \approx 10^{-4}$ eV in the XUV. This shows that the NIR field strongly drives electron quiver motion and distorts the atomic potential, whereas the XUV interaction remains perturbative.

Once an electron is removed from the parent atom or molecule, the oscillating laser field can drive it back toward the ion, a process known as recollision [36]. In HHG, the maximum photon energy is given by

$$E_{\mathrm{cutoff}} = I_p + 3.17\,U_p \tag{2.6}$$

where I_p is the ionization potential and U_p is the ponderomotive energy of the electron in the laser field. This relation follows from the semiclassical three-step model, where the factor 3.17 represents the maximum kinetic energy an electron can gain before recombining with the parent ion [37].

In molecular systems, SFI is further influenced by molecular orientation and orbital symmetry [38]. Although ionization often occurs from the highest occupied molecular orbital (HOMO), lower-lying orbitals can contribute significantly when their spatial orientation enhances their coupling to the external field. This orbital selectivity provides valuable insight into molecular electronic structure and dynamics [39, 40].

Multiphoton Ionization

Multiphoton ionization (MPI) occurs when an atom or molecule absorbs multiple photons in a single laser pulse to overcome its ionization potential I_p. When driven by NIR laser fields at moderate intensities, MPI can be described within perturbation theory [30]. In this regime, the n-photon absorption probability scales as

$$\Gamma_n = \sigma_n I^n, \tag{2.7}$$

where σ_n is the n-photon ionization cross section and I is the laser intensity.

Two distinct MPI pathways can be distinguished: sequential ionization (SI) and non-sequential ionization (NSI). In SI, ionization proceeds stepwise through the absorption of single photons via real intermediate ionic states. In contrast, NSI involves the correlated absorption of multiple photons through virtual intermediate states, leading to the simultaneous removal of more than one electron. As illustrated in Fig. 2.2, both channels can be energetically allowed; however, their relative importance depends on the photon energy and laser intensity.

In synchrotron-based experiments, the comparatively low photon flux typically limits the interaction to single-photon absorption per atom within a pulse [41]. In contrast, experiments employing high-intensity FEL pulses can reach photon fluxes sufficiently high that both SI and NSI become accessible.

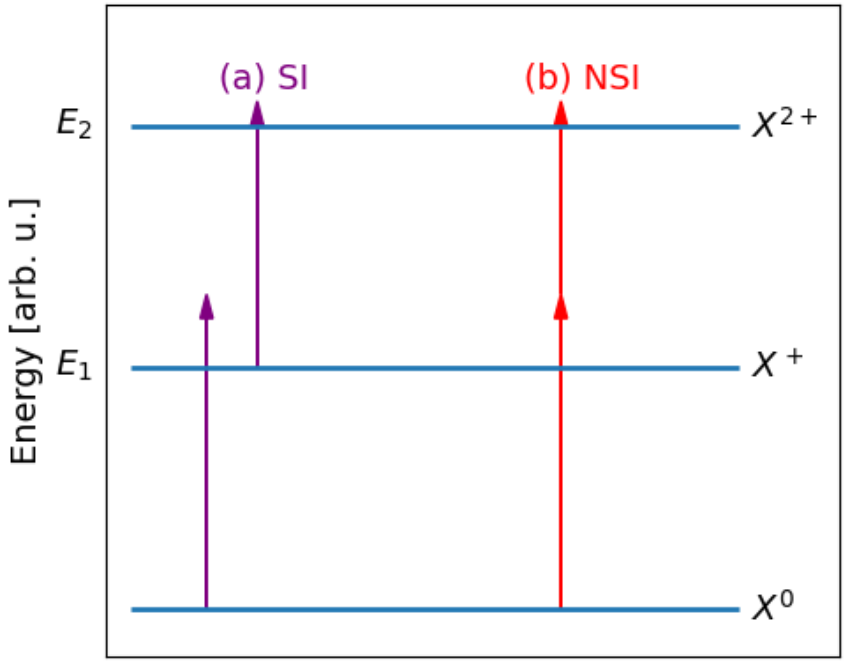

Figure 2.2: Multiphoton ionization of an atom X: (a) sequential ionization (SI) and (b) non-sequential ionization (NSI).

Above-Threshold Ionization (ATI)

ATI is an extension of multiphoton ionization in which atoms or molecules absorb more photons than the minimum number required to exceed the ionization threshold. The excess photon energy is transferred to the liberated electron as kinetic energy, resulting in a series of discrete peaks in the photoelectron spectrum separated by the photon energy $h\nu$, as illustrated in Fig. 2.3.

The ATI ionization rate can be written as

$$\Gamma_{n+s} = \sigma_{n+s} I^{n+s}, \tag{2.8}$$

where Γ_{n+s} represents the partial ionization rate for the ATI channel involving the absorption of $n+s$ photons, σ_{n+s} is the corresponding multiphoton ionization cross section, and s denotes the number of excess photons absorbed beyond the minimum requirement. Each ATI channel corresponds to a distinct peak in the photoelectron spectrum.

The kinetic energy of the emitted electron is given by

$$E_k = (n+s)\hbar\omega - I_p - U_p, \tag{2.9}$$

where I_p is the ionization potential and U_p is the ponderomotive potential, which accounts for the average quiver motion of the electron in the oscillating laser field.

Tunneling Ionization

In the strong-field regime, the laser field substantially distorts the Coulomb potential, reducing and narrowing the potential barrier, thereby enabling electron emission via tunneling even when the photon energy is below the ionization potential. This process, known as tunneling ionization, dominates in the regime where the Keldysh parameter satisfies $\gamma \ll 1$.

A closely related mechanism is over-the-barrier ionization (OBI), in which the laser field completely suppresses the Coulomb barrier, allowing electrons to escape directly rather than

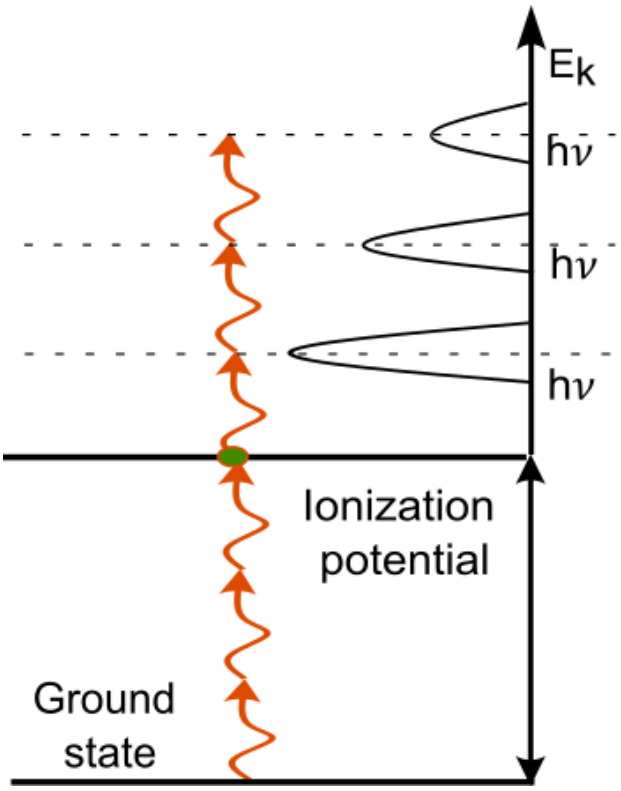

Figure 2.3: Schematic illustration of ATI. Absorption of additional photons beyond the ionization threshold produces a series of photoelectron peaks separated by the photon energy.

tunnel. Both tunneling ionization and OBI are inherently quantum-mechanical processes and cannot be explained within a purely classical framework.

The tunneling ionization rate can be described by the Ammosov–Delone–Krainov (ADK) theory, which provides the probability per unit time for electron emission [34]. In a simplified form, the width of the ion momentum distribution along the laser polarization is given by

$$\Gamma(p_{\parallel}) = A \exp\left[-\frac{(p_{\parallel} - p_0)^2 \omega^2 (2I_p)^{3/2}}{3I^{3/2}}\right], \tag{2.10}$$

where $p_{\parallel}$ is the ion momentum parallel to the laser polarization, p_0 is the central momentum, I_p is the ionization potential, I is the laser intensity, ω is the laser angular frequency, and A is a normalization constant. The ADK approach can be used to estimate the intensity of the NIR laser. During the experiment at REMI, the peak intensity at the target was estimated by measuring the argon charge-state ratio, as described in Appendix A.

2.1.2 Core Ionization

When photons of sufficiently high energy interact with atoms or molecules, inner-shell (core) electrons can be ionized by absorption of a single photon. Compared to valence-shell ionization, core ionization requires significantly higher photon energies, typically from a few tens to several hundreds of electron volts. For example, sulfur $2p$ ionization occurs near 170 eV, while xenon $4d$ ionization occurs near 90 eV; these photon energies are readily accessible at FELs and synchrotron facilities (see Fig. 1.1), and more recently with HHG.

The photoionization cross section decreases with increasing photon energy, except near shell-specific ionization thresholds, where pronounced absorption edges appear. These edges are characteristic of specific elements and electronic shells, such as the sulfur $2p$ and $2s$ edges and the carbon $1s$ edge shown in Fig. 2.4.

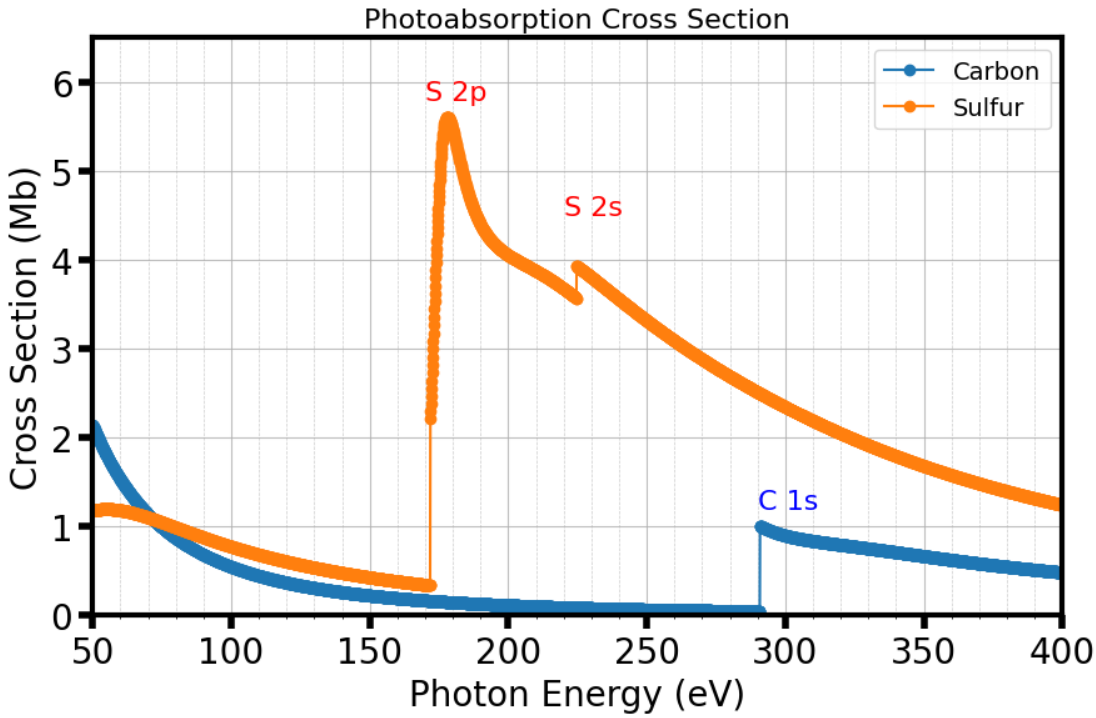

Figure 2.4: Total photoabsorption cross sections of atomic sulfur and carbon calculated with XATOM (XRAYPAC) [42]. Sulfur $2p$ and $2s$ thresholds appear near 170 eV and 230 eV, respectively, while the carbon $1s$ edge is near 290 eV.

Decay Processes

Ionization of a core-level electron leaves the atom or molecule in a highly excited state with a vacancy in the inner electronic shell. Such a configuration is intrinsically unstable, and relaxation proceeds through various decay pathways that redistribute the excess energy either radiatively or non-radiatively. The dominant decay channel depends strongly on the atomic number, the shell involved, and the available final states.

Fluorescence Decay

In fluorescence decay, a higher-lying electron fills a core hole, and the excess energy is emitted as an X-ray photon, as illustrated in Fig. 2.5 (a).

$$h\nu = E_i - E_f \tag{2.11}$$

Here, E_i and E_f denote the total electronic energies of the atom in the initial core-hole state and the final relaxed state after radiative decay, respectively.

The fluorescence yield increases with atomic number due to higher radiative transition rates. For elements such as sulfur and xenon, the AM decay process dominates.

Auger-Meitner Decay

AM decay is a non-radiative relaxation process following core ionization, in which the energy released by filling a core hole is transferred to another electron, causing its emission.

AM transitions are labeled by the shell containing the initial vacancy, followed by the shells of the electron filling the vacancy and the emitted electron. An example of a KLL AM transition is shown in Fig. 2.5(b). In this case, an electron from the L_1 shell fills the K-shell vacancy, while an electron from the L_2 shell is emitted.

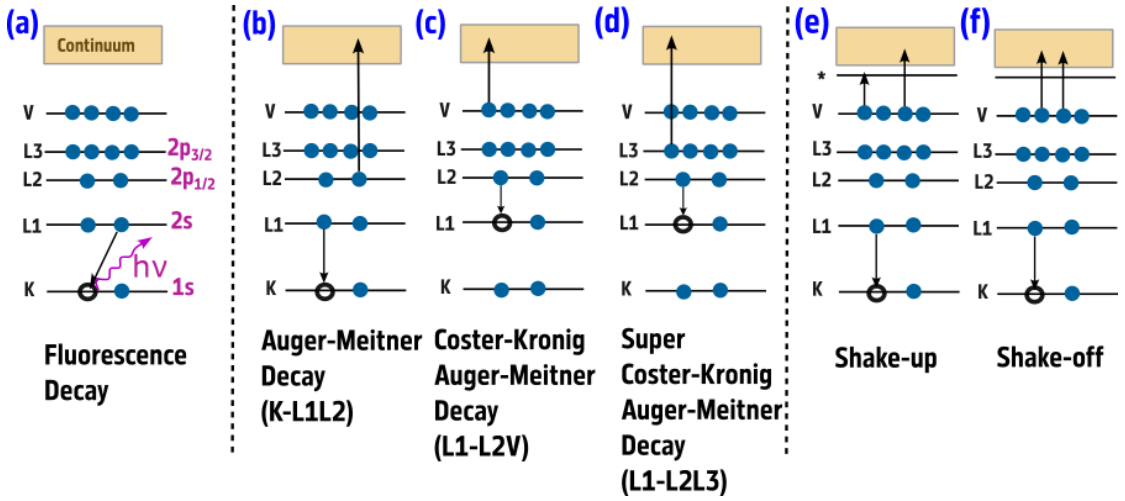

Figure 2.5: Schematic overview of the de-excitation pathways following the creation of an inner-shell vacancy in an atom. The primary relaxation mechanisms, fluorescence emission and Auger–Meitner decay, are shown. In addition, higher-order ionization processes accompanying the sudden creation of the core hole, including shake-up excitation and shake-off ionization of outer-shell electrons, are illustrated.

The kinetic energy of the emitted electron is given by

$$E_{\text{kin}} = E_K - E_{L1} - E_{L2} - \Delta, \tag{2.12}$$

where E_K, E_{L1}, and E_{L2} are the binding energies of the respective shells, and Δ accounts for electronic relaxation and Coulomb interaction in the final doubly ionized state.

If part of the excess energy is transferred to excite an additional outer-shell electron rather than being fully converted into kinetic energy, the process is referred to as a satellite AM transition. When the available energy is sufficient to eject two electrons simultaneously, the process is known as double AM decay.

If the electron filling the inner-shell vacancy originates from the same shell as the initial vacancy, while the emitted electron comes from an outer shell, the process is referred to as Coster–Kronig decay, for example, the LLM transition shown in Fig. 2.5 (c). If the emitted electron also originates from the same shell, the process is called super Coster–Kronig decay, as in the LLL transition shown in Fig. 2.5 (d).

Shake-Up and Shake-Off Processes

When a core electron is suddenly removed, the effective potential experienced by the remaining electrons changes abruptly, which can induce additional electronic excitations. In a shake-up process, a valence electron is promoted to a higher unoccupied orbital, whereas in a shake-off process, an electron is ejected into the continuum, resulting in double ionization (see Fig. 2.5 (d) and (f)).

In photoelectron spectra, shake-up and shake-off processes appear as satellite peaks shifted towards higher binding energies relative to the main core-level line.

2.2 Coulomb Explosion Imaging

A central goal of ultrafast molecular science is to construct time-resolved “molecular movies” that visualize atomic motion during chemical reactions. Because reactions proceed through short-lived intermediate geometries on femtosecond timescales, direct structural mapping of

transient configurations, such as isomerization [43] and hydrogen migration [44], is essential to resolve the underlying reaction mechanisms. CEI addresses this challenge by converting the instantaneous molecular geometry into measurable fragment momenta.

CEI can be realized with any ionization source that produces rapid multiple ionization on a timescale shorter than nuclear motion. Implementations include few-cycle femtosecond lasers, FELs, energetic ion beams, and electron-impact ionization. Despite differences in the ionization mechanism, all approaches rely on the same principle: sudden multiple ionization projects the molecule onto a repulsive Coulomb potential energy surface, and the resulting fragment momenta encode the initial geometry.

In pump–probe CEI (Fig. 2.6), a pump pulse prepares an ionized electronic state and initiates nuclear dynamics. After a delay Δt, a probe pulse removes additional electrons, thereby projecting the molecule onto a repulsive Coulomb potential. Under the frozen-nuclei approximation, the geometry is assumed unchanged during ionization. The charged fragments then separate under Coulomb repulsion, converting electrostatic potential energy into kinetic energy. Coincident detection of all fragments and reconstruction of their three-dimensional momentum vectors yield the molecular geometry at the probe time. Repeating the measurement for different delays provides time-resolved structural snapshots.

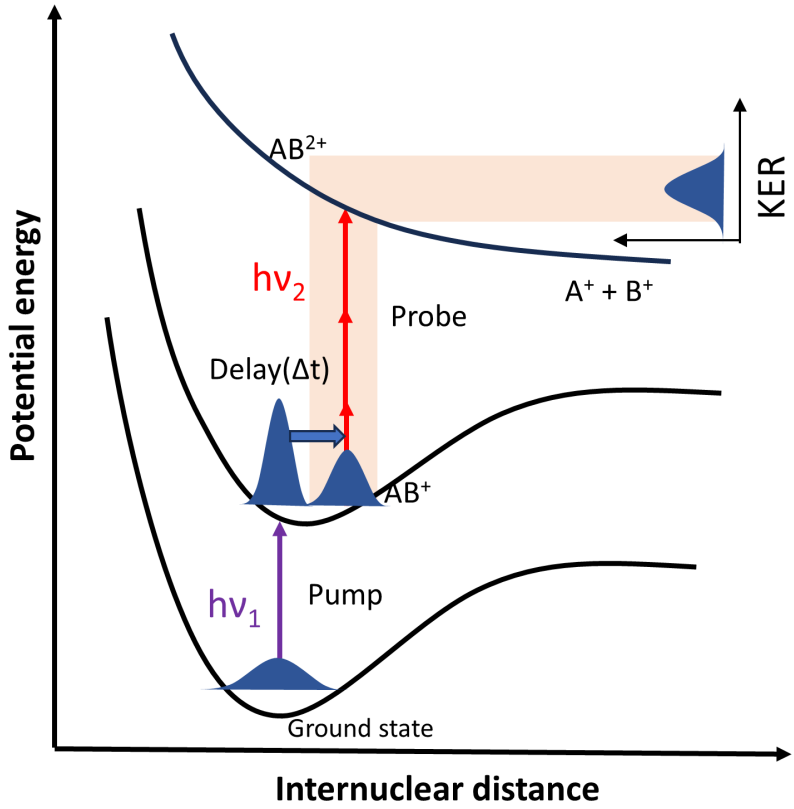

Figure 2.6: Schematic illustration of pump–probe Coulomb explosion imaging. A pump pulse prepares a neutral AB molecule from a singly ionized state AB^+. After a controlled delay, a probe pulse further ionizes the molecule to the dissociative state AB^{2+}, projecting it onto a repulsive Coulomb potential-energy surface. The molecule subsequently dissociates along the Coulomb curve, and the measured fragment momenta and kinetic energy release encode the internuclear separation, and thus the molecular geometry, at the probe time.

2.2.1 Principles of Coulomb Explosion Imaging

The theoretical description of CEI follows from energy and momentum conservation. For a diatomic molecule, sudden ionization produces two fragments with charges q_1 and q_2 separated by an initial distance R_0. The resulting Coulomb repulsion drives rapid fragmentation. The interaction potential between fragments i and j separated by R_{ij} is given by the Coulomb potential,

$$V_{ij}(R_{ij}) = \frac{1}{4\pi\epsilon_0}\frac{q_i q_j}{R_{ij}}, \tag{2.13}$$

where q_i and q_j denote the fragment charges, R_{ij} is the internuclear separation, and ϵ_0 is the permittivity.

As the fragments separate, this potential energy is converted into kinetic energy release (KER). In the center-of-mass frame, momentum conservation requires

$$m_1 v_1 = m_2 v_2, \tag{2.14}$$

and using the reduced mass $\mu = m_1 m_2/(m_1 + m_2)$, the KER is

$$\mathrm{KER} = \frac{1}{2}\mu v_{\mathrm{rel}}^2. \tag{2.15}$$

These relations establish a direct mapping between measured fragment velocities and initial internuclear separations. Since experiments measure velocity distributions rather than distances, the probability density functions in real space and velocity space are related by conservation of probability,

$$P(v)\,dv = P(R)\,dR, \tag{2.16}$$

where $P(R)$ represents the probability density of the initial internuclear separation at the moment of ionization, and $P(v)$ represents the probability density of the measured relative fragment velocity following Coulomb explosion.

Using the velocity–distance relation derived from Coulomb repulsion, the velocity distribution can be expressed as

$$P(v) = \sqrt{\frac{q_1 q_2}{2\mu}}\, R^{-3/2} P(R), \tag{2.17}$$

which provides a direct connection between the experimentally measured velocity distribution and the initial molecular structure.

For polyatomic molecules, multiple charged fragments interact simultaneously. The total Coulomb potential is the sum of all pairwise interactions,

$$V = \sum_{i<j} \frac{1}{4\pi\epsilon_0}\frac{q_i q_j}{r_{ij}}. \tag{2.18}$$

By measuring all fragment momenta in coincidence and using classical Coulomb dynamics, the initial molecular geometry can be reconstructed. This framework is valid when ionization occurs much faster than nuclear motion, fragment charges remain approximately constant, and external forces are negligible. While these conditions are reasonably well satisfied for CEI using ∼10 fs pulses, they are not strictly fulfilled. Nuclear motion can begin during ionization, particularly for light atoms such as hydrogen, and sequential ionization may alter fragment charge states during dissociation. These effects introduce deviations from the ideal Coulomb explosion model and limit the accuracy of the reconstructed geometry.

In addition, CEI becomes increasingly challenging for larger molecules, as complete reconstruction requires detecting all fragments in coincidence, and the multi-fold coincidence yield decreases with size. Achieving sufficient ionization of all atomic sites also becomes more difficult in larger systems, making short pulses essential to ensure rapid ionization before significant nuclear motion occurs. Consequently, smaller and lighter molecules are generally more favorable for accurate structural reconstruction using CEI.

2.3 Pump–Probe Model and Fitting Procedure

The pump–probe measurement principle is illustrated schematically in Fig. 2.6. In a pump–probe experiment, an initial pump pulse excites the atomic or molecular system and initiates electronic and/or nuclear dynamics. A time-delayed probe pulse subsequently interrogates the evolving state. By varying the delay between the two pulses and recording observables such as transient absorption or ion and electron yields, the temporal evolution of the system can be reconstructed. In this work, ion and electron signals are recorded using VMI or coincidence measurements as a function of the pump-probe delay.

The pump–probe delay defines three characteristic temporal regimes, as illustrated in Fig. 2.7.

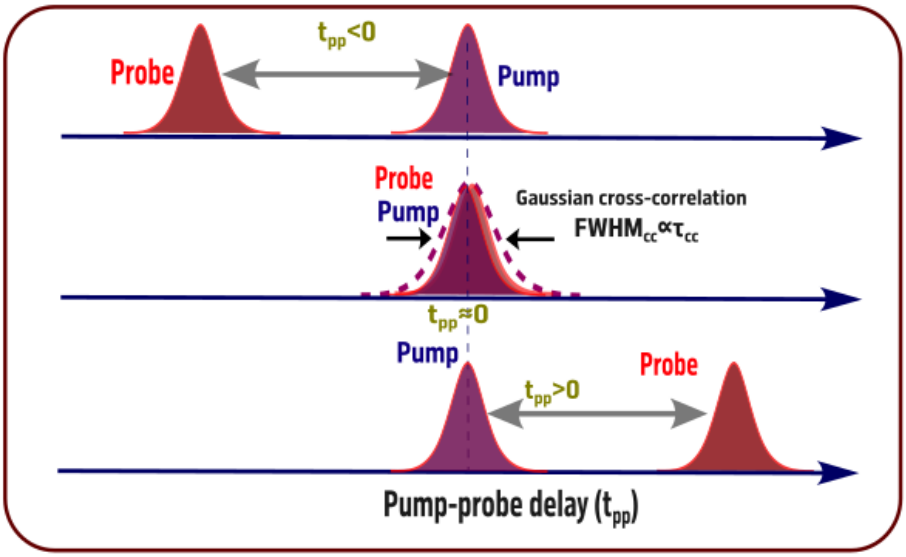

Figure 2.7: Schematic representation of the pump–probe delay. Negative delay corresponds to the probe pulse arriving before the pump pulse, temporal overlap indicates simultaneous interaction, and positive delay corresponds to the probe pulse arriving after the pump pulse.

- **Negative delays** ($t_{pp} < 0$)**:** The probe pulse arrives before the pump and interacts with the system in its ground state. The measured signal serves as a baseline reference that is independent of pump-induced excitation.
- **Temporal overlap** ($t_{pp} \approx 0$)**:** The pump and probe pulses overlap in time. The measured response is governed by their cross-correlation and determines the experiment's effective temporal resolution.
- **Positive delays** ($t_{pp} > 0$)**:** The pump pulse prepares an excited state, and the probe interrogates the system after a controlled evolution time. The delay-dependent signal reflects the relaxation and decay dynamics of the excited-state population.

2.3.1 Pump–Probe Fitting Model

Model Assumptions

Consider an idealized pump–probe experiment in which both pump and probe pulses are infinitely short in time (delta-like). Each pulse instantaneously transforms the atomic or molecular system, and the measured signal depends only on the pump–probe delay t_{pp}. The system dynamics are described using simple photochemical reaction schemes and first-order kinetics, which provide a reasonable approximation for gas-phase ultrafast experiments [45, 46].

Step-Like Model: Long-Lived Excited State

The first model describes the formation of a long-lived excited state whose lifetime greatly exceeds the experimental time window. In the delta-pulse limit, the intrinsic response is represented by a Heaviside step function.

Reaction scheme

$$\begin{cases} \mathrm{M} \xrightarrow{\text{pump}} \mathrm{A}, \\ \mathrm{A} \xrightarrow{\text{probe}} \mathrm{B} \end{cases} \tag{2.19}$$

If the probe arrives before the pump ($t_{pp} < 0$), no product B is formed. For $t_{pp} \geq 0$, the probe converts a fraction of the excited-state population into the observable product, resulting in a step-like increase in the signal. The response function is therefore written as

$$f(t_{pp}) = f_0 + f_1\,\theta(t_{pp}), \tag{2.20}$$

where $\theta(t)$ is the Heaviside step function defined as

$$\theta(t) = \begin{cases} 0, & t_{pp} < 0, \\ 1, & t_{pp} \geq 0. \end{cases} \tag{2.21}$$

This model describes a population created by the pump pulse that remains constant during the probe interaction.

Transient Model: Exponential Decay of a Metastable State

The second model describes a metastable state created by the pump pulse that decays exponentially with decay rate constant k_r.

Reaction scheme

$$\begin{aligned} \mathrm{M} + \text{pump} &\longrightarrow \mathrm{A}^* \\ \mathrm{A}^* &\xrightarrow{k_r} \mathrm{C} \\ \mathrm{A}^* + \text{probe} &\longrightarrow \mathrm{B} \end{aligned} \tag{2.22}$$

The population of the metastable intermediate follows first-order decay kinetics [45],

$$[\mathrm{A}^*](t) = [\mathrm{A}^*]_0 \exp\left(-\frac{t}{\tau_r}\right), \tag{2.23}$$

where $\tau_r = \frac{1}{k_r}$ is the relaxation time constant and $[\mathrm{A}^*]_0$ is the initial population created by the pump pulse.

The corresponding pump–probe delay-dependent signal is

$$f(t_{pp}) = f_0 + f_1\,\theta(t_{pp})\exp\left(-\frac{t_{pp}}{\tau_r}\right), \tag{2.24}$$

which reflects the exponential decay of the metastable intermediate population probed as a function of delay time.

Transient-Limited Model: Instantaneous Dynamics

The third model applies when the intrinsic system dynamics are much faster than the experimental time resolution. In this case, the response can be approximated by a Dirac delta function.

Reaction scheme

$$\mathrm{M} \xrightarrow{\text{pump+probe}} \mathrm{A} \tag{2.25}$$

The signal is localized at zero delay and is given by

$$f(t_{pp}) = f_0\,\delta(t_{pp}), \tag{2.26}$$

where $\delta(t)$ is the Dirac delta function. This indicates that the signal appears only when the pump and probe pulses temporally overlap.

Finite Pulse Duration and Convolution

In real experiments, the pump and probe pulses have finite duration. The measured signal is therefore the convolution of the intrinsic system response function $R(t)$ with the instrumental response function $G(t)$,

$$S(t) = \int_{-\infty}^{\infty} R(t')\,G(t-t')\,dt'. \tag{2.27}$$

Assuming Gaussian pulse shapes, the instrumental response function is

$$G(t) = \exp\left(-\frac{t^2}{\tau_{cc}^2}\right), \tag{2.28}$$

where τ_{cc} is the cross-correlation time given by

$$\tau_{cc}^2 = \frac{\tau_{\text{pump}}^2}{n_{\text{pump}}} + \frac{\tau_{\text{probe}}^2}{n_{\text{probe}}} + \tau_{\text{jitter}}^2. \tag{2.29}$$

Here, τ_{pump} and τ_{probe} are the pulse durations, n_{pump} and n_{probe} are the number of photons involved in the process, and τ_{jitter} is the timing jitter.

Convolved Response Functions

In real pump–probe experiments, the measured signal is the convolution of the intrinsic system response with the Gaussian instrumental response function. Assuming a Gaussian cross-correlation function with width τ_{cc} and temporal overlap at t_0, the analytical forms of the convolved response functions are illustrated in Fig. 2.8.

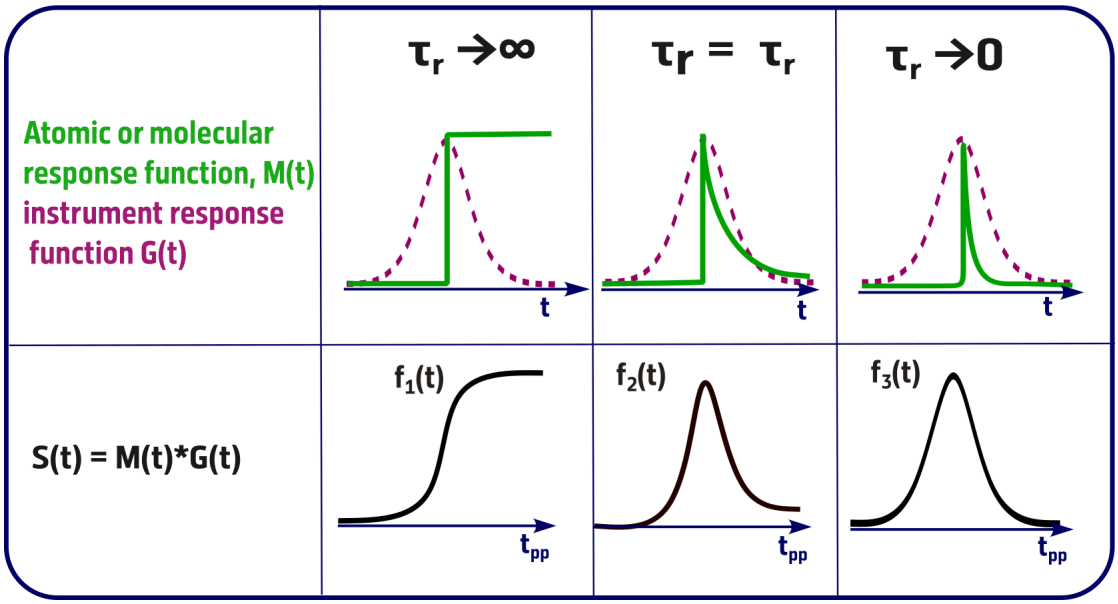

Figure 2.8: Schematic illustration of the three relaxation mechanisms and their corresponding convolved pump–probe signals. In each case, the intrinsic atomic or molecular response function is convolved with a Gaussian instrumental response that represents the pump–probe cross-correlation. The resulting observed signals are shown as $f_1(t)$, corresponding to a step-like response for a long-lived excited state ($\tau_r \to \infty$), $f_2(t)$, corresponding to an exponentially decaying metastable state with finite relaxation time τ_r, and $f_3(t)$, corresponding to an instantaneous response ($\tau_r \to 0$) limited by the experimental temporal resolution.

Step-like response function For a long-lived excited state ($\tau_r \to \infty$), the intrinsic response is a Heaviside step function. After convolution with the Gaussian instrumental response, the measured signal becomes

$$f_1(t) = \frac{1}{2}\left[1 + \mathrm{erf}\left(\frac{t - t_0}{\tau_{cc}}\right)\right], \tag{2.30}$$

where $\mathrm{erf}(z)$ is the error function. This describes a step-like rise broadened by the finite experimental resolution.

Exponentially decaying response function For a metastable state with finite relaxation time τ_r, the intrinsic response is an exponential decay multiplied by a Heaviside step function. The convolved response is

$$f_2(t) = \frac{1}{2}\exp\left(\frac{\tau_{cc}^2}{4\tau_r^2} - \frac{t - t_0}{\tau_r}\right)\left[1 + \mathrm{erf}\left(\frac{t - t_0}{\tau_{cc}} - \frac{\tau_{cc}}{2\tau_r}\right)\right]. \tag{2.31}$$

This function describes an exponentially decaying population observed with finite temporal resolution.

Instantaneous response function When the intrinsic dynamics are much faster than the instrumental response ($\tau_r \to 0$), the system response is approximated by a Dirac delta function. The convolution yields a Gaussian profile:

$$f_3(t) = \exp\left(-\frac{(t - t_0)^2}{\tau_{cc}^2}\right). \tag{2.32}$$

This function represents the temporal profile of the instrumental response and is used to model instantaneous processes.

The final fit function observed in the experiment $S(t)$ can be represented as a linear combination of all response functions observed in the processes. This could be written as follows.

$$S(t) = A_0 + A_1 \cdot f_1(t) + A_2 \cdot f_2(t) + A_n \cdot f_n(t) \tag{2.33}$$

2.3.2 Numerical Fitting Strategy

Because the analytical expressions used in this work are nonlinear and involve correlated parameters, appropriate fitting methods are required to obtain reliable and physically meaningful results. For the CO_2 and xenon photoionization studies, described in Chapters 6 and 5, a Markov Chain Monte Carlo (MCMC) fitting algorithm based on the Metropolis sampling scheme is employed. The implementation of these fitting procedures follows the methodology described in Ref. [47].

For the UV-induced fragmentation dynamics of 1-butanethiol, as presented in Chapter 7, the fitting procedure is performed using a nonlinear least-squares method implemented through the SciPy optimization package in Python.

Chapter 3

Experimental Techniques using Free-Electron Laser FLASH

3.1 Introduction

This chapter details the experimental methods applied in this thesis at the FLASH facility, with a primary focus on the use of a FEL source for femtosecond X-ray pump–probe spectroscopy to investigate ultrafast atomic and molecular dynamics. Section 3.2 provides an overview of the working principles of FELs, covering the main FEL components, the microbunching and self-amplified spontaneous emission (SASE) process, the FLASH facility, and photon beam diagnostics. Essential diagnostic tools, namely the gas monitor detector (GMD) for measuring FEL pulse energy and beam position, and the FEL pulse duration diagnostics, are discussed in terms of their roles in FEL pulse characterization and experiment monitoring.

The experiments presented in Chapters 4, 5, 6, and 7 employ two-color pump–probe spectroscopy to investigate atomic and molecular systems, using either an FEL pump with an optical laser probe or an optical laser pump with an FEL probe. Two end stations at FLASH, namely the REMI and the CFEL-ASG Multi-Purpose instrument (CAMP), were used to study the reaction pathways of atomic and molecular systems.

The REMI end station was used to investigate both atomic and molecular systems (see Chapters 5 and 6). Section 3.3 describes the pump–probe experimental setup at the REMI end station, comprising a molecular source, a reaction microscope spectrometer, and position- and time-sensitive particle detectors for measuring charged fragments, as well as the data analysis scheme used for REMI. For atomic targets such as xenon (Xe), time-of-flight mass spectrometry (TOF-MS) measurements were used to probe photoionization dynamics. For molecular systems, including CO_2 and CS_2, ion–ion coincidence detection provided access to coincident fragmentation channels, enabling detailed insight into dissociation dynamics and reaction mechanisms.

A second set of experiments was carried out at the CAMP end station on the BL1 beamline at FLASH1, focusing on the UV-induced fragmentation dynamics of 1-butanethiol (see Chapter 7). Section 3.4 describes the pump–probe experimental setup at the CAMP end station, including the molecular source and the VMI spectrometer, and introduces the principles of VMI and Abel inversion.

These experimental methods demonstrate the capability of FEL-based pump-probe techniques to resolve transient states in atomic and molecular systems, giving insights into fundamental reaction mechanisms, dissociation pathways, and fragmentation dynamics detailed in the following chapters 5,6 and 7.

3.2 Free-Electron Laser

The FEL concept was introduced by Madey [20] in 1971 as an accelerator-based light source in which coherent radiation is generated by relativistic electrons propagating through a periodic magnetic structure known as an undulator (or wiggler) [48]. Unlike conventional lasers, which rely on bound electronic transition in solid, liquid, or gaseous gain media, FELs do not require a material gain medium and offer wavelength tunability determined by the electron beam energy and undulator parameters. Following Madey's original proposal, FELs were realized in two principal operating regimes: low-gain and high-gain configurations [48].

In the low-gain regime, FELs are typically operated as oscillators, in which the radiation is amplified over multiple passes through an optical cavity with relatively small single-pass gain. Such oscillator-based FELs are well suited for long-wavelength operation, from the microwave to the infrared and visible spectral ranges, where high reflectivity optical components are available for the cavity [49]. In contrast, extending the oscillator concept to shorter wavelengths is hindered by strong material absorption and the lack of suitable X-ray cavities. As a result, short-wavelength FELs operate in the high-gain regime, in which coherent radiation is generated and exponentially amplified in a single pass through a long undulator without the need of a cavity. In this regime, the dominant radiation mechanism is self-amplified spontaneous emission [50–52]. The underlying physics and characteristic properties of the SASE process are discussed in detail later.

Compared to third-generation synchrotron radiation sources, which produce broadband, partially coherent emission originating from relativistic electrons in bending magnets or insertion devices [53], high-gain FELs provide orders-of-magnitude higher peak brilliance, a high degree of spatial coherence, and femtosecond pulse durations [54]. These laser-like properties enable the investigation of nonlinear phenomena and ultrafast dynamics in atomic, molecular, and condensed-matter systems [55]. Furthermore, the high peak brightness and coherence of FELs have enabled single-shot coherent diffractive imaging and femtosecond crystallography, advancing structural studies of biological samples to near-atomic resolution [56].

SASE FEL facilities span a broad photon-energy range from the XUV to the hard X-ray regime. Facilities operating in the XUV and soft X-ray range, such as FLASH in Germany and FERMI in Italy, as well as large-scale X-ray facilities including the LCLS (LCLS-I and LCLS-II) at SLAC in the United States, the EuXFEL in Germany, SwissFEL in Switzerland, PAL-XFEL in Korea, and SACLA in Japan, operate from the soft to the hard X-ray regime and are commonly referred to as X-ray free-electron lasers (XFELs), with their primary focus on hard X-ray generation and applications.

The XUV and soft X-ray regimes are particularly well suited for spectroscopic investigation due to strong resonant interactions with valence and shallow-core electronic states, whereas hard X-rays, owing to their short wavelength and high penetration depth, enable diffraction and imaging techniques with atomic resolution. The scientific programs of these facilities overlap significantly, and experiments in AMO physics, condensed matter, structural biology [57], and high-energy-density physics are conducted across the accessible photon-energy range [58].

3.2.1 FEL Components

Fig. 3.1 presents a schematic diagram of a single-pass FEL operating in the SASE mode. An FEL has three primary components: an electron source, an accelerator, and an undulator.

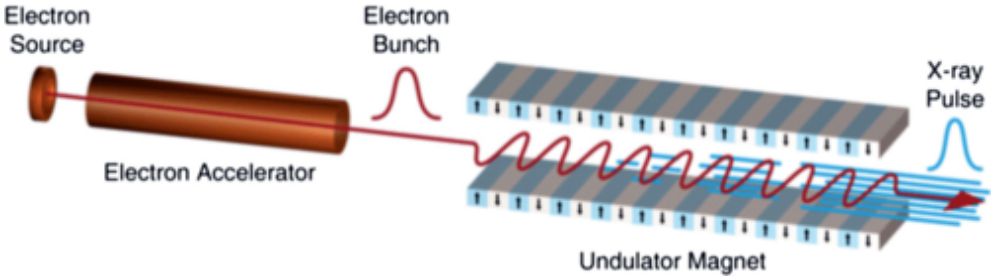

Figure 3.1: Basic components of an FEL: Electron source, linear accelerator, and undulator. Adapted from Ref.[59]

Electron Source

The electron source is an initial and essential part of a FEL. It generates high-quality electron bunches, which remain essential for the SASE process discussed later. At FLASH, electron bunches are generated in a superconducting radio frequency (RF) gun equipped with a cesium telluride (Cs_2Te) photocathode. The photocathode, illuminated by a UV laser pulse, emits electrons through the photoelectric effect. The RF gun accelerates the emitted electrons to an initial energy of approximately 5 MeV. The electron gun employs superconducting technology to achieve high stability and efficiency while minimizing beam degradation due to space-charge effects. This setup produces high-brightness electron bunches, which are important for the stable performance of the FEL.

Superconducting Accelerator

Following their generation, the electron bunches are further accelerated through superconducting 1.3 GHz TESLA (Teraelectronvolt Energy Superconducting Linear Accelerator) Test Facility (TTF) modules. These accelerating structures consist of superconducting linear RF cavities that produce electric field gradients of up to 40 MV/m, accelerating electrons to relativistic velocities [60]. As a result, the superconducting modules increase the electron energy from an initial 5 MeV to 1.35 GeV by the end of the accelerator, following the FLASH2020+ upgrade [61]. The use of superconducting RF cavities minimizes power losses and enables operation at high repetition rates, enabling FLASH to deliver thousands of pulses per second and thereby significantly enhancing data-collection efficiency.

Undulator Radiation

As electrons pass through the superconducting accelerating modules, they gain relativistic energies, reaching velocities close to the speed of light, where relativistic effects become significant. At these relativistic beam energies, electron beam dynamics is characterized by the Lorentz factor.

$$\gamma = \frac{1}{\sqrt{1 - \frac{v^2}{c^2}}}, \tag{3.1}$$

where v is the electron velocity and c is the speed of light, the electrons enter the undulator. The undulator comprises a periodic array of magnetic dipoles that generates an

alternating magnetic field. As the relativistic electrons traverse this field, they experience the Lorentz force,

$$\vec{F} = q\left(\vec{E} + \vec{v} \times \vec{B}\right), \tag{3.2}$$

where q is the electron charge, $\vec{E}$ is the electric field vector, and $\vec{B}$ is the magnetic field vector. In the undulator, the magnetic components force the electrons into a sinusoidal oscillatory trajectory. This oscillatory motion results in the emission of synchrotron radiation, which is predominantly confined to a narrow cone along the direction of electron propagation, with an angular divergence of approximately

$$\theta \approx \frac{1}{\gamma}. \tag{3.3}$$

Two key relativistic effects govern the wavelength of the radiation emitted by an undulator. First, due to the relativistic motion of the electrons, the undulator period undergoes length contraction in the electron rest frame, effectively reducing the undulator wavelength from λ_u to $\lambda_u' = \lambda_u/\gamma$. Second, the radiation emitted by the oscillating electrons is blue-shifted in the laboratory frame as a result of the relativistic Doppler effect. These two effects together lead to emission at significantly shorter wavelengths, enabling FELs to generate high-energy photons.

The wavelength of the undulator radiation emitted in the forward direction, including the reduction in longitudinal electron velocity caused by transverse oscillatory motion, is given by

$$\lambda_l = \frac{\lambda_u}{2\gamma^2}\left(1 + \frac{K^2}{2}\right), \tag{3.4}$$

where λ_l is the emitted radiation wavelength, λ_u is the undulator period (the distance between identical magnetic poles), γ is the Lorentz factor of the electrons, and K is the undulator parameter defined as

$$K = \frac{eB_0\lambda_u}{2\pi m_e c}, \tag{3.5}$$

with e denoting the elementary charge, B_0 the peak magnetic field, m_e the electron mass, and c the speed of light.

The emitted wavelength λ_l depends strongly on both the undulator period λ_u and the Lorentz factor γ, with relativistic effects compressing the radiation wavelength by several orders of magnitude. This scaling allows FELs to produce short-wavelength, high-energy radiation—such as X-rays—even when the undulator period is substantially larger than the emitted wavelength.

Interaction of Electrons and the Radiation Field

A one-dimensional theoretical framework can be employed to describe the interaction between relativistic electrons and the radiation field in a single-pass undulator [62]. This simplified model shows the generation of coherent radiation in a FEL and illustrates how energy is transferred from the electron beam to the electromagnetic field. During this interaction, electrons lose kinetic energy, which is converted into emitted radiation.

The radiation field is described using a plane-wave approximation propagating along the z-direction, as illustrated in Fig. 3.2. The transverse electric field component is given by

$$E_x = E_0 \cos(k_l z - \omega_l t + \phi), \quad \text{with} \quad k_l = \frac{\omega_l}{c} = \frac{2\pi}{\lambda_l}, \tag{3.6}$$

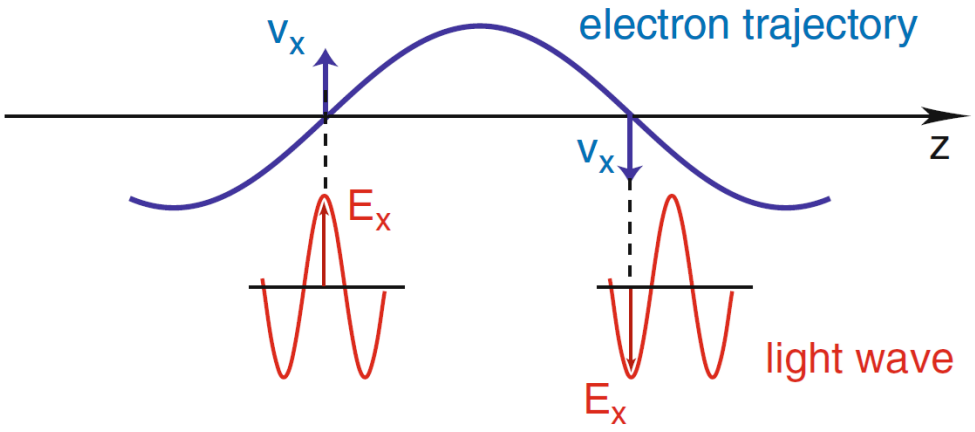

Figure 3.2: Energy is transferred from the electron to the light wave. The electron velocity and the electric field are in the same direction.

where E_0 denotes the field amplitude, ω_l the angular frequency, and λ_l the radiation wavelength.

The transverse electric field exerts a Lorentz-force on an electron, thereby modifying its energy. The rate of energy exchange between an electron and the radiation field can be expressed as

$$\frac{dW_e}{dt} = -e\vec{v} \cdot \vec{E} = -ev_x(t)E_x(t), \tag{3.7}$$

where W_e denotes the kinetic energy of the electron, e is the elementary charge and $v_x(t)$ is the transverse velocity of the electron. For the radiation field to gain energy, the quantity $\frac{dW_e}{dt}$ must be negative, indicating a continuous transfer of energy from the electron beam to the electromagnetic wave. This condition requires that the transverse electron velocity and the electric field remain suitably phase-matched.

From Eqs. 3.6 and 3.7, the average longitudinal velocity of an electron in the undulator can be written as

$$v_z = c\left(1 - \frac{1}{2\gamma^2}\left(1 + \frac{K^2}{2}\right)\right), \tag{3.8}$$

where γ is the relativistic Lorentz factor and K is the undulator parameter, which characterizes the strength of the magnetic field. The longitudinal velocity is therefore slightly smaller than the speed of light, and the electron follows a sinusoidal trajectory due to the periodic magnetic field of the undulator.

The time required for an electron to traverse half of the undulator period ($\lambda_u/2$) and the corresponding time required for the radiation field to propagate the same distance are given by

$$t_e = \frac{\lambda_u}{2v_z}, \quad \text{and} \quad t_l = \frac{\lambda_u}{2c}. \tag{3.9}$$

The difference between these times leads to a phase slippage between the electron and the light wave, which is a key factor in sustaining coherent energy exchange during the FEL interaction.

Continuous energy transfer occurs when the phase condition is satisfied.

$$\omega_l(t_e - t_l) = \pi \tag{3.10}$$

Under this condition, the transverse electron velocity and the electric field remain aligned, as shown in Fig. 3.2, such that the light wave advances by half an optical wavelength ($\lambda_l/2$) during half a period of the electron oscillation. This yields the resonance condition for amplified radiation with wavelength λ_l,

$$c\Delta t = \frac{\lambda_l}{2}, \quad \lambda_l = \frac{\lambda_u}{2\gamma^2}\left(1 + \frac{K^2}{2}\right). \tag{3.11}$$

In the forward direction, the emitted radiation wavelength corresponds to the fundamental undulator wavelength. When the phase condition satisfies $\omega_l(t_e - t_l) = 3\pi, 5\pi, 7\pi, \ldots$, odd higher harmonics $\lambda_l/3, \lambda_l/5, \lambda_l/7, \ldots$ can be generated. In contrast, even-order harmonics are not amplified, as the net energy transfer from the electron beam to the radiation field vanishes in these cases.

3.2.2 Microbunching and SASE

The previous section described the interaction of a single electron with a radiation field, resulting in spontaneous undulator radiation. In a realistic FEL, radiation is produced by an ensemble of electrons within a bunch. The spontaneous emission originating from individual electrons provides the initial seed for the self-amplified spontaneous emission (SASE) process.

As an electron bunch propagates through the undulator, each electron undergoes transverse oscillatory motion and emits radiation at the resonant wavelength λ_r. At the entrance of the undulator, this radiation is incoherent, and the total radiated power scales linearly with the number of electrons N_e,

$$P_{\text{incoherent}} \propto N_e. \tag{3.12}$$

As the interaction between the electron beam and the radiation field develops, collective effects become significant. The longitudinal electric-field component of the radiation induces energy modulation in the electron bunch. This modulation causes the electrons to reorganize into microbunches with a spatial periodicity approximately equal to the radiation wavelength λ_r. The formation of these microbunches is a key mechanism for the development of coherence in an FEL. Once microbunching occurs, electrons emit radiation in phase, leading to constructive interference and a rapid increase in the emitted power.

In the SASE process, the radiation originates from shot noise in the electron beam and grows exponentially as microbunching becomes more pronounced along the undulator. This amplification continues until saturation is reached, resulting in the intense, ultrashort radiation pulses characteristic of FELs.

Energy Modulation

As the radiation field copropagates with the electron beam through the undulator, the transverse electric-field component E_x interacts with the electrons, inducing an energy modulation. This energy modulation can be expressed as

$$\Delta\gamma \propto \cos(k_r z), \tag{3.13}$$

where $k_r = 2\pi/\lambda_r$ is the radiation wave number. The periodic modulation of the electron energy is the first step in the development of longitudinal density modulation.

Density Modulation

The energy modulation is converted into a density modulation because the electron longitudinal velocity depends on energy. Electrons with higher energies advance relative to the bunch, while lower-energy electrons lag behind. As a result, the initially uniform electron distribution evolves into a density-modulated structure with a period matching the radiation wavelength λ_r. This process leads to the formation of microbunches, as illustrated in Fig. 3.3.

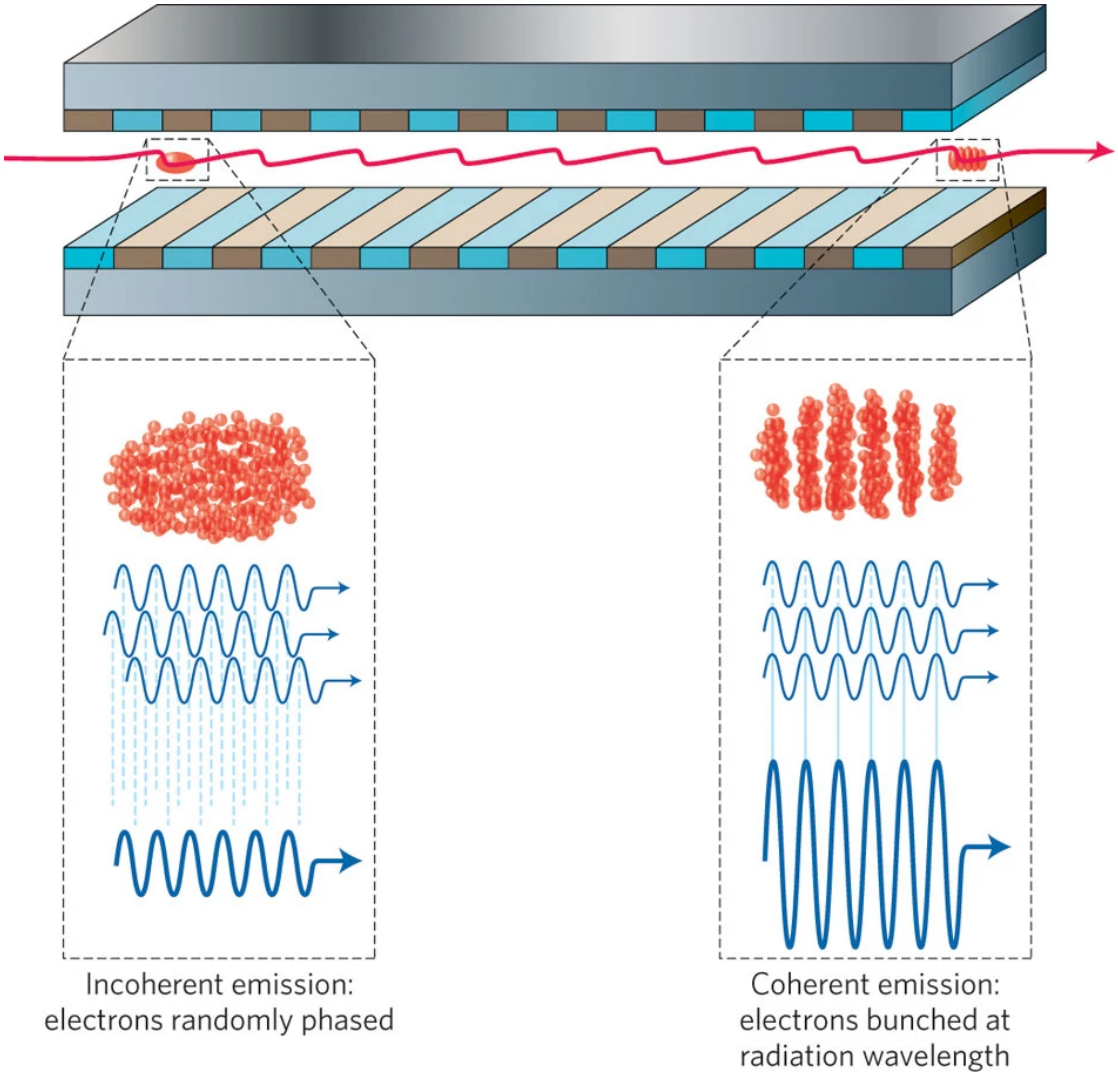

Figure 3.3: Schematic representation of microbunching in an undulator. Initially, the electron bunch is uniformly distributed and emits spontaneous radiation. Through the SASE mechanism, energy and density modulation leads to microbunching and coherent emission. Adapted from Ref. [63].

Coherent Emission and Amplification

Once microbunching is established, the electrons emit radiation that is phase-aligned with the existing electromagnetic field. Under these conditions, the radiated power scales quadratically with the number of electrons,

$$P_{\text{coherent}} \propto N_e^2, \tag{3.14}$$

reflecting the coherent nature of the emission. The constructive interference between the emitted radiation and the existing field leads to exponential amplification of the radiation intensity along the undulator, as shown in Fig. 3.4.

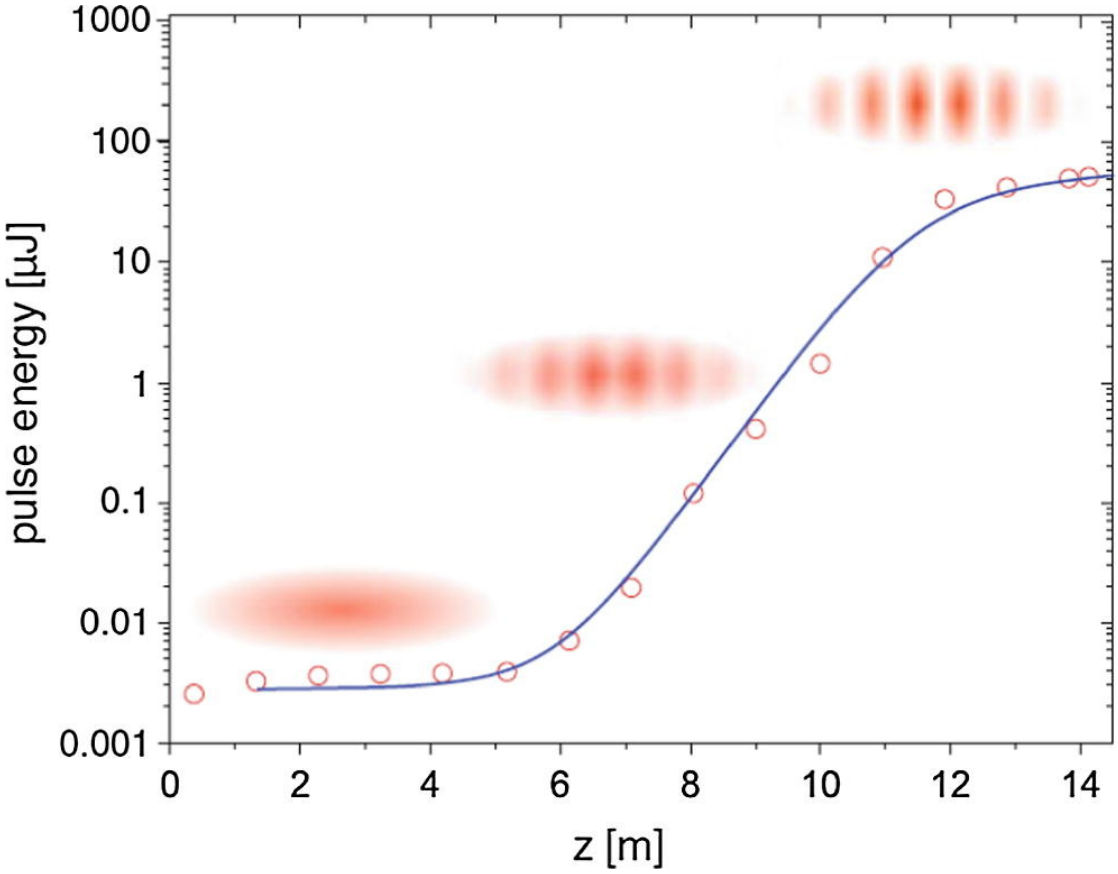

Figure 3.4: Evolution of the FEL pulse energy and electron-beam microbunching as a function of undulator length z, showing exponential growth followed by saturation. Adapted from Ref. [64].

The evolution of the radiation field amplitude $A(z)$ along the undulator can be described by

$$\frac{dA(z)}{dz} \propto A(z), \tag{3.15}$$

which has the solution

$$A(z) = A_0 e^{z/L_g}, \tag{3.16}$$

where L_g is the gain length, a characteristic parameter of the FEL that determines the distance over which the radiation intensity grows exponentially.

The exponential amplification continues until saturation is reached. At saturation, a significant fraction of the electron beam energy has been transferred to the radiation field, and further amplification is suppressed. The saturation intensity I_{sat} depends on both the electron beam properties and the undulator parameters.

3.2.3 Free-Electron-Laser in Hamburg (FLASH)

The Free-Electron Laser in Hamburg (FLASH) originated from the TESLA test facility. It was the first FEL in the extreme ultraviolet (XUV) and soft X-ray regions worldwide and began its user operations in 2005. FLASH operates using the SASE process. Currently, it can cover wavelengths from 3.4 nm to 51 nm at the first harmonic, with peak power in the gigawatt (GW) range and pulse durations from less than 10 fs to 200 fs.

FLASH has two experimental halls: FLASH1, named after Albert Einstein, and FLASH2, named after Kai Siegbahn, which was constructed as an extension of the existing FLASH1 facility. The first lasing from FLASH2 occurred in 2014, allowing parallel operation with FLASH1. FLASH2 is equipped with a variable gap undulator, enabling it to cover a wide range of fundamental wavelengths from 3.3 to 90 nm.

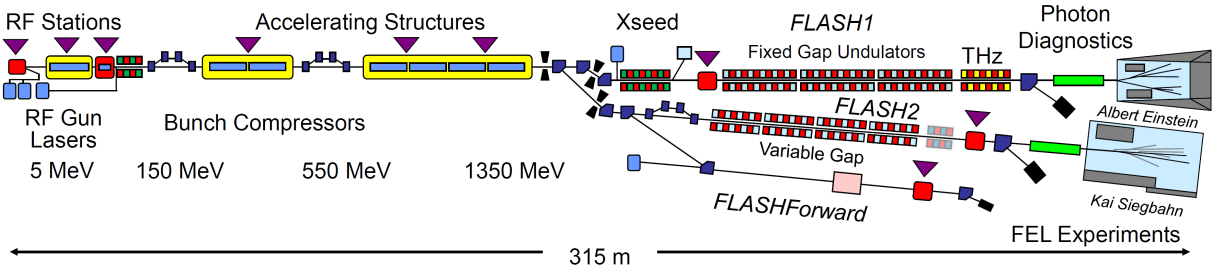

Figure 3.5: Schematic layout of FLASH. Not to scale. The two main SASE beamlines, FLASH1 and FLASH2, are in operation for user experiments. A third beamline runs the FLASH Forward plasma acceleration experiment. Adapted from Ref.[61]

3.2.4 FEL Photon Beam Diagnostics

FLASH operates in SASE mode; the emitted radiation fluctuates significantly due to the inherent stochastic nature of the amplification process. Therefore, it becomes essential to install pulse-resolved diagnostics to characterize the properties of the FEL pulses.

FEL Pulse Energy

The Measurement of the single-shot pulse energy is an essential parameter in many FELs experiments, as it directly relates to the number of photons in the pulse. Many phenomena in AMO physics depend strongly on the number of photons involved in the excitation. A non-invasive device, a gas monitor detector (GMD) [65, 66] is integrated into the FLASH beamline to measure the intensity and position of the FELs beam. This device operates by photo-ionizing rare gases at low gas pressure. Due to this low gas pressure, the interaction region remains effectively transparent, allowing the FEL beam to pass through with negligible attenuation. When the FEL beam passes through the chamber, it ionizes the gas. The electric field inside the chamber accelerates ions upward and electrons downward. The Faraday cup measures electron and ion currents. The number of photons can be calculated from a simple photoionization formula shown in Fig. 3.6. Furthermore, the FEL pulse passes between two electrode plates, enabling us to measure its position.

Two pairs of GMDs devices have been integrated into the beamline to ensure reliable, continuous monitoring of intensity and position: one set installed at the end of the undulators and another in the experimental hall before the beam is distributed to the instruments/beamlines.

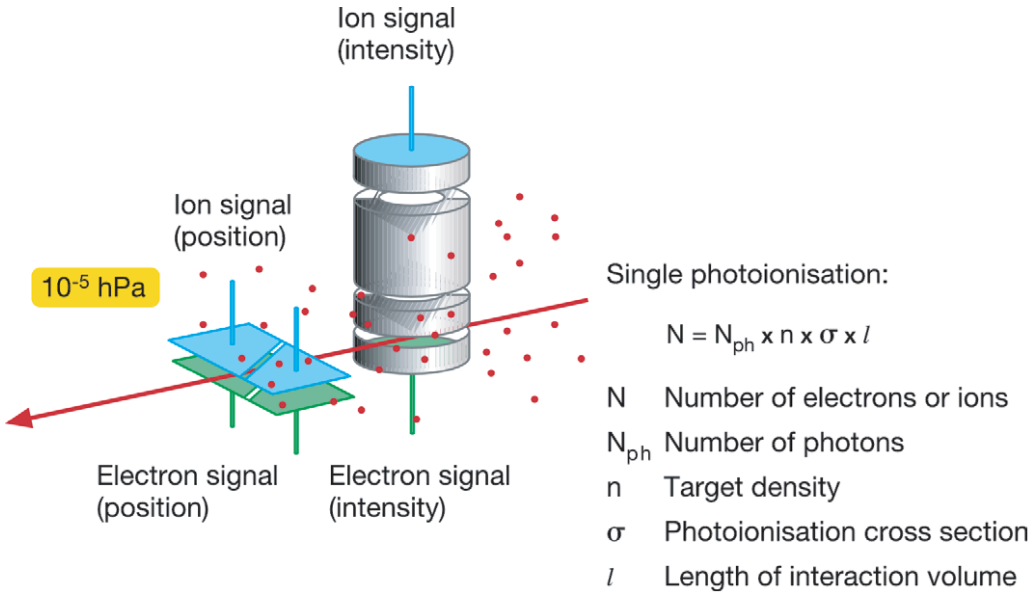

Figure 3.6: Schematic illustration of the GMDs, which provides non-invasive, shot-to-shot measurements of the FEL pulse intensity. A Faraday cup detects and counts the electrons and ions generated as the FEL pulse traverses an ionization chamber filled with rare gases at very low pressure. On the left-hand side, a pair of split electrodes is used to determine the horizontal position of the FEL beam based on the charge asymmetry induced by the ionization signal. Adapted from Ref.[67]

3.3 The Reaction Microscope Setup

REMIs [68] are multi-particle spectrometers, also known as cold-target recoil-ion momentum spectrometers (COLTRIMS). They were developed to investigate correlated many-particle dynamics in atoms, molecules, and clusters following interactions with femtosecond laser pulses, HHG, FEL radiation, and electron and ion collisions [69]. This enables kinematically complete atomic and molecular fragmentation experiments by coincident, momentum-resolved detection of recoiling target ions and emitted electrons. Kinematic completeness refers to the ability to measure the momenta, energy, and angles of all charged particles observed in coincidence [70].

The REMI used in this thesis is located at beamline FL26 FLASH2, a permanent endstation. Fig. 3.7 provides a schematic representation of the FL26 REMI endstation. The REMI setup includes an ionization source, FLASH2 pump-probe laser, and FLASH2 SASE FEL beam (depicted in purple), an ultrahigh vacuum (UHV) system, a supersonic jet containing atoms or molecules (represented by green balls), and a spectrometer.

Charged particles—ions (red) and electrons (blue)—are guided by the spectrometer fields: the ions are accelerated toward the ion detector by a uniform electric field, while the electrons are steered toward the electron detector by a magnetic field. The combination of a homogeneous electric field and magnetic fields provides 4π solid-angle acceptance for both ions and electrons.

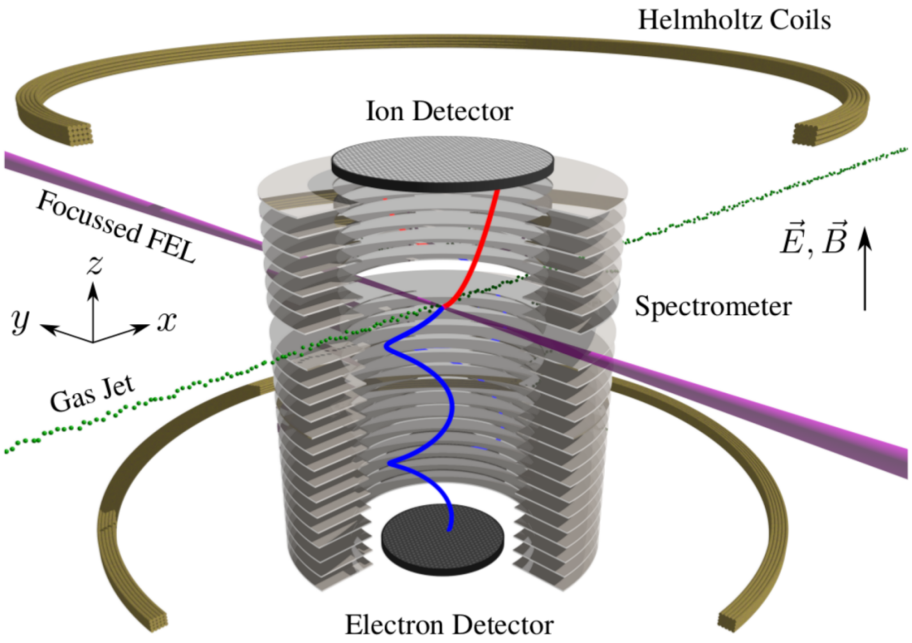

Figure 3.7: Sketch of reaction microscope (REMI) endstation at FLASH. Adapted from Ref. [71]

3.3.1 Vacuum Requirement for REMI Experiment

An ultrahigh-vacuum (UHV) environment is essential for the spectrometer. In the XUV and soft X-ray regime, photoionization cross sections are large for both the target gas and residual background gases. As a result, background molecules can be ionized not only in the focal region but also along the entire FEL beam path inside the spectrometer, leading to false coincidence signals. To maximize the signal-to-noise ratio (SNR)—defined as the ratio of ionization events originating from the target gas to those from residual background

gases—the pressure in the main chamber must be maintained below 10^{-10} mbar. Under these conditions, detected electrons and ions can be reliably attributed to the target species.

Such vacuum levels are achieved through a differential pumping scheme that progressively reduces the pressure from the molecular source nozzle to the interaction region, in combination with turbomolecular pumps, the use of low-outgassing materials [72], and thorough bake-out procedures [73].

3.3.2 Gas Jet Source

The gas-jet system typically comprises a gas reservoir, a nozzle, multiple skimmer assemblies, and differential vacuum stages, as shown in Fig. 3.8. These stages, using skimmers and apertures, produce a collimated stream of atoms and molecules. This setup is designed to meet experimental requirements, including low thermal energy, precise target localization, and low density, which are essential for achieving high-resolution momentum measurements.

One of the key benefits of the supersonic gas jet is its ability to reduce thermal energy. Adiabatic cooling during supersonic expansion significantly lowers the gas temperature down to just a few kelvins. At these low temperatures, the particles' thermal and rotational motion becomes negligible, enabling precise momentum measurements.

Secondly, the interaction volume in the REMI setup is highly localized, confined to the laser focus ($\sim 50\,\mu$m) and the FEL beam ($\sim 20\,\mu$m). The small, well-defined interaction volume ensures a precisely known initial position of the charged particles, which is essential for accurately reconstructing their initial momenta originating from molecular dynamics rather than from acceleration in the spectrometer.

Another essential requirement that the gas jet source addresses is the low target density. The gas jet density is kept below 10^{10} particles/cm^3, in the interaction region essential for coincidence measurements. A higher density could lead to excessive counts per laser shot, complicating momentum reconstruction and coincident-channel analysis. The main thing is that for coincidences, one wants at most one molecule ionized per shot.

Employing skimmers and differential pumping collimates the gas jet, thereby confining the interaction volume and selecting the coldest and most central part of the beam. This improves the definition of the target density distribution in the interaction region, thereby enhancing the precision and reproducibility of the experimental measurements.

In a supersonic expansion, gas flows from a high-pressure reservoir (1–10 mbar) through a nozzle of diameter 10–100 μm into a low-pressure region. Initially, the flow remains subsonic ($\mathrm{Ma} \ll 1$), but as the pressure drops rapidly beyond the nozzle, it transitions to supersonic speeds ($\mathrm{Ma} \gg 1$). Here, the Mach number is defined as

$$\mathrm{Ma} = \frac{v}{c}\,, \tag{3.17}$$

where v is the flow velocity and c is the local speed of sound in the gas.

Two skimmers are used in this experiment to further collimate the beam. The expansion process produces a gas jet with a sharp momentum distribution along the jet axis and an even smaller transverse momentum spread. For an ideal gas undergoing such expansion, the maximum jet velocity is given by:

$$v_{\mathrm{jet}} = \sqrt{\frac{2k_B T_0}{m} \cdot \frac{\gamma}{\gamma - 1}} \tag{3.18}$$

Here, $k_B = 1.38 \times 10^{-23}$ J/K is the Boltzmann constant, T_0 is the gas temperature before the expansion, m is the particle mass, and γ is the adiabatic index, defined as $\gamma = \frac{f+2}{f}$, with f being the degrees of freedom of the gas particle.

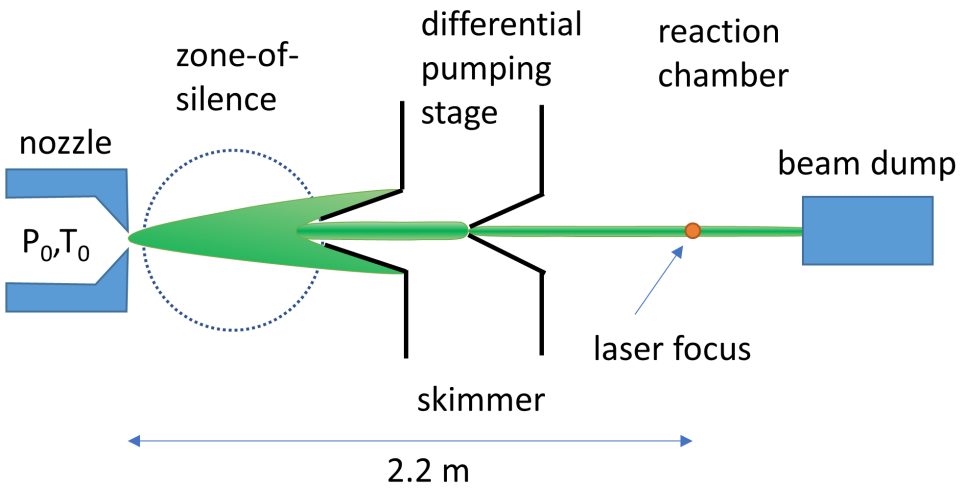

Figure 3.8: Schematic of supersonic gas jet. The gas expands through the nozzle inside the chamber. Two skimmers, in ring-shaped form, produce a collimated beam of ions after 2.2 m, ionized by a laser. Not ionized gas samples are captured by the beam dump.

3.3.3 Spectrometer and Detectors

Fig. 3.9 schematically shows the spectrometer used in this REMI setup. Atomic or molecular samples in the supersonic jet entering from left to right are exposed to the laser and FEL in the center of the spectrometer. The charged particles are guided into the spectrometer, where a uniform electric field accelerates them and a magnetic field confines them toward the ion and electron detectors, respectively.

The spectrometer generates a tunable electric field by applying a high-voltage bias to a stack of cylindrical steel rings. A uniform electric field is achieved by connecting a series of resistors between the rings. Since ions are much heavier than electrons, electrons attain significantly higher velocities and therefore exhibit much shorter time-of-flight (TOF). The distance from the interaction region to the electron detector is twice that on the ion side. A magnetic field is applied parallel to the electric field to guide the fastest electrons toward the detector. Rather than reducing their speed, the magnetic field changes only the direction of the electron's velocity, forcing them to follow cyclotron trajectories within the spectrometer and enabling detection over the full solid angle 4π. The motion of charged particles is described by the Lorentz force 3.2.

The spectrometer consists of 22 rings of annealed stainless steel, stacked along the z-axis and separated by 10 mm. The spectrometer rings are 1 mm thick, with an inner diameter of 120 mm and an outer diameter of 200 mm. The individual rings are electrically connected via a 100 k Ω resistor, which maintains a constant potential across the spectrometer.

Detectors

The charged particle is guided to an ion and electron detector, respectively. The REMI combines a Micro-channel plate (MCP) with a delay-line detector. The detection scheme consists of two steps: In the first step, the signal is amplified by a MCP, and the impact time is measured. In the second step, the anode of the delay line determines the particle's impact position. Fig. 3.10 shows an ion and electron detector system scheme.

Micro-Channel Plate

Ions passing through the grid reach the end of the spectrometer, where they strike the MCP. Fig. 3.10(a) illustrates the MCP, which consists of a thin plate made of glass or ceramic

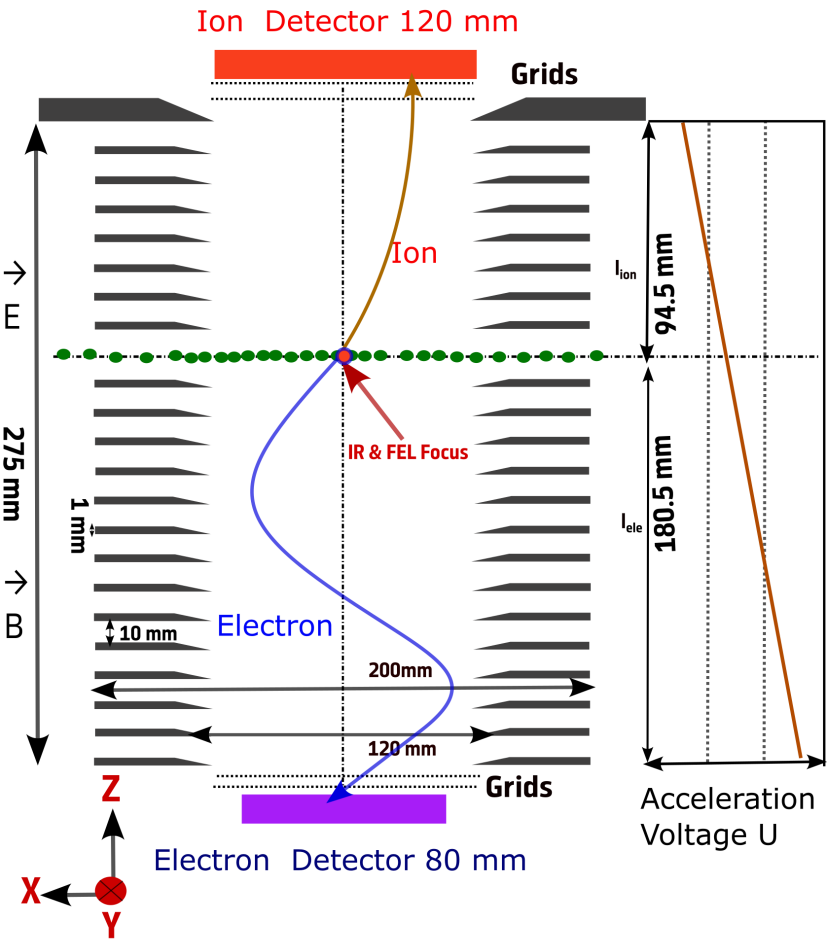

Figure 3.9: Schematic of the spectrometer.

material embedded with millions of tiny micro-channels, each with a diameter between 5-25 μm. The plate is cut at a slight angle to ensure that incoming particles strike the channel walls.

When a charged particle collides with the wall of a channel, it ejects secondary electrons from the surface. These secondary electrons are accelerated by a high voltage applied along the channel, initiating an avalanche process as they move downward. This electron cascade significantly amplifies the signal. The MCPs can amplify the signal by up to a factor of 10^6, making them highly sensitive detectors.

The impact time of a particle on the MCP is recorded and used to calculate the TOF. By combining the timing signal from the MCP (t_{MCP}) with the FEL trigger time (t_{trigger}), the TOF is calculated as:

$$t_{\mathrm{TOF}} = t_{\mathrm{MCP}} - t_{\mathrm{trigger}}$$

t_{trigger} is the input provided by the FLASH facility, indicating the arrival time of the photons.

Delay-line Anode

When a particle (such as an ion or electron) hits the MCPs above the delay line, an electron cloud emerging from the back of the MCPs interacts with the delay-line anode, generating an electrical signal. Fig. 3.10(c) illustrates how the signal travels along the wires to both ends of each wire layer. The time difference between these signals (from one end to the

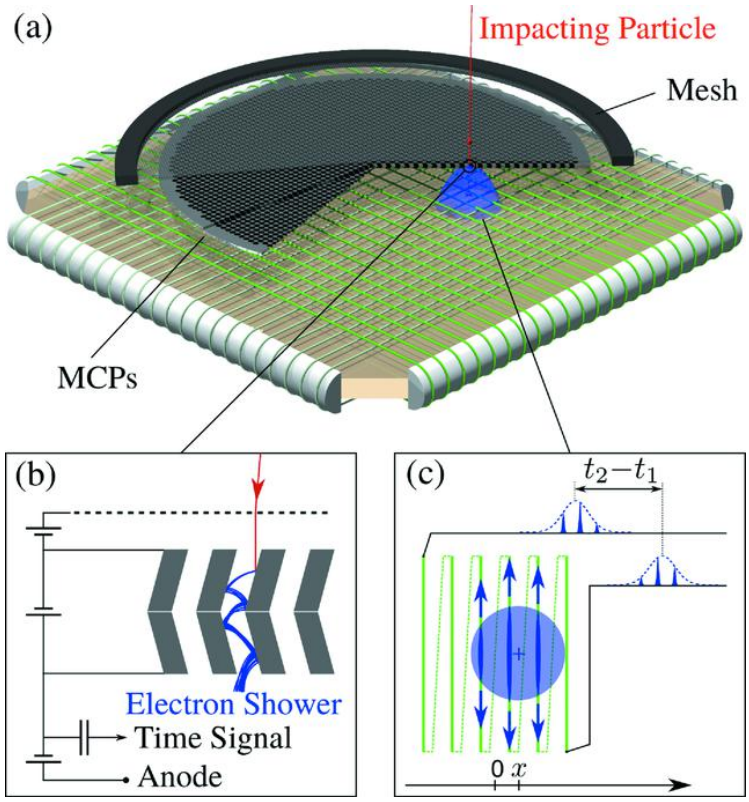

Figure 3.10: (a) Schematic representation of an MCP working principle and a delay-line anode. (b) An incident particle impacts the inner wall of the MCP, generating secondary electrons that initiate a cascade amplification process, resulting in an electron cloud. (c) The spatial position of the particle impact is determined using a delay-line anode. The generated signals propagate along the delay-line wires in opposite directions and are detected at the ends. The time difference (Δt) between the signals is used to calculate the spatial coordinates of the particle's impact. Adapted from Ref. [71].

other) provides information about the exact position of the particle impact in both the X and Y coordinates. The difference in arrival times across wire layers (e.g., X and Y) is used to triangulate the precise two-dimensional position of the impact point on the detector. The signal is processed by software [69].

If the timing information along the x- and y-directions is obtained, then the two-dimensional information on the impact position can be calculated as:

$$X \propto (t_{x1} - t_{\mathrm{MCP}}) - (t_{x2} - t_{\mathrm{MCP}})$$

$$Y \propto (t_{y1} - t_{\mathrm{MCP}}) - (t_{y2} - t_{\mathrm{MCP}})$$

Here, t_{x1} and t_{x2} are the arrival times of the signals at both ends of the wire in the x-direction, while t_{y1} and t_{y2} represent the corresponding times for the y-direction. These time differences determine the precise X and Y coordinates of the particle's impact.

This method offers several advantages over charge-coupled device (CCD) cameras, including high spatial resolution, improved timing accuracy, and minimal dead time.

3.3.4 Reconstruction of Ion momenta

The ion momentum can be decomposed into longitudinal and transverse components depending on the spectrometer geometry. The longitudinal momentum (p_z) is parallel to the spectrometer axis or in the z-direction, and transverse momentum (p_x) and (p_y) are perpendicular to the z-axis.

Longitudinal Ion momentum

The longitudinal momentum (p_z) corresponds to the ion's motion along the z-direction. It is primarily determined by the spectrometer's electric field. The total flight time $t_{m,q}(p_z)$ is the sum of the acceleration region and drift region.

$$t_{m,q}(p_z) = m\left(\underbrace{\frac{2a_z}{\sqrt{p_z^2+2mq\Delta U}\pm p_z}}_{\text{Acceleration Region}} + \underbrace{\frac{d}{\sqrt{p_z^2+2mq\Delta U}}}_{\text{Drift Region}}\right) \tag{3.19}$$

In the following, m and q are assumed to be known. If there is no drift region present ($d = 0$), the analytical solution is given by

$$p_z(t) = \frac{ma}{t} - \frac{q\Delta U}{2a}t \tag{3.20}$$

Approximation of Small Momenta

When the initial momentum p_z is small compared to the momentum gained in the extraction field,

$$p_z \ll \sqrt{2mq\Delta U},$$

an approximation can be derived. For small p_z, the term

$$\sqrt{p_z^2+2mq\Delta U}$$

can be expanded as a Taylor series:

$$p_z(t) \approx q\Delta U\frac{(t_0-t)}{a} + \mathcal{O}\left((t_0-t)^2\right), \tag{3.21}$$

where the zero-momentum flight time t_0 is defined as:

$$t_0 = \sqrt{\frac{m}{q\Delta U}}\left(\sqrt{2}\,a + \frac{d}{\sqrt{2}}\right). \tag{3.22}$$

This approximation is valid for small initial momenta $p_z \ll \sqrt{2mq\Delta U}$, and provides a closed-form analytical expression for $p_z(t)$.

Transverse Momentum

The transverse momentum ($p_\perp$) lies in the plane perpendicular to the spectrometer axis and is not unaffected by the electric field. The transverse components p_x and p_y represent the ion's motion in the x- and y-directions, respectively.

The impact position on the detector depends on the initial transverse momenta p_x and p_y, as well as the TOF (t). Additionally, there is a constant offset mv_{jet} due to the jet velocity v_{jet} along the x-axis.

The positions x and y on the detector are expressed as:

$$x = \frac{t}{m}\left(p_x + mv_{\text{jet}}\right), \quad y = \frac{t}{m}p_y. \tag{3.23}$$

Rearranging these equations to solve for the transverse momenta:

$$p_x = m\left(\frac{x}{t} - v_{\text{jet}}\right), \quad p_y = m\frac{y}{t}. \tag{3.24}$$

Thus, the transverse momentum $p_\perp$ is reconstructed as:

$$p_\perp = \sqrt{p_x^2 + p_y^2}. \tag{3.25}$$

3.3.5 Data Analysis of REMI

The REMI data analysis was performed using the Grand unifiEd reactioN microscopE souRce Code (GENERiC), developed during this work [74]. GENERiC is implemented as a shared library within the GSI Object Oriented On-line Off-line system (Go4) framework [75], which is itself based on CERN's ROOT data analysis framework [76]. Since its initial implementation, the software has been further developed in several thesis projects, where general analysis procedures and calibration strategies were established and documented [77, 78].

Within Go4, the list-mode data files were processed, and the data acquisition (DAQ) performance was monitored throughout the experiment. The data analysis consists of four main steps: acquire, unpack, calculate, and merge. In these steps, raw detector signals are converted into timing information, reconstructed into TOF and position data, transformed into calibrated three-dimensional momentum vectors and derived physical observables, i.e., KER and angular distributions, and finally merged with the FLASH DAQ dataset to enable time-resolved analysis.

In the following subsections, the individual analysis steps are described in more detail. The final merged datasets were further processed and visualized in Python using several scientific computing packages, particularly those listed in Refs [79–87].

Acquire Step: From Voltage Traces to Timing

In the acquire step, the raw voltage traces from all individual detector channels are converted into timing information. To determine the arrival time of the voltage trace with high accuracy, a constant fraction discriminator (CFD) is applied to each channel's raw voltage signal. A CFD reduces timing errors by triggering at a fixed fraction of the pulse amplitude, making the timing largely independent of signal amplitude fluctuations.

Unpack Step: Reconstruction of Detector Hits

In the unpack step, the timing information from each detector channel is used to reconstruct the TOF and the impact position on the delay-line detector. The output of this step contains the TOF and the ion's spatial position.

Calc Step: Identification of Ions and Coincidence Analysis

In this step, the reconstructed TOF and position information are used to identify the ions and to calculate their momentum vectors. The ions are then grouped into coincidence channels based on momentum conservation. If the vector sum of the momenta of the group of ions is close to zero, the ions are identified as fragments originating from the same

dissociation event. The output of the calc step comprises two datasets: one containing the identified ions with their reconstructed momenta, and another containing the ions sorted by coincidence channel.

Kinetic Energy Release and Angular Variables

From the reconstructed momentum vectors, the kinetic energy (or particle energy) of each ion is calculated as

$$\mathrm{KER} = \frac{p^2}{2m}, \tag{3.26}$$

where m is the mass of the particle and p is the magnitude of the particle's total momentum.

The emission angle of an individual ion is measured relative to the spectrometer axis. In the case of multi-ion fragmentation, the relative angles between momentum vectors are obtained from the corresponding scalar products:

$$\cos\theta_{ij} = \frac{\mathbf{p}_i \cdot \mathbf{p}_j}{|\mathbf{p}_i|\,|\mathbf{p}_j|}. \tag{3.27}$$

Coincidence Detection

To identify coincidence fragmentation channels, an ion–ion coincidence map, as a photoion–photoion coincidence (PIPICO) map, is constructed. A distinct diagonal line can appear in the map, corresponding to a specific molecular fragmentation channel. The momentum sum in the z direction is already very narrow, as expected when selecting ion pairs with correlated TOF values, which imply correlated z momenta. However, a false coincidence can still occur and still fulfill this filter/condition.

The PIPICO map is based solely on TOFs information; consequently, ions with similar TOFs can be misassigned. For example, in triatomic molecules such as OCS, O^+ and S^{2+} ions cannot be distinguished based on their mass-to-charge ratio (and thus TOF). However, when momentum-conservation conditions are applied to filter coincidence events, this ambiguity is reduced: in the case of a single ionization event per FEL pulse, only one oxygen ion and one sulfur ion can be produced. Therefore, to suppress random coincidences, a momentum-sum condition was applied in all three spatial directions. The resulting three-dimensional momentum-sum distribution for the $CO^+ + O^+$ coincidence channel is shown in Fig. 3.11 to illustrate the procedure.

Merging with FLASH Data

The FLASH DAQ system records FEL and laser parameters on a shot-to-shot basis, required, for example, for time-dependent normalization of ion yields. The FLASH DAQ and REMI DAQ datasets are merged using their common event identifiers called "TrainID". The resulting merged dataset contains, for each Train ID, the complete set of relevant FLASH parameters together with the corresponding REMI observables from the Acqiris, unpack, and calc stages. In particular, the FLASH DAQ parameters used in this work include the FEL pulse energy, pump–probe laser pulse energy, the delay between the pump–probe laser and the FEL, and timing diagnostics from the bunch arrival-time monitor (BAM) and Laser arrival monitor (LAM).

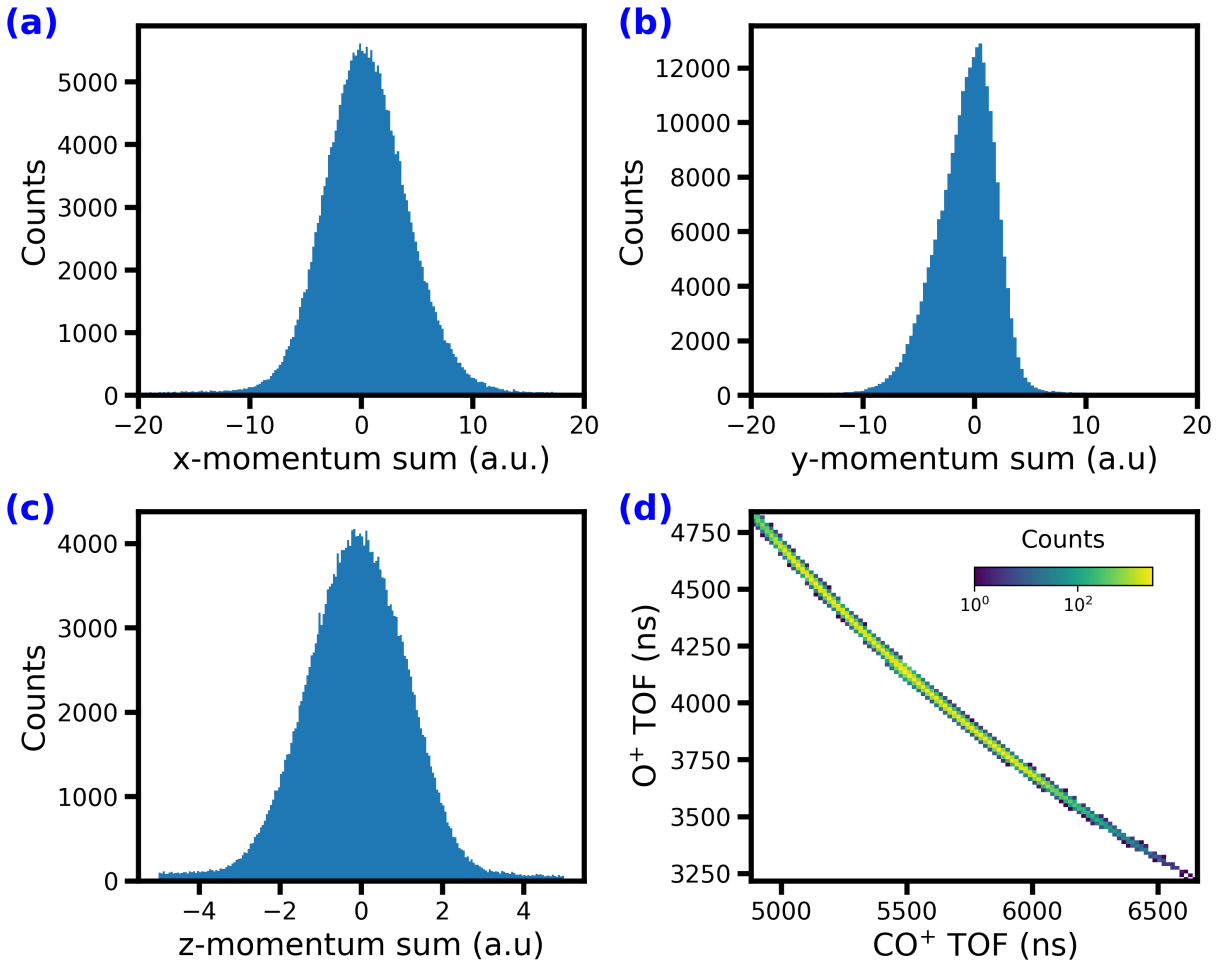

Figure 3.11: Momentum-sum spectra of the coincidence channel CO^+/O^+ obtained from the CO_2 data set. Panels (a)–(c) show the summed momentum components along the x, y, and z directions, respectively. Panel (d) displays the PiPiCo histogram after applying the two-dimensional momentum-sum condition used to isolate the coincidence line.

3.4 CAMP End-Station

The UV-induced fragmentation experiments of 1-butanethiol (see Chapter 7) were conducted at the CFEL ASG Multi-Purpose (CAMP) end-station [88], located at the FLASH1 beamline FL12, formerly known as BL1. The CAMP end-station is a versatile instrument that enables a range of experimental techniques, including coherent diffraction imaging and electron-ion spectroscopy [89]. These experiments are often executed in a pump-probe scheme that combines FEL pulses with a synchronized pump-probe laser [90].

3.4.1 Layout of the Experimental Hall

Fig. 3.12 illustrates the schematic layout of the FLASH1 hall and BL1 beamline. At FLASH, electron bunches are distributed between the two experimental halls FLASH1 and FLASH2, *via* a kicker system [91]. FLASH1 employs a fixed-gap undulator. This BL1 beamline has a split-and-delay mirror unit (SDU) for XUV-pump/XUV-probe experiments [92].

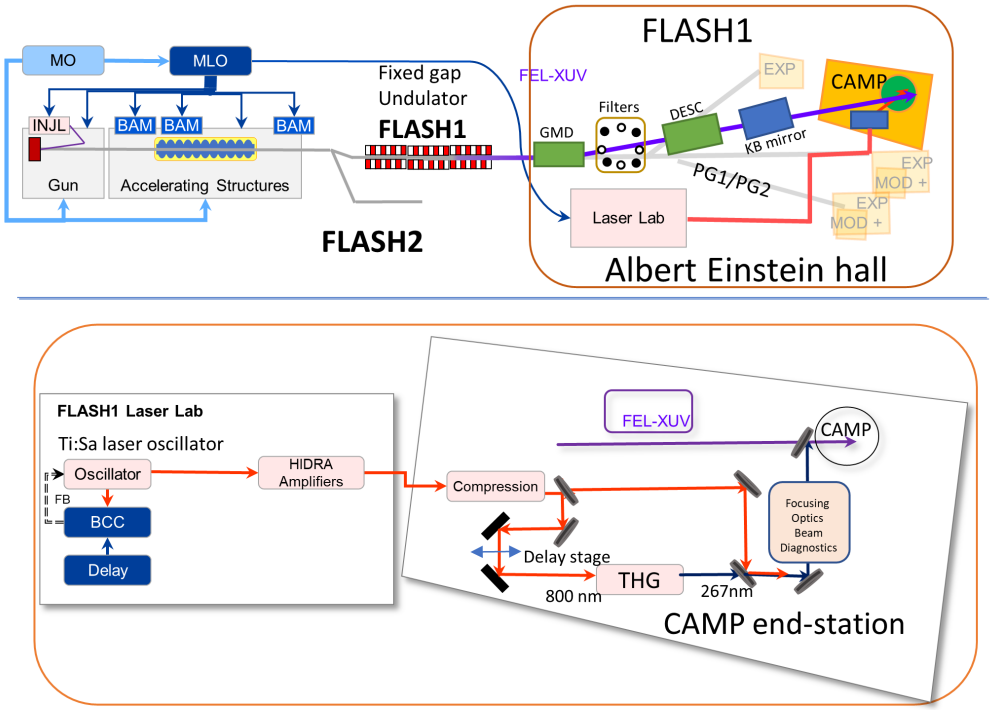

Figure 3.12: Schematic layout of the FLASH1 facility and the CAMP end-station. The upper panel shows an overview of the FLASH1 experimental hall and the BL1 beamline. The lower panel illustrates the optical pump–probe laser system used in the experiment. The electron beam passes through a fixed-gap undulator to generate FEL pulses, which are transported to the CAMP end-station *via* a series of beamline mirrors. Diagnostic instruments, including the GMD,BAM, and variable-line-spacing (VLS) spectrometer, are positioned along the beamline. An optional delay stage and split-and-delay (SDU) unit enables FEL-pump/FEL-probe experiments. The FEL beam is focused onto the interaction region using Kirkpatrick–Baez (KB) mirrors. The Ti:sapphire-based FLASH1 laser system includes synchronization, harmonic generation, and beam diagnostics. The optical pump–probe laser beam is transported through evacuated beamlines to the CAMP end-station. At the end station, the laser pulses are compressed, frequency-converted to the second, third, and fourth harmonics, and characterized using diagnostic tools. The system also enables two-color pump–probe experiments using only optical laser pulses.

3.4.2 FLASH1 Optical Laser System

Two laser systems are located in the FLASH1 experimental hall: one is used for pump-probe experiments at BL1 (CAMP endstation) and BL3, and the other is used for the PG1 and PG2 beamlines. For the BL1 and BL3 endstations, the laser system based on Ti-Sapphire technology delivers a central wavelength of 800 nm (up to 10 mJ, 50 fs FWHM) and a repetition rate of 10 Hz. Second-, third-, and fourth-harmonic pulses at 400 nm, 267 nm, and 200 nm can be generated near the end station.

The Fig. 3.12 shows an overview of the FLASH1 Pump-probe laser system. The Ti:Sa oscillator is locked to the FEL accelerator's master oscillator clock. A balanced cross-correlator is installed to stabilize timing and measure the oscillator's arrival time. A detailed explanation is provided in the Chapter. 4. The laser beam from the Ti:Sa oscillator is directed to the high-power amplifier (HIDRA), which operates at a 10 Hz repetition rate and delivers a pulse energy of up to 10 mJ after amplification.

The FLASH1 laser system is located in a separate climate-controlled laser hutch in the FLASH1 experimental hall. Under vacuum conditions, the laser beam is transported from the hutch to the BL1 end station. Near the end station, an optical table is used to diagnose the laser and guide it to the coupling window, where the beam is sent to the CAMP end-station.

For the pump-probe experiment, synchronization between the FEL and IR pulses from different sources is not possible. The synchronization of FEL and PP laser is discussed in the timing chapter.

3.4.3 Molecular Source

The 1-butanethiol sample is a liquid at ambient conditions with a vapor pressure of 61 hPa at 25 °C. Its boiling point ranges between 97 and 99 °C. To conduct gas-phase experiments, the sample was vaporized. This was achieved by placing the sample in a bubbler and heating it to an elevated temperature, achieving the necessary vapor pressure for phase transition. A continuous supersonic jet was used to deliver molecules in the experiment. The supersonic expansion was achieved using helium as the carrier gas, enabling rapid cooling and sample expansion. This molecular gas jet source is elaborated in Subsection 3.3.2. The molecular beam setup at REMI and CAMP is very similar

3.4.4 Electron and Ion Spectrometer

The molecular beam is aligned perpendicular to both the FEL and optical laser beams within the interaction region. This geometry is illustrated in Fig. 3.13, which shows a schematic of the CAMP double-sided VMI spectrometer. In the present configuration, the optical laser beam intersects the FEL beam at a small angle of approximately 1.5°.

Upon interaction with the laser and FEL pulses, the molecules undergo ionization and fragmentation, leading to electron emission and the formation of ionic fragments. An electrostatic extraction field accelerates these charged particles in opposite directions toward their respective detectors. The spectrometer electrodes are configured to satisfy velocity-focusing conditions, such that particles with identical initial velocity vectors are mapped to the same detector positions, largely independent of their initial spatial coordinates. This arrangement enables simultaneous measurement of the kinetic energy and angular distributions of both electrons and ions.

The detection system consists of MCP detectors coupled to phosphor screens and CCD cameras. Electrons and ions are detected on separate detector assemblies positioned at the bottom and top of the spectrometer, respectively. The total current signal from the MCP is

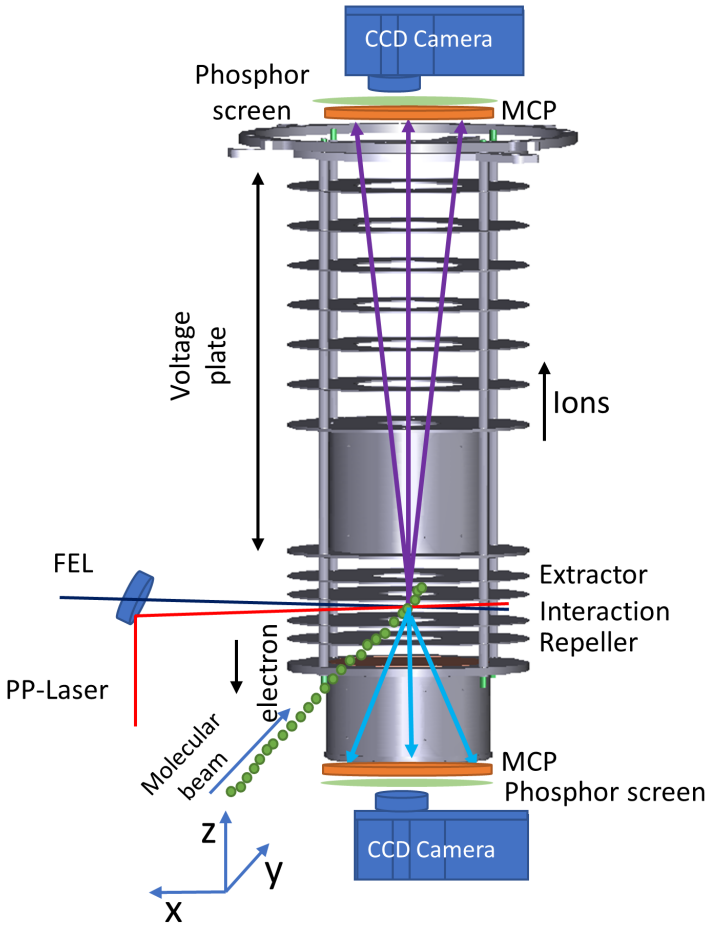

Figure 3.13: Schematic of the double-sided VMI spectrometer. The experimental setup involves supersonic expansion of the molecular sample, which is cooled to low temperatures to reduce thermal motion. This sample interacts perpendicularly with the FEL beam and the pump–probe laser beam. The experiment employs a double-sided VMI configuration to detect electrons and ions simultaneously. The charged particles are guided to the respective top (ion) and bottom (electron) detectors, each comprising a MCP, a phosphor screen, and a CCD camera to image the phosphor screen from outside the vacuum.

digitized using a 2 GHz analog-to-digital converter (ADQ2AC-4GMTCA). The arrival times of the ions are recorded and used to obtain TOF-MS.

3.4.5 Velocity Map Imaging

The concept of velocity map imaging was first proposed by Chandler and Houston in 1987 [93], and was subsequently refined by Eppink and Parker [94]. Fig. 3.13 shows a VMI spectrometer imaging the velocity distributions of ions or electrons, making it a powerful technique for investigating the structure and dynamics of atoms, molecules, and clusters. In VMI experiments, ionization and fragmentation processes generate charged particles in a localized interaction region, which are guided toward a position-sensitive detector by electrostatic fields.

The integration of electrostatic imaging optics with TOF-MS enables simultaneous measurement of the kinetic energy and angular distribution of ions and electrons. This capability allows discrimination and quantitative analysis of ions with identical mass-to-charge ratios. Advanced configurations, such as double-sided VMI spectrometers, further

enable simultaneous detection of electrons and ions, facilitating coincidence and correlation measurements.

Fig. 3.14 shows a conventional single-sided VMI spectrometer consisting of parallel electrodes: a repeller, an extractor, a lens, and a ground electrode. Charged particles are created in the interaction region between the repeller and extractor plates and are subsequently accelerated toward the detector by the electrostatic lens field. The electrode voltages are adjusted to satisfy velocity-focusing conditions, such that particles with identical initial velocity vectors are mapped to the same detector positions, largely independent of their initial spatial coordinates.

The electrostatic lens system projects the three-dimensional velocity distribution of the particles onto a two-dimensional detector plane. Consequently, the recorded image represents a two-dimensional projection of the three-dimensional velocity space. Assuming cylindrical symmetry about the laser polarization axis, the original three-dimensional velocity distribution can be reconstructed from this projection using inverse Abel transformation techniques.

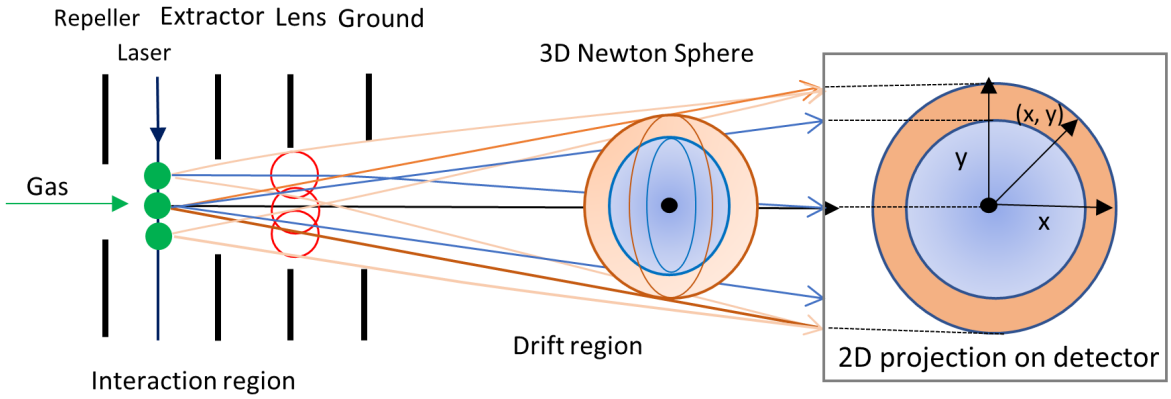

Figure 3.14: Schematic of the VMI spectrometer and the VMI image formation principle. The interaction of the molecular beam (green) with the laser and FEL pulse produces a three-dimensional Newton sphere of ions or electrons. The electrostatic lens system maps the three-dimensional velocity distribution onto a two-dimensional detector plane under velocity-focusing conditions. Particles possessing identical initial velocity vectors are focused to the same position on the detector, largely independent of their initial spatial coordinates within the interaction volume.

3.4.6 Abel Inversion

In VMI experiments, the detector records a two-dimensional projection of the three-dimensional velocity distribution of charged particles (Fig. 3.15(a). The VMI spectrometer axis is aligned with the laboratory z-axis, while the detector lies in the (x, y) plane. Assuming cylindrical symmetry about the spectrometer axis, the three-dimensional velocity distribution depends only on the radial coordinate.

$$\rho = \sqrt{x^2 + y^2 + z^2}. \tag{3.28}$$

The measured image intensity $I(x, y) \equiv I(r)$, with $r = \sqrt{x^2 + y^2}$, corresponds to the projection of the three-dimensional distribution along the z-axis,

$$I(r) = \int_{-\infty}^{+\infty} F\left(\sqrt{r^2 + z^2}\right) dz. \tag{3.29}$$

This expression can be written in the form of the Abel transform,

$$I(r) = 2 \int_{r}^{\infty} \frac{\rho\, F(\rho)}{\sqrt{\rho^2 - r^2}}\, d\rho. \tag{3.30}$$

The three-dimensional velocity distribution is recovered *via* the inverse Abel transform [95, 96] (Fig. 3.15b).

$$F(\rho) = -\frac{1}{\pi} \int_{\rho}^{\infty} \frac{dI(r)}{dr} \frac{dr}{\sqrt{r^2 - \rho^2}}. \tag{3.31}$$

pBASEX Method for Abel Inversion

Although the inverse Abel transform provides an exact analytical solution for reconstructing the original radial distribution $f(\rho)$ from the projection $I(r)$, its direct numerical implementation is highly sensitive to experimental noise. This sensitivity arises primarily from the presence of the derivative term and the square-root singularity at $y = r$. To overcome these limitations, several stable numerical algorithms have been developed for practical Abel inversion. In this work, the pBASEX (polar basis set expansion) method was employed for all Abel inversion procedures due to its numerical stability and robustness against noise [97]. Fig. 3.15 shows how the VMI image is processed for recorded pump–probe delays.

The pBASEX method is an extension of the BASEX algorithm, specifically optimized for velocity-map imaging data expressed in polar coordinates. In this approach, the measured projection $F(y, \theta)$ is expanded in a set of analytical basis functions and Legendre polynomials:

$$F(y, \theta) = \sum_{n,l} a_{nl}\, B_n(y)\, P_l(\cos\theta), \tag{3.32}$$

where $B_n(y)$ are radial basis functions, $P_l(\cos\theta)$ are Legendre polynomials describing the angular dependence, and a_{nl} are expansion coefficients determined through a least-squares fitting procedure.

Because the Abel transform of each basis function $B_n(y)$ is known analytically, the original three-dimensional distribution can be reconstructed without numerical differentiation. The reconstructed radial distribution $f(r, \theta)$ is obtained as

$$f(r, \theta) = \sum_{n,l} a_{nl}\, b_n(r)\, P_l(\cos\theta), \tag{3.33}$$

where $b_n(r)$ are the inverse-Abel-transformed radial basis functions.

This basis-set expansion approach significantly reduces noise amplification and provides a numerically stable reconstruction of both radial and angular distributions.

Implementation of the pBASEX Method

Several steps are taken to implement the pBASEX method.

Image preprocessing Raw CCD images contain contributions from electronic offsets, scattered light, and detector background. Therefore, each image was first background-corrected by applying a Gaussian blur to remove the background. Residual hot pixels and low-intensity background contributions were removed using threshold-based filtering. These steps improved the signal-to-noise ratio while preserving the image features relevant to quantitative inversion.

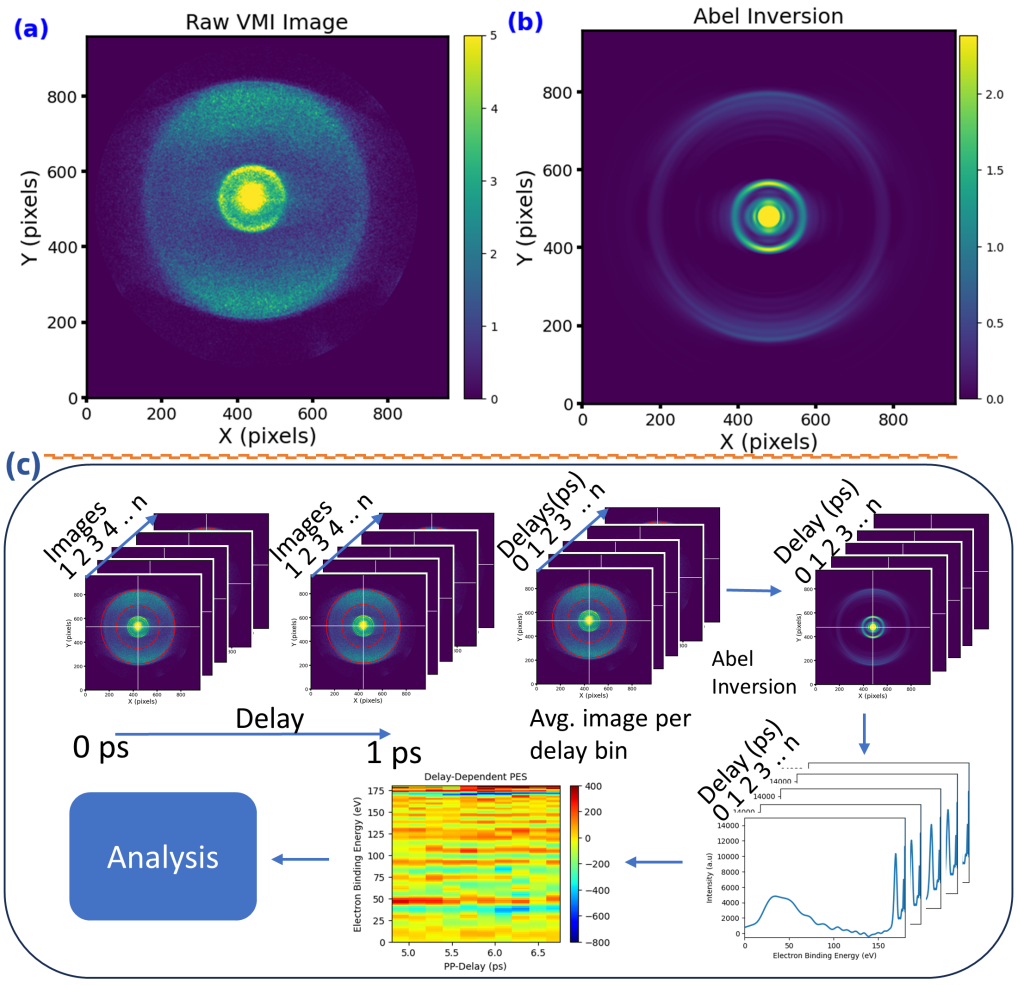

Figure 3.15: The top panel shows a raw VMI image and its corresponding Abel-inverted image from the 1-butanethiol dataset. The bottom panel illustrates the processing steps for VMI images acquired in a pump–probe scheme. Images are first binned by delay stage, and an average image is computed for each delay bin. Abel inversion is then applied, after which the kinetic (or binding) energy distributions are extracted for each delay. These data are collected and visualized as two-dimensional histograms and one-dimensional energy distributions for each delay.

Delay binning and averaging For pump–probe measurements, individual images were recorded as a function of the pump–probe delay. The images were grouped into discrete delay bins according to the experimental timing resolution. For each delay bin, all images were averaged to yield a single representative image, thereby reducing statistical fluctuations and

improving the robustness of the subsequent Abel inversion. The resulting set of delay-binned, averaged images served as input to the pBASEX analysis.

Basis-function definition and reconstruction parameters Prior to the inversion, a precomputed pBASEX basis set was loaded from an `HDF5` file. The basis set is characterized by the maximum image radius and the truncation parameters used in the basis expansion (e.g., the number of radial basis functions and the maximum Legendre order). In the present analysis, a basis set corresponding to a maximum radius of $R = 480$ pixels and a maximum angular order of $l_{\max} = 4$ was used. The reconstruction further requires defining the image center (x_0, y_0), selecting a quadrant for symmetry averaging, and specifying a regularization parameter α that balances numerical stability and spatial resolution.

Centering, quadrant folding, and resizing Accurate image centering is essential because the image center corresponds to zero transverse velocity. The center coordinates (x_0, y_0) were determined and kept fixed throughout the analysis to ensure consistency between delay bins. Assuming cylindrical symmetry about the laser polarization axis, quadrant folding was applied using all four quadrants. The folded images were then resized to a fixed radius of $R = 480$ pixels to match the dimensionality of the selected basis set.

pBASEX inversion and extraction of observables For each delay bin, the algorithm returned the reconstructed inverse-Abel image, the fitted projection, and the corresponding radial intensity distribution. The radial coordinate was converted into kinetic energy using a calibration constant determined from helium photoelectron reference spectra.

Overall, the combination of background correction, delay binning and averaging, symmetry enforcement *via* quadrant folding, and stable pBASEX inversion enabled reproducible, quantitatively reliable reconstruction of energy- and angle-resolved distributions from the measured VMI data.

Chapter 4

Achieving Sub-50 fs Temporal Resolution at FLASH2

Observing and controlling matter on its intrinsic timescale represents a central goal of ultrafast science. Fundamental processes in physics, chemistry, and biology, including electronic rearrangement, charge migration, and nonadiabatic relaxation, occur on femtoseconds or attoseconds timescales [9]. In a typical pump-probe experiment, a pump pulse excites the system and initiates a dynamical process, while a second time-delayed probe pulse probes the transient atomic or molecular state. By scanning the relative delay between the pulses and recording observables such as ion yields, photoelectron spectra, or transient absorption spectra [99], the temporal evolution of the underlying processes can be reconstructed.

The most challenging aspect of FEL pump-probe experiments is the precise synchronization of the FEL and the external pump-probe laser. In conventional tabletop ultrafast laser pump-probe experiments, pump and probe pulses originate from the same oscillator or amplifier system and are transported over short distances. Even in these compact setups, beam transport can introduce timing jitter or slow drift due to mechanical vibrations, pointing instability, and environmental fluctuations. However, at large-scale facilities such as FLASH, synchronization challenges are substantially greater.

The external femtosecond pump-probe laser system must be synchronized with the accelerator-generated XUV pulse, which extends over 100 meters [100]. Long-distance transport of laser pulses along the beam path, uncommon in FEL facilities, increases sensitivity to temperature fluctuations, humidity, air-pressure changes, and mechanical vibrations. Since pump-probe experiments often involve data acquisition over extended periods, maintaining stable temporal overlap over timescales of several days is essential.

Various FEL facilities worldwide have thus implemented multiple strategies to achieve accurate control of the relative timing between FEL and external laser, employing dedicated diagnostics and feedback systems. For instance, the European EuXFEL has demonstrated sub-20 fs temporal precision in short-pulse operation during soft X-ray photoelectron spectroscopy experiments [101]. At the LCLS, temporal resolutions in the approximately 30 fs regime have been achieved [102], while typical optical-laser/X-ray pump-probe experiments report resolutions around 60 fs (full width at half maximum (FWHM)) [103]. The externally seeded FEL facility FERMI [104] provides X-ray pulses with timing jitter below 5 fs [105] relative to the optical laser; however, the overall experimental temporal resolution remains on the order of 100 fs (FWHM) [106, 107], primarily limited by pulse durations rather than residual jitter or drift. These cases demonstrate that achievable time resolution is strongly dependent on facility configuration and experimental conditions.

This chapter is based on work published in Optics Express; see Ref. [98]. The author of this thesis is a co-first author on the published work with Atia-Tul-Noor and was involved in the experiment, data analysis, and manuscript preparation.

At the FLASH2 FEL beamlines, temporal resolution in two-color pump-probe experiments has historically been limited to approximately 150-300 fs (FWHM), which is substantially larger than the jitter and cross-correlation time of the two pulses [108–110]. This observation suggests that residual jitter and long-term drift are the primary factors limiting effective time resolution achieved in the experiment. Enhancing synchronization performance is therefore crucial for fully utilizing the capabilities of FEL-based ultrafast spectroscopy at FLASH.

This chapter presents a detailed investigation of FLASH timing information and the achievable temporal resolution at the FLASH2 beamline FL26. An optical LAM is implemented to actively compensate for slow drifts in the pump-probe laser arrival time using a feedback loop, while simultaneously measuring the timing jitter of each laser pulse. Additionally, the timing jitter of the FEL and the optical laser is independently measured using the BAM and LAM, respectively, and employed to correct the relative arrival time of the two pulses [108, 111], resulting in an effective temporal resolution below 50 fs (FWHM) in a benchmark xenon photoionization measurement.

4.1 Experimental Setup

The experiments presented in this chapter were performed at the FLASH using the REMI end-station at the FL26 beamline [71, 112]. A detailed description of the FLASH facility, its operation in SASE mode, and the REMI setup is given in Chapter 3. Here, only aspects relevant to the pump-probe configuration are summarized, with emphasis on the FLASH timing and the LAM system used to measure and stabilize the laser timing jitter.

FLASH is a 315 m long FEL facility delivering intense femtosecond pulses in the XUV and soft X-ray range [51, 113]. The measurements were carried out at FLASH2 [114], which offers variable-gap undulators that enable wavelength tuning within a limited range for a given electron-beam energy. For the data presented here, the accelerator was tuned to an electron-beam energy of 925 MeV, and the undulator was configured to generate XUV pulses at a photon energy of 160 eV (7.7 nm). The pulse energy shows significant shot-to-shot fluctuations, with an average of approximately 2.5 μJ in the interaction region. From the statistical fluctuations of the FEL pulse energy and the accelerator settings, the pulse duration is estimated to be (20 ± 10) fs (FWHM), corresponding to only a few temporal modes [115–117]. An overview of the FLASH facility, including the timing and diagnostics infrastructure and the delivery of the external pump-probe laser to the experimental end station, is shown in Fig. 4.1.

FLASH operates in burst mode at 10 Hz. Each burst consists of an 800 μs RF pulse during which a train of electron bunches generates FEL radiation in the undulators. The bunch trains for FLASH1 and FLASH2 are separated downstream of the last accelerating module by a kicker-septum system, with a gap of 50 μs (sometimes 70 μs) to accommodate the kicker rise time and the transition of the RF system. Up to 800 FEL pulses can be produced within a burst with intra-burst repetition rates of up to 1 MHz [118]. In the present experiment, the FLASH2 FEL was operated at 100 kHz, corresponding to a bunch spacing of 10 μs. The macropulse structure is illustrated in Fig. 4.2. For the measurements, 45 FEL pulses were synchronized with 77 NIR laser pulses. The first 45 pulses overlapped with the FEL for FEL-NIR pump-probe measurements, while the remaining pulses, containing only the NIR pulses, served as references.

The presented pump-probe experiments employed a wavelength-tunable optical parametric chirped-pulse amplification (OPCPA)-based NIR laser system synchronized to the FEL burst pattern [119, 120]. The oscillator output is amplified by ytterbium-based fiber pre-amplifiers and a high-power chirped-pulse amplification (CPA) stage, which pumps a

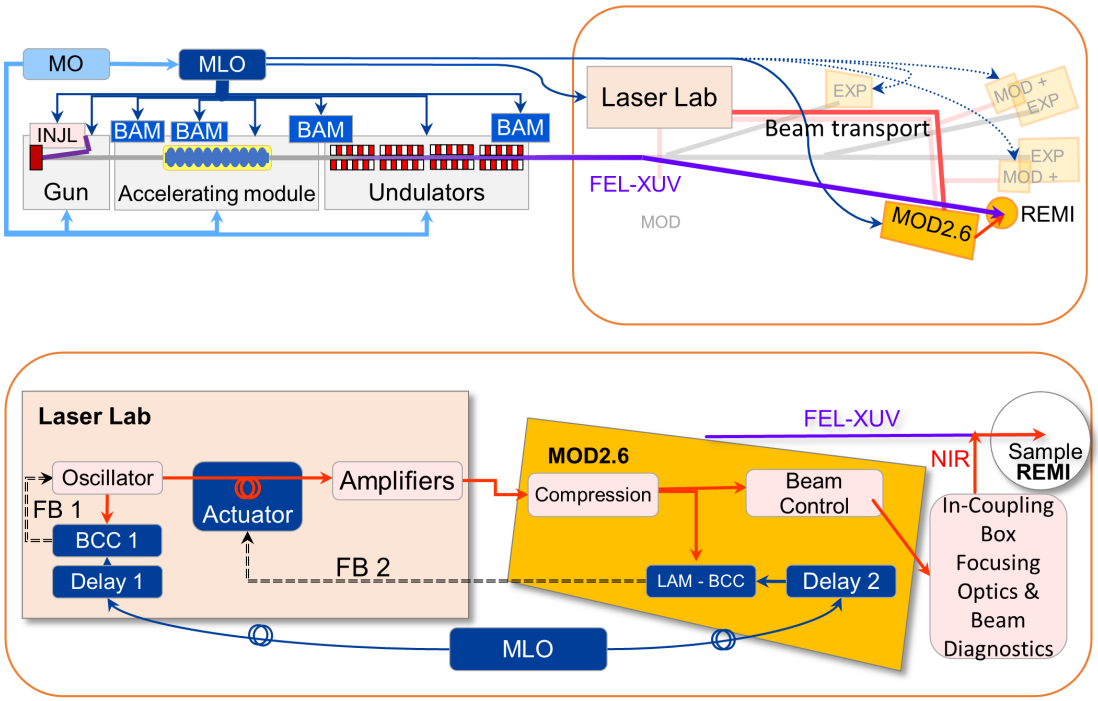

Figure 4.1: Schematic layout of the FLASH facility and the FLASH2 experimental hall. The laser laboratory is indicated in light yellow, and the MOD2.6 in yellow (the bottom section shown enlarged). The RF main oscillator (MO) provides the reference timing signals for the gun and the accelerator of FLASH, as well as for the master laser oscillator (MLO). BAMs are installed at timing-critical locations along the linear accelerator to measure the arrival time of the electron bunches and provide feedback for stabilizing their timing relative to the optical reference. The balanced cross-correlatorss (BCCs) are important components of the synchronization system, enabling synchronization of the pump–probe laser with the MLO. In particular, the LAM, which is based on a BCC, compensates timing drifts arising during laser amplification and transport. The pump–probe laser system is located in the laser laboratory within the experimental hall and is transported through

multi-stage OPCPA seeded by a supercontinuum source. The system delivers wavelength-tunable femtosecond pulses with durations below 15 fs.

The pump-probe laser system is located in an environmentally stabilized laser hutch within the FLASH2 experimental hall. From there, the laser beam is transported to the MOD2.6 next to the REMI endstation at beamline FL26 via an approximately 40 m long vacuum beamline. While the laser laboratory provides relatively stable environmental conditions, with typical temperature fluctuations of about ±0.1 K and relative humidity variations of about ±5%, the larger hall where the end stations are located experiences larger fluctuations of approximately ±0.5 K and ±10% relative humidity over the course of a week.

After laser pulse compression, the NIR pulses pass through several diagnostic sections and dispersive glass wedges to control pulse duration. The laser beam is transported from MOD2.6 to the in-coupling box located near the REMI end station. In the in-coupling box, the NIR beam is focused by two spherical mirrors, and a photodiode measures the laser pulse energy and the far-field focus. The NIR and XUV beams are then combined through the in-coupling window of the REMI spectrometer. The laser beam is coupled into the vacuum chamber through a 3.5 mm-thick BK7 window and overlapped with the FEL beam using a mirror with a central aperture that enables collinear propagation of the FEL and

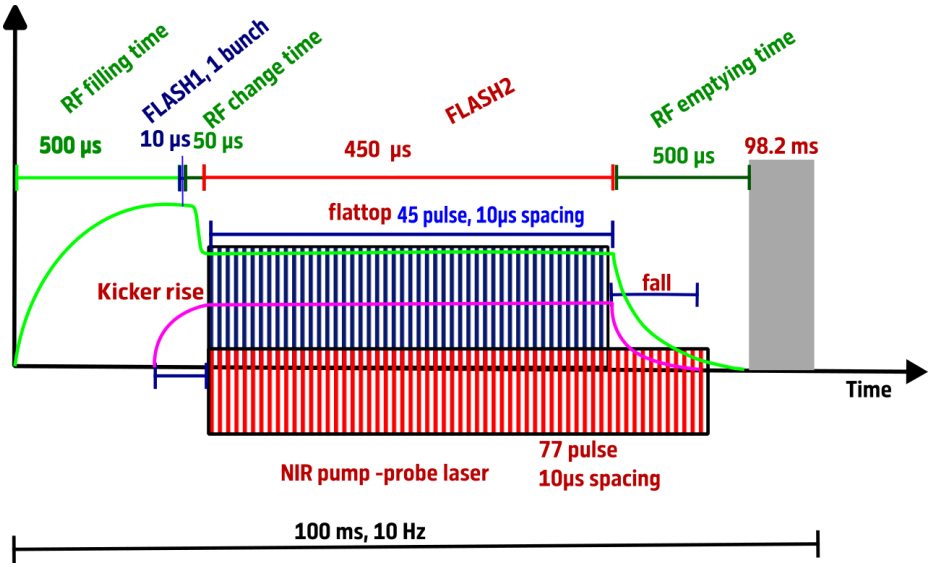

Figure 4.2: Timing structure of the FLASH RF pulse showing RF filling, bunch trains for FLASH1 and FLASH2, kicker rise and fall for beam switching, and RF emptying within the 10 Hz cycle. In this experiment, 45 FEL pulses overlapped with NIR laser pulses for pump-probe measurements, while the remaining laser pulses served as references without FEL overlap.

NIR beams. In the present experiment, the NIR laser operated at a central wavelength of 800 nm with a pulse duration of 18 fs (FWHM), a pulse energy of 110 μJ, and a focal spot size of approximately 50 μm.

The sample is introduced via supersonic expansion in a continuous gas jet[112]. The gas beam propagates perpendicular to both the XUV and NIR laser beams and intersects them in the interaction region at the center of the REMI spectrometer. The generated ions are extracted by a homogeneous electric field and directed onto a time- and position-sensitive detector. A detailed description of the gas jet source and the REMI spectrometer is provided in section 3.3.

4.1.1 FLASH Timing Infrastructure

Precise synchronization between the FEL and the external laser is important for high-time-resolution pump-probe experiments at FLASH. To achieve femtosecond-level timing stability across the entire facility, FLASH employs a hierarchical timing architecture that combines an RF system with an optical synchronization network and dedicated arrival-time diagnostics for the FEL and laser. This section describes the main components of the FLASH timing system and their roles in maintaining the temporal stability at the experimental end station.

FLASH timing infrastructure is based on the RF MO, which provides the master reference for accelerator subsystems, including the electron gun and superconducting accelerator modules. While RF synchronization is sufficient for accelerator operation, femtosecond pump-probe experiments require significantly higher timing precision. For this purpose, an optical MLO serves as a very stable optical reference clock.

The MLO generates trains of 200-fs ultrashort pulses at 217 MHz at 1550 nm, distributed throughout the facility via actively stabilized optical fiber links. The fiber links are designed to suppress path-length fluctuations caused by environmental changes, such as temperature variations and mechanical vibrations. As a result, the arrival time of the optical reference pulse is stabilized to the femtosecond level over long distances. All timing-critical subsystems, including the electron-bunch arrival time and the external pump-probe lasers, are referenced

to this common optical clock, thereby ensuring a unified timing network.

Several diagnostics are used to monitor and stabilize the timing of the accelerator and external lasers relative to the optical reference. BAMs installed at timing-critical sections of the accelerator measures the electron bunch arrival time and provides feedback to stabilize their timing relative to the MLO. In addition, BCCs are used to synchronize the external pump-probe laser oscillator to the optical timing network. BCC is explained in the Appendix Section A. A LAM, also based on a BCC, is installed close to the experimental end station to measure and compensate timing drifts arising from laser amplification and transport discussed in the following section.

Bunch Arrival Monitors

The BAM is an important diagnostic system for measuring the arrival time of electron bunches relative to an optical reference clock and thus plays an important role in synchronizing FEL pulses with external pump-probe laser systems or stabilizing the FEL. The arrival time of the electron bunches, and thus of the FEL pulses, is measured on a shot-to-shot basis using BAM.

The BAM operates via electro-optic sampling of the transient electric field generated by a passing electron bunch. This timing signal is referenced to the MLO, providing femtosecond-level arrival-time precision. BAMs are installed at timing-critical sections along the accelerator and integrated into longitudinal feedback systems to stabilize electron-bunch timing during FEL operation. Details can be found in [121, 122]. In pump–probe experiments, the recorded BAM data enable post-analysis correction of fast shot-to-shot timing jitter, thereby improving the effective temporal resolution.

4.1.2 Laser Arrival Monitor

To compensate for timing drifts of the pump-probe laser, a LAM is installed at MOD2.6 near the REMI end station. As illustrated in Fig. 4.3, the LAM utilizes a BCC to measure the relative timing between the pump–probe laser pulses and the optical reference from the MLO. A small fraction of the compressed NIR beam is sampled and spatially and temporally overlapped with the reference pulses in a nonlinear beta-barium borate (BBO) crystal, generating a sum frequency generation (SFG) signal. The signals from the two passes through the BBO crystal are detected by a balanced photodiode pair (PD1 and PD2), and the difference between their outputs yields a differential error signal proportional to the timing offset between the laser pulses and the reference.

The feedback actuator consists of a temperature-controlled fiber section of approximately 30 m and an additional 5 m polarization-maintaining single-mode fiber that serves as the actuator in the optical path. Adjusting the fiber temperature changes the optical path length through thermal expansion and the thermo-optic effect, thereby shifting the arrival time of the laser pulses. This configuration enables continuous tuning of the laser timing with a coefficient of approximately 330 fs/K, providing a delay adjustment range of several picoseconds with sub-femtosecond resolution.

The error signal from the LAM is used in an active feedback loop (FB2) to compensate for timing drifts and slow timing fluctuations of the pump–probe laser. Based on the LAM error signal, the arrival time of the laser pulses is stabilized by adjusting the optical path length between the oscillator and the laser amplifier using the temperature-controlled fiber actuator.

For FEL–laser pump–probe experiments, both stable and precisely controllable laser arrival times relative to the FEL pulses are required. The arrival time of the laser pulses can be scanned by delaying the LAM reference using Delay 2, while the FB2 feedback loop

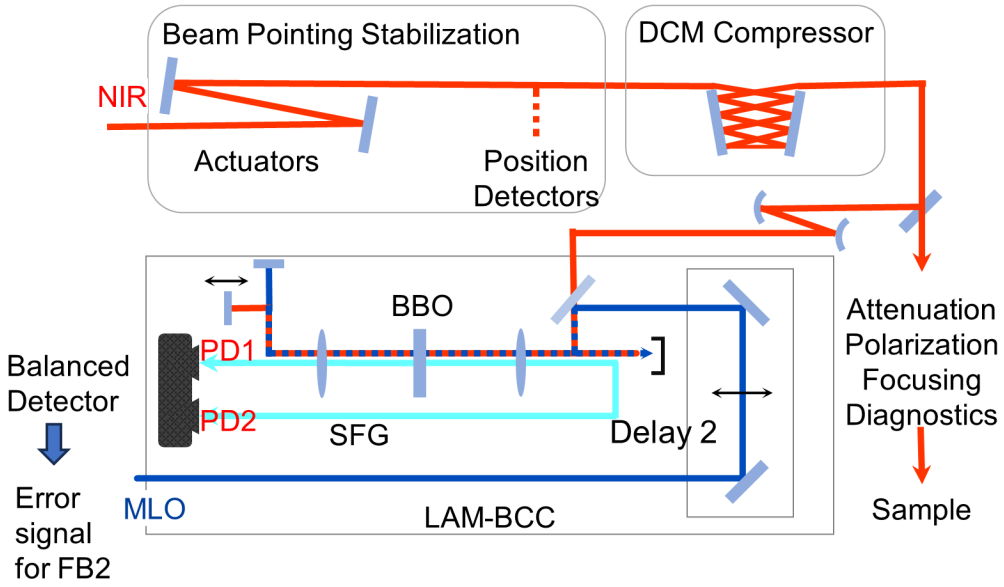

Figure 4.3: Schematic of the laser setup at MOD2.6. The laser beam is transported from the laser hutch to MOD2.6 via a vacuum beam transport pipe. The NIR laser (red) is stabilized for pointing and compressed using a double-chirped mirror (DCM) compressor. A small fraction of the beam is directed to the LAM, while the main beam passes through control and diagnostic stages before reaching the experimental end station. In the LAM, the laser pulses are combined with the MLO reference (blue) and focused into a BBO crystal to generate SFG. Temporal overlap is adjusted using Delay 2 in the reference beam path. After the first pass through the crystal, the laser pulse is slightly delayed relative to the reference, and both beams are reflected for a second pass. The resulting SFG signals are detected by a balanced photodiode pair (PD1 and PD2), from which the feedback signal (FB2) is derived.

adjusts the fiber temperature accordingly. This approach translates the reference delay into a controlled shift of the pump–probe laser arrival time.

4.1.3 Active Drift Compensation

Figure 4.4 presents the performance of the LAM feedback over a 12-hour measurement period. The dataset includes several experimental runs, during which the pump-probe delay was scanned for approximately 7 hours. The gaps observed in Figure 4.4 (a) correspond to interruptions in data acquisition between individual runs. The initial experimental run lasts approximately 4 hours.

The actively stabilized laser arrival time, as measured with FB2 feedback, is depicted in green and yellow. The feedback loop regulates the temperature of the fiber coil in FB2 to minimize the LAM error signal, which quantifies the relative timing difference between the MLO reference and the pump-probe laser pulses. With active feedback, the in-loop arrival-time stability reaches approximately 10 fs rms, and drifts averaged over five minutes are reduced to below 1 fs rms (yellow trace).

To estimate the drift expected without active stabilization, the compensated drift is reconstructed from the temperature changes applied to the fiber actuator (blue curve). This analysis indicates that, without feedback, the laser arrival time would drift by up to approximately 500 fs peak-to-peak over the 12-hour measurement period. After subtracting a five-minute rolling average, the residual jitter of the reconstructed drift is approximately 21 fs rms (red trace).

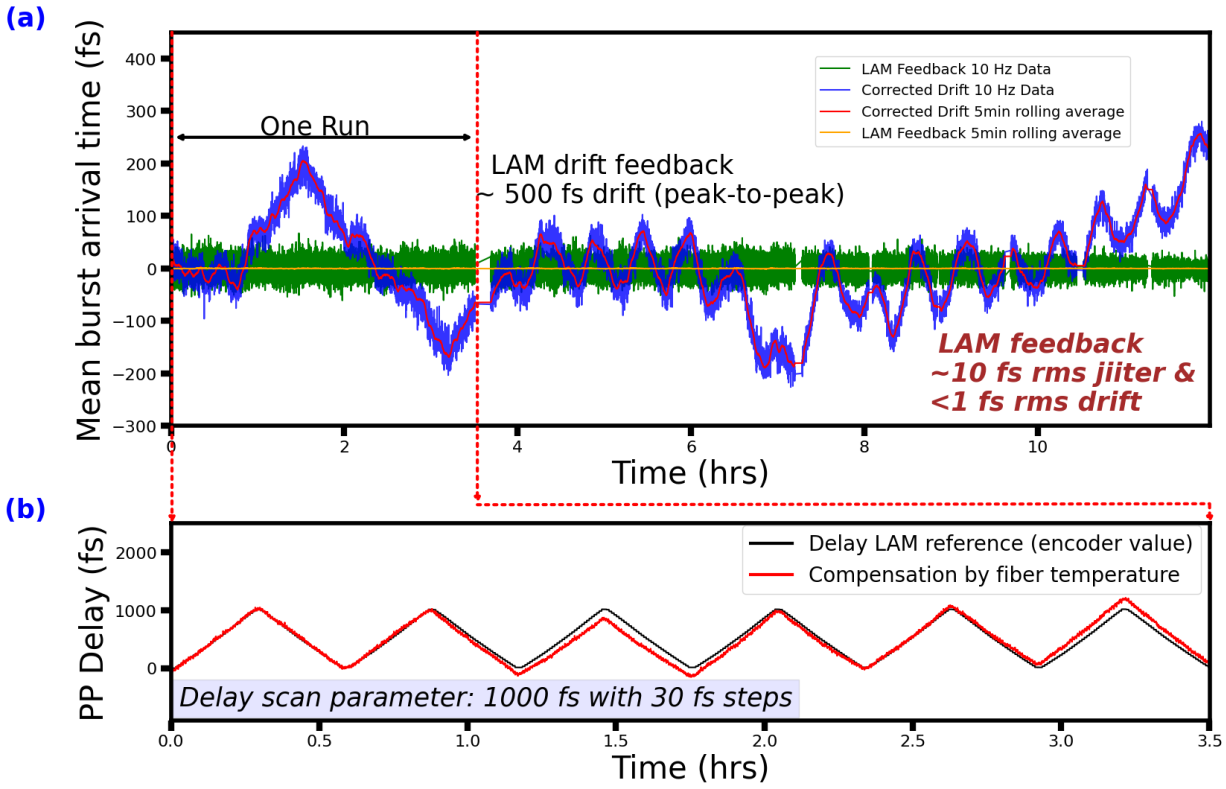

Figure 4.4: In-loop drift measurement of the LAM with internal feedback (FB2) over 12 hours. The mean arrival time values for each burst, recorded at a repetition rate of 10 Hz, are shown in green, while the yellow curve represents the five-minute rolling average. The blue trace shows the compensated drift, obtained by converting the applied fiber temperature changes into timing shifts. The measurement indicates a peak-to-peak drift of approximately 500 fs over the 12-hour period. (b) Measured delay stage position (black) and corresponding fiber temperature (red) over approximately four hours of laser operation, corresponding to the period labeled "one run" in panel (a). The scan range is 1 ps with a step size of 30 fs. The laser arrival time is scanned by delaying the LAM reference via FB2, thereby shifting the pump–probe laser arrival time through corresponding adjustments to the fiber temperature.

The oscillatory behavior observed in the timing drift likely results from independent feedback loops within the laser system and from thermal relaxation of the temperature-controlled fiber actuator. Additionally, environmental variations along the extended beam transport path to the experimental end station can accumulate over time and contribute to the observed timing drifts. Active LAM feedback is therefore essential for compensating these effects.

Fig. 4.4 (b) shows the effect of a delay scan on the relative arrival time during a single experimental run lasting approximately 4 hours. The LAM timing reference is shifted by Delay 2 (black curve), while the pump-probe laser arrival time follows this shift via FB2 feedback, adjusting the fiber temperature (red curve). The small difference between the two traces arises from the simultaneous compensation of slow timing drifts.

The delay scan spans 1 ps with a step size of 30 fs. Because the FB2 feedback responds without significant delay, the delay scan does not noticeably affect the in-loop jitter or drift shown in Figure 3(a). The pump-probe laser arrival time reliably tracks the LAM reference throughout the scan, demonstrating that the FB2 feedback and the temperature-controlled fiber actuator are effective for both drift stabilization and controlled-delay scans in typical user experiments.

4.2 Results

The performance of the implemented LAM stabilization scheme was evaluated using a pump–probe experiment on xenon. Laser-assisted xenon X-ray photoionization [123] provides a reliable method for quantifying the temporal resolution. Xenon is particularly well-suited for this purpose because its well-characterized photoionization dynamics and subsequent AM decay produce a clear temporal response. This allows precise determination of the temporal overlap between the FEL and optical laser pulses, providing a direct measure of the effective time resolution.

In this experiment, XUV pulses from the FEL with photon energies at 160 eV act as the pump. Photoionization of the 4*d* and 4*p* shells generates a core hole that relaxes within a few femtoseconds via AM decay, resulting in Xe^{2+} ions and a range of excited intermediate states [124]. Several of these states lie below the Xe^{3+} ionization threshold and exhibit lifetimes ranging from a few femtoseconds to several hundred picoseconds [125, 126]. A detailed discussion of xenon photoionization at this photon energy is provided in Chapter 5.

A delayed NIR probe pulse can further ionize these intermediate states, resulting in higher final charge states. Consequently, the Xe^{2+} yield decreases when the probe arrives after the pump pulse. Measuring the Xe^{2+} ion yield as a function of the XUV-NIR delay therefore provides a direct probe of the temporal response of the pump–probe interaction.

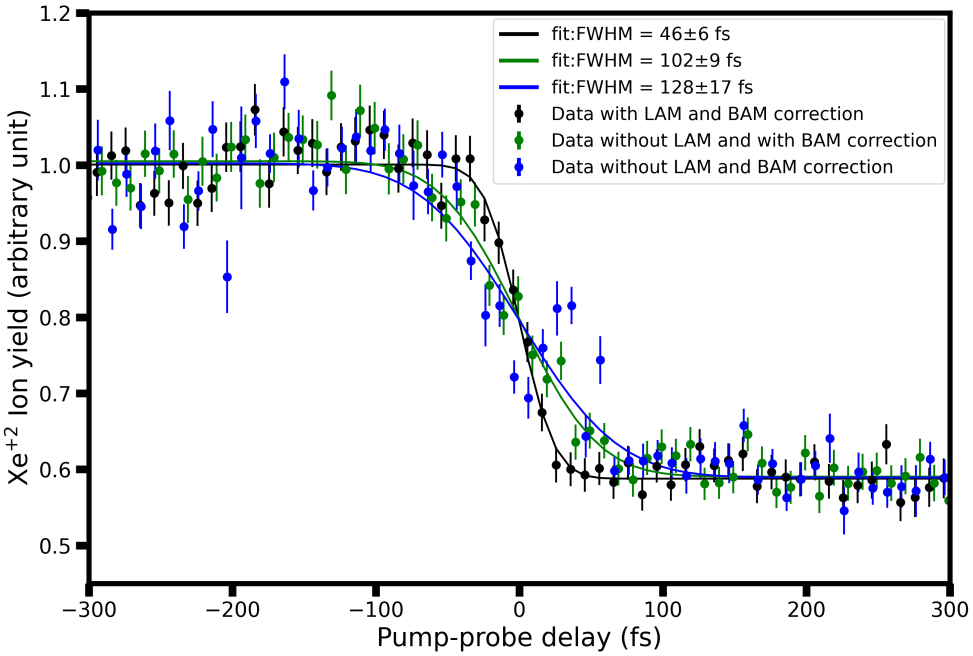

Figure 4.5: Xe^{2+} ion yield as a function of the delay between the XUV pump and the NIR probe. The curves are fitted with step functions convolved with a Gaussian to account for pulse duration and timing jitter. Without feedback, the intrinsic timing stability at FLASH2 yields a width of 130 fs FWHM (blue). Shot-to-shot timing correction using the BAM reduces this to 104 fs FWHM (green). With additional optical laser stabilization via LAM feedback, the width decreases to 46 ± 5 fs FWHM (black).

The data points shown in Fig. 4.5 correspond to Xe^{2+} yields averaged over 10 fs delay bins, with error bars representing the standard error of the mean. The corrected delays were grouped into 10 fs intervals and normalized by the number of shots per bin. To evaluate the impact of timing corrections, three delay definitions were compared: (i) the raw delay-stage

position, (ii) delays corrected shot-by-shot using the BAM, and (iii) delays corrected using the BAM with additional active stabilization of the laser with laser jitter.

For this measurement, the delay stage was scanned bidirectionally over a range of approximately ±0.5 ps. The delay was incremented in 30 fs steps, with data collected for 30 s at each position, resulting in a total acquisition time of approximately 1 h. Ion signals from the REMI DAQ were combined with FEL machine parameters from the FLASH control system, including LAM, BAM, FEL pulse energy (GMD), fiber temperature, and the raw pump–probe delay. The datasets were synchronized on a shot-by-shot basis during post-processing (see Section 3.3.5).

To remove unstable FEL and laser conditions, events were filtered by selecting the central regions of the LAM and FEL energy distributions (Fig. 4.6). This procedure suppresses outliers and ensures that only shots recorded under stable FEL and laser conditions are included in the analysis.

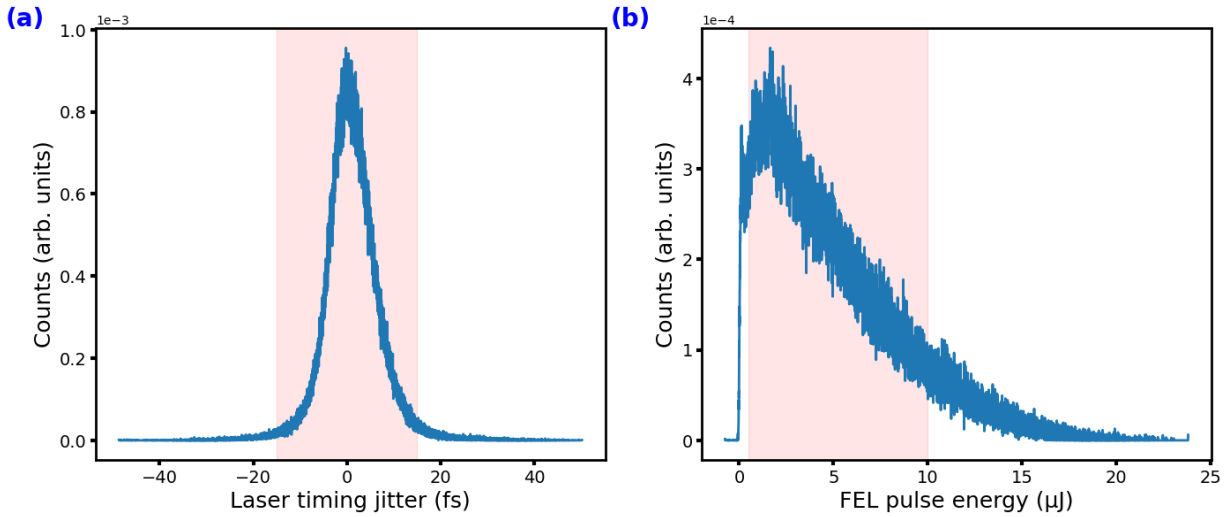

Figure 4.6: Event selection based on laser timing and FEL pulse energy. (a) Distribution of the laser arrival monitor (LAM) timing jitter. (b) Distribution of the FEL pulse energy. The red shaded regions indicate the selection windows used in the data analysis.

The delay-dependent signal was fitted using an error function of the form

$$f(t) = a + b\left[1 + \mathrm{erf}\left(\frac{t - t_0}{\sqrt{2}\sigma}\right)\right], \tag{4.1}$$

where a and b represent the baseline and amplitude, respectively, t_0 denotes the temporal overlap between the pulses, and σ corresponds to the standard deviation of the Gaussian instrument response. The extracted temporal width reflects the convolution of the temporal profiles of the XUV and NIR pulses, as well as residual timing jitter and slow temporal drifts in the experimental setup. A more detailed description of the fitting procedure is provided in Section 2.3.1.

Without timing correction, the fitted width is (130±17) fs FWHM (blue curve). Applying shot-to-shot BAM timing correction reduces the width to (104 ± 9) fs FWHM (green curve). When both BAM correction and active LAM feedback stabilization are applied, the width further decreases to (46 ± 5) fs FWHM (black curve), corresponding to an approximately two-fold improvement in temporal resolution.

To understand the achieved temporal resolution and its remaining limitations, the known sources of timing jitter and drift are considered. In this context, jitter refers to short-term fluctuations in pulse arrival time on a shot-to-shot basis, whereas drift describes slower

variations on timescales of minutes to hours. By averaging the experimental data over individual pulse trains, long-term drifts can be separated from the pulse-to-pulse jitter.

The electron bunch arrival time is measured on a shot-to-shot basis using the BAM. This allows correction of the relative timing between the electron bunch and the MLO, leaving a residual uncertainty determined by the BAM resolution of approximately $\sigma_{\mathrm{BAM}} \approx 5$ fs rms, limited by measurement noise. In addition, intrinsic arrival time fluctuations associated with the SASE process contribute an estimated jitter of $\sigma_{\mathrm{SASE}} \approx 3$ fs rms at a wavelength of 7 nm [127].

A dominant contribution to the temporal resolution originates from fluctuations in the arrival time of the optical laser pulses. In the absence of stabilization, slow drifts of several hundred femtoseconds can occur over timescales of minutes to hours, as illustrated in Fig. 3(a). The implemented active LAM feedback compensates these slow variations within the laser transport system, reducing drifts from approximately 500 fs peak-to-peak to about 1 fs peak-to-peak. Analysis of the LAM data indicates a residual pulse-to-pulse timing jitter of approximately 10 fs rms, which is comparable to the intrinsic timing jitter of the laser oscillator relative to the optical reference, $\sigma_{\mathrm{Osc-MLO}} \approx 6$ fs rms. This observation suggests that the amplification and transport stages of the optical laser mainly introduce slow timing drifts while contributing negligibly to the overall timing jitter.

The optical reference distribution itself contributes only a minor timing uncertainty of approximately $\sigma_{\mathrm{OptRef}} \approx 1$ fs rms [100]. Taking these contributions into account, the total timing jitter after sorting the data using the BAM signal can be estimated as

$$\sigma_{\mathrm{jitter}} = \sqrt{\sigma_{\mathrm{OptRef}}^2 + \sigma_{\mathrm{BAM}}^2 + \sigma_{\mathrm{SASE}}^2 + \sigma_{\mathrm{LAM-jitter}}^2}. \tag{4.2}$$

This results in an estimated total timing jitter of approximately 12 fs rms, corresponding to about 29 fs FWHM.

The overall experimental temporal resolution is obtained by combining this timing jitter with the durations of the XUV and NIR pulses. Assuming pulse durations of $\tau_{\mathrm{XUV}} \approx (20 \pm 10)$ fs FWHM and $\tau_{\mathrm{Laser}} \approx (18 \pm 10)$ fs FWHM, the effective temporal resolution can be approximated by

$$\tau_{\mathrm{resolution}} = \sqrt{\tau_{\mathrm{XUV}}^2 + \tau_{\mathrm{Laser}}^2 + \sigma_{\mathrm{jitter}}^2}. \tag{4.3}$$

This yields a temporal resolution of approximately (40 ± 12) fs FWHM, which is in good agreement with the experimentally measured values within the given uncertainties.

Potential sources of residual timing drift and jitter of the laser may lie outside the active feedback loop. In particular, approximately 4 m of the NIR beam path from the MOD2.6 (see Fig.4.1) to the interaction region remains outside the stabilization scheme. In addition, mechanical vibrations of the optical component in the attached in-coupling box with the REMI setup, for example, those induced by vacuum pumps, may contribute to residual timing instabilities.

The length and temperature variations of the remaining 4 m beam path are monitored during the experiment using an interferometer (SIOS SP 15000 NG, SIOS Messtechnik GmbH) with sub-nanometer precision. The additional timing jitter introduced by this section of the beam path was measured to be below 1 fs rms, while the drift observed during the measurements presented here was approximately 6 fs peak-to-peak. A detailed analysis is provided in Appendix B.2.

4.3 Summary

An active feedback stabilization scheme based on drift correction using the LAM, which measures laser timing jitter and compensates timing drifts, has been successfully implemented and characterized. This scheme was first realized at the FLASH2 beamline FL26. Using the LAM system, a benchmark two-color XUV–NIR pump–probe experiment on xenon was performed, achieving a temporal resolution of 46 ± 5 fs FWHM over an hour-long measurement period. This performance was enabled by the combination of long-term drift suppression via active feedback, shot-to-shot laser and FEL timing jitter. Prior to the implementation of the LAM system, the effective time resolution at the FLASH2 beamlines typically ranged from 150 to 300 fs FWHM, highlighting the substantial improvement achieved.

The enhanced temporal resolution demonstrated in the FEL-NIR pump-probe experiment significantly extends the range of ultrafast phenomena accessible at FLASH. It enables real-time investigations of fundamental processes, including molecular vibrations, charge migration [128], and short-lived transient excited states [125] that evolve on femtosecond timescales. Furthermore, the LAM feedback loop maintains timing stability of approximately ± 30 fs over extended periods, enabling long data acquisition runs without frequent realignment, timing-overlap scans, or experimental interruptions. This stability significantly improves the efficiency and throughput of experimental data, particularly for complex or statistically demanding measurements.

Further improvements in timing diagnostics are anticipated, particularly through the installation of the LAM feedback loop closer to the interaction region. Such developments are expected to further reduce residual timing errors and improve overall synchronization performance. With these enhancements, achieving a temporal resolution below 10 fs appears feasible, thereby opening access to an entirely new class of ultrafast dynamics for experimental investigation.

Looking ahead, future developments at FLASH include the implementation of seeded FEL operation, which is expected to provide significantly improved temporal coherence and stability compared to SASE operation. Seeded FLASH pulses offer enhanced control over temporal pulse shape, reduced pulse duration, and lower timing jitter, enabling more precise and reproducible pump-probe delay scans. Together, these advances position FLASH as a leading platform for high-precision ultrafast science, facilitating studies of dynamical processes spanning the femtoseconds-to-attoseconds regime.

Chapter 5

Xenon Photoionization Dynamics in the Vicinity of the $4d$ Giant Resonance and Cooper Minimum

5.1 Introduction

Time-resolved X-ray spectroscopy can provide insights into the dynamics of electronic structure and relaxation processes in atoms and molecules. A fundamental process that governs many dynamical processes and thus motivates numerous studies is the creation and decay of core holes. When atoms and molecules absorb high-energy photons, a core electron is ejected, creating a highly excited ionic state (see Fig. 2.5). This excited, unstable state rapidly relaxes, often via AM decay [130]. In this non-radiative process, outer-shell electrons fill the core vacancy, releasing energy by emitting an AM electron. Probing the dynamics of this core-hole creation and its subsequent decay on the timescale of a few femtoseconds is essential for understanding electron correlation.

Xenon (Xe) serves as a benchmark atomic system for studying these ultrafast phenomena in the XUV regime. Xe has complex multielectron dynamics, particularly in the $4d$ subshell, with a pronounced maximum in its photoionization cross-section, well known as the "giant resonance". This resonance significantly enhances absorption and profoundly affects subsequent relaxation dynamics, making Xe an ideal candidate for theoretical models. Another significant feature in Xe photoionization is the Cooper minimum near the photon energy of 160 eV. At this energy, the photoionization cross-sections for the $4d$ and $4p$ subshells become comparable. Studying Xe, especially around the Cooper minimum, thus provides critical insights into the fundamental photoionization process.

A variety of experimental techniques have been employed to investigate the ionization dynamics of xenon following inner-shell ionization, including multielectron coincidence measurements [131], ion–electron coincidence spectroscopy [132], time-resolved multielectron spectroscopy [133], and ion TOF spectroscopy [134], as well as measurements of charge-state distributions and ion yields as a function of incident photon energy [135–138]. These studies have provided valuable insight into the production probabilities of multiply charged ions and the cascade pathways associated with AM decay.

Particular interest has focused on the formation and decay of double-core-hole states in Xe, such as the $4d^{-2}$ configuration. These states may be produced through strongly correlated electronic processes involving $4p$ orbitals [139] or through sequential AM decay following

This chapter is based on work published in Physical Review A; see Ref. [129]. Sonu Kumar, the author of this thesis, is the first author of the publication and was involved in the experiment, data analysis, and preparation of the manuscript.

the formation of a $4s^{-1}$ core hole [140]. Previous investigations employing multielectron–ion coincidence spectroscopy have resolved several ionization pathways leading to these configurations and have provided detailed insight into their formation mechanisms [141, 142]. However, experimental access to the temporal sequence and lifetimes of the intermediate states involved in these decay cascades remains challenging due to their extremely short lifetimes and the limited temporal resolution of earlier experimental approaches.

In this chapter, the AM decay dynamics of xenon following inner-shell ionization are investigated using ion TOF spectroscopy in combination with XUV pump NIR probe measurements. In the first part of this chapter, the relative ion yields of multiply charged xenon ions are measured at two photon energies, 90 eV and 160 eV. The photon energy of 90 eV serves as a reference point due to the large photoabsorption cross section associated with the well-known xenon giant resonance [143]. In contrast, 160 eV lies near the Cooper minimum, where the photoionization cross sections of the $4d$ and $4p$ subshells are similar [144]. A comparison of the resulting charge-state distributions provides insight into the dominant decay pathways following inner-shell ionization.

In the second part of the chapter, time-resolved XUV pump-NIR probe measurements are performed to investigate the temporal evolution of the intermediate states involved in the AM decay cascade. By analyzing the delay-dependent ion yields, characteristic lifetimes of transiently populated states can be extracted. These measurements provide further insight into the relaxation dynamics of xenon following inner-shell ionization and allow direct comparison with previously reported results obtained at similar photon energies for 90 eV [125, 145]. The results presented in this chapter, therefore, contribute to a deeper understanding of correlated electron dynamics and ultrafast decay processes in atomic systems.

5.2 Experimental Methods

The experiments were performed at the FLASH FEL facility using the REMI end-station at the FL26 beamline during two separate beam times. A detailed description of the REMI apparatus, the FLASH source, and the pump–probe configuration is provided in Chapter 3. The two beam times were conducted at photon energies of 90 eV and 160 eV, respectively. These photon energies were selected to investigate xenon photoionization dynamics in the vicinity of the $4d$ giant resonance and the Cooper minimum.

A detailed description of the FEL and NIR laser pulse parameters is provided in the Appendix A. The XUV SASE pulses had a duration of approximately (20 ± 10) fs (FWHM) and were synchronized with NIR laser pulses of wavelength centered at 800 nm with a duration of (15 ± 3) fs (FWHM). The corresponding average XUV pulse energies were about 1.5 μJ at 90 eV and 2 μJ at 160 eV, yielding peak intensities on the order of 10^{13} W/cm^2. The overall temporal resolution of the experiment, determined from cross-correlation measurements (see Chapter 4), was (46 ± 5) fs (FWHM).

The xenon dynamics were investigated using ion TOF-MS. Both beams were spatially and temporally overlapped and focused onto a supersonic xenon gas jet located at the center of the REMI spectrometer. The XUV focal spot size was approximately 25 μm (FWHM), while the NIR focal spot size was about 50 μm (FWHM). Ions generated in the interaction region were extracted by a homogeneous electric field and detected using a time- and position-sensitive detector (see chapter section 3.3) for more details.

5.2.1 Data Acquisition and Analysis

Xenon ions were detected using a delay-line REMI detector, which records the impact position (x, y) and TOF for each detected ion in list-mode files. The experiments were performed during two separate beam times, with consistent data analysis procedures applied in both cases. Data acquisition and online monitoring were carried out using the Go4 software framework. A detailed description of the data acquisition system, including the merging of REMI and FLASH DAQ data and the subsequent analysis, is provided in subsection 3.3.5.

The data analysis was carried out in several stages. In the first stage, the detector coordinates and the TOF offset were calibrated. In the second stage, background removal was performed, and the calibrated, filtered data were merged with the FLASH DAQ for further time-resolved analysis.

Background suppression was achieved by applying TOF-dependent filters to the detector signals. Linear boundaries of the form $y = mx + c$ were used to constrain the valid region in the X-position (jet direction), while constant limits $y = \pm c$ were applied along the Y-direction (FEL direction) as shown in Fig. 5.1(a) and (b). These conditions define a region of interest (ROI) for the ions and suppress background contributions from other ions with similar TOF. The figure corresponds to data recorded at a photon energy of 160 eV; the same filtering procedure was also applied to the 90 eV dataset.

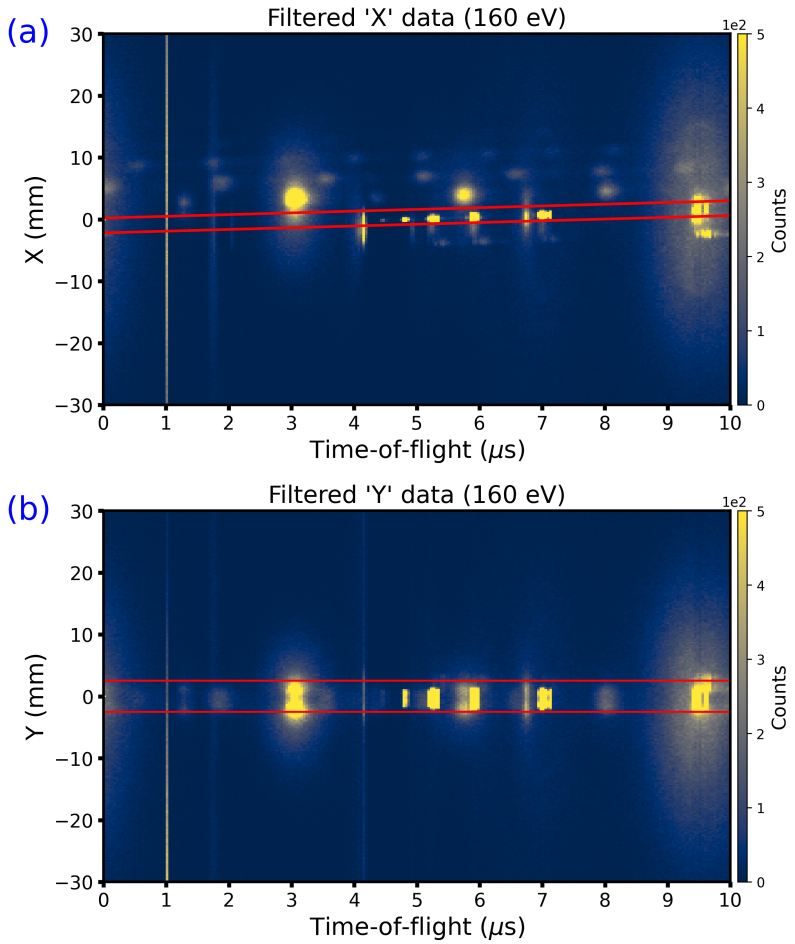

Figure 5.1: Filter applied to 2D histograms of detector position versus TOF. The red lines indicate the selection boundaries used to define the region of interest (ROI): (a) filtering in the X-direction and (b) filtering in the Y-direction. Only events within these boundaries are retained for further analysis.

After background filtering, the cleaned REMI data were merged with the FLASH DAQ data based on the TrainID. Pump–probe delay was corrected using single pulse BAM and LAM data to account for timing jitter between the pump and probe pulses. The corrected delays were grouped into 20 fs-wide bins to improve statistical reliability, analogous to the procedure described in Chapter 4. The pump–probe scan was performed by varying the NIR delay stage in 30 fs steps, with 25,000 shots recorded at each delay point.

Ion yields for different xenon charge states were extracted by selecting and summing counts within the corresponding ion TOF ranges. The yields were normalized to the number of shots per delay step. To account for pulse-to-pulse fluctuations inherent to the SASE, only pulses within the 1-5 μJ energy range were considered, and the ion yields were further normalized to the FEL pulse energy on a shot-by-shot basis. To further improve temporal resolution, additional slicing based on the LAM and BAM distributions was performed to remove outliers.

5.3 Results

5.3.1 Mass Spectra and Relative Ion Yields

The mass spectra of multiply charged xenon ions obtained following interaction with XUV pulses at photon energies of 90 eV and 160 eV are presented in Fig. 5.2(a) and (b), respectively. The presence of multiple peak structures within individual charge states is attributed to the natural isotopic distribution of xenon. At a photon energy of 90 eV (Fig. 5.2(a)), xenon charge states Xe^{q+} (q = 2-4) are clearly observed in the mass spectrum. The measured mass spectrum closely matches that reported in earlier studies under low-FEL irradiance conditions [145, 146]. Among the observed species, Xe^{2+} constitutes the dominant contribution (56%), followed by Xe^{3+} (43%) [146]. These relative ion yields provide an estimate of the branching ratios, defined as the yield of a particular charge state relative to the total ion yield resulting from the decay of core-hole excited Xe^{+}. The corresponding branching ratios for 90 eV are summarized in Table 5.1.

Fig. 5.3 shows the energy-level scheme and possible transition responsible for the formation of higher charge states after XUV photoionization, along with the additional transition accessible by the NIR probe pulse discussed later section. At 90 eV, the photoionization process is dominated by single photon absorption via the giant $4d \rightarrow \varepsilon f$ continuum resonance. The resulting core-hole excited $4d^{-1}$ state primarily decays to Xe^{2+} through a single AM process leading to a $5p^{-2}$ configuration, and to Xe^{3+} via a subsequent second AM decay also known as double AM decay.

The AM decay of Xe 4d core-hole states ($4d^{-1}_{3/2}$ and $4d^{-1}_{5/2}$), as well as 4d shake-up satellites in configurations such as $4d^{-1}5p^{-1}nl$, predominantly produces intermediate Xe^{2+} states. These states are denoted as "a" and "b" in Fig.5.3 (likely corresponding to the $5s^{-1}5p^{-2}7p$ configuration) located above, and "c" below, the Xe^{3+} threshold (associated with Rydberg series such as $5s^{-1}5p^{-2}6p$ or $5p^{-3}nl$ [125]). These intermediate Xe^{2+} states subsequently decay via a second AM process to various Xe^{3+} states [147, 148]. Additionally, direct double AM decay, in which two electrons are emitted simultaneously, contributes to the Xe^{3+} yield (not shown) [149]. The very small fraction of Xe^{4+} ($< 1\%$) observed at 90 eV indicates that single-photon absorption is the dominant mechanism [148].

At a higher photon energy of 160 eV, the mass spectrum shows the formation of higher charge states, Xe^{q+} (q = 2–6), as shown in Fig. 5.2(b). The most abundant species is Xe^{3+} (38%), followed by Xe^{4+} (33%) and Xe^{2+} (29%), as listed in Table 5.2. This photon energy exceeds the ionization threshold of the 4p subshell (binding energy 145.6 eV [8]) but remains below that of the 4s subshell (213.32 eV [140]). A single XUV photon can ionize electrons

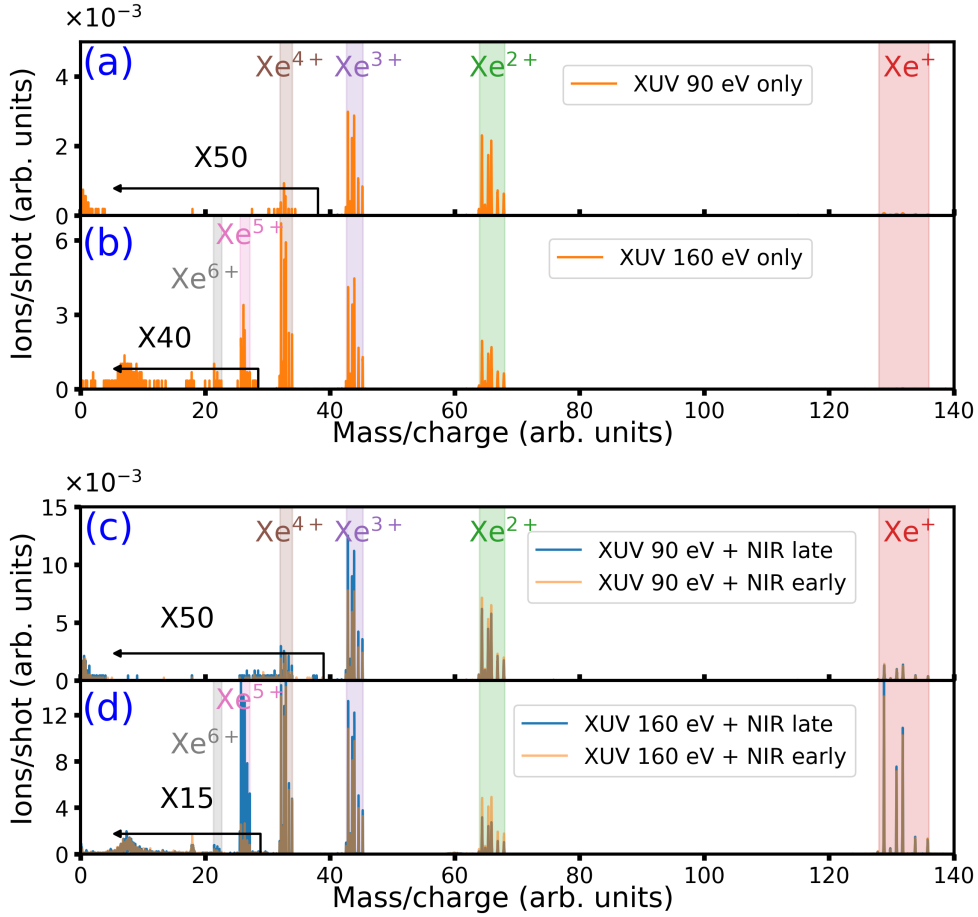

Figure 5.2: Mass-to-charge (m/q) spectra of xenon ions recorded at photon energies of (a) 90 eV and (b) 160 eV. The lower panels show spectra obtained in the presence of both XUV and NIR pulses at early and late delays of 100 fs: (c) 90 eV XUV with NIR and (d) 160 eV XUV with NIR. For better visibility in the low-m/q region, the ion intensities were scaled by factors of 50 in (a), 40 in (b), 50 in (c), and 15 in (d), corresponding to $m/q < 40$ in (a,c) and $m/q < 30$ in (b,d). The multi-peak structure arises from the natural isotopes of xenon.

Ion	XUV (90 eV)	XUV+NIR (early)	XUV+NIR (late)
Xe^{2+}	57%	59%	48%
Xe^{3+}	43%	41%	52%
Xe^{4+}	$\ll 1\%$	$\leq 1\%$	$\leq 1\%$

Table 5.1: Relative ion yields of xenon following 4*d* ionization at a photon energy of 90 eV. The yields are shown for XUV-only excitation and for combined XUV+NIR excitation at early (negative delay) and late (positive delay) of approximately 100 fs. The values are extracted from the ion yield intensities of the TOF spectra shown in Fig. 1(a,c). The measurement uncertainty is on the order of a few percent.

from both the 4*d* and 4*p* subshells, and subsequent AM decay processes lead to final charge states of Xe^{2+}, Xe^{3+}, and Xe^{4+}.

The 4*d* ionization cross section at 160 eV is approximately one order of magnitude lower than at 90 eV [143] and approaches a minimum near 180 eV, known as the Cooper minimum [139, 151]. In the vicinity of this minimum ($\sim$ 160 eV), the ionization cross sections of the 4*d* and 4*p* subshells become comparable [144]. As a result, Xe^{3+} and Xe^{4+} ions are predominantly produced through AM cascades following ionization of both subshells.

Ion	XUV (160 eV)	XUV+NIR (early)	XUV+NIR (late)
Xe^{2+}	29%	30%	17%
Xe^{3+}	38%	38%	46%
Xe^{4+}	33%	31%	34%
Xe^{5+}	$\ll 1\%$	$\leq 1\%$	3%
Xe^{6+}	$\ll 1\%$	$\ll 1\%$	$\leq 1\%$

Table 5.2: Relative ion yields of xenon following combined $4d$ and $4p$ ionization at a photon energy of 160 eV. The yields are shown for XUV-only excitation and for XUV+NIR excitation at early (negative delay) and late (positive delay).

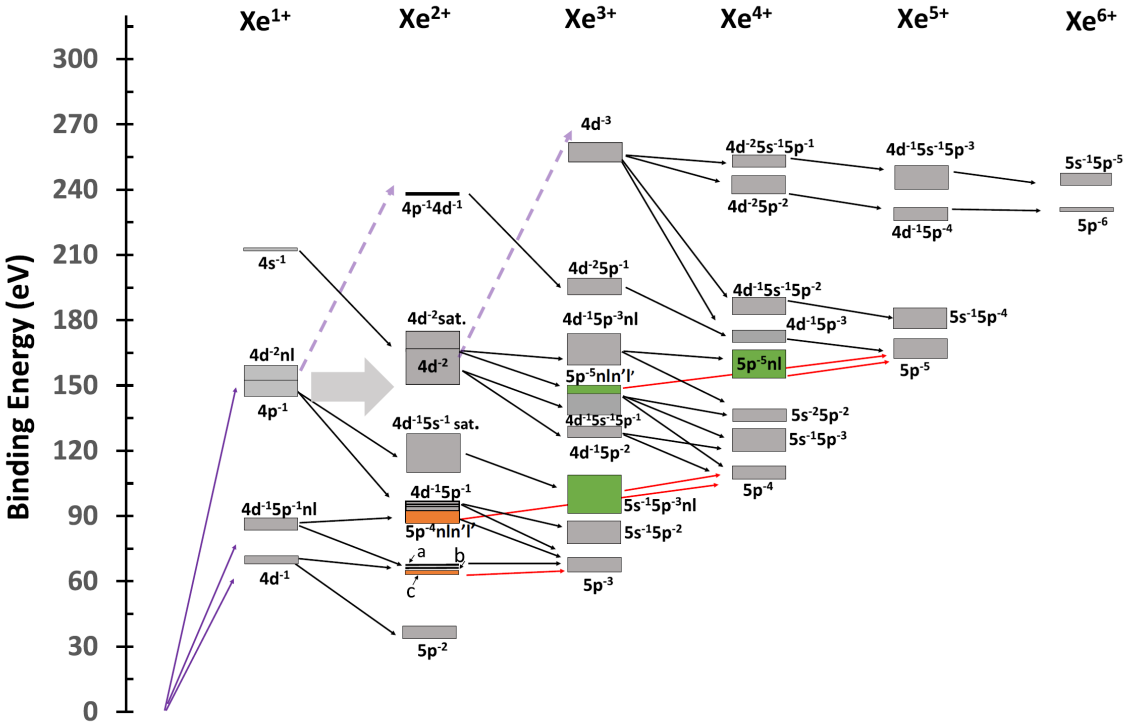

Figure 5.3: Energy-level diagram of the most relevant states of Xe^{q+} ($q = 1$–6) lying below a binding energy of 320 eV. Neutral xenon is excited or ionized by XUV radiation (purple solid arrow). The subsequent AM transitions most relevant to this study are indicated by black arrows. The gray boxes represent the binding-energy ranges of the corresponding states, with AM transitions taken from Refs. [8, 124, 131, 132, 140, 141, 150]. The light-gray horizontal arrow denotes the super-Coster–Kronig (sCK) transition (see text). The green and orange boxes indicate possible intermediate states probed by the NIR field, as shown by the red arrows. The dashed purple arrow represents a possible second-photon absorption leading, for example, to the $4d^{-3}$ state.

Recent theoretical studies [152] support the dominant formation of Xe^{3+} associated with primary $4p$ photoionization, as also observed in multielectron coincidence experiments [132]. The potential pathway for the formation of Xe^{4+} involves the population of $4d^{-2}$ states via super-Coster–Kronig (sCK) [139] transitions following $4p$ ionization, followed by subsequent AM decay. Therefore, two distinct decay pathways originating from $4p^{-1}$ and $4d^{-2}$ configurations must be considered at 160 eV.

The $4p^{-1}$ vacancy decays via single and cascaded AM processes, predominantly populating satellite states such as $4d^{-1}5p^{-1}$ and $4d^{-1}5s^{-1}$, as well as configurations of the

form $4d^{-1}5p^{-2}(5d, 6s)^1$ [8]. In contrast, the decay of doubly ionized $4d^{-2}$ states, previously investigated in soft x-ray photoabsorption experiments [124, 141], proceeds via Xe^{2+} to Xe^{3+} ($4d^{-1}5p^{-2}$), which further decays into configurations such as $5s^{-1}5p^{-3}$ or $5p^{-4}$, ultimately leading to Xe^{4+}.

The comparatively large yields of Xe^{4+} indicates that ionization pathways involving excitation and subsequent decay of $4d^{-2}$ states play a dominant role in the formation of higher charge states under these conditions.

5.3.2 Intensity-Dependent Ion Yields

The observation of Xe^{4+} at 90 eV and Xe^{5+} and Xe^{6+} at 160 eV, as shown in Fig. 5.2, indicates that at least two photons must be absorbed, since a single photon does not have sufficient energy to reach the corresponding ionization thresholds. The higher harmonic spectral content in the FEL could, in principle, contribute to the formation of such high charge states; however, the reflectivity of the FL26 beamline mirrors strongly suppresses the second- and third-harmonic components to the 10^{-4}–10^{-5} level relative to the fundamental, thereby ruling out any significant harmonic contribution.

The dependence of the ion yields on the XUV pulse energy provides insight into the underlying ionization mechanisms. The ion yields Y as a function of pulse energy I were analyzed using a double-logarithmic representation, where the data were fitted with a linear function.

$$\log(Y) = m \log(I) + c, \tag{5.1}$$

with the slope m corresponding to the effective number of absorbed photons.

At a photon energy of 90 eV, low charge states such as Xe^{2+} and Xe^{3+} exhibit an approximately linear dependence on intensity over a broad range, as shown in Fig. 5.4(a). This behavior is characteristic of single-photon ionization followed by AM decay. In contrast, the Xe^{4+} yield shows a steeper slope ($m > 1$), indicating the involvement of multiphoton ionization.

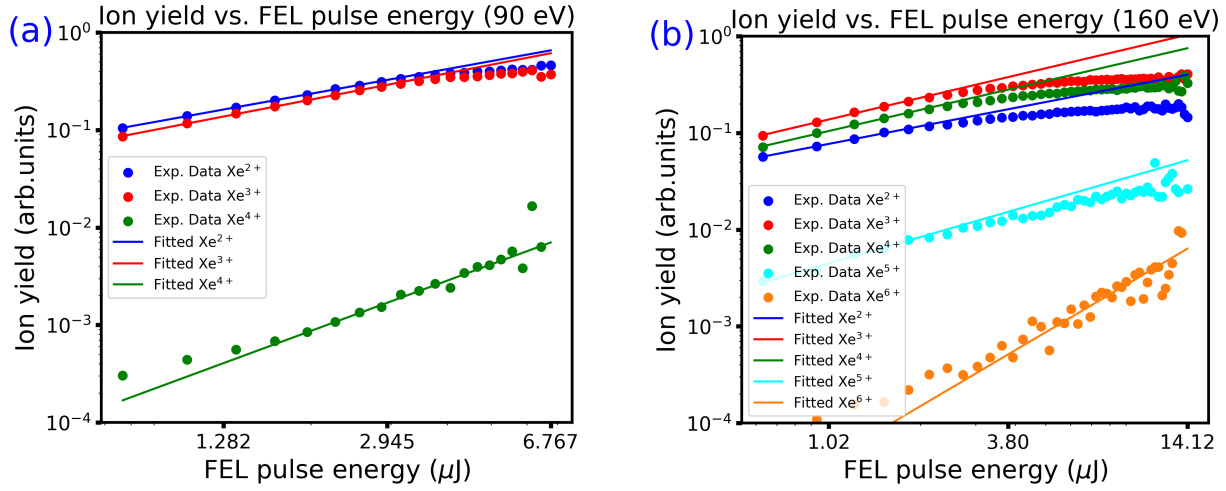

Figure 5.4: Ion yield as a function of the FEL pulse energy for xenon ions recorded at photon energies of 90 eV (a) and 160 eV (b). The data are fitted with a linear function on a double-logarithmic scale. At 160 eV, the formation of Xe^{6+} is observed from pulse energies of approximately 2 μJ.

A similar feature is observed at 160 eV (Fig. 5.4(b)), where the Xe^{5+} and Xe^{6+} ion yields show nonlinear scaling with intensity, with slopes exceeding unity. These observations

indicate that the formation of higher charge states proceeds predominantly via sequential multiphoton ionization rather than through contributions from higher harmonics of the XUV beam.

At the higher FEL pulse energy, the ion yield tends to saturate, attributed to the depletion of neutral xenon atoms within the interaction volume.

5.3.3 Delay-dependent Ion Yields at 90 eV

The delay-dependent mass spectra at 90 eV are shown in Fig. 5.2(c), and the corresponding relative ion yields obtained in the pump-probe scheme are listed in Table 5.1. Here, NIR pulses arriving 100 fs before and after the XUV pulse are referred to as "early" and "late", respectively. The delay range of ±0.5 ps was scanned multiple times in both directions for each measurement set. By convention, positive delays correspond to the NIR pulse arriving after the XUV pulse, and negative delays to the opposite case. Details of the data analysis and normalization procedures are described in the previous section 5.2.1.

Compared to the mass spectrum obtained with XUV-only excitation (Fig. 5.2(a)), the relative ion yields Xe^{q+} ($q = 2$–4) remain largely unchanged for negative delays. In contrast, for positive delays, the Xe^{3+} yield increases by approximately 25%, while the Xe^{2+} yield decreases by about 18%. This behavior is attributed to the ionization of intermediate Xe^{2+} states by the NIR pulse, as indicated by the red arrows in Fig. 5.3. The Xe^{+} ion yield is predominantly generated by the NIR pulse alone.

Fig. 5.5 shows the delay-dependent ion yields for Xe^{2+}, Xe^{3+}, and Xe^{4+} at 90 eV. In Fig. 5.5(a), the Xe^{2+} (left axis) and Xe^{3+} (right axis) yields are plotted as a function of the XUV-NIR delay. For positive delays, a pronounced decrease in the Xe^{2+} signal (black dots with error bar) is observed near zero delay, where the pump and probe pulses temporally overlap. This decrease is accompanied by a rapid increase in the Xe^{3+} yield (blue dots with error).

The delay-dependent change in the Xe^{2+} signal arises from XUV-induced creation of a $4d^{-1}$ core hole in Xe^{+}, followed by an ultrafast AM decay (lifetime ~ 6 fs [153]), which populates intermediate Xe^{2+} states within the cross-correlation time $\tau_{cc} \approx 30$ fs of the pump and probe pulses. These intermediate states are susceptible to further ionization by the NIR pulse. For large positive delays, Xe^{2+} predominantly relaxes to its ground-state $5p^{-2}$ configuration.

The observed increase in the Xe^{3+} yield is attributed to NIR-induced ionization of excited Xe^{2+} states, such as $5s^{-1}5p^{-2}6p$ [149] and $5p^{-3}nl$ configurations (denoted by "c" in Fig. 5.3), which lie just below the Xe^{3+} threshold and cannot decay spontaneously. These states have long lifetimes exceeding ~ 100 ps [125, 126]. Consequently, the delayed NIR pulse efficiently ionizes these states, leading to a sustained increase in the Xe^{3+} yield. No decrease in the Xe^{3+} signal is observed at large positive delays, consistent with the long lifetime of the intermediate states relative to the experimental timescale and in agreement with previous studies [125]. The resulting Xe^{3+} ions predominantly occupy the ground-state $5p^{-3}$ configuration.

For negative delays, where the NIR pulse precedes the XUV excitation, the relaxation pathways of the $4d^{-1}$ and $4d^{-1}5p^{-1}nl$ states are only weakly affected by the probe pulse. These features observed in the Xe^{2+} and Xe^{3+} signals arise from the interplay between the initial AM decay and the subsequent NIR-induced ionization, and are convolved with the finite temporal resolution of the experiment. To quantify this behavior, the data are fitted using a Gaussian error function.

$$f_1(t) = A_0 + A_1 \left[1 + \mathrm{erf}\left(\frac{t - t_0}{\tau_{cc}} \right) \right], \tag{5.2}$$

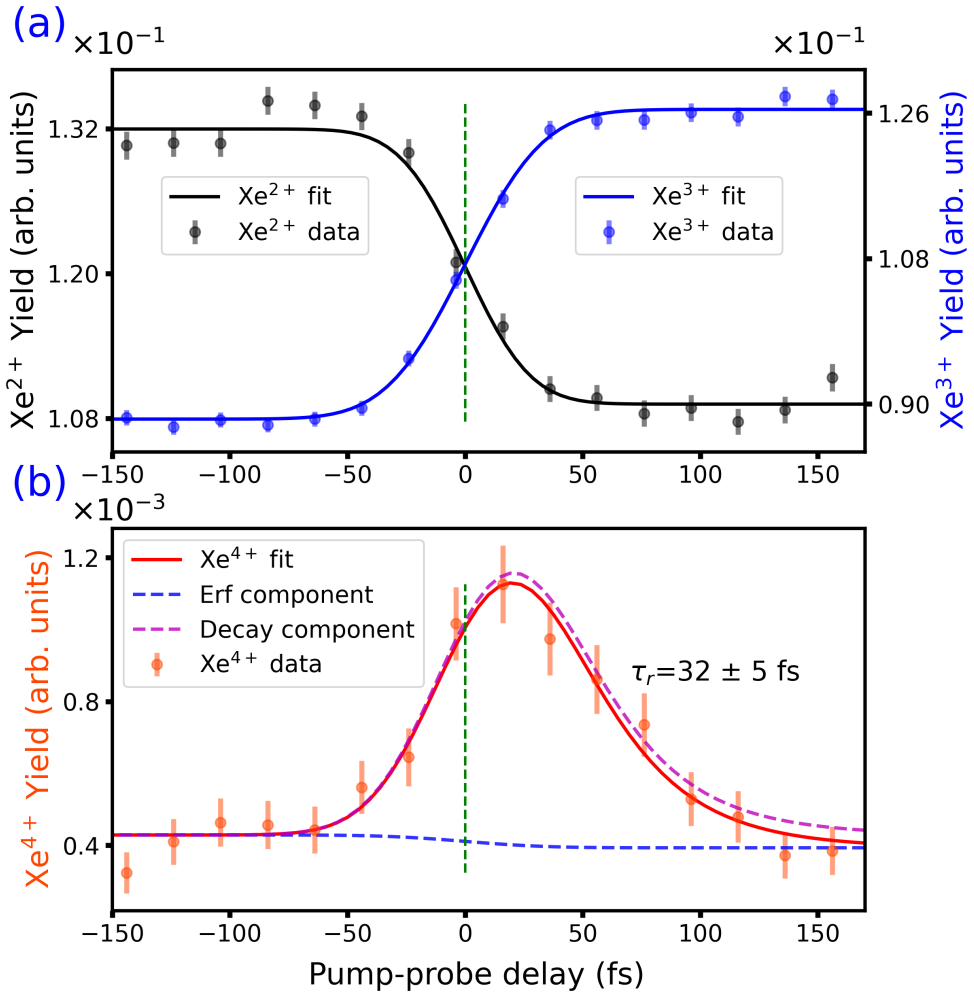

Figure 5.5: Ion yields of Xe^{q+} (q = 2–4) as a function of the delay between the 90 eV XUV pump and NIR probe pulses. (a) Ion yields of Xe^{2+} (left) and Xe^{3+} (right) as a function of the pump–probe delay. Over the same delay range, the Xe^{2+} yield decreases while the Xe^{3+} yield increases. The dots and error bars represent the average values and the corresponding standard errors of the measurements, respectively. The solid black and blue curves correspond to fits using the function given in Eq.5.2, yielding cross-correlation times of (30 ± 3) fs for Xe^{2+} and (37 ± 2) fs for Xe^{3+}, respectively. (b) For Xe^{4+}, the ion yield as a function of delay is fitted with an exponential model5.3, showing an average lifetime of (32 ± 5) fs. The purple and blue curves represent the exponential and step-function components of the fit, respectively, while the solid red curve shows their combined contribution.

where A_0 represents the baseline, A_1 the amplitude, t_0 the temporal offset, and τ_{cc} the cross-correlation time determined by the pulse durations, timing jitter, and experimental drifts. From the fit to the Xe^{2+} data, $\tau_{cc} = (30 \pm 3)$ fs is obtained.

At a photon energy of 90 eV, Xe^{4+} cannot be efficiently produced via single-photon absorption (threshold $\sim$ 106 eV). While less than 1% Xe^{4+} is observed under XUV-only conditions, its yield increases by approximately a factor of two in the pump-probe experiment. In addition to this overall enhancement, a pronounced transient feature is observed in the Xe^{4+} signal. As shown in Fig. 5.5(b), the Xe^{4+} yield initially rises and subsequently decays rapidly.

This transient behavior in Xe^{4+} is attributed to NIR-induced double ionization of short-lived doubly excited $5p^{-4}nl$ states of Xe^{2+} (indicated in Fig. 5.3), which decay to Xe^{3+} in the

$5p^{-3}$ configuration via a second AM process [125, 138]. The temporal evolution of the Xe^{4+} yield is described by a model combining the Gaussian error function with an exponential decay (see Sec. 2.3.1 for details),

$$f(t) = f_1(t) + A_2 \exp\left(-\frac{t-t_0}{\tau_r}\right)\left[1 + \mathrm{erf}\left(\frac{t-t_0}{\tau_{cc}} - \frac{\tau_{cc}}{2\tau_r}\right)\right]\exp\left(\frac{\tau_{cc}^2}{4\tau_r^2}\right), \tag{5.3}$$

where A_2 defines the amplitude of the transient contribution and τ_r represents the effective decay time of the intermediate states. The fit to the data is shown in Fig. 5.5(b) (orange solid line) and yields an average lifetime of (32 ± 5) fs. This value is attributed to the doubly excited intermediate Xe^{2+} states involved in the decay cascade, primarily of the $5p^{-4}nl\,n'l'$ configuration, and is in excellent agreement with previous time- and energy-resolved measurements [125, 147].

5.3.4 Delay-dependent Ion Yields at 160 eV

At photon energy of 160 eV, ionization occurs from both $4p$ and $4d$ subshells, whose cross sections are comparable. As a result, the branching ratios of the ion yields differ from 90 eV. The relative ion yields of Xe^{q+} ($q = 2$–6) remain nearly unchanged for XUV-only excitation and for negative pump-probe delays. In contrast, for positive delays, a clear redistribution of the ion yields is observed. The yield of Xe^{2+} decreases by approximately 41%, while the yields of Xe^{3+} and Xe^{4+} increase by about 21% and 3%, respectively. The most pronounced changes occur for Xe^{5+} and Xe^{6+}, which show strong relative increases of roughly 200% and 100%.

Fig.5.6 shows the delay-dependent ion yields measured at 160 eV. As in the 90 eV case, the Xe^{2+} signal exhibits a step-function behavior. This indicates that intermediate states are formed by the XUV pulse and are subsequently ionized by the delayed NIR pulse. The yields of Xe^{3+} and Xe^{4+} increase for positive delays, suggesting that long-lived intermediate states play an important role.

The behavior of Xe^{3+} can be understood as arising mainly from NIR-induced ionization of intermediate states created after $4d$ core-hole ionization, as discussed in the last section. However, the overall change in Xe^{3+} is less pronounced than at 90 eV. This is because, at 160 eV, a significant fraction of Xe^{3+} is already produced via $4p$ ionization pathways, which are not strongly affected by the NIR pulse.

The time-dependent Xe^{4+} yield can be attributed to ionization of intermediate Xe^{3+} states, such as those in the $5s^{-1}5p^{-3}nl$ and $5p^{-4}nl$ configurations, which lie below the Xe^{4+} ionization threshold. The delay dependence of both Xe^{3+} and Xe^{4+} is fitted using the model described in Eq.5.2. Their temporal evolution reflects contributions from both $4p$- and $4d$-initiated processes, as well as the interplay between AM decay and NIR-induced ionization. These contributions, however, cannot be fully separated using ion TOF measurements alone.

A particularly strong transient feature is observed in the Xe^{5+} yield, as shown in Fig. 5.6(c). The signal rises within a few tens of femtoseconds and then decays. This behavior can be understood in terms of competing processes involving intermediate states in the decay cascade. Long-lived states, such as $5p^{-5}nl\,n'l'$, can be further ionized by the NIR pulse. The initial rise in the Xe^{5+} signal is attributed to NIR-induced double ionization of these states, leading to the formation of Xe^{5+}. The subsequent decay reflects the competition between this ionization pathway and AM decay into Xe^{4+}. As the delay increases, the population of intermediate states decreases due to AM decay, resulting in a reduced Xe^{5+} yield for delays beyond approximately 90 fs. The remaining enhancement at large positive delays indicates that some of these intermediate states have lifetimes longer than the maximum experimental delay of about 0.5 ps.

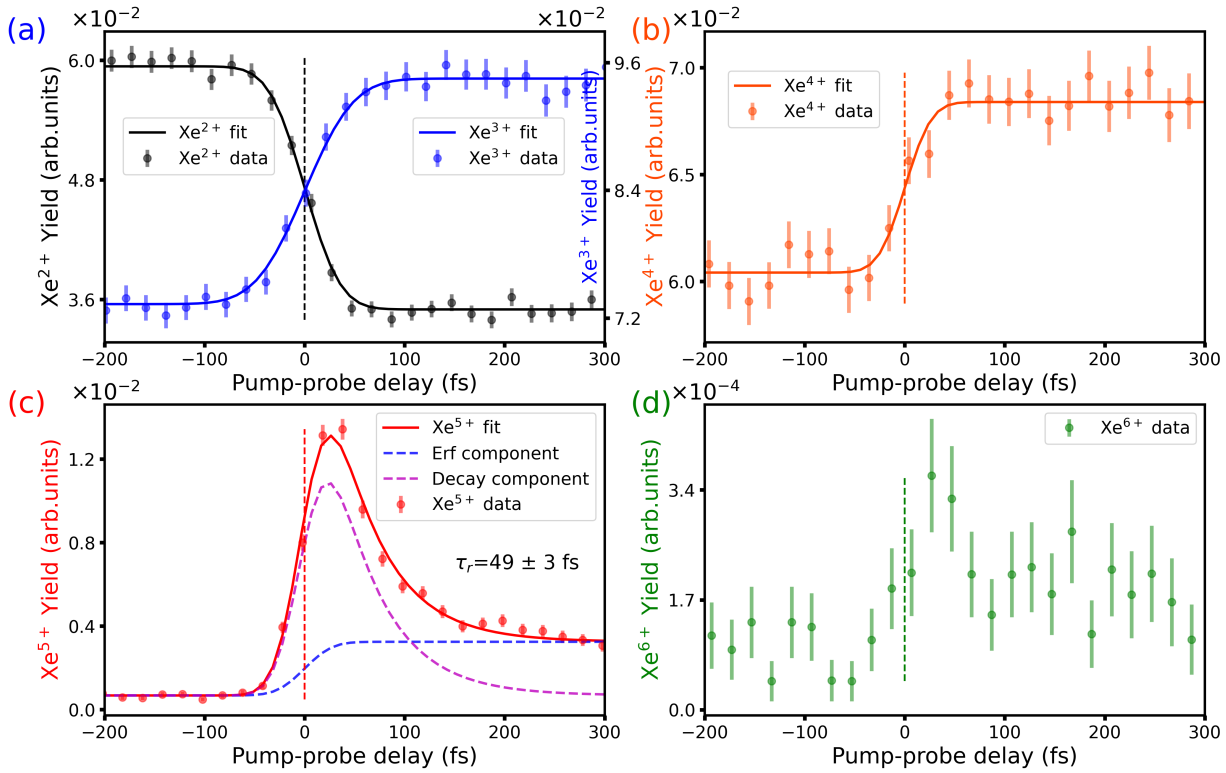

Figure 5.6: (a)–(d) Ion yields of Xe^{q+} (q = 2–6) as a function of delay at 160 eV XUV pump and NIR probe pulses. In (a), the left and right y-axes correspond to Xe^{2+} and Xe^{3+}, respectively. The yields of Xe^{2+}–Xe^{4+} are fitted using the step function defined in Eq.5.2, yielding cross-correlation times of (37 ± 3) fs, (44 ± 5) fs, and (31 ± 7) fs, respectively. The Xe^{5+} yield in (c) is fitted using Eq.5.3, resulting in a cross-correlation time of (30 ± 1) fs and a lifetime of (49 ± 3) fs. In (c), the purple and blue curves represent the exponential and step-function components, respectively, while the red solid line shows the combined fit.

To quantify this behavior, the Xe^{5+} data are fitted using the transient function 5.3. The fit shows an average lifetime of (49 ± 3) fs, which can be attributed to the decay of intermediate states dominated by $5p^{-5}nl\,n'l'$ configurations. This value is about a factor of two shorter than previously reported [123], likely due to differences in experimental conditions, in particular the shorter instrumental response time in the present measurements.

Finally, the Xe^{6+} yield, shown in Fig. 5.6(d), exhibits a similar but weaker transient behavior. Due to limited statistics, no reliable lifetime can be extracted. Nevertheless, the general trend of an increase near zero delay followed by a gradual decrease suggests a mechanism similar to that of Xe^{5+}. In this case, highly excited configurations such as $5p^{-6}nl\,n'l'$ are populated, decay via AM processes to Xe^{5+}, and are subsequently ionized by the NIR pulse to form Xe^{6+}.

5.4 Summary

This chapter investigates the ionization and relaxation dynamics of xenon atoms exposed to an intense, ultrashort XUV pulse from the FEL at photon energies of 90 eV and 160 eV, corresponding to the 4*d* giant resonance and the vicinity of the Cooper minimum, respectively. At 90 eV, the ionization process is dominated by 4*d* single ionization followed by AM decay, whereas at 160 eV both 4*p* single ionization and 4*d* double ionization contribute significantly, leading to altered branching ratios of the resulting charge states. These processes are studied using ion TOF spectroscopy using the REMI end-station.

Analysis of the ion yields as a function of XUV pulse energy shows that the formation of higher charge states Xe^{5+} and Xe^{6+} at 160 eV, and Xe^{4+} at 90 eV cannot be explained by single-photon absorption and is instead governed by multiphoton processes, most likely arising from sequential two-photon ionization. Pump-probe measurements were performed using a two-color XUV pump-NIR probe scheme with improved temporal resolution. In this approach, the NIR pulse probes the transient population of intermediate excited states by promoting them to higher-lying configurations, thereby providing insight into the intermediate steps of the relaxation pathways leading to different final charge states.

From the analysis of the delay-dependent ion yields, an average decay time of (49 ± 3) fs is obtained for the processes leading to Xe^{5+}. This value is approximately a factor of two shorter than previously reported results, which can be attributed to the improved temporal resolution achieved in the present experiment. Furthermore, a distinct decay pathway leading to the formation of Xe^{6+} is identified. This pathway originates from NIR-induced ionization of Xe^{5+} ions produced via sequential two-photon absorption.

Overall, the results show that intense XUV pulses from the FEL enable selective excitation of core-hole states and, when combined with synchronized NIR pulses, provide direct time-domain access to ultrafast decay dynamics in atomic systems. Future investigations employing time-resolved ion-electron coincidence techniques will enable more detailed and state-selective characterization of AM decay dynamics in xenon. In addition, further improvements in temporal resolution will be essential for resolving the fastest decay channels and gaining deeper insight into correlated electron dynamics.

Chapter 6

Fragmentation Dynamics of CO_2 and CS_2 using an FEL Pump–NIR Probe Technique

6.1 Introduction

The ionization and fragmentation dynamics of carbon dioxide (CO_2) and carbon disulfide (CS_2) are of broad scientific importance in atmospheric chemistry, astrophysics, and strong-field physics [27, 154, 155]. In planetary atmospheres such as those of Mars [156] and Venus [157], where CO_2 is a major constituent, exposure to high-energy radiation, such as UV light and highly charged particles from the solar wind, leads to ionization and dissociation, shaping the upper-atmospheric chemistry. Understanding these dynamics under intense XUV radiation from a FEL is therefore essential for radiation chemistry.

CEI in a pump–probe configuration provides an excellent method for probing transient molecular structure by analyzing the correlated momenta of the ionic fragments [71]. An XUV pump pulse removes one or several valence electrons, initiating rapid Coulomb-driven dissociation, while a time-delayed NIR pulse interrogates the evolving nuclear dynamics. By varying the pump–probe delay, one can effectively obtain a time-resolved movie of the molecular breakup. In our experiment, CEI was implemented using a REMI, which records all the charged fragments in ion coincidence and reconstructs their three-dimensional momentum vectors. The temporal and spatial evolution of the molecular geometry is then inferred from time-resolved KER and the correlated momentum distribution of the fragments [44, 158].

The ionization and fragmentation dynamics of CO_2 and CS_2 have been extensively studied using various experimental techniques, including electron-ion impact and femtosecond laser excitation [159–161]. In this work, the response of these triatomic molecules to intense 90 eV XUV FEL pulses is examined. At this energy, XUV efficiently populates the dicationic and tricationic species, and the resulting strong Coulomb repulsion between the ions drives complex fragmentation dynamics.

For photon energies above 37 eV, CO_2 undergoes double ionization to form the metastable dication CO_2^{2+}, which can persist briefly due to potential energy barriers that delay dissociation, whereas excited dicationic states are dissociative [162]. Under the same excitation conditions, CS_2 also forms a metastable dication CS_2^{2+} and its excited states are dissociative [163], but its heavier sulfur atoms and its different electronic structure give rise to a broader range of dissociation pathways compared with CO_2 [164]. At 90 eV, triple ionization to CO_2^{3+} and CS_2^{3+} becomes accessible. For CO_2^{3+}, the potential energy surface is purely dissociative and dominated by Coulombic repulsion, leading to prompt fragmentation [165].

In contrast, CS_2^{3+} exhibits a barrier on the potential-energy surface (PES) in addition to the Coulombic repulsion, which originates from the bound trication state; as a result, CS_2^{3+} is clearly observed in the mass spectrum.

Tricationic molecular ions can undergo *three-body* dissociation—for example, $CO_2^{3+} \longrightarrow C^+ + O_a^+ + O_b^+$. Such a breakup proceeds *via* two mechanisms: sequential and non-sequential (concerted) [161]. In the sequential mechanism, one bond breaks first, producing a rotating intermediate dication that subsequently dissociates after a short delay. In contrast, the non-sequential mechanism involves the nearly simultaneous breaking of multiple bonds, ejecting all ionic fragments in a single step from an essentially intact molecular geometry. The relative contributions of these pathways depend on both molecular properties and the total energy deposited into the molecular ion. Lighter systems, such as CO_2, exhibit significant contributions from both mechanisms, whereas heavier systems, such as CS_2, tend to favor non-sequential fragmentation. A comparative investigation of CO_2 and CS_2 under identical excitation conditions, therefore, provides critical insight into how atomic substitution and molecular composition influence ultrafast Coulomb-explosion dynamics in linear triatomic molecules.

6.2 Experimental Setup

This experiment was performed at the REMI endstation at FL26 FLASH2 beamline [71]. A brief overview is presented here, while a detailed description of the REMI apparatus and the FEL–NIR pump–probe setup can be found in Chapter 3. Briefly, the FEL was tuned to 90 eV, while NIR pulses from the pump–probe laser, synchronized with FLASH [100], were wavelength centered around 800 nm with a repetition rate of 100 kHz per burst. The FEL and NIR pulses had durations of less than 20 fs, and both lasers operated at a common repetition rate of 10 Hz. The FEL delivered 45 pulses per train at a rate of 450 pulses per second, while the NIR laser delivered 75 pulses per train at a rate of 750 pulses per second. A synchronized pump–probe delay scan was performed using the NIR laser. In the pump–probe experiment, the first 30 pulses consisted of NIR only, the next 40 pulses involved overlapping FEL and NIR, and the final 5 pulses were FEL only. The FEL and pump–probe laser pulse patterns and overlap are described in Chapter 4. The average FEL pulse energy, measured using a (GMD)[66], was 1.5 µJ, with approximately 10% shot-to-shot variation. The FEL beam was focused into the interaction region using an ellipsoidal mirror, achieving a nominal spot size of 2.7 µm × 3.1 µm[71]. In our experiment, however, the actual focal spot size was approximately 20 µm, yielding an estimated peak intensity of $1 \times 10^{13}\,\mathrm{W\,cm^{-2}}$ based on the xenon or argon charge state in the mass spectrum. The NIR laser pulse was focused at the interaction region using two spherical mirrors, yielding a focal spot size of approximately 50 µm, as measured by a near-field camera that imaged the beam profile at the focus. The peak intensity was determined to be $8 \times 10^{13}\,\mathrm{W\,cm^{-2}}$ and was verified through TOF measurements of argon charge-state ratios (see Appendix A.

The CO_2 and CS_2 molecules were introduced into the vacuum chamber *via* supersonic expansion through a 50 µm-diameter nozzle, forming a molecular jet. Upon expansion into ultra-high vacuum, the molecules are cooled and form a forward-directed beam, which is subsequently collimated by two skimmers. The resulting jet is directed into the REMI interaction region, where the collinear FEL and NIR beams intersect it perpendicularly. Fragment ions produced by the XUV and laser pulses are accelerated by a homogeneous electric field of 10 V/cm toward the ion detectors.

The resulting photoions were recorded using a REMI spectrometer. Ions were detected with large-area MCP detectors equipped with a delay-line anode, which provided the TOF and impact positions (x, y) of each fragment. From these, the three-dimensional momenta

were reconstructed: the TOF gives the velocity along the spectrometer axis, and the impact position yields the transverse velocities in x and y. For more details, see Section 3.3.

6.2.1 Data Acquisition and Analysis

For CO_2 and CS_2, ions were detected using a delay-line anode REMI detector, recording the impact position (x, y) and TOF for each hit (event) in list-mode files. The Go4 software was used for both online monitoring during beam time and offline data analysis [166]. The REMI CO_2 and CS_2 data analyses are detailed in Section 3.3.5

Two-fold Coincidence

In the two-fold ion–ion coincidence channels, the doubly ionized molecule (CO_2 or CS_2) undergoes a two-body fragmentation into two charged fragments, for example

$$CO_2^{2+} \longrightarrow CO^+ + O^+, \quad \text{or} \quad CS_2^{2+} \longrightarrow CS^+ + S^+.$$

These channels appear as distinct islands in the ion–ion photoion-photoion coincidence (PIPICO) maps, where the TOF of the two ions from the same event are plotted against each other.

To ensure that the detected ion pairs originate from the same parent molecule, a momentum conservation filter is applied to the dataset. Only events satisfying

$$\vec{p}_1 + \vec{p}_2 \approx 0$$

within the experimental resolution are retained, where $\vec{p}_1$ and $\vec{p}_2$ are the momentum vectors of the two detected ions. This condition eliminates accidental coincidences arising from fragments of different molecules or from background signals.

From these selected ion pairs, the KER distributions are extracted. The KER provides insight into the potential energy surfaces involved at the instant of fragmentation.

Three-fold Coincidence

In the three-fold ion–ion–ion coincidence channels, the triply ionized parent molecule undergoes a complete Coulomb explosion into three charged fragments, for example:

$$CO_2^{3+} \longrightarrow C^+ + O^+ + O^+, \quad \text{or} \quad CS_2^{3+} \longrightarrow C^+ + S^+ + S^+.$$

Experimentally, these triple-coincidence channels are visualized in a PIPICO-sum representation, where the sum of the TOF of two fragments is plotted against the TOF of the third fragment.

For a true triple-coincidence event, momentum conservation must hold simultaneously for all three fragments in three dimensions:

$$\vec{p}_1 + \vec{p}_2 + \vec{p}_3 \approx 0.$$

This criterion ensures that all detected ions originate from a single molecular dissociation event.

Momentum-Space Visualization: Newton and Dalitz Plots

In addition to the PIPICO and KER analyses, the fragmentation dynamics of both CO_2^{3+} and CS_2^{3+} were studied using Newton and Dalitz plots [167]. These momentum-space tools provide complementary information about the geometric arrangement and energy sharing of the fragments in multi-body breakup channels.

The Newton plot is employed to analyze momentum correlations among the three fragments produced by the dissociation of CO_2^{3+} or CS_2^{3+}. In this representation, the momentum vector of the first outer atom (O_a^+ in CO_2 or S_a^+ in CS_2) is aligned along the x axis and serves as a reference direction. The momentum vectors of the remaining fragments are then plotted in the upper and lower halves of the coordinate frame, providing a clear and intuitive visualization of the breakup geometry. This representation is particularly useful for three-body Coulomb explosion, distinguishing between non-sequential and sequential fragmentation pathways, as each mechanism produces characteristic, readily identifiable patterns in the Newton plot.

For three-body dissociation channels, Dalitz plots were additionally used to quantify the partitioning of the total kinetic energy among the fragments, thereby complementing the geometric breakup information obtained from the Newton plot. In this two-dimensional plot, the difference between the normalized kinetic energies of the two identical outer atoms (O^+ in CO_2 or S^+ in CS_2) is mapped onto the x axis, whereas the normalized kinetic energy of the central C^+ ion is represented on the y axis. The Dalitz coordinates are defined as

$$x = \frac{\epsilon_{A_1} - \epsilon_{A_2}}{\sqrt{3}}, \tag{6.1}$$

$$y = \epsilon_C - \frac{1}{3}, \tag{6.2}$$

where ϵ_{A_1}, ϵ_{A_2}, and ϵ_C denote the normalized kinetic energy of the two outer fragments (O^+ or S^+) and the central C^+ fragment, respectively. These normalized energies are obtained from

$$\epsilon_i = \frac{E_i}{k}, \qquad k = E_{A_1} + E_{A_2} + E_C, \tag{6.3}$$

with k representing the total kinetic energy in the three-body fragmentation channel.

The resulting Dalitz plot provides a clear visualization of the energy-sharing dynamics, effectively distinguishing the symmetric linear breakup pathways characteristic of molecules such as CO_2 and CS_2 from more asymmetric or sequential dissociation processes.

The distinction between these non-sequential and sequential mechanisms is made by analyzing momentum-correlation maps, Dalitz plots, and Newton diagrams, which reveal characteristic geometric patterns and energy partitioning among fragments. Sequential breakup typically yields asymmetric energy sharing and elongated momentum structures, whereas concerted breakup produces more symmetric distributions and higher total kinetic energy.

6.3 Results

6.3.1 Fragmentation Dynamics of CO_2

Mass Spectrum of CO_2

Fig. 6.1 summarizes the ion signals recorded with the REMI detector for CO_2 under different ionization conditions (XUV+NIR, XUV-only, and NIR-only).

Fig. 6.1(a) shows a two-dimensional histogram of the ion signal, plotted as the radial distance R (mm) from the detector center versus the ion TOF (proportional to $\sqrt{m/z}$). This representation directly visualizes the correlation between the ion-impact radial position and the mass spectrum for CO_2 exposed to combined XUV and NIR pulses. The localized spot at the center of the detector corresponds to ions with almost zero kinetic energy, i.e., intact doubly ionized parent ions such as bound CO_2^{2+} ($m/z = 22$) states that do not dissociate. Inner rings arise from neutral-dissociation channels, where only one fragment is charged and carries small kinetic energy, for example O^+ ($m/z = 16$). The pronounced outer ring is attributed to the Coulomb explosion of multiply charged CO_2, which produces highly energetic fragment ions such as C^+ ($m/z = 12$), O^+, and CO^+.

Fig. 6.1(b) shows the corresponding one-dimensional mass spectrum for the XUV+NIR configuration, obtained by integrating the 2D distribution in Fig. 6.1(a) over the radial coordinate. The spectrum is dominated by the singly charged parent CO_2^+, with additional peaks from CO^+ and O^+, and a small contribution from CO_2^{2+}. The dication can dissociate via

$$CO_2^{2+} \longrightarrow CO^+ + O^+,$$

and this two-body Coulomb explosion shows as larger-radius rings in Fig. 6.1(a), reflecting the high KER.

Fig. 6.1(c) compares the XUV-only and NIR-only mass spectra. The XUV pulse produces single- and multiple-charge states of CO_2, but no distinct CO_2^{3+} peak at the expected $m/z \approx 14.7$. This is because the highly unstable trication undergoes prompt Coulomb explosion into $C^+ + O^+ + O^+$. A small C^{2+} peak appears at $m/z = 16$ only in the XUV-present condition, and a weak H_2O^+ peak is observed at $m/z = 18$. In contrast, the NIR-only spectrum is dominated by the parent CO_2^+ peak, with only a very weak dication contribution. Taken together with panel (b), these observations show that ionization and fragmentation are driven mainly by XUV absorption, while the NIR pulse primarily perturbs the branching between parent and fragment channels.

Pump–Probe Ion Yields of CO_2 Fragments

The CO_2 fragment ion yield is obtained by integrating the counts within the TOF window of the fragment for each delay bin and normalizing by the total number of laser shots. To account for XUV intensity fluctuations, the yield is further normalized to the FEL pulse energy. The pump–probe delay was scanned repeatedly over a range of ±500 fs, with positive delay defined such that the NIR pulse arrives after the XUV pulse and *vice versa* for negative delay.

Fig.6.2 shows the delay-dependent ion yields of CO^+ and CO_2^{2+} as a function of pump–probe delay. For positive delay, the CO^+ ion yield increases like a positive error function near the temporal overlap of the XUV and NIR pulses, while the CO_2^{2+} channel show transient feature.

The CO_2^{2+} yield displays a pronounced maximum close to temporal overlap, followed by an exponential decay at positive delays. This behavior indicates that CO_2^{2+} is formed

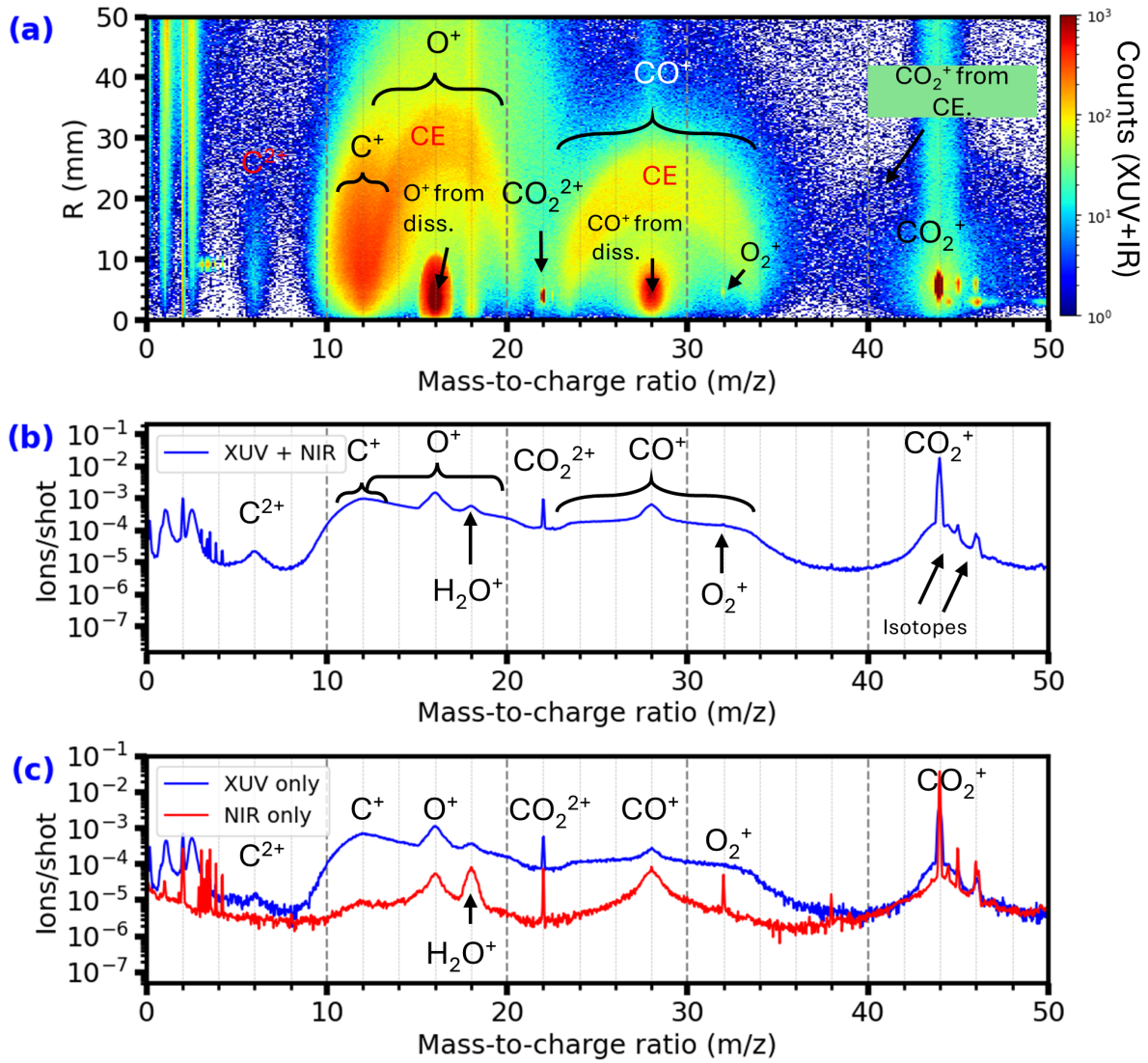

Figure 6.1: Ion signals from CO_2. (a) 2D histogram of detector radius R versus mass-to-charge ratio (m/z) for the XUV+NIR pulse together, average over all pump–probe delays. (b) Mass spectrum obtained by integrating panel (a) over R. (c) Comparison of NIR-only (red) and XUV-only (blue) mass spectra.

via a transient intermediate state prepared by the XUV pulse. In a simplified picture, the XUV pulse first populates an excited molecular cation,

$$CO_2 + h\nu_{XUV} \longrightarrow {CO_2}^{+*} + e^-,$$

which subsequently evolves and decays on a characteristic timescale τ. The delayed NIR pulse probes this population by further ionizing or promoting ${CO_2}^{+*}$ onto metastable dicationic states (${CO_2}^{2+}$).

$$ {CO_2}^{+*} + h\nu_{NIR} \longrightarrow {CO_2}^{2+} + e^- $$

The ${CO_2}^{2+}$ ion yield as a function of pump–probe delay (Δt) is well described by the convolution of the instrument response function with an exponential decay; fitting the transient yields an intermediate-state lifetime of $\tau = 62 \pm 10\,\mathrm{fs}$ for the excited states of ${CO_2}^{+*}$. The fitting procedure is described in Section 2.3.1.

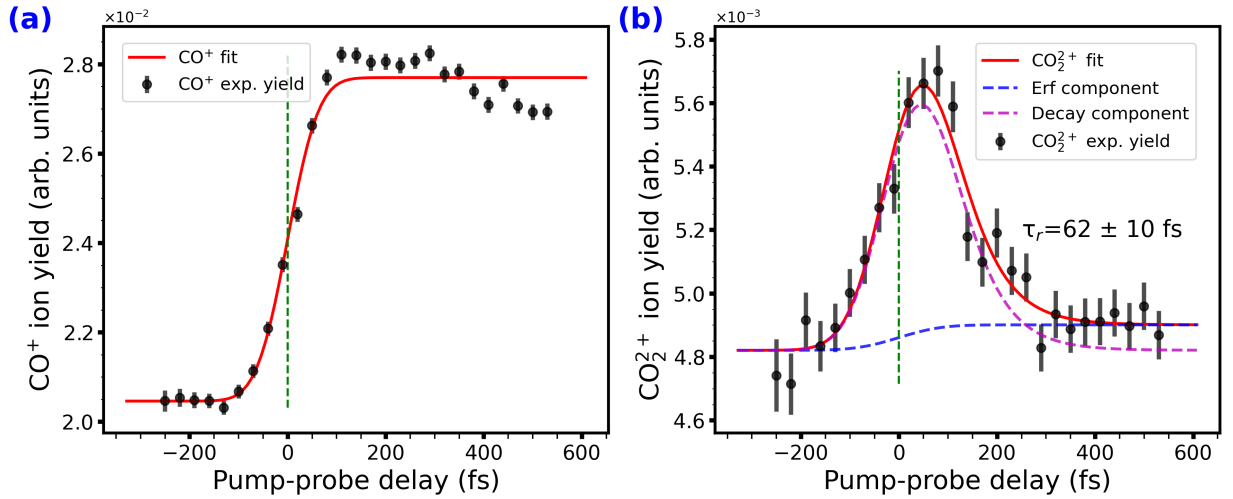

Figure 6.2: Ion yields vs. Δt. (a) CO^+: black points with error bars are the exp. data; the red curve is the instrument cross-correlation or error function. (b) ${CO_2}^{2+}$: black points with error bars are the exp. data; the red curve is the total fit (error function response (blue), exponential decay component (pink dotted).

The CO^+ ion yield exhibits a positive error function increase around the temporal overlap of the XUV and NIR pulses and then remains approximately constant for positive delays. This behavior is characteristic of a long-lived intermediate state.

In a simplified picture, the XUV pulse first prepares an excited molecular cation,

$$CO_2 + h\nu_{XUV} \longrightarrow {CO_2}^+$$

which has a long lifetime compared to the pump–probe delay range. When the NIR pulse arrives (for $\Delta t \geq 0$), it couples this population into dissociative or higher-lying dicationic states that eventually yield

$${CO_2}^+ + h\nu_{NIR} \longrightarrow CO^+ + O \quad \text{or} \quad {CO_2}^+ + h\nu_{NIR} \longrightarrow CO + O^+$$

Because the ${CO_2}^+$ population is essentially constant over the scanned delays, the NIR pulse finds nearly the same amount of intermediate population for all $\Delta t > 0$. As a result, the CO^+ yield increases sharply once the pulses start to overlap and then saturates, appearing as a step function in the delay-dependent ion yield.

Photo-ion Photo-ion Coincidence (PIPICO)

The PIPICO map of CO_2 is shown in Fig. 6.3. Panel (a) displays the TOF correlation between the first-hit and second-hit ions, corresponding to a two-fold ion–ion coincidence. Panel (b) shows the correlation between the TOF of the first-hit ion and the sum of the TOFs of the other two fragments, representing a three-fold coincidence and allowing access to three-body fragmentation channels.

Coincident ion detection enables detailed investigation of fragmentation dynamics and ion–ion correlations in molecular breakup processes.

Time-Resolved KER of the $CO^+ + O^+$ Channel

Fig. 6.4(a) shows the KER of $CO^+ + O^+$ as a 2D histogram $I(\text{KER}, \Delta t)$. Two main features are evident: (i) true ion–ion coincidences from ${CO_2}^{2+} \longrightarrow CO^+ + O^+$ (red dotted line in region 2), and (ii) contribution attributed to false coincidences, where ions originating from

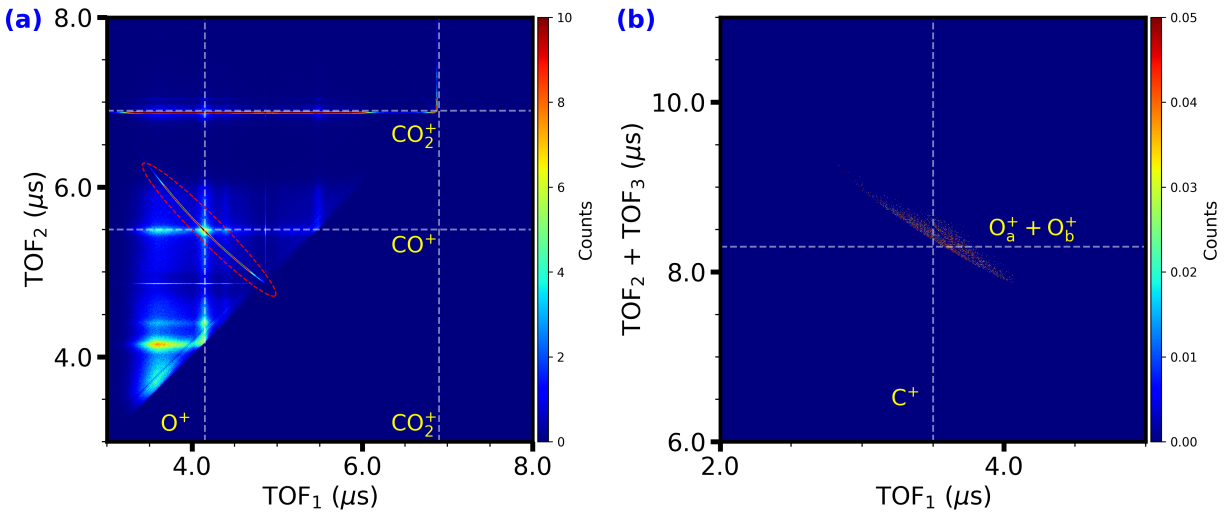

Figure 6.3: PIPICO map of CO_2 showing different dissociation channels: (a) TOF correlation between the first and second ions (two-fold ion–ion coincidence); (b) correlation between the TOF of the first-hit ion and the sum of the TOFs of the other two fragments (three-fold coincidence).

independent ion–neutral channels, such as $CO^+ + O$ and $CO + O^+$, pass the momentum conservation filter (region 1).

It can be simplified using the following equation.

$$CO_2 + h\nu_{XUV} \longrightarrow {CO_2}^{+*} + e^-, \tag{6.4}$$

$${CO_2}^{+*} + h\nu_{NIR} \longrightarrow {CO_2}^{2+} + e^- \longrightarrow CO^+ + O^+. \tag{6.5}$$

Fig. 6.4(c) shows that the KER yield from false coincidence in the range from (0 eV to 1 eV) show postive error function after NIR pulse arrives. This can be explained by the fact that the behavior increases with temporal overlap, consistent with NIR-induced ion–neutral dissociation of ${CO_2}^+$; the onset is described by the instrument cross-correlation (FWHM ∼70 fs). In contrast, the high-KER trace in panel (d) (4 eV to 9 eV) exhibits a transient characteristic of dication formation followed by Coulomb explosion. The delay dependence is modeled by the instrument response convolved with an exponential decay, yielding an intermediate-state lifetime of $\tau = (57 \pm 8)$ fs, which is a similar lifetime obtained by fitting ${CO_2}^{2+}$ ion yield vs pump–probe delay.

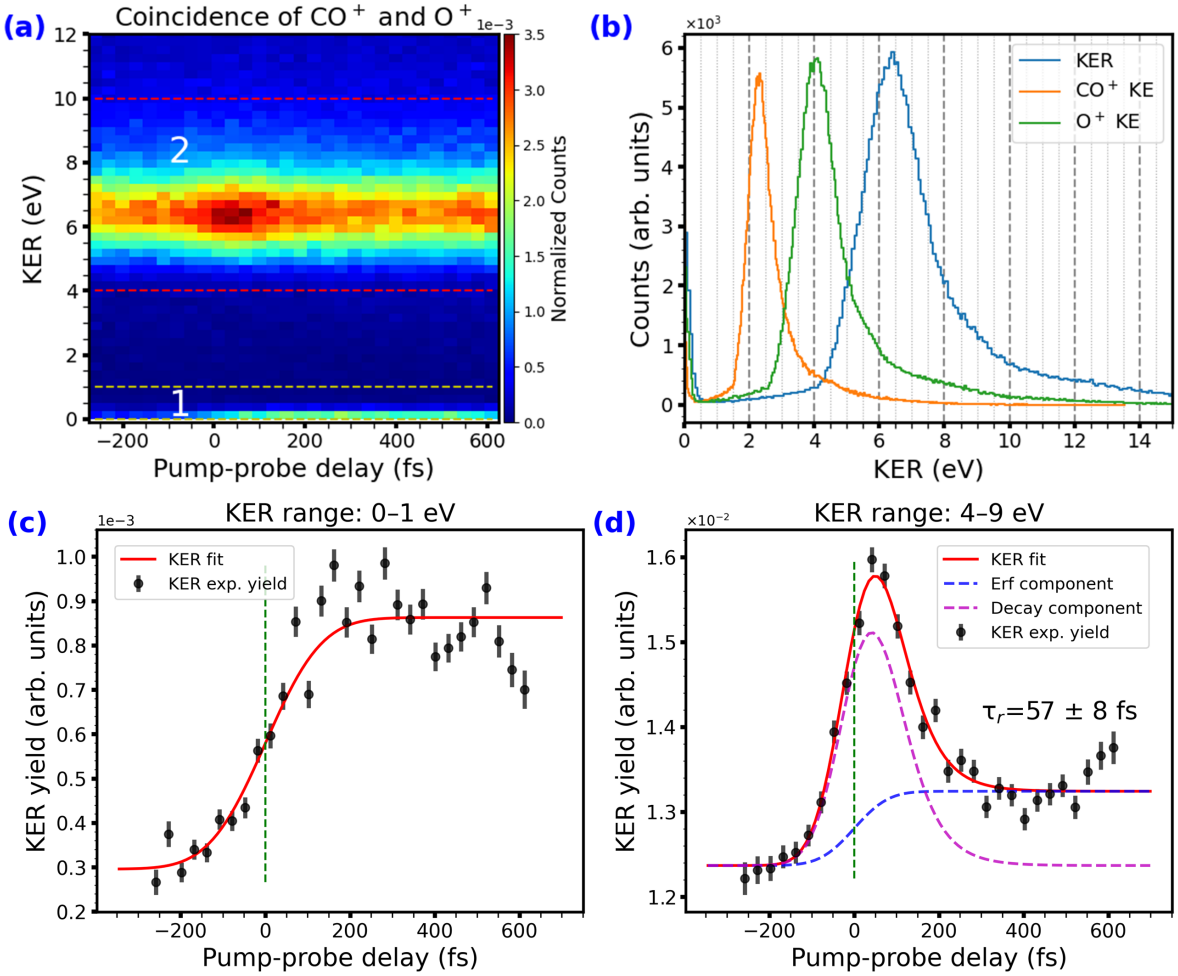

Figure 6.4: Time-resolved KER for $CO^+ + O^+$. (a) Two-dimensional map of KER as a function of pump–probe delay. (b) KER distribution of the $CO^+ + O^+$ channel, peak at 6.2 eV (blue curve); the green and orange curves show the individual fragment kinetic energies of O^+ and CO^+, respectively. (c) Delay-dependent KER yield integrated over the region (0 eV to 1 eV, Region 1), dominated by ion–neutral dissociation from excited $CO_2{}^{+*}$ states, fitted with an error function. (d) KER yield integrated over the Coulomb-explosion window (4 eV to 9 eV, Region 2), reflecting the formation and dissociation of $CO_2{}^{2+}$ into $CO^+ + O^+$.

Three-Body Dissociation Channel $CO_2{}^{3+} \longrightarrow C^+ + O_a{}^+ + O_b{}^+$

The three-body breakup of $CO_2{}^{3+}$ into $O_a{}^+ + C^+ + O_b{}^+$ occurs via two pathways. In the non-sequential (direct) breakup, both C–O bonds break nearly simultaneously,

$$CO_2^{3+} \rightarrow O_a^+ + C^+ + O_b^+, \tag{6.6}$$

whereas in the sequential pathway, a CO^{2+} fragment is formed first and subsequently dissociates,

$$CO_2^{3+} \rightarrow CO^{2+} + O_a^+ \rightarrow O_a^+ + C^+ + O_b^+. \tag{6.7}$$

The three-body coincidence channel can be analyzed using Dalitz and Newton plots. Fig. 6.5(a) shows the geometrical representation of the Dalitz plot, where each point corresponds to a specific momentum correlation among the three fragments. Different regions in this diagram correspond to distinct dissociation mechanisms. Events located near the central, symmetric region correspond to non-sequential (concerted) breakup, in which

both C–O bonds rupture nearly simultaneously. In contrast, elongated structures along the characteristic axes (indicated by the red dotted line) arise from sequential fragmentation, in which the molecule dissociates stepwise via a transient CO^{2+} intermediate.

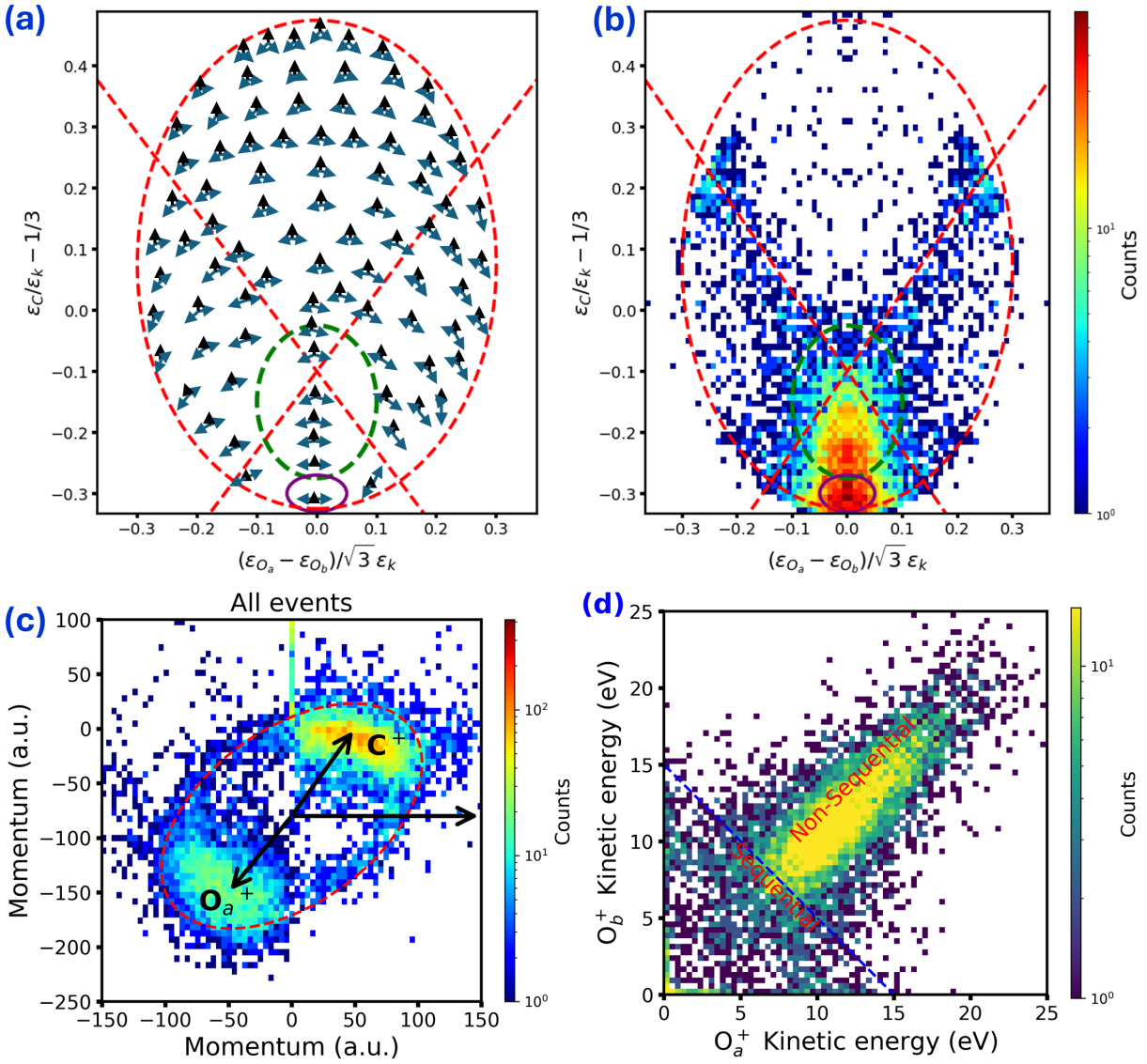

Figure 6.5: (a) Schematic momentum-correlation features at representative points of the Dalitz plot. (b) Experimental Dalitz plot for the three-body channel $CO_2^{3+} \longrightarrow C^+ + O_a{}^+ + O_b{}^+$. (c) The Newton plot for all events. (d) KER correlation between the two O^+ ions produced in the fragmentation of CO_2^{3+}. Two regions are identified: Region 1 (blue), below the $y = x$ line, corresponds to sequential fragmentation, while Region 2, above the line, is dominated by non-sequential breakup.

The experimental Dalitz plot for the $C^+ + O_a{}^+ + O_b{}^+$ channel is shown in Fig. 6.5(b). The same characteristic features are observed: a small island near the bottom corresponds to nearly linear dissociation with very little bending excitation, while events along the green dotted line are associated with non-sequential fragmentation. A more extended band is attributed to the sequential pathway. From the relative population distributions in these regions, the two fragmentation mechanisms can be clearly distinguished and their relative contributions quantified.

Complementary information is obtained from the Newton diagram. Fig. 6.5(c) shows the Newton plot for the $C^+ + O_a{}^+ + O_b{}^+$ channel, where the momentum of $O_b{}^+$ is fixed along

the x axis, and the momenta of C^+ and ${O_a}^+$ are plotted in the upper and lower halves of the frame, respectively. Sequential events form a circular band (indicated by the red elliptical curve), providing evidence of a two-step decay: first ${CO_2}^{3+} \longrightarrow {O_a}^+ + CO^{2+}$, followed by the delayed dissociation of CO^{2+}. Because the first dissociation occurs near the equilibrium bond angle ($\sim 170°$), the departing O^+ imparts angular momentum to the CO^{2+} fragment, producing the characteristic ring structure.

The above Dalitz and Newton plots include all events, consisting of both sequential and non-sequential contributions. To separate these pathways, a correlation plot of the kinetic energies of the two terminal O^+ ions was used. As shown in Fig. 6.5(d), a pronounced diagonal island reflects the strong kinetic energy correlation expected for non-sequential breakup, whereas a diffuse off-diagonal region corresponds to sequential fragmentation. Sequential events are selected below the $y = x$ line, while the remaining events are non-sequential.

Fig. 6.6 presents the Newton diagrams after separating the sequential and non-sequential events. In the non-sequential case, the Newton plot shows well-separated distributions of C^+ and O^+ in the upper and lower halves of the frame, reflecting a concerted breakup. In contrast, for sequential events, the first dissociation step imparts angular momentum to the intermediate CO^{2+} fragment, leading to the characteristic ring structure observed in the Newton plot.

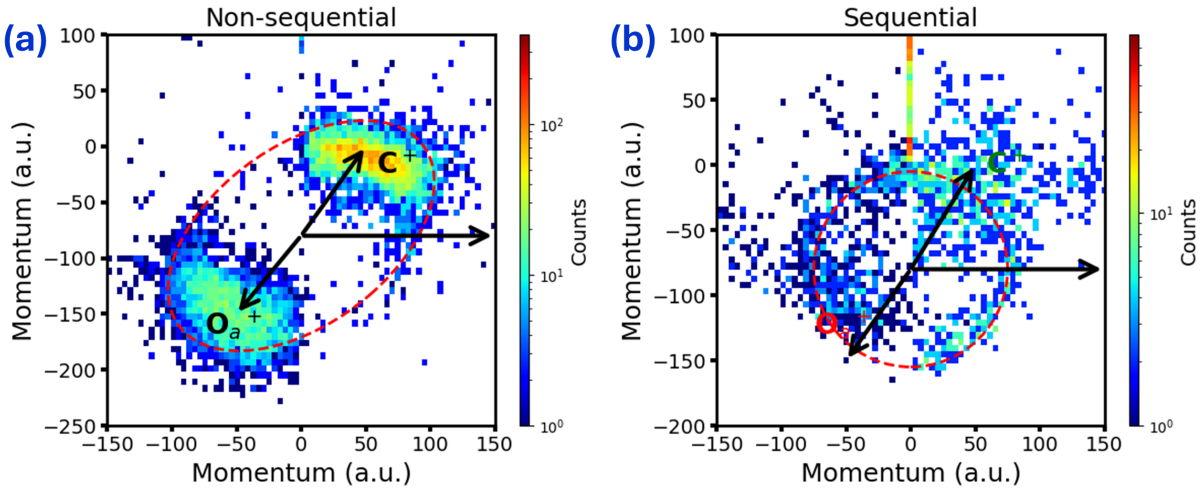

Figure 6.6: Newton plots for events selected based on the kinetic energy correlation of the two terminal O^+ ions: (a) non-sequential and (b) sequential.

The asymptotic angle between the momentum vectors of the two O^+ ions is expected to be less than 180° due to Coulombic repulsion between the positively charged fragments. Fig. 6.7(a) shows the distribution of this asymptotic O^+–O^+ angle, featuring a broad peak in the range of 100°–150° for the sequential process and a narrow distribution centered around 160° for the non-sequential process. The smaller angles observed in the sequential process arise because the first O^+ ion is ejected earlier, allowing the intermediate ${CO_2}^{2+}$ to rotate before the second bond breaks.

Fig. 6.7(b) shows the kinetic energy of the C^+ ion. The C^+ ions show higher kinetic energy in the sequential process than in the non-sequential process. This increase arises from the stepwise breakup, where Coulomb repulsion in the intermediate stage (CO^{2+}) contributes additional kinetic energy to the C^+ fragment. In contrast, in the non-sequential process, dissociation occurs in a nearly linear geometry, with the two O^+ ions emitted back-to-back. As a result, the momentum of the C^+ ion approaches zero, since the momenta of the O^+ ions balance each other. This reflects conservation of linear momentum, and

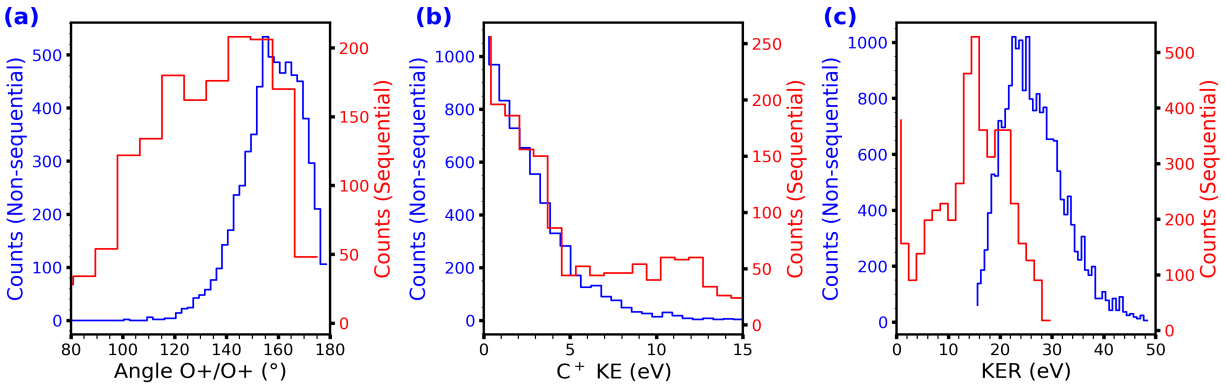

Figure 6.7: (a) Asymptotic O^+–O^+ angle between the momentum vectors of the two O^+ ions, (b) kinetic energy of C^+, and (c) KER from the fragmentation of CO_2^{3+}. Non-sequential fragmentation (blue solid line) and sequential fragmentation (red solid line) are shown.

the kinetic energy of the C^+ ion is minimized in such a symmetric dissociation. Fig. 6.7(c) shows the KER for the sequential and non-sequential processes. In the sequential case, the KER is approximately 10 eV, whereas in the non-sequential case it is around 26 eV. In the sequential process, part of the available energy is transferred into rotational excitation of the CO^{2+} intermediate state.

Time-Resolved KER of CO_2^{3+}

In the pump–probe sequence, the XUV pulse prepares an excited dication CO_2^{2+*}, which can be further ionized by the delayed NIR pulse to form CO_2^{3+}:

$$CO_2^{2+*} + h\nu_{\mathrm{NIR}} \rightarrow CO_2^{3+}. \tag{6.8}$$

The formation of CO_2^{3+} opens the three-body fragmentation channel

$$CO_2^{3+} \longrightarrow C^+ + O_a^+ + O_b^+, \tag{6.9}$$

The subsequent dissociation proceeds via two distinct pathways: (i) a non-sequential breakup, in which both C–O bonds rupture nearly simultaneously, and (ii) a sequential process proceeding via a transient CO^{2+} intermediate. Triple-coincidence events $C^+ + O_a^+ + O_b^+$ are separated into non-sequential and sequential contributions based on the kinetic energy correlation of the two O^+ ions. For each class, the events are binned as a function of pump–probe delay Δt, and a two-dimensional histogram $I(\mathrm{KER}, \Delta t)$ is plotted.

Fig. 6.8(a) shows the delay-dependent KER map for the non-sequential channel, while Fig. 6.8(b) shows the corresponding map for the sequential channel. From these plots, the KER-integrated yields, $Y_{\mathrm{nonseq}}(\Delta t)$ and $Y_{\mathrm{seq}}(\Delta t)$, are obtained by integrating over all KER and are shown in Fig. 6.8(c–d), respectively.

The non-sequential KER yield exhibits a prompt, step-like rise at the temporal overlap of the XUV and NIR pulses, followed by a slow saturation for positive delays. In contrast, the sequential yield rises more gradually and shows a pronounced increase only after delays of approximately 250 fs, indicating a delayed population and rotational evolution of the CO^{2+} intermediate prior to its breakup. The rotational dynamics can be verified by constructing time-resolved Newton plots (see Fig. 6.9). A small tail in the C^+ momentum distribution is observed for time delays between 0 and 250 fs, with the NIR pulse arriving later. No arc-like feature appears in this other time window, indicating that the CO^{2+} intermediate state subsequently dissociates into C^+ and O^+. The rotational time of the CO^{2+} ion can be theoretically estimated to be approximately 89 fs for half a rotational period [161]. The

secondary breakup of this rotating CO^{2+} wave packet gives rise to the circular feature observed in Fig. 6.9(b).

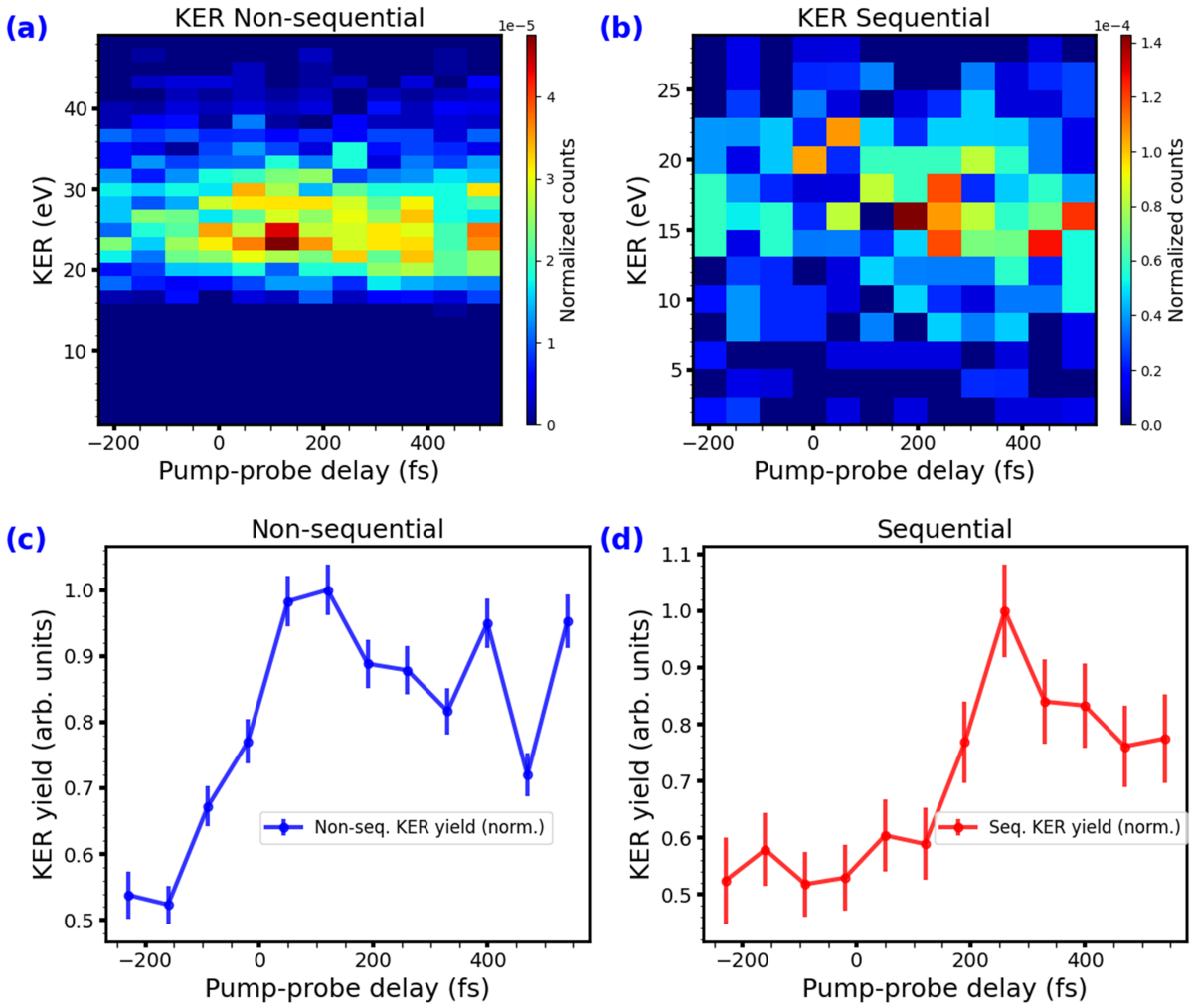

Figure 6.8: Time-resolved KER of triple-coincidence events: (a) non-sequential and (b) sequential 2D histogram (KER vs. pump–probe delay); (c,d) corresponding delay-dependent KER-integrated yields.

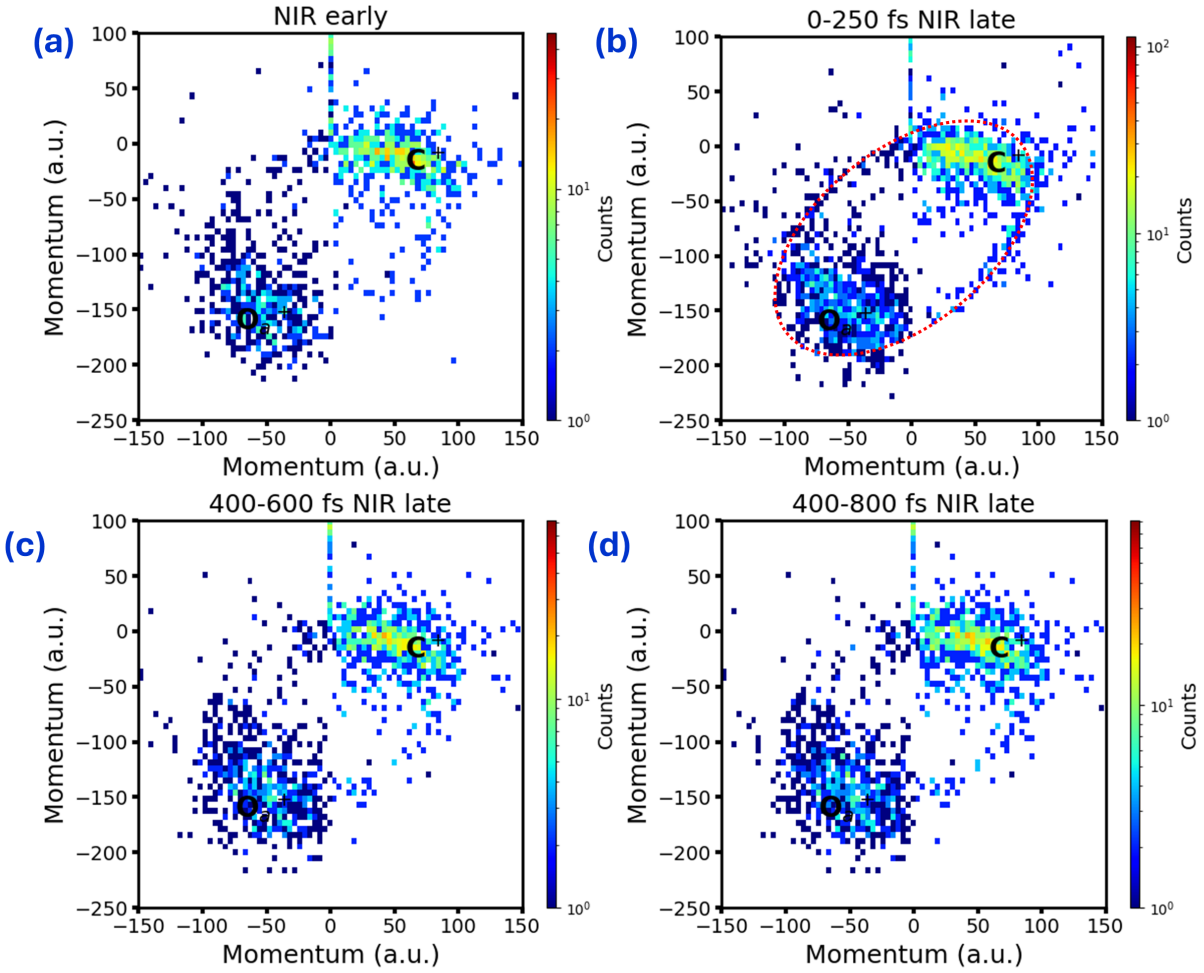

Figure 6.9: Time-resolved Newton plots of all detected events, including both sequential and non-sequential contributions. (a) Early NIR delay. (b) Late NIR delay, 0–250 fs. (c) Late NIR delay, 400–600 fs. (d) Late NIR delay, 400–800 fs

6.3.2 Fragmentation Dynamics of CS_2

Mass Spectrum of CS_2

Fig. 6.10(a) shows a two-dimensional histogram of the ion yield for CS_2 recorded with combined XUV+NIR pulses, plotted as detector radius R (mm) versus mass-to-charge ratio m/z. Localized counts at the detector center correspond to fragments with negligible KER, whereas features at small R (inner rings) arise from low-energy dissociation pathways such as neutral dissociation accompanied by a charged partner fragment. In contrast, the outer rings originate from Coulomb explosion following breakup of multiply charged ${CS_2}^{q+}$ ($q \geq 2$), which shows high KER. This R–m/z map separates low- and high-energy fragmentation at a glance.

Fig. 6.10(b) shows the corresponding one-dimensional mass spectrum obtained by integrating panel (a) over R. Narrow peaks from metastable and bound states of ${CS_2}^{+}$ ($m/z = 76$), ${CS_2}^{2+}$ ($m/z = 38$), and ${CS_2}^{3+}$ ($m/z \approx 25.3$) indicate intact molecular ions in the cold beam, while broader features originate from energetic fragments. Prominent fragment peaks include CS^+ ($m/z = 44$) and S^+ ($m/z = 32$) from two-body breakup, as well as lighter ions such as C^+ ($m/z = 12$). The spectrum shows that single ionization is the dominant channel, although higher charge states are also populated via multiple ionization followed by two- or three-body dissociation.

Fig. 6.10(c) compares the XUV-only and NIR-only spectra. The XUV pulse produces substantial single-, double-, and triple-ionization of CS_2; notably, a distinct ${CS_2}^{3+}$ peak is observed. In contrast, the NIR-only spectrum is dominated by the parent ${CS_2}^{+}$ with a much weaker dication signal. Together, these observations indicate that XUV absorption drives the production of higher charge states and associated multi-body breakup in CS_2, while the NIR pulse primarily modifies branching fragment channels.

CS_2 PIPICO

The PIPICO map for CS_2 is shown in Fig. 6.11, providing a two-fold coincidence representation in which the TOF of one ion is plotted against that of the second ion for each event. Correlation identifies specific two-body breakup channels. In Fig. 6.11(b), the TOF of one ion is plotted against the sum of the TOFs of the other two ions, i.e., TOF_i vs. $\mathrm{TOF}_j + \mathrm{TOF}_k$, revealing triple-coincidence fragmentation channels.

Several coincident channels arising from dications and trications, as well as from dimers of the CS_2 molecule, are observed as sharp lines in the PIPICO map within the region marked by the white dotted line.

$$ {CS_2}^{2+} \longrightarrow CS^+ + S^+, \tag{6.10} $$

$$ {CS_2}^{2+} \longrightarrow C^+ + {S_2}^+, \tag{6.11} $$

$$ {(CS_2)_2}^{2+} \longrightarrow {CS_2}^+ + {CS_2}^+, \tag{6.12} $$

$$ {CS_2}^{3+} \longrightarrow CS^{2+} + S^+, \tag{6.13} $$

$$ {CS_2}^{3+} \longrightarrow CS^+ + S^{2+}, \tag{6.14} $$

$$ {CS_2}^{3+} \longrightarrow C^+ + {S_a}^+ + {S_b}^+. \tag{6.15} $$

Here, ${S_a}^+$ and ${S_b}^+$ denote the two sulfur ions in the three-body channel (6.15); the subscripts indicate detection order. In the data analysis, true-coincidence events are selected using a momentum-conservation filter that ensures all fragments originate from the same dissociation event.

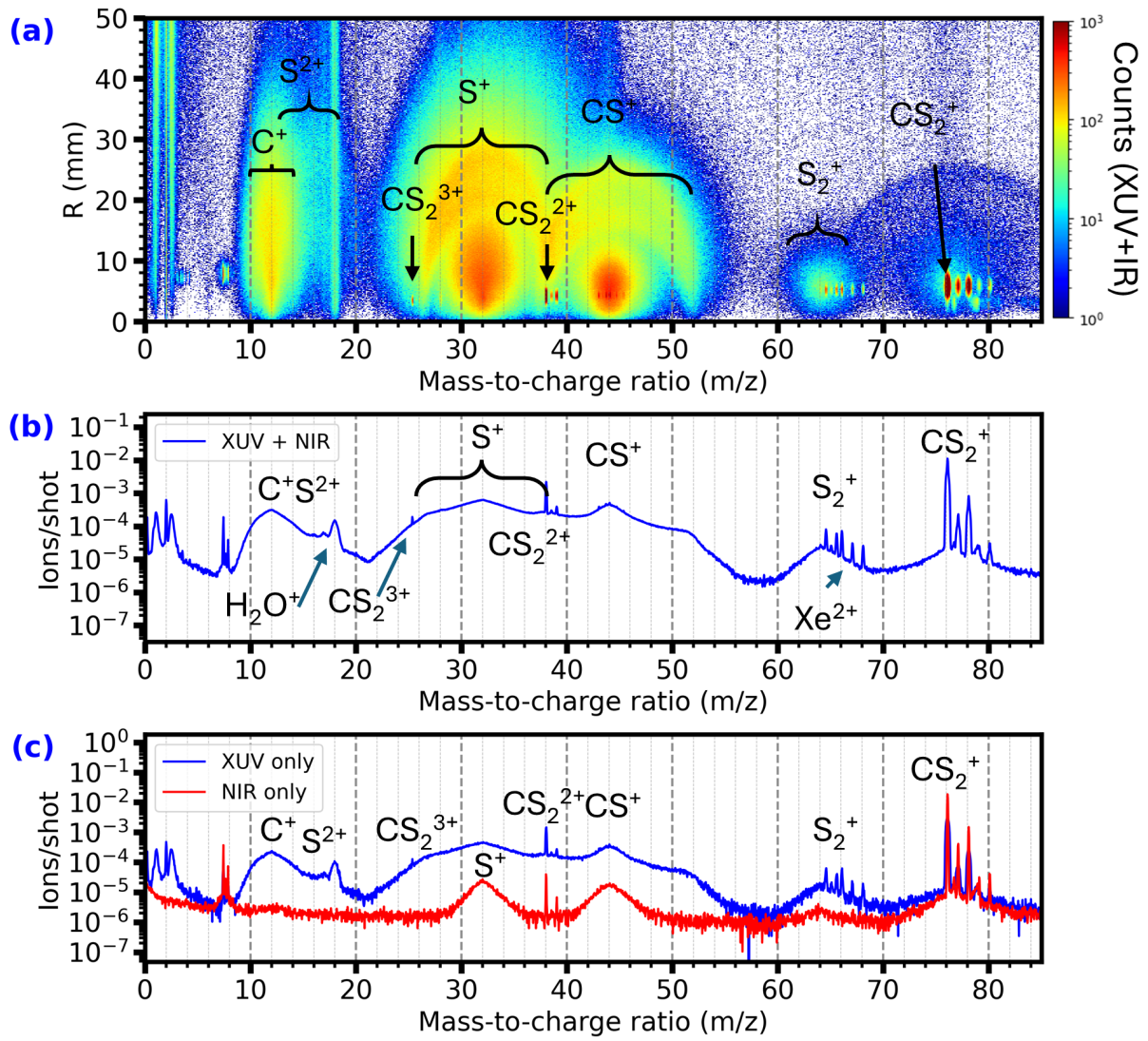

Figure 6.10: Ion signals from CS_2. (a) 2D histogram of detector radius R versus mass-to-charge ratio $[m/z]$ for the XUV+NIR pulse together, average over all pump–probe delays. (b) Mass spectrum (Counts/shot vs. m/z) obtained by integrating panel (a) over R. (c) Comparison of NIR-only (red) and XUV-only (blue) mass spectra.

Branching ratios of coincidence channels

The branching ratio BR_i of a given coincidence channel i is defined as

$$\mathrm{BR}_i = \frac{N_i}{\sum_j N_j} \times 100\%\,, \tag{6.16}$$

where N_i is the number of coincidence events observed in channel i and $\sum_j N_j$ is the total number of coincidence events in all considered channels. The total number of coincidence events is calculated by summing all the coincident events, and the branching ratio values are summarized in Table 6.1.

$$\sum_j N_j = 306\,653 \tag{6.17}$$

The $CS^+ + S^+$ channel clearly dominates with a branching ratio of 82.09%, indicating that it is the most favorable two-body dissociation pathway. Its high yield enables reliable delay-dependent analysis.

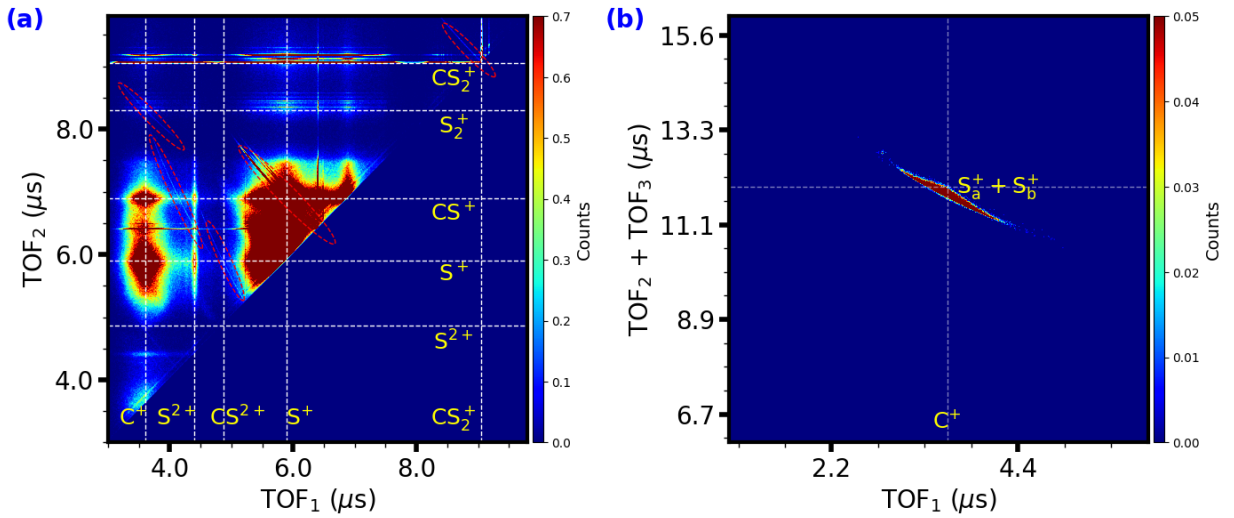

Figure 6.11: PIPICO map of CS_2 showing different dissociation channels: (a) TOF correlation between the first and second ions (two-fold ion–ion coincidence), (b) correlation between the TOF of the first-hit ion and the sum of the TOFs of the other two fragments (three-fold coincidence).

Table 6.1: Branching ratios of the coincidence channels.

Channel	N_i	BR_i [%]
$S^+ + CS^+$	251 722	82.09
$CS_2^+ + CS_2^+$	11 274	3.68
$CS^+ + S^{2+}$	3 628	1.18
$C^+ + S_2^+$	1 420	0.46
$CS^{2+} + S^+$	2 810	0.92
$C^+ + S_a^+ + S_b^+$	35 799	11.67
Total	306 653	100.00

In contrast, the $C^+ + S_2{}^+$ channel exhibits a very small branching ratio (0.46%), making it the least probable two-body dissociation pathway and preventing meaningful time-resolved analysis. Similarly, the low yields of the other minor channels limit the scope of delay-dependent studies. In addition, three-body breakup $C^+ + S_a{}^+ + S_b{}^+$ (11.67%) is observed, reflecting the formation and fragmentation of higher charge states.

KER of Two-Body Breakup Channels

Fig. 6.12(a–d) shows the KER distributions for the two-fold ion–ion coincidence channels identified in the CS_2 data. Two prominent channels originate from the dication.

$$CS_2{}^{2+} \longrightarrow CS^+ + S^+ \quad \text{and} \quad CS_2{}^{2+} \longrightarrow C^+ + S_2{}^+.$$

For the $CS^+ + S^+$ channel shown in Fig. 6.12(a), the KER exhibits a pronounced peak near 4.2 eV, with a tail extending to 10 eV. The $C^+ + S_2{}^+$ channel shown in Fig. 6.12(b) also peaks at 4.2 eV, but with a narrower KER distribution. This channel likely originates from a bending motion in which the two sulfur atoms approach each other, form a transient S–S bond (near-triangular geometry), and subsequently detach from the carbon atom, producing $S_2{}^+$. Because the charge-separation distance at breakup is similar to that in the CS^+-S^+ channel, the KER values are comparable. Momentum conservation then leads to a strongly asymmetric energy partitioning: the lighter C^+ fragment carries most of the kinetic energy,

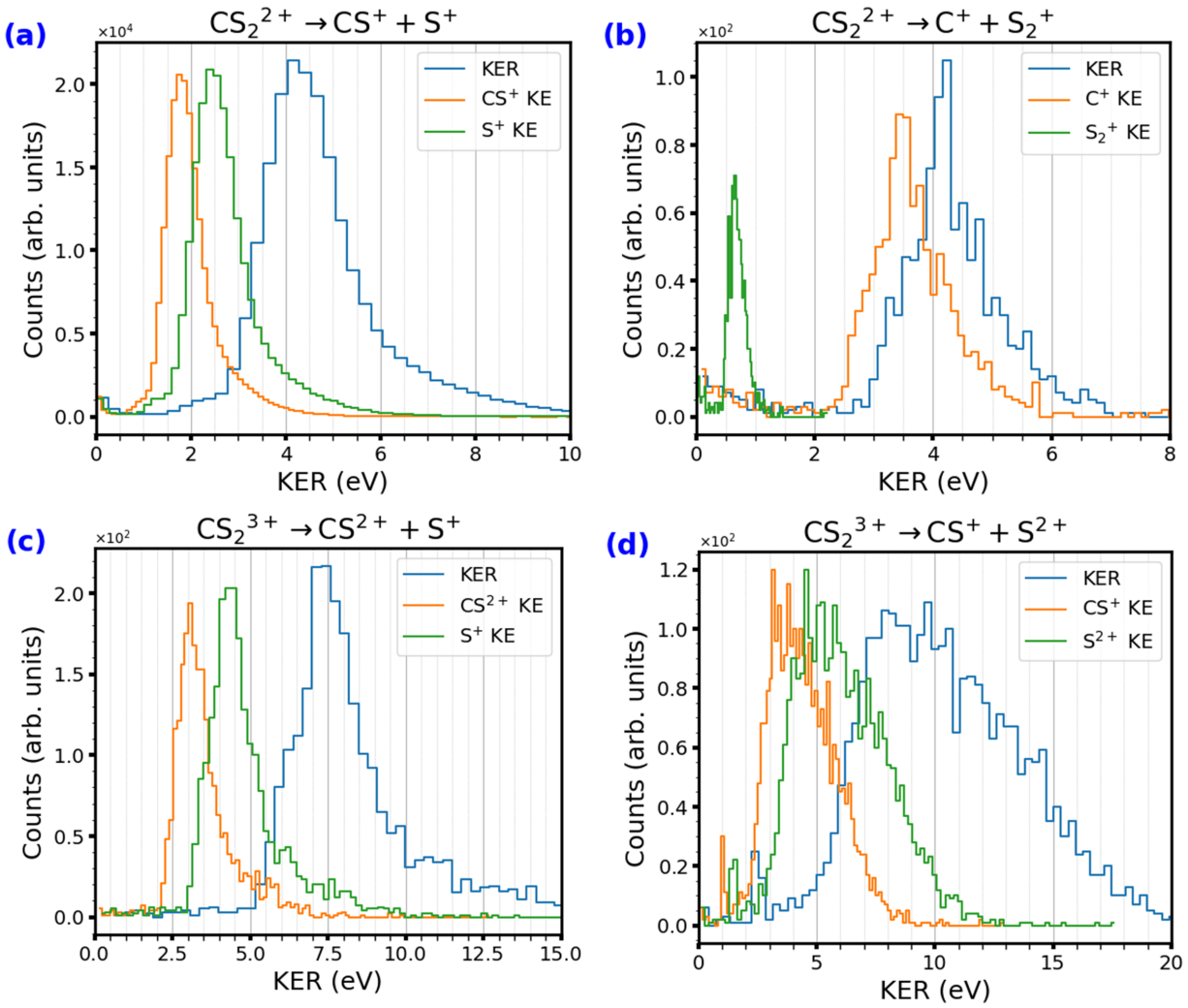

Figure 6.12: KER distributions for two-fold ion–ion coincidence channels: (a) $CS_2^{2+} \longrightarrow CS^+ + S^+$, (b) $CS_2^{2+} \longrightarrow C^+ + S_2^+$, (c) $CS_2^{3+} \longrightarrow CS^{2+} + S^+$, (d) $CS_2^{3+} \longrightarrow CS^+ + S^{2+}$.

while the heavier S_2^+ ion is correspondingly slower.

Two additional two-body breakup channels arise from the trication and are shown in Fig. 6.12(c–d):

$$CS_2^{3+} \longrightarrow CS^{2+} + S^+ \quad \text{and} \quad CS_2^{3+} \longrightarrow CS^+ + S^{2+}\,.$$

As expected for a higher total charge, their KER distributions are shifted to larger energies and are generally broader than the dication channels, reflecting a stronger Coulomb drive and a range of breakup geometries at the instant of fragmentation. For the channel $CS_2^{3+} \longrightarrow CS^{2+} + S^+$, the KER peaks at around 7 eV and extends up to 12 eV. In contrast, for $CS_2^{3+} \longrightarrow CS^+ + S^{2+}$ (Fig. 6.12d), the KER is more broadly distributed, spanning roughly 5 eV to 20 eV with a peak near 9 eV. This broadening likely arises from low barriers on the relevant PESs along C–S bond stretching, which permit fragmentation over a wide range of geometries and can support bound states at low vibrational excitation [168].

Time-Resolved KER of the $CS^+ + S^+$ Channel

A time-resolved KER map was plotted for the $CS^+ + S^+$ two-body breakup, with sufficient statistics for delay-dependent analysis. Fig. 6.13(a) shows the 2D histogram $I(\mathrm{KER}, \Delta t)$. Binning was chosen to balance temporal resolution, and errorbar counts are normalized per laser shot and corrected for FEL pulse energy.

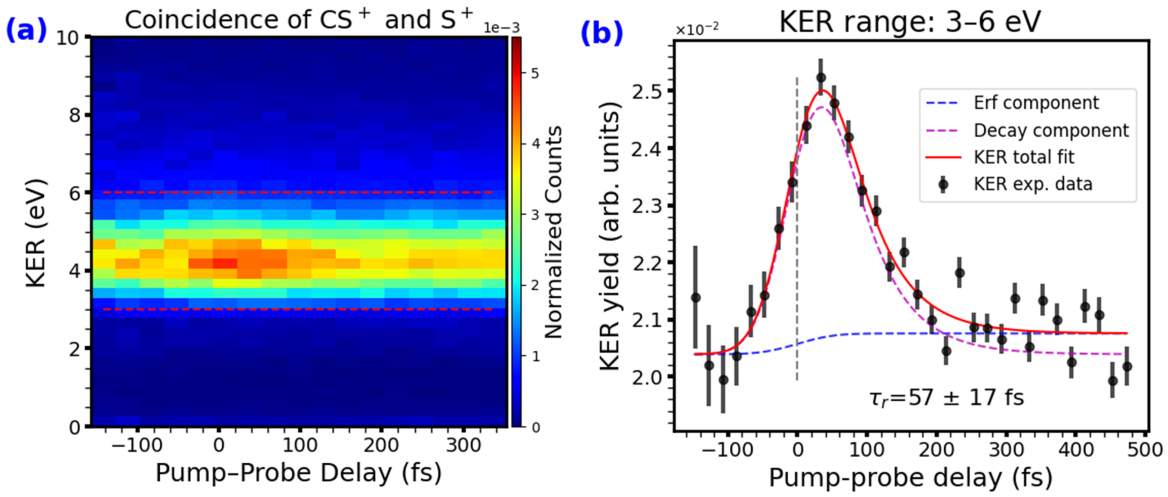

Figure 6.13: Time-resolved KER of $CS^+ + S^+$. (a) 2D histogram of KER vs. pump–probe delay. (b) Delay-dependent yield integrated over 3 eV to 6 eV. Black points with error bars show the measured KER integrated yield; the red curve is the total fit. The blue dotted curve is the error-function (cross-correlation) component, and the pink dotted curve is the exponential decay component. The vertical dotted lines mark the temporal overlap.

To quantify the dynamics, Fig. 6.13(b) plots the KER yield integrated over 3 eV to 6 eV. A clear transient is observed: the yield rises during the XUV–NIR temporal overlap and decays at positive delays, indicating that the NIR pulse probes a short-lived intermediate prepared by the XUV pulse.

$$CS_2 + h\nu_{XUV} \longrightarrow {CS_2}^{+*} + e^- + h\nu_{NIR} \longrightarrow CS^+ + S^+ + e^-$$

The delay dependence is well described by an exponential convolved with the instrument cross-correlation, showing a characteristic timescale of $\tau_r = (57 \pm 17)$ fs from the 1D fit.

The ${CS_2}^{2+} \longrightarrow CS^+ + S^+$ channel shows the same transient behavior like ${CO_2}^{2+}$ dissociation into $CO^+ + O^+$. In CS_2 data, ion–neutral channels such as $CS^+ + S$ or $S^+ + CS$ are not observed.

Three-Body Dissociation Channel ${CS_2}^{3+} \longrightarrow C^+ + {S_a}^+ + {S_b}^+$

Fig. 6.11(b) shows the PIPICO map for CS_2 in the three-body breakup regime. A distinct triple-coincidence island is observed for the complete Coulomb explosion channel,

$${CS_2}^{3+} \longrightarrow C^+ + {S_a}^+ + {S_b}^+,$$

where subscripts a, b label the two indistinguishable sulfur ions.

Fig. 6.14(a) shows the geometrical representation of the Dalitz plot, where the marked regions indicate the expected signatures of different mechanisms. The experimental Dalitz distribution is shown in Fig. 6.14(b), in which each point corresponds to one $C^+ + {S_a}^+ + {S_b}^+$ event and encodes the sharing of the KER among the three fragments. The axes are normalised according to Eqs. (6.1) and (6.2). Distinct regions can be associated with specific pathways: events enclosed by the green dotted oval correspond to molecular bending, and the bottom central area, marked in dotted purple, indicates nearly linear dissociation, in which carbon has nearly zero energy, and the other two atoms carry all the energy and separate. Two other lobes, marked by the black oval shape, reflect the asymmetric stretching of CS_2, where one C–S bond stretches more than the other at the time of Coulomb explosion. The

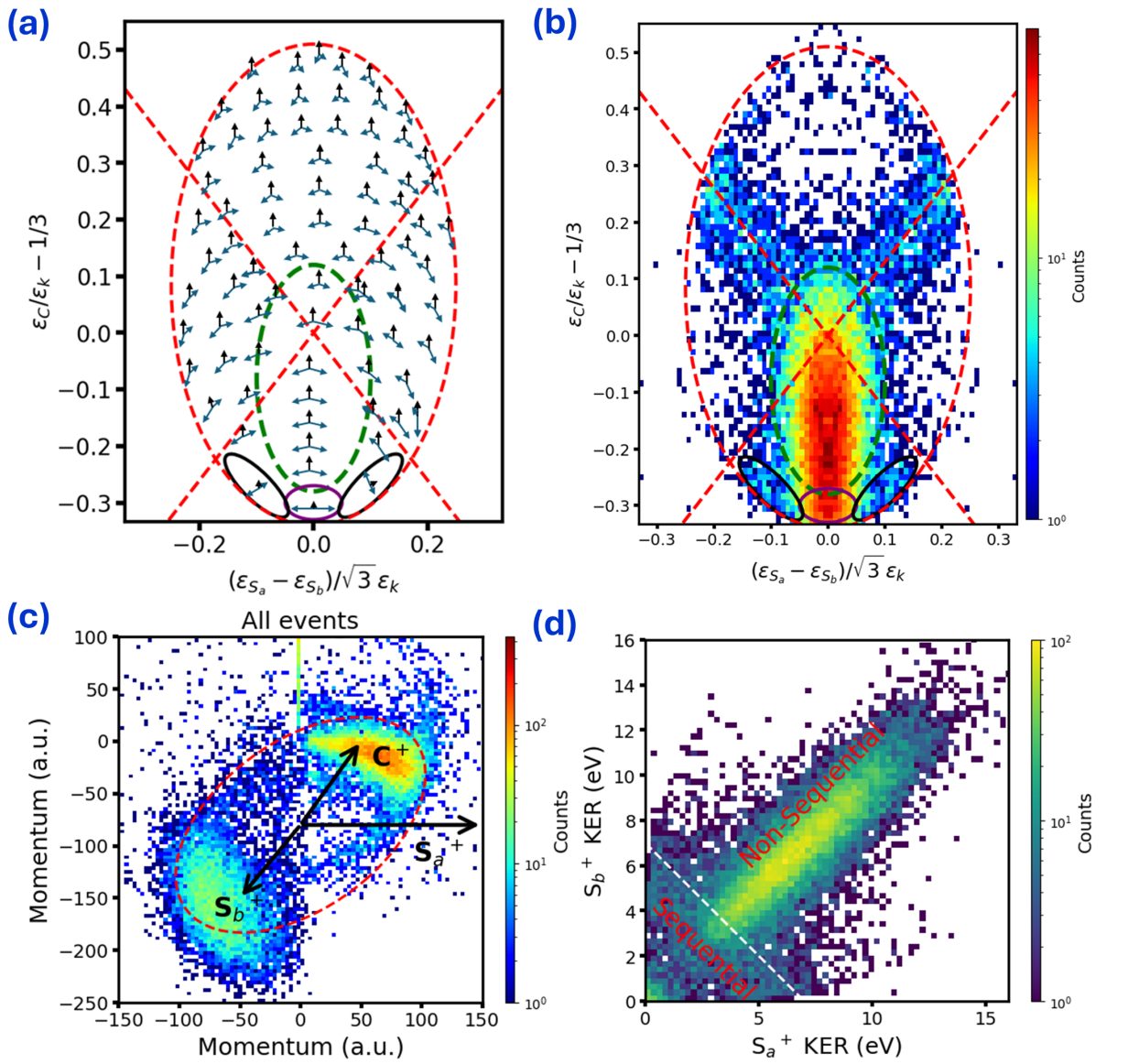

Figure 6.14: (a) Schematic momentum-correlation features at representative points of the Dalitz plot. (b) Experimental Dalitz plot for the three-body channel $CS_2{}^{3+} \longrightarrow C^+ + S_a{}^+ + S_b{}^+$. (c) Newton plot for all events(including sequential and non-sequential). (d) Energy-correlation plot for the two sulfur ions.

event located along the two crossing dashed red-lined elongated band along the characteristic axis (indicated by the red dashed line) signals sequential fragmentation, in which the two C–S bonds break stepwise *via* a transient CS^{2+} intermediate. Compared with $CO_2{}^{3+}$—where linear, symmetric breakup is often dominant than $CS_2{}^{3+}$ here molecular bending dominates. This difference arises from the larger mass of sulfur compared to oxygen, which modifies the momentum and kinetic energy partitioning during fragmentation.[169, 170]. There is a higher probability of a higher-vibrational-frequency population, thus favoring the molecular bending fragmentation mechanism [168].

The Newton plot for the triple-coincidence channel is shown in Fig. 6.14(c). The momentum vector of $S_a{}^+$ is fixed along the x axis, while the momenta of C^+ and $S_b{}^+$ are plotted in the upper and lower half-planes, respectively. Two intense islands are observed, corresponding to non-sequential dissociation of $CS_2{}^{3+}$. A weak half-circular arcs are visible between the islands; these ring-like features are characteristic of sequential

breakup, reflecting a two-step decay in which $CS_2^{3+} \longrightarrow S_a^+ + CS^{2+}$ is followed, after a finite delay, by $CS^{2+} \longrightarrow C^+ + S_b^+$.

To separate these two mechanisms quantitatively, the correlation between the kinetic energies of S_a^+ and S_b^+ is shown in Fig. 6.14(d). Two structures are clearly distinguished: a strong diagonal band, indicating a pronounced correlation between the sulfur-ion energies (non-sequential), and a diffuse off-diagonal region with weak correlation (sequential breakup). The dotted white boundary marks the selection used for subsequent analysis: events within the off-diagonal region are assigned to the sequential pathway, while the complementary region along the diagonal defines the non-sequential set. This energy correlation also confirms the coexistence of concerted and stepwise fragmentation mechanisms.

After filtering the events based on the kinetic energy correlation, the non-sequential and sequential contributions are separated, and the corresponding Newton diagrams are shown in Fig. 6.15(a–b), respectively. In the non-sequential case, the Newton plot exhibits two distinct islands, whereas the sequential Newton plot shows a tail-like feature. Due to limited statistics, a clear ring structure cannot be resolved in the sequential Newton plot.

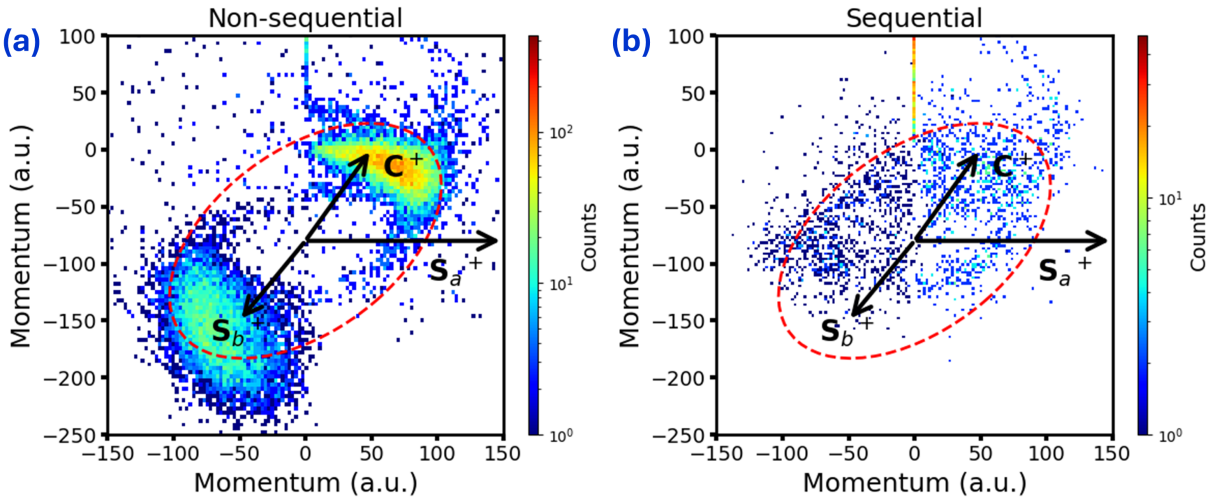

Figure 6.15: Newton diagram of (a) Non-sequential (b) and sequential fragmentation for $CS_2^{3+} \longrightarrow C^+ + S_a^+ + S_b^+$

Fig. 6.16(a) shows the KER distribution of all events, including sequential and non-sequential, for CS_2^{3+} together with the corresponding fragment energies. The KER is broadly distributed and peaks at approximately 19 eV. For comparison, strong-field measurements using longer NIR pulses ($\sim$ 60 fs, $\sim 5 \times 10^{14}$ W cm^{-2}) report smaller KER (15 eV) values. This reduction is plausibly attributed to molecular deformation (e.g., bond stretching/bending, bond softening) during the longer pulse, which increases the charge-separation distance at breakup. In the present experiment, the FEL pulse duration is < 20 fs, limiting nuclear rearrangement prior to Coulomb explosion and yielding a higher KER peak. The $\sim$ 19 eV value is consistent with prior measurements reported by Rjagara *et al.* using 120 keV Ar^{8+} ion impact [171] and by Wang *et al.* using 1 keV electron impact [168].

Fig. 6.16(b) compares the KER for sequential and non-sequential three-body fragmentation. The sequential mechanism KER range from 0 eV to 17 eV with a peak near 14 eV, whereas the non-sequential pathway peaks around 19 eV. The reduced KER in the sequential case is consistent with a two-step breakup in which the second dissociation occurs at a larger internuclear separation, thereby reducing Coulomb repulsion and the released kinetic energy.

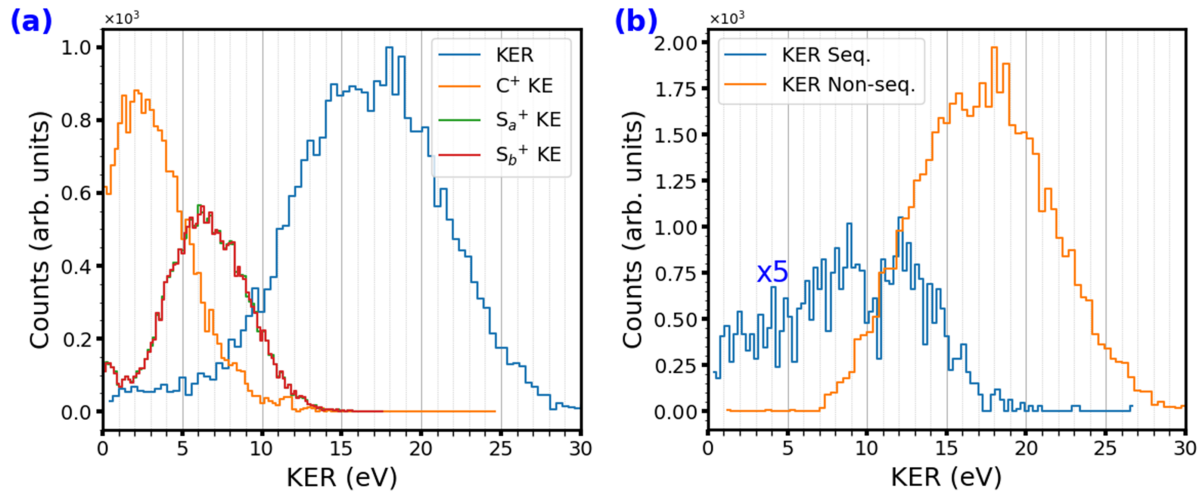

Figure 6.16: (a) KER distribution for the three-body breakup $CS_2^{3+} \longrightarrow C^+ + S_a^+ + S_b^+$. (b) Comparison of KER distributions for non-sequential and sequential mechanisms.

Time-Resolved KER of CS_2^{3+}

Fig. 6.17(a) shows the time-resolved KER map for triple-coincidence events ($C^+ + S_a^+ + S_b^+$), plotted as a 2D histogram of KER (eV) versus pump–probe delay. Owing to the low triple-coincidence count rate, coarser binning in both delay and energy is used than for the two-body channels. Each bin is normalized to the laser shot and corrected for the FEL pulse energy.

A clear delay-dependent signal is visible: the mean KER decreases from approximately 19 eV at temporal overlap to 15 eV at positive delays, consistent with a coulombic potential energy curve. Because of limited statistics, sequential and non-sequential contributions cannot be reliably separated; consequently, the aggregate KER is reported.

Given the low counts, a robust fit of the delay-dependent yield integrated over 10 eV to 30 eV is not feasible, and quantitative lifetimes for this channel cannot be extracted.

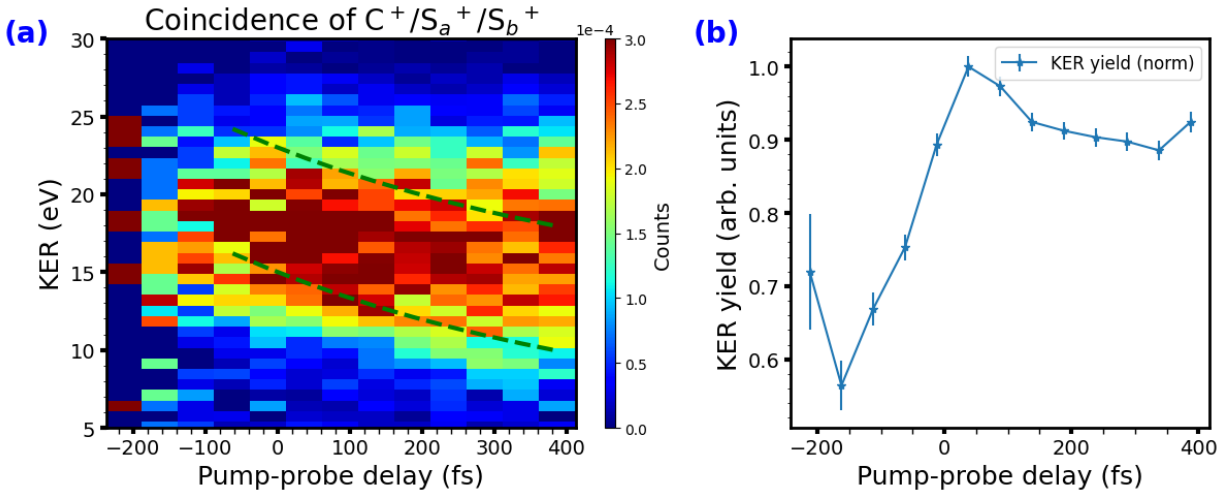

Figure 6.17: Time-resolved KER of $C^+ + S^+ + S^+$. (a) 2D map of KER versus pump–probe delay. (b) Integrated KER yield over the selected KER window as a function of delay.

6.4 Summary and Conclusions: Comparative Dynamics of CO_2 and CS_2

This chapter provides a comparative analysis of the ultrafast ionization and fragmentation dynamics of CO_2 and CS_2 using time-resolved CEI with an XUV-pump and an NIR-probe in a REMI setup.

In CO_2, XUV FEL pulses induce single and double ionization, thereby populating both bound and dissociative states. Triple ionization leads exclusively to dissociative states; consequently, the triple-ionized species (CO_2^{3+}) does not appear as a distinct peak in the mass spectrum, reflecting its high instability and rapid Coulomb-driven fragmentation. Coincidence analysis identifies two principal fragmentation pathways: a two-body channel ($CO^+ + O^+$) and a three-body channel ($C^+ + O^+ + O^+$). The KER for the two-body channel exhibits a transient dependence on the pump–probe delay, which is attributed to a dissociative cationic state (CO_2^{+*}) with a lifetime of 62 ± 10 fs.

Dalitz and Newton plot analyses of the three-body fragmentation channel in CO_2 provide detailed insight into dissociation dynamics. These triple-coincidence data reveal both sequential and non-sequential fragmentation pathways. Energy correlation analysis between the two O^+ ions enables clear differentiation between concerted (non-sequential) and stepwise (sequential) breakup mechanisms. Newton plots show distinct momentum distributions: the sequential pathway exhibits well-defined lobes, indicating a delayed emission of the second O^+ ion after formation of a rotating CO^{2+} intermediate, whereas the non-sequential pathway shows a more symmetric distribution. Time-resolved Newton plot analysis further elucidates the rotational dynamics of the intermediate CO^{2+} fragment, with an estimated rotational timescale of approximately 250 fs. The three-body channel is further enhanced by ionization from the delayed NIR pulse, which promotes the formation of ${CO_2}^{2+*}$ and its subsequent conversion to ${CO_2}^{3+}$. This highly charged state subsequently undergoes Coulomb explosion, resulting in fragmentation into C^+ and two O^+ ions through both sequential and non-sequential processes, with a clear dependence on the pump–probe delay.

In CS_2, XUV FEL pulses induce single, double, and triple ionization, populating both bound and dissociative states, as evidenced by the mass spectrum. Coincidence analysis identifies several two-body fragmentation channels, with the $CS^+ + S^+$ channel being dominant, as well as a three-body channel ($C^+ + S^+ + S^+$). The KER for the dominant $CS^+ + S^+$ channel exhibits a transient dependence on the pump–probe delay, attributed to a dissociative excited cation state (${CS_2}^{+*}$) with an exponential decay time of 57 ± 17 fs.

Dalitz and Newton plot analyses of the three-body fragmentation channel $C^+ + S^+ + S^+$ in CS_2 indicate the presence of both sequential and non-sequential breakup mechanisms. Separation of these pathways is achieved by measuring energy correlations between the two sulfur ions (S^+). The analysis indicates that the non-sequential (concerted) mechanism is dominant. Additionally, the mean KER decreases from approximately 19 eV to 15 eV as the positive delay increases, suggesting structural evolution of the molecule. However, limited statistics restrict more detailed separation and quantitative analysis of the individual contributions.

The comparison of CO_2 and CS_2 underscores the impact of molecular mass and electronic structure on fragmentation dynamics. In CO_2, the atomic masses are relatively similar, while in CS_2, the heavier sulfur atoms significantly influence nuclear motion. Additionally, sulfur's greater electron count compared to oxygen leads to differences in electronic structure and ionization behavior. Consequently, CS_2 displays more pronounced bending dynamics, as observed in Dalitz plot distributions, whereas CO_2 remains comparatively linear. This increased bending in CS_2 facilitates the observation of minor channels such as $C^+ + {S_2}^+$, while CO_2 exhibits only a very weak ${O_2}^+$ signal. Furthermore, CS_2 shows a clear trication

signature in the mass spectrum, whereas in CO_2 the trication state dissociates too rapidly to be directly detected.

Despite these differences, the lifetimes of the states $CO_2{}^{+*}$ and $CS_2{}^{+*}$ are approximately similar within experimental uncertainty. However, the low triple-coincidence count rate limits a more detailed analysis of three-body fragmentation dynamics. Future experiments utilizing higher-repetition-rate free-electron lasers or extended acquisition times under stable conditions will be necessary to clearly distinguish between sequential and non-sequential breakup mechanisms.

Chapter 7

UV-Induced Dissociation of 1-Butanethiol

7.1 Introduction

Sulfur-containing organic compounds play a significant role in the photochemistry of the Earth's atmosphere, despite their low concentration [172]. These compounds act as secondary air pollutants, influencing air quality, climate regulation, and ecosystem health [173]. Within this family of chemicals, small-carbon-chain thiol (R-SH) molecules such as methanethiol (CH_3SH), ethanethiol (C_2H_5SH), propanethiol (C_3H_7SH), and the linear-chain of four-carbon 1-butanethiol (C_4H_9SH) are common and reactive, playing an important role in atmospheric sulfur cycling [174]. These thiol molecules enter the atmosphere from both anthropogenic and natural sources, with contributions from fossil fuel combustion, petroleum refining, biomass burning, and biologically mediated marine fluxes [173]. Thiol groups in the atmosphere can undergo photolysis under UV radiation, where absorption of light leads to cleavage of sulfur–hydrogen (S−H) and carbon–sulfur (C−S) bonds and the formation of sulfur radicals [175]. These radicals can initiate a series of atmospheric reactions, ultimately leading to the formation of harmful compounds, such as sulfur dioxide (SO_2) and sulfuric acid (H_2SO_4). These products are responsible for environmental problems such as acid rain and smog [176].

Photodissociation of organosulfur molecules governs the formation of reactive sulfur-containing radicals, with implications ranging from atmospheric chemistry to biomolecular photoprotection. However, a detailed, real-time understanding of how S−H and C−S bonds break, when they do, and how the charge redistributes during bond breaking and rearrangement in the gas phase is an active area of research [177].

Traditional optical pump–probe techniques provide excellent temporal resolution but lack element specificity. In contrast, synchrotron-based X-ray probes with picosecond pulse durations provide chemical sensitivity but lack time resolution for studying ultrafast processes and suffer from limited photon flux for low-density gas-phase targets, making site-specific studies on femtosecond timescales challenging [178]. Recent advancements in X-ray FEL sources have overcome these limitations by delivering short, high-intensity X-ray pulses [51]. This enables time-resolved inner-shell photoelectron spectroscopy in the gas phase with both element and site specificity, allowing, for example, the direct tracking of sulfur-centered electronic and nuclear dynamics during UV-driven dissociation [109, 177, 179–182].

Probing the sulfur (S) 2p edge leverages the locality and chemical sensitivity of inner-shell ionization: the S (2p) binding energy shift is influenced by the immediate bonding environment. Therefore, a time-delayed sulfur-edge X-ray probe provides insight into the evolving local structure as S-H and C-S bonds depart from their equilibrium geometries and

fragments form.

Time-resolved X-ray photoelectron spectroscopy (TR-XPS) exploiting the S (2p) edge has been used to disentangle the ultrafast UV dissociation of CS_2, directly assigning the emergence of CS and S photoproducts from the time-dependent S (2p) photoelectron lines, validating the sulfur-site specificity for bond-selective breakup [177, 183]. Another complementary study, using time-resolved X-ray Auger-Meitner spectroscopy (TR-AMS) at the S (2p) level, monitors the Auger-Meitner (AM) electron spectra of UV-excited CS_2, resolving from bound excited molecule to CS + S fragment and provides a dissociation time constant of 1.2 ps consistent with prior S (2p) TR-XPS result [183].

Here, the UV-induced dissociation of 1-butanethiol was studied using an UV pump pulse at a center wavelength of 267 nm, corresponding to 4.65 eV photon energy to initiate dissociation, followed by a delay-controlled XUV probe pulse at 179 eV photon energy to investigate sulfur-centered dynamics with femtosecond resolution (see Fig. 7.1). Experiments were conducted at the CAMP endstation (beamline BL1, FLASH1), employing an ion time-of-flight spectrometer and an electron velocity map imaging (VMI) spectrometer; see Chapter 3 for more details. Time-resolved experiments provide information on fragmentation pathways and on the evolution of FEL-induced charge states, where charge transfer stops as the molecular fragments separate. As the C-S bond dissociates and the 1-butanethiol moiety evolves towards atomic sulfur, the S (2p) binding energy shifts to higher values, directly reflecting the transition from molecular to an atomic sulfur environment. This increase in binding energy corresponds to a decrease in the photoelectron and AM kinetic energy.

7.2 Experimental Method

The time-resolved UV/XUV pump–probe experiments described in this chapter were carried out at the permanent CAMP endstation at beamline BL1 at FLASH1, as described in Chapter 3. The XUV probe pulse was generated by the FLASH1 fixed-gap undulator and set to a photon energy of 179 eV to ionize the S (2p) core level states. The FEL operated at 10 Hz, synchronized with the optical laser system. The XUV pulse has a temporal duration of approximately 50 fs (FWHM) and was focused into the interaction chamber using a KB mirror setup, producing a focal spot of roughly 10 µm diameter [88].

Because of the stochastic nature of the SASE process and accelerator fluctuations—i.e., variations in the electron bunch energy and timing—both the FEL pulse energy and arrival time fluctuate from shot to shot. To correct for these variations, the pulse energy was recorded on a shot-by-shot basis using a GMD [66], while the timing jitter was measured using a BAM setup [121]. These diagnostics were used in the post-analysis to normalize the data and correct for timing jitter, thereby improving temporal resolution [98, 108, 111, 185].

A Ti:Sapphire pump–probe laser synchronized to FLASH delivered 800 nm NIR pulses; a fraction of the beam was frequency tripled in a BBO crystal to produce UV pump pulses with pulse durations on the order of about 150 fs and a peak intensity of 5×10^{12} W cm^{-2}. The UV and XUV pulses were spatially and temporally overlapped in the interaction region. Temporal delay scans were performed using a motorized delay stage, varying the relative delay between −1 ps and 1 ps in 100 fs steps. Background datasets, FEL-only and UV-only, were acquired intermittently at 0.25 Hz during the scans.

Gas-phase 1-butanethiol samples were introduced into the interaction region via supersonic expansion. The sample (Sigma-Aldrich, >98 % purity) was vaporized in a resistively heated reservoir integrated with an injection valve. The reservoir was maintained at approximately 100 °C—about 2 °C above the sample's boiling point (98 °C)—to ensure sufficient vapor pressure. The molecules were seeded in a helium carrier gas at a backing pressure of 3 bar and expanded into vacuum through a continuous nozzle. The resulting molecular

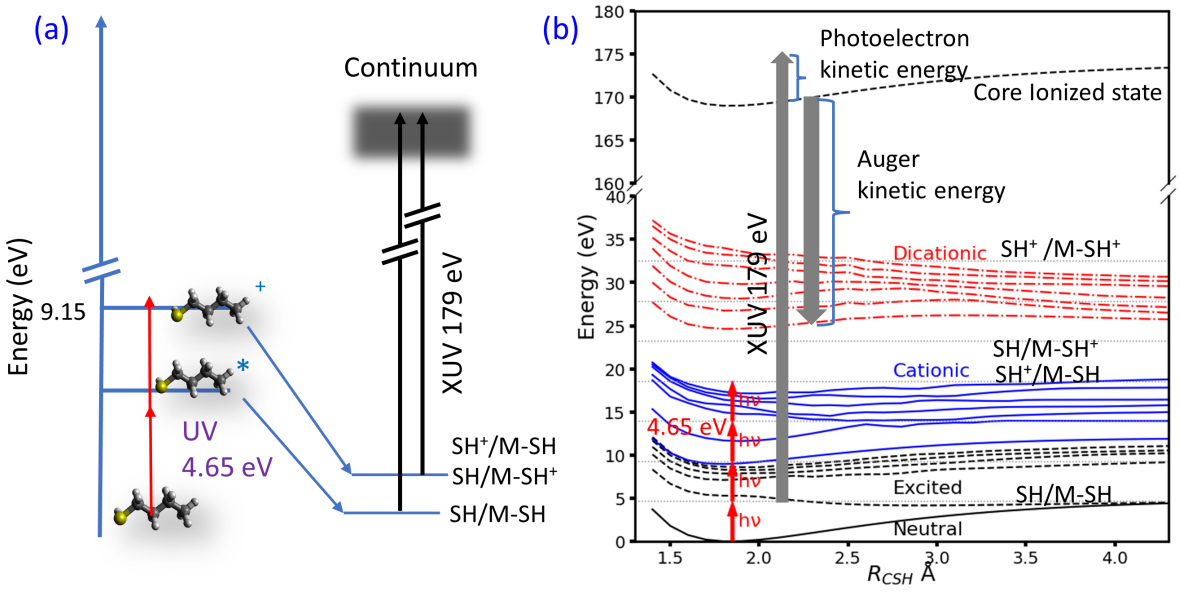

Figure 7.1: Schematic of the UV/XUV pump–probe experiment on 1-butanethiol. (a) A 267 nm (4.65 eV) UV pump pulse photoexcites the molecule via a two- or multiphoton absorption pathway, initiating dissociation along the C–S coordinate toward neutral fragments, including atomic sulfur (S) and sulfur-loss channels (SH/M–SH), as well as cationic sulfur-containing fragments (SH^+/M–SH^+). A delayed 179 eV XUV FEL probe pulse ionizes the S 2p core level, enabling femtosecond-resolved tracking of the evolving sulfur electronic structure via electron VMI.(b) Time-dependent density functional theory (TD-DFT) potential energy curves (PECs) along the C–S coordinate for selected neutral, excited, cationic, and dicationic states. These curves illustrate the dissociative pathways and the increase in S (2p) binding energy as the fragments separate, corresponding to a decrease in photoelectron kinetic energy. The quantum-chemical calculations were performed using ORCA 6.1.0 [184]. The S_0 ground state of 1-butanethiol was optimized at the B3LYP/def2-QZVP level with D3(BJ) dispersion corrections. Starting from the lowest-energy conformer, potential-energy curves were computed as a function of the C–S bond distance for the lowest 25 electronically excited states of the neutral, cationic, and dicationic species using the TD-DFT (B3LYP/def2-TZVPD). During these scans, all other geometric parameters were kept fixed except S−C bond length.

jet underwent adiabatic cooling and was collimated by two skimmers before entering the interaction chamber, which was maintained at a pressure below 5×10^{-9} mbar.

The CAMP endstation housed a double-sided VMI spectrometer capable of simultaneously detecting ions and electrons [88]. Ion TOF and VMI electron images were recorded at the same time, and the ion VMI detector was gated to selectively record the momenta of specific molecular fragments in a separate run. Following interaction with the laser pulse, the resulting ions and electrons are accelerated and guided by an electric field, which maps their velocities onto a dual MCP detector equipped with a phosphor screen and a CCD camera for imaging. Ion TOF information was recorded via an analog-to-digital converter (ADC).

7.2.1 Data Analysis

This section provides a detailed analysis of the experimental data obtained from a double-sided VMI setup. In this experiment, electron and ion VMI images and ion TOF spectra were recorded during a pump-probe delay scan, along with reference measurements using FEL-only and UV laser-only pulses. The main data processing steps are outlined here. All electron and ion data were analyzed in JupyterLab notebooks using Python, based on analysis scripts developed for this work.

Ion TOF-MS Data

In this experiment, time-resolved ion-yield information was obtained by recording mass spectra at different delay times. At each delay point, multiple single-shot TOF spectra were collected, binned, and averaged to improve the signal-to-noise ratio. Since the actual arrival time of the FEL is subject to timing jitter due to arrival-time fluctuations, each delay point was corrected using BAM data to determine the accurate delay between the FEL and the pump–probe laser pulse.

Ion yields were extracted from the TOF spectra by integrating the signal over selected TOF intervals. First, the TOF axis was calibrated to mass-to-charge ratio (m/z) using reference peaks from ions of known m/z (e.g., He^+ and the 1-butanethiol parent ion). Integration windows corresponding to the fragments of interest were then defined based on their m/z values, and the signal integrated within each window was taken as the ion yield as a function of time delay between pump and probe pulses. To correct for shot-to-shot FEL energy fluctuations, the extracted ion yields were normalized to the number of photons absorbed in the ionization process. In cases of low FEL peak intensity, single-photon absorption is generally a good approximation for most XUV experiments.

This analysis provided ion-yield traces as a function of pump–probe delay for each fragment; the discussion here focuses on the most relevant channels. The temporal overlap (t_0) of the pump and probe pulses was obtained by fitting the delay-dependent ion or electron yield using the fitting procedure described in Section 2.3.1.

Electron VMI Data

Electron spectra were recorded with the electron side of the double-sided VMI spectrometer. At each pump–probe delay, multiple single-shot images were acquired. The raw images were first processed shot-by-shot using a Gaussian blur filter and then thresholded to remove background noise, hot pixels, and detector artifacts. Subsequently, data is binned and averaged, yielding an electron image for each delay bin. All delay values were also corrected using BAM values.

The averaged 2D electron images were symmetrized and then Abel-inverted using the pBasex algorithm [97] to reconstruct the central slice of the 3D photoelectron distribution, as described in Section 3.4.5. Angular integration of the inverted images yields kinetic-energy spectra of the emitted electrons. Energy calibration of the electron detector was performed using the well-known He $1s$ ionization line ($E_I = 24.5$ eV) [186] and the krypton $3d$ spin–orbit doublet (Kr $3d_{5/2}$ at 93.8 eV and Kr $3d_{3/2}$ at 95.0 eV) [187], ensuring accurate assignment of spectral features (Fig. 7.2).

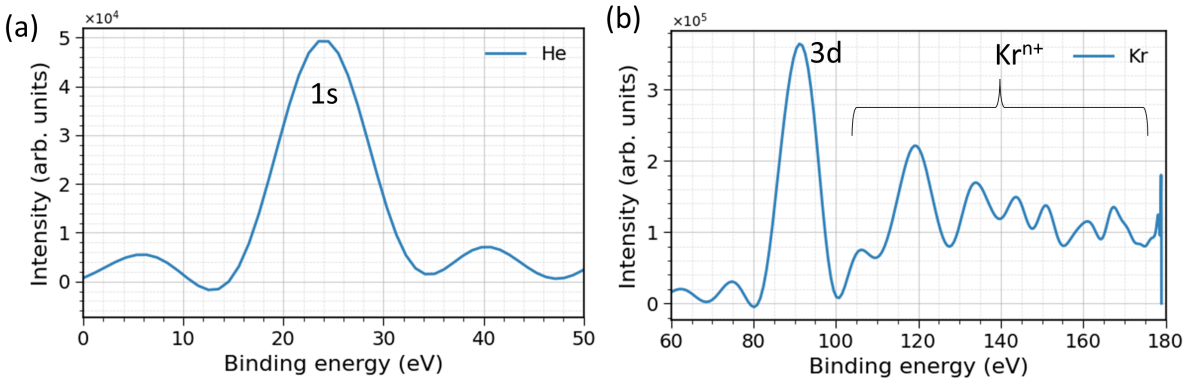

Figure 7.2: Reference binding energies extracted from the electron VMI data and used for electron kinetic energy calibration: (a) He 1*s* and (b) Kr 3*d*. The corresponding electron VMI and their Abel-inverted image are shown in Appendix C.3.

7.3 Results

7.3.1 Time-Resolved Ion Spectroscopy

Mass Spectra

The ionization and fragmentation dynamics of 1-butanethiol induced by XUV and UV pulses were investigated using the pump–probe setup. Fig. 7.3(a) shows the mass spectra of 1-butanethiol following interaction with the XUV pulse (blue trace) and the UV pulse alone (red trace). Fig. 7.3(b) compares the UV-early (black) and UV-late (green) mass spectra. High-resolution mass spectra of 1-butanethiol, shown in Appendix C.2, help to identify overlapping ion TOF signals.

Reaction Channels in 1-Butanethiol under UV Excitation

Static experiments on 1-butanethiol under UV excitation at 248 nm have revealed several reaction channels [188]. The main pathways are summarized as follows.

1. **Cleavage of the S–H bond:**

$$CH_3CH_2CH_2CH_2SH \longrightarrow CH_3CH_2CH_2CH_2S + H$$

2. **Cleavage of the C–S bond:**

$$CH_3CH_2CH_2CH_2SH \longrightarrow CH_3CH_2CH_2CH_2 + SH$$

3. **Dissociation after hydrogen transfer:**

$$CH_3CH_2CH_2CH_2SH \longrightarrow 2\,C_2H_4 + SH_2$$

4. **Cleavage of a C–C bond:**

$$CH_3CH_2CH_2CH_2SH \longrightarrow CH_3CH_2 + CH_2CH_2SH$$

The UV mass spectrum in Fig. 7.3(a) (red trace) shows a strong parent-ion signal at $m/z = 90$. A single UV photon of 4.65 eV is well below the ionization potential (IP) of 1-butanethiol (≈9.15 eV [189]), so the observed parent ion must originate from a two-photon

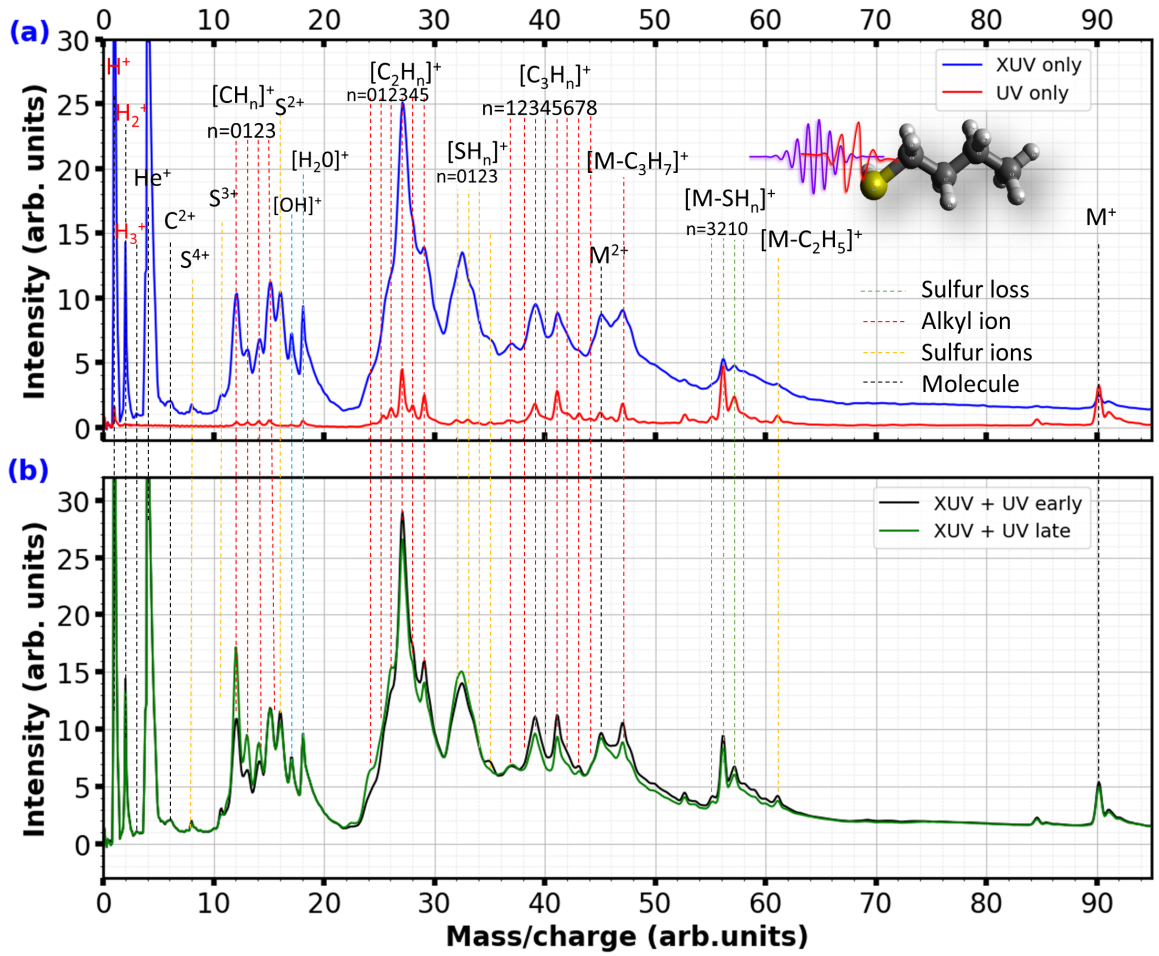

Figure 7.3: Mass spectra of 1-butanethiol obtained under different excitation/ionization conditions. (a) Fragment ions produced by XUV-only (blue) and UV-only (red) laser pulses. (b) UV-early (black) and UV-late (green) spectra from the pump–probe experiment, highlighting the temporal evolution of fragmentation channels.

ionization pathway. A prominent group of fragments appears at $m/z = 54$–58, corresponding to $C_4H_n^+$ ($n = 6$–10) fragments produced after breaking off of S^+ or SH_n^+ ($n = 0$–3). A very small peak at $m/z = 32$–35 indicates that sulfur is formed predominantly in neutral form, with only minor channels in which sulfur departs as SH_2. Clear evidence for C–C bond cleavage is provided by the most intense peak in the TOF-MS spectrum near $m/z = 24$–29, attributable to $C_2H_n^+$ fragments ($n = 0$–5), consistent with UV-induced carbon–carbon bond scission.

Overall, the UV pulse induces fragmentation through both C–S and C–C bond cleavage. Low peak signals include a weak H^+ peak and a very faint H_2^+ peak, the latter consistent with the high IP of neutral H_2 (15.37 eV [190]) or alternatively attributable to fragmentation of the molecule itself. This implies that multiphoton absorption processes at 4.65 eV are required to produce these hydrogen-containing ions under the applied UV conditions.

Fig. 7.1(b) shows calculated PECs for 1-butanethiol, indicating that two to four UV photons are required to excite and dissociate the molecule, consistent with the rich fragmentation observed in the UV-only mass spectrum. At least two UV photons are required to ionize the molecule and produce the parent cation. Within the singly ionized manifold, several dissociative states lie at significantly higher energies; absorption of four UV photons would be required to access these dissociative cationic states.

A distinct dicationic (M^{2+}) peak cannot be unambiguously identified, most likely due

to overlap with the SCH^+ fragment, which appears at the same m/z. The IP of M^{2+} is approximately 25 eV, as suggested by the above theoretical calculations. It is also possible that the dication is too short-lived to be detected. Overall, the PECs suggests that more than three UV photons are required to access strongly ionized dissociative states of the molecule. The UV-intensity-dependent mass spectrum is shown in the Appendix (see Section C.1).

XUV: Core Ionization of Sulfur

When a 1-butanethiol molecule is exposed to XUV photons with an energy of 179 eV, the dominant process is ionization of the S (2p) core level, which has an IP of approximately 169 eV. Ionization occurs on a sub-femtosecond time scale, leaving a core hole localized on the sulfur atom. Within just a few sub-10 fs vacancy decays primarily via the AM process [191], in which a valence or inner electron (from the HOMO, HOMO-1, or Sulfur 3s,3p shells) fills the 2p hole, and an additional AM electron will be emitted from the outer shell. As nuclear motion begins to couple to the evolving charge distribution, the S–H and C–H bonds weaken. Within approximately 30 fs to 100 fs after XUV absorption, Coulomb-driven fragmentation sets in, leading to hydrogen loss, cleavage of the C–S bond, and the formation of small carbon-chain fragments. These processes are summarized schematically in Fig. 7.4, which illustrates the sequential evolution of 1-butanethiol following XUV-induced core ionization.

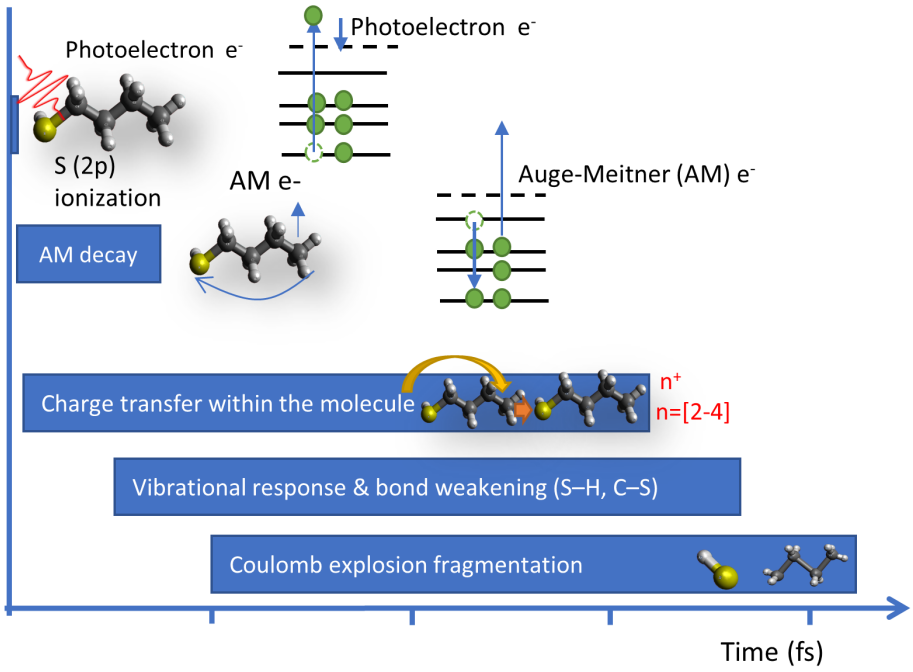

Figure 7.4: Schematic illustration of the processes following XUV ionization of 1-butanethiol. XUV absorption creates a sulfur 2p core hole and emits a photoelectron, followed by AM decay that redistributes charge within the molecule. Subsequent intramolecular charge transfer and increasing Coulomb repulsion lead to fragmentation and Coulomb explosion.

The mass spectra reveal the effects of S (2p) ionization at 179 eV and the subsequent AM decay. The cascade AM process localizes charge at the sulfur site, producing highly charged sulfur ions (up to S^{4+}) and driving Coulomb-induced fragmentation. The peak at m/z=56 corresponds to the loss of SH_2 ($[M–SH_2]^+$), indicating sulfur-centered bond cleavage. Peaks at m/z=33–35 arise from sulfur-containing fragments formed after rapid one- or two-hydrogen-transfer processes within the molecular ion.

In addition to sulfur ions, numerous carbon-containing fragment ions are observed, including small hydrocarbons such as CH_3^+ and C_2H^+, as well as larger fragments like $C_3H_6^+$. The most intense low-mass fragment, m/z=27 ($C_2H_3^+$), originates from carbon–carbon bond cleavage and subsequent dehydrogenation. Overall, the mass spectra indicate that sulfur-core ionization initiates ultrafast charge redistribution, hydrogen migration, and extensive fragmentation, yielding both highly charged sulfur ions and characteristic hydrocarbon fragments.

Delay-Dependent Ion Fragment

The delay value between the UV and XUV pulses is defined relative to time zero (t_0), which corresponds to their temporal overlap (Fig. 7.5). Negative delays ($t < 0$) correspond to UV pump – XUV probe ordering, where the UV pulse initiates excitation or dissociation before the XUV pulse probes the sulfur 2p level. Positive delays ($t > 0$) correspond to XUV pump – UV probe ordering, where the XUV pulse first ionizes the sulfur 2p core level, followed by UV interaction with the resulting transient states.

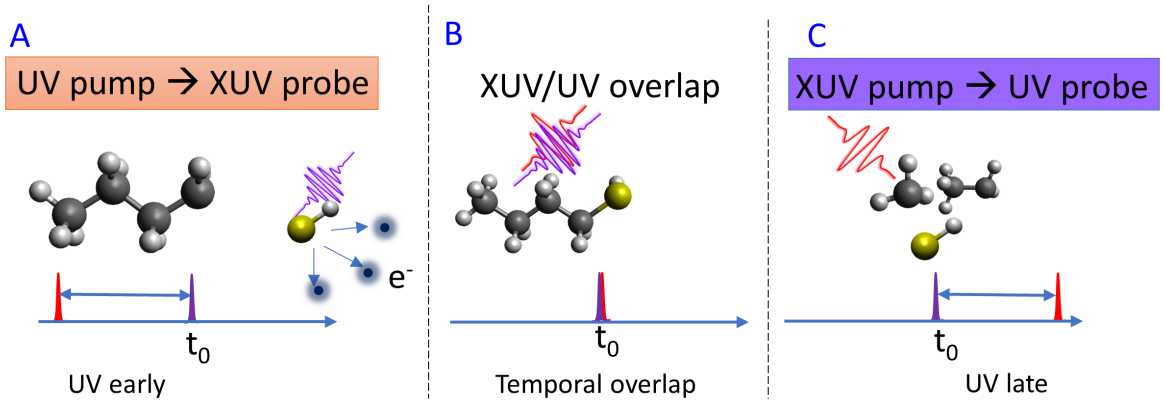

Figure 7.5: Three-panel schematic illustrating the UV/XUV delay-dependent pulse sequence: (A) UV pump – XUV probe ($t < 0$): the UV pulse excites or dissociates the molecule before XUV ionization; (B) Time zero (t_0): temporal overlap of UV and XUV pulses; (C) XUV pump – UV probe ($t > 0$): the XUV pulse ionizes the S (2p) core level before the UV pulse interacts. This schematic captures the three delay regimes of the dissociation and charge-transfer dynamics of 1-butanethiol.

UV pump – XUV probe ($t < 0$, Fig. 7.5A): The UV pulse excites 1-butanethiol from its ground state to electronically excited states and, if its photon energy and intensity are sufficiently high, can also ionize and induce dissociation of the parent molecule. A delayed XUV pulse then ionizes the sulfur 2p level, and Auger decay proceeds from an excited or fragmented ion state.

Time zero (t_0, Fig. 7.5B): The UV and XUV pulses overlap, defining the reference point for all pump–probe delays.

XUV pump – UV probe ($t > 0$, Fig. 7.5C): The XUV pulse ionizes the S (2p) core first, creating a highly unstable core-ionized state that decays via AM processes. The subsequent UV pulse interacts with the many transient and excited states resulting from or following AM decay, thereby enhancing fragmentation yields.

Charge Transfer

The UV pump–XUV probe experiment (Fig. 7.6) illustrates how charge redistributes between the alkyl and sulfur fragments during C–S bond dissociation in 1-butanethiol. The UV pump pulse (red) launches dynamics along the repulsive C–S coordinate, producing neutral fragments whose separation increases with delay. A time-delayed XUV pulse (purple) ionizes the S (2p) core level, and the AM cascade rapidly produces two-three valence holes centered near sulfur within a few femtoseconds, producing S^{2+} and S^{3+} ions.

As illustrated schematically in Fig. 7.6(a), the charge-transfer efficiency depends strongly on the internuclear distance. At short delays, when the fragments remain close, electron density can flow from the alkyl group to the sulfur site, resulting in a shared final-state charge distribution. At intermediate separations, this transfer becomes partial and distance-dependent. At long delays, once the fragments are effectively isolated, charge transfer is quenched, and sulfur ionizes locally while the alkyl fragment remains neutral.

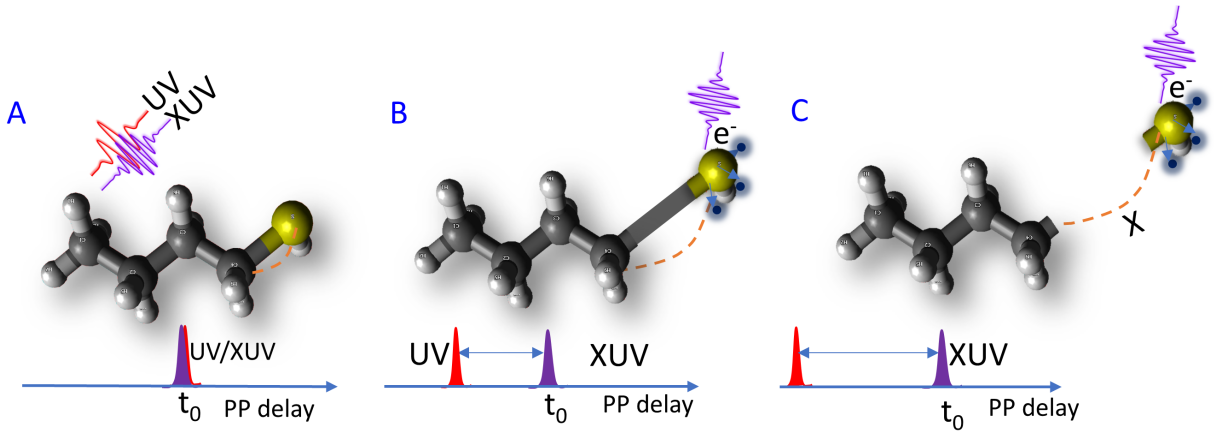

Figure 7.6: Schematic of the charge transfer between the alkyl and sulfur fragment as a function of pump-probe delay. The 267 nm UV pump pulse (red) dissociates the molecule along the C–S bond, and the time-delayed XUV pulse (purple) ionizes the sulfur 2p core level. Panels (A–C) represent short, intermediate, and long pump–probe delays corresponding to increasing C–S separations, where the charge localization evolves from shared to fully isolated.

This interpretation is supported by the measured S^{2+} and S^{3+} ion yields shown in Fig. 7.7. The ion yield of S^{2+} exhibits a temporal onset delayed by approximately 300 fs, whereas the S^{3+} signal appears after roughly 500 fs. These systematic shifts indicate that sulfur reaches higher charge states only after the fragments have separated sufficiently for the charge-transfer channel to close, consistent with dissociation along a repulsive C–S coordinate.

Hydrogen Migration and Roaming–H_2 Dynamics in 1-Butanethiol

There are several delay-dependent fragmentation channels that provide clear evidence of hydrogen migration in 1- butanethiol most notably the ion yields of H_n^+ ($n = 1$–3) and SH_n^+ ($n = 0$–3), which are discussed in detail in this section. As shown schematically in Fig. 7.8, the XUV pulse initiates S (2p) ionization of C_4H_9SH, followed by AM decay leading to a dication, launching nuclear motion that leads to the formation of a roaming H_2 neutral precursor on a timescale of tens to a few hundred femtoseconds [192–194]. This transient species branches mainly along three pathways: (a) hydrogen abstraction/association to yield H_3^+ [195],(b) electron transfer with the 1-butanethiol cation to form H_2^+, and (c) H_2

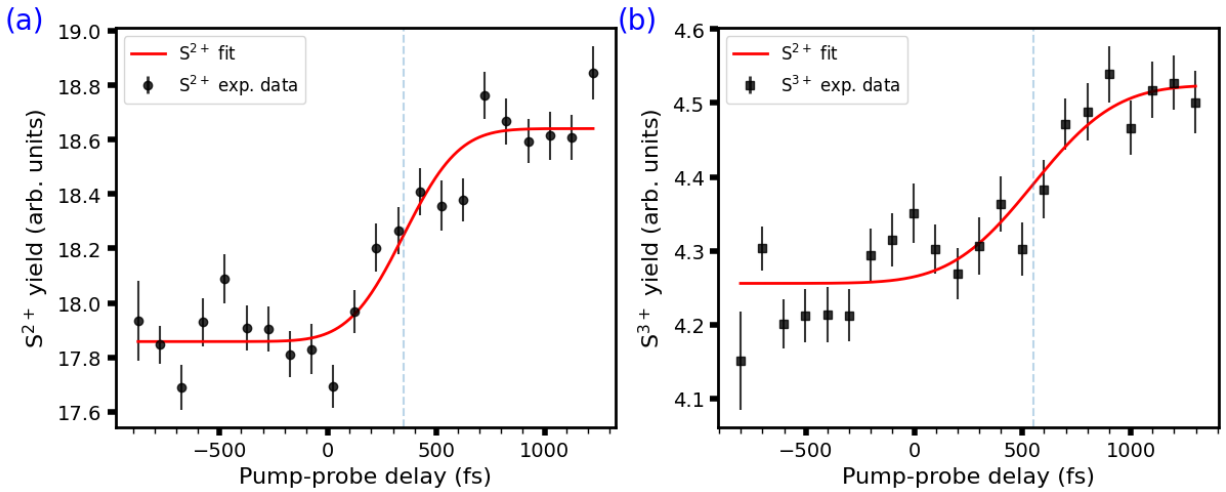

Figure 7.7: (a) S^{2+} ion yield and (b) S^{3+} ion yield as a function of pump–probe delay for 1-butanethiol. The S^{2+} yield is shifted by approximately 300 fs, while the S^{3+} yield is shifted by approximately 500 fs, reflecting the dissociative dynamics of 1-butanethiol along the repulsive C–S coordinate. These temporal offsets indicate that higher charge states emerge only after the charge-transfer channel closes, consistent with a transition from delocalized to localized ionization as the internuclear separation increases.

transfer to the sulfur site producing SH_3^+ [196]. The roaming-mediated H_3^+ channel gives rise to a pronounced transient peak near t_0, whereas depletion of H_2^+ and SH_3^+ is observed when the UV probe arrives at later delays, as discussed in the following paragraphs.

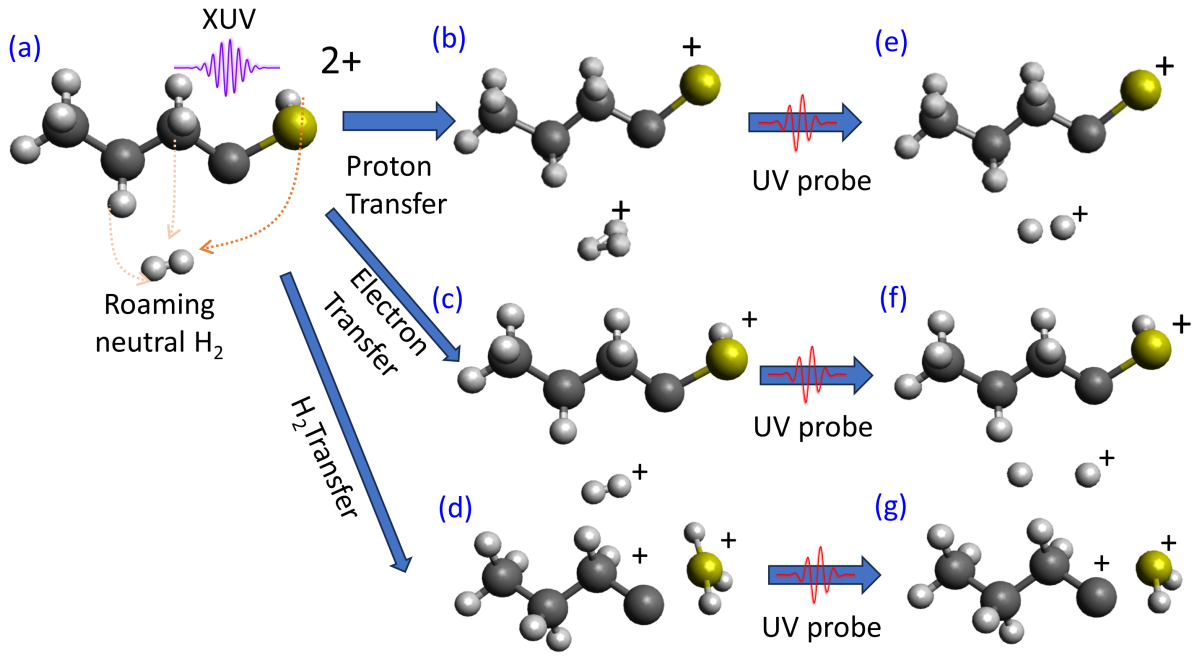

Figure 7.8: Schematic illustration of H_2 roaming and product formation channels in C_4H_9SH. (a) The XUV pulse initiates S (2p) ionization, generating the dicationic state $C_4H_9SH^{2+}$, followed by dissociation to produce a neutral roaming H_2 fragment. (b) Proton transfer forms $H_3^+ + C_4H_7S$, (c) electron transfer yields $H_2^+ + C_4H_8S^+$, and (d) H_2 migration leads to SH_3^+. (e–f) The UV probe pulse can further perturb or ionize the roaming H_2, thereby modifying the yields of H_3^+, H_2^+, and SH_3^+ through UV-induced fragmentation.

Formation of H_3^+ Following AM decay, the parent molecule forms a dication that undergoes ultrafast charge redistribution, weakening the α-C–H bonds and narrowing the H–C–H angle so that two α-hydrogens (i.e., the hydrogens attached to the α-carbon, the carbon atom directly adjacent to the sulfur-bearing carbon) combine into neutral H_2. This neutral H_2 roams within the dication's electrostatic field and subsequently abstracts the S–H proton, yielding free H_3^+ (m/z=3)—a mechanism analogous to that previously established for ethanethiol by Ekanayake *et al.* [197]. Such pathways provide fundamental insight into H_3^+ formation; one of the universe's most abundant ions and its huge role in the interstellar medium[198].

Ab initio quantum chemical calculations show that doubly ionized sulfur withdraws electron density less effectively than doubly ionized oxygen, resulting in a smaller positive charge increase on α-hydrogens, reduced α-C–H elongation, narrower H–C–H angles, and a longer α-H···H distance. Together, these effects suppress neutral H_2 formation and thus H_3^+ yield in thiols relative to alcohols [197].

Consistently, ethanethiol exhibits an eclipsed SH geometry relative to the forming H_2 at the dication minimum and a slower H_3^+ formation time (365 ± 10 fs) compared to ethanol (220 ± 6 fs). These trends are expected to persist in 1-butanethiol, given the same α-site origin of H_2 and the S–H deprotonation endpoint [197].

Ion Yield of H_3^+ Formation Following XUV-induced S 2p ionization, AM decay led to a dicationic state of 1-butanethiol. This highly excited state rapidly evolves to generate a transient, roaming neutral H_2 precursor. When the UV probe pulse arrives near the temporal overlap (t_0), it efficiently couples to these short-lived geometries, promoting proton-transfer and association reactions that yield H_3^+.

The delay-dependent H_3^+ Ion yield, shown in Fig. 7.9(a), exhibits an asymmetric rise and decay that is well described by a Gaussian–exponential convolution model. This fitting yields a lifetime for the H_3^+-forming configuration, determined to be 100 ± 100 fs.

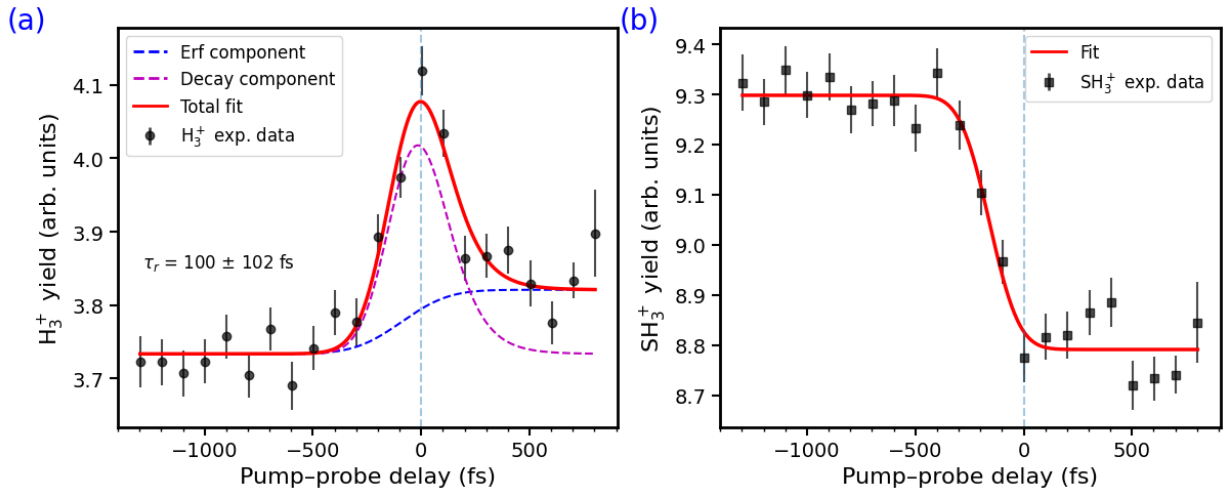

Figure 7.9: Ion yield as a function of pump–probe delay for (a) H_3^+ and (b) SH_3^+. In panel (a), the experimental data (black) are fitted using a Gaussian–exponential convolution, shown as the sum of an error-function component (blue dotted), a decay component (purple), and the total fit (red). Panel (b) shows the SH_3^+ yield (black with error bars) fitted with a negative error function (red), capturing the UV-induced depletion of the SH_3^+ precursor.

Ion yield of SH_3^+ Formation of SH_3^+ requires both a sulfur-centered positive charge and access to a mobile H_2. The UV pulse can reduce the SH_3^+ yield by either:

- consuming the roaming H_2 precursor (diverting it into H_2^+ or H_3^+ channels), or
- The UV pulse can further ionize the SH_3^+ (or its intermediate precursor) and/or induce dissociation. Either pathway decreases the yield of SH_3^+ with pump–probe delay.

Fig. 7.9(b) shows the delay-dependent SH_3^+ yield. The UV-induced decrease near t_0 suggests that the probe pulse either ionizes the neutral H_2 precursor or induces the dissociation. This behavior is modeled using a negative error function that captures the UV-driven depletion of the SH_3^+ signal.

Ion yield of H^+ Fragments The H^+ fragments arise from two main contributions:

- Direct S−H or C−H bond cleavage of the XUV-prepared cation/dication, and
- UV ionization of neutral H atoms generated by XUV-induced dissociation.

The delay-dependent H^+ yield, shown in Fig. 7.10(a), exhibits a clear enhancement near t_0, demonstrating that the UV pulse couples efficiently to short-lived reactive geometries created immediately after XUV ionization. As the system evolves beyond these geometries, the H^+ yield decays with a characteristic timescale of ~ 200 fs, consistent with the loss of the H_2 roaming precursor that feeds these channels.

Ion Yield of SH_2^+ Formation of SH_2^+ originates from intramolecular hydrogen transfer within the XUV-ionized 1-butanethiol cation. The initial S (2p) ionization, followed by AM decay, produces a highly excited, multiply charged state that drives proton migration toward the sulfur atom, transiently forming SH_2^+-like configurations.

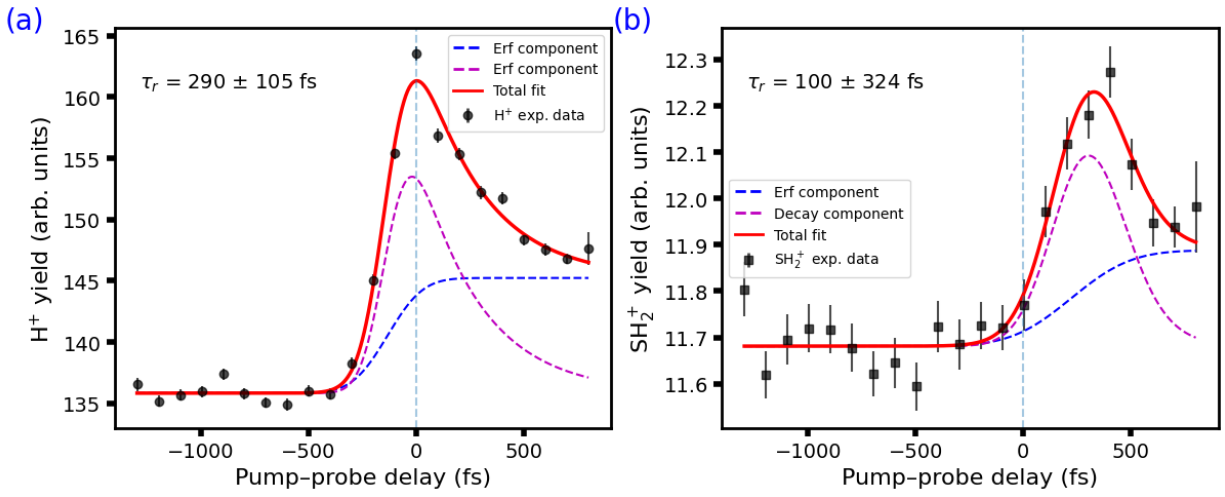

Figure 7.10: Ion yield as a function of pump–probe delay for (a) H^+ and (b) SH_2^+. (a) The experimental H^+ signal (black) is fitted using a Gaussian–exponential convolution model, shown as the sum of an error-function component (blue dotted), a decay component (purple), and the total fit (red). (b) The SH_2^+ yield (black with error bars) is fitted with the same Gaussian–exponential convolution function, capturing the ultrafast formation and decay of the transient SH_2^+ configuration.

The corresponding ion yield, shown in Fig. 7.10(b), reflects both this XUV-driven hydrogen migration and the interaction with the UV pulse. When the UV probe interacts with the short-lived SH_2^+, it either further ionizes them or disrupts the weakly bound configuration. At longer delays, the ion yield of SH_2^+ decreases on a sub-picosecond

timescale ($\sim$ 100 fs), consistent with the very short-lived nature of the migrating-hydrogen configuration.

Ion Yield of H_2^+ Fig. 7.11 shows the delay-dependent ion yield of H_2^+, which is primarily generated by the XUV pulse through ionization of neutral roaming H_2 precursors formed during early fragmentation of 1-butanethiol. When UV pulse arrives after the t_0, it can further excite the already formed H_2^+ to repulsive electronic states, leading to dissociation into $H^+ + H$. This UV-induced depletion of H_2^+ ions yields a negative error function in the measured H_2^+ yield at positive delays.

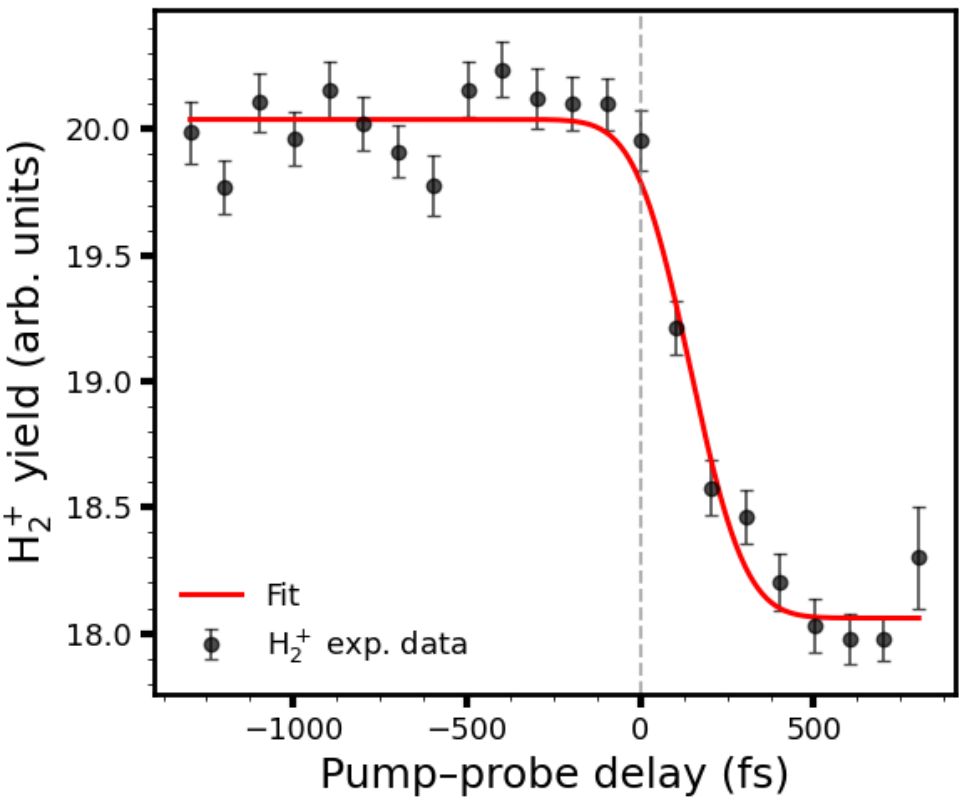

Figure 7.11: Ion yield as a function of pump–probe delay for H_2^+. The experimental H_2^+ signal (black) is fitted using an error function (red).

7.3.2 Electron VMI: Probing Site-Specific Dynamics with TR-XPS and TR-AMS

Time-resolved TOF-MS spectroscopy provides an overall picture of fragmentation dynamics but does not reveal electronic state evolution [199]. Such information is essential for understanding excited-state processes, where the Born–Oppenheimer approximation (BOA) breaks down, and strong electron–nuclear coupling can drive rapid population transfer between electronic states, particularly near conical intersections (CIs), where potential energy surfaces become degenerate [4, 200].

In the UV-pump / XUV-probe scheme used here, a UV pump pulse initiates excited-state dynamics in 1-butanethiol, followed by an FEL probe pulse that ionizes the S (2p) core level. The resulting photoelectrons and AM electrons are recorded as a function of pump–probe delay. The delay-dependent kinetic energy (KE) distributions provide a sensitive probe of ultrafast changes in charge localization and local bonding as the molecule evolves on the excited-state potential energy landscape.

In the following section, a detailed analysis of the delay-dependent VMI electron spectra focuses on two key aspects: (i) the appearance of short-lived electron features immediately following UV excitation, and (ii) the temporal evolution of the photoelectron and AM electron kinetic energies.

X-ray photoelectron and Auger-Meitner process

A schematic representation of X-ray photoelectron spectroscopy (XPS) and Auger-Meitner spectroscopy (AMS) processes is shown in Fig. 7.12. In the electronic ground state (bottom panel), absorption of an incident X-ray photon ionizes a core-level electron, creating a core hole. This system relaxes through the electronic transition in which an electron from a higher-lying orbital fills the vacancy. The excess energy released in this relaxation process is transferred to a second electron, known as a AM electron. The characteristic time scale of such a process is of the order of a few femtoseconds. Although radiative decay channels such as fluorescence can, in principle, compete with the AM mechanism, their contribution to the S (2p) studied here is negligible [201].

In the time-resolved method (top panel), the molecular system is first excited by a UV pump. This excitation changes the valence electronic configuration, and the subsequent X-ray ionization, XPS, and AMS decay pathways may differ significantly from those observed in the ground state.

In TR-XPS, a UV pulse excites the system, and a delayed XUV pulse ionizes the chosen core level. The resulting photoelectron kinetic energy directly reflects the instantaneous binding energy of the probed orbital. Because core levels, such as S (2p), are highly localized, their binding energies are highly sensitive to the local environment. This enables TR-XPS to monitor bond cleavage or rearrangement at the sulfur site in real time, a capability that cannot be achieved with ion detection alone.

The KE of the emitted photoelectron is given by

$$E_{\text{kin}} = h\nu_{\text{probe}} - \text{BE}, \tag{7.1}$$

where $h\nu_{\text{probe}}$ is the probe photon energy and BE is the binding energy (BE).

Following S (2p) photoionization in 1-butanethiol, the resulting core hole decays via the AM process: a valence electron from the molecular orbital fills the S (2p) vacancy, and the released energy ejects a second valence electron or AM electron.

The kinetic energy of the AM electron is primarily determined by the energy difference between the core-ionized state and the final dicationic state reached upon decay. This can be expressed approximately as

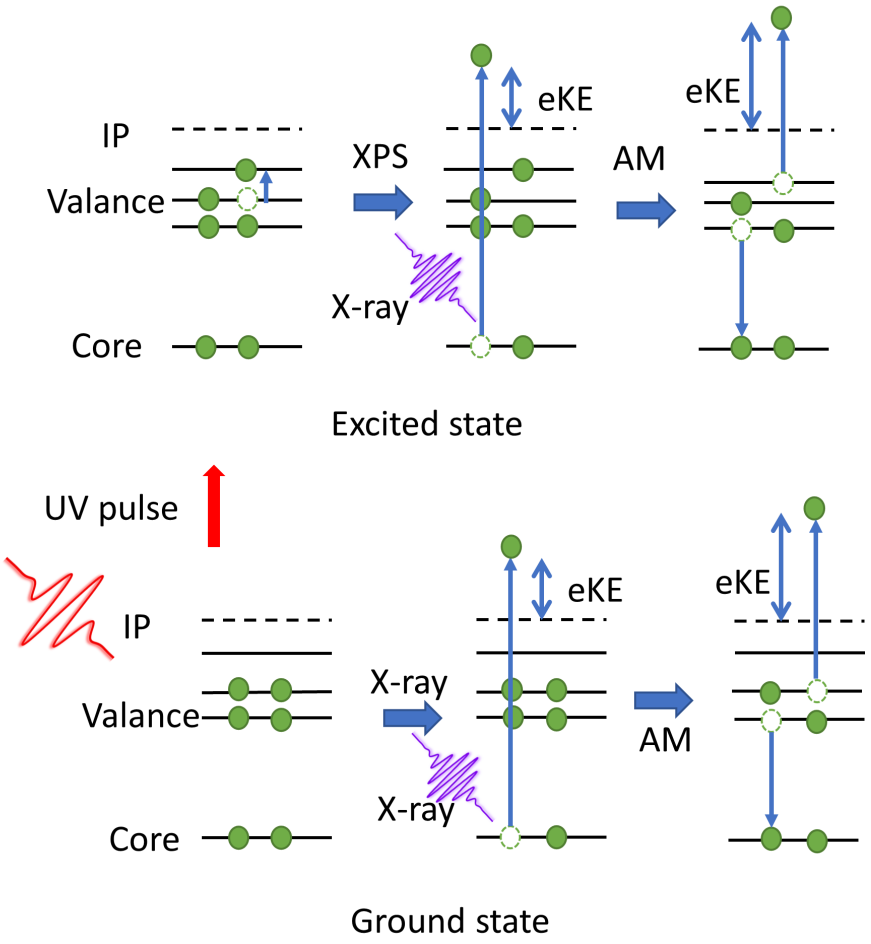

Figure 7.12: Schematic illustration of XPS and AMS processes in the ground state (top) and UV-excited state (bottom). An X-ray photon ejects a core electron, creating a core-ionized state that relaxes when a higher-lying electron fills the vacancy and an AM electron is emitted. Differences in the valence structure of ground- and UV-excited molecules are reflected in the resulting AM electron kinetic energies.

$$E_{\text{kin}}^{\text{Auger}} \approx E_{\text{core-ionized}} - E_{\text{dication}}. \tag{7.2}$$

The above equation indicates that the kinetic energy of AM electrons depends on the molecular electronic structure rather than on photon energy once the photon energy exceeds the resonance threshold. Unlike in TR-XPS, the AM electron kinetic energy is independent of the probe photon energy, making TR-AMS inherently non-resonant and robust against probe-pulse bandwidth and photon-energy jitter at FELs. The energy resolution is instead governed by intrinsic factors, such as the core-hole lifetime broadening, and by experimental factors, such as the spectrometer resolution.

The TR-AMS technique has been successfully applied to track ultrafast dynamics in photochemically relevant systems. McFarland et al. investigated thymine at the oxygen K-edge and showed that UV excitation produces a distinct feature, attributed to changes in the electronic structure during the non-adiabatic relaxation [202]. In sulfur-containing nucleobases, Lever et al. applied TR-AMS to 2-thiouracil, observing characteristic shifts in the S (2p) AM spectrum linked to C-S bond elongation. These results demonstrate the ability of TR-AMS to simultaneously capture nuclear motion and electronic-state dynamics with element specificity [179].

UV Early and Late Electron Spectra

Fig. 7.13 shows the photoelectron spectra of 1-butanethiol recorded with a FEL photon energy of 179 eV with a bandwidth of approximately 4 eV. The spectra include contributions from both direct photoionization and AM decay processes and are displayed for two characteristic delay conditions: UV-early (black) and UV-late (red).

In the UV-late configuration, the XUV pulse arrives first and ionizes the molecule before the UV excitation pulse. Thus, the observed electrons originate from the ground-state (unexcited) molecule, representing the static photoemission reference, as shown in the bottom panel of Fig. 7.12. In the UV-early condition, the UV pulse arrives before the XUV probe, probing transient ionization from the UV-excited electronic state. Comparison of these two spectra, therefore, highlights how the molecule's electronic and nuclear dynamics evolve upon photoexcitation.

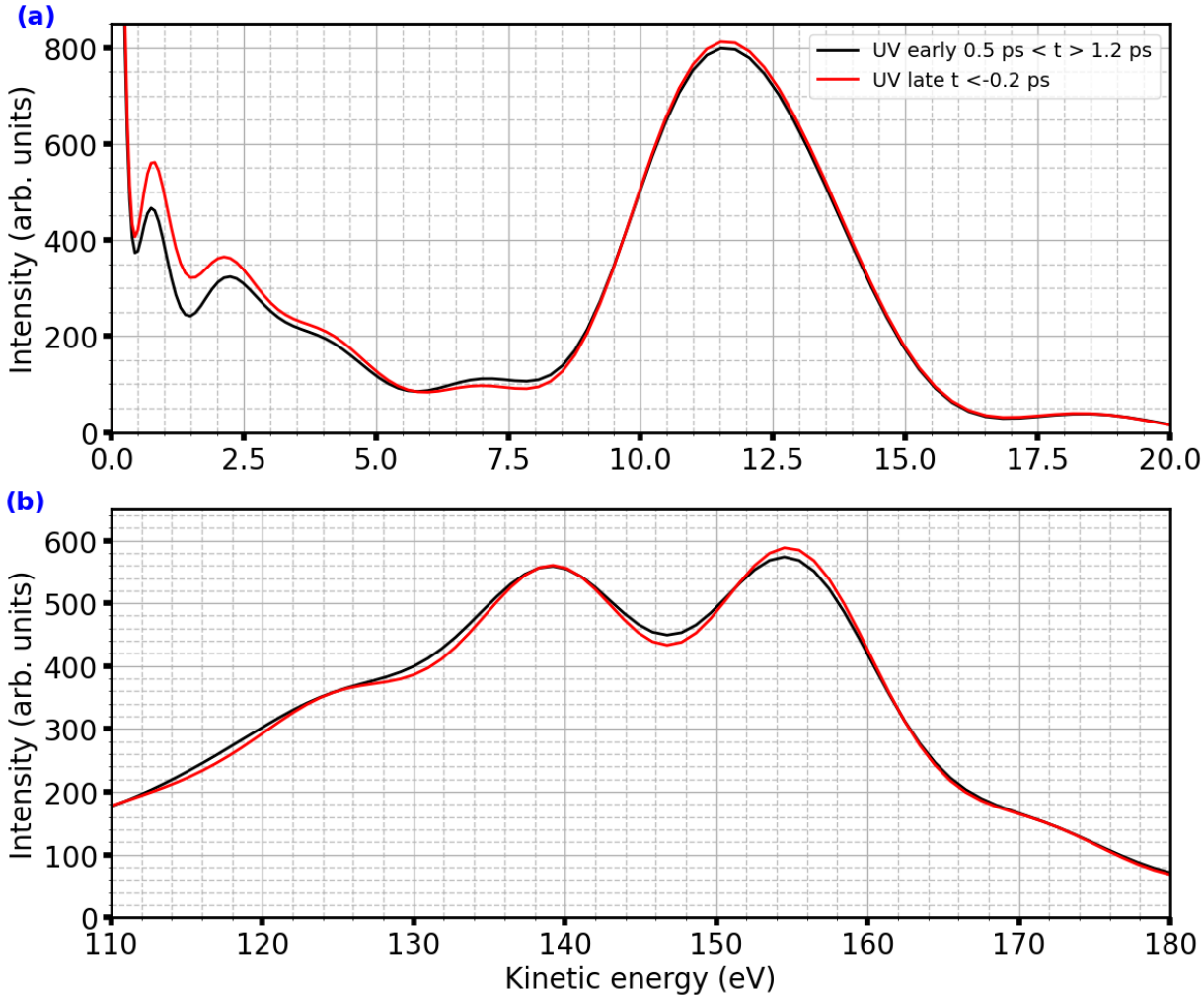

Figure 7.13: Early (red) and late (black) photoelectron spectra of 1-butanethiol recorded at 179 eV photon energy. The top panel shows the XPS region (0–20 eV kinetic energy) with S (2p) photoemission peaks, and the bottom panel shows the AMS region (125–145 eV) corresponding to sulfur LMM decay. The helium 1s line at 155 eV serves as a reference for electron spectra.

The upper panel of Fig. 7.13(a) shows the XPS region (0–20 eV kinetic energy), which is dominated by S (2p) photoemission. The S (2p) peaks appear near 11.5 eV kinetic energy, corresponding to binding energies of 168.81 eV ($2p_{3/2}$) and 170.08 eV ($2p_{1/2}$), consistent with previously reported gas-phase sulfur-edge measurements on thiol-containing molecules

[196, 203]. To the best of my knowledge, specific S (2p) binding energies for gas-phase 1-butanethiol have not been reported. A theoretical calculation was performed using the GAMESS software to estimate the S (2p) binding energy and its molecular fragments, showing good agreement with the experimental values (see Appendix, Section C.4 for details). Comparison of the late-delay (red) and early-delay (black) spectra shows a slight decrease in the S (2p) photoemission intensity accompanied by a corresponding increase in the sulfur-fragment signal under UV-early conditions. This behavior indicates a perturbation of the local electronic environment at the sulfur site following UV excitation.

The lower panel of Fig. 7.13(b) shows the AMS region (125–150 eV kinetic energy), where multiple features arise from sulfur LMM AM decay. In LMM decay, a vacancy created in the L shell is filled by an M-shell electron, and the released energy ejects a second M-shell electron. A sharp line at 155 eV corresponds to helium 1s ionization (binding energy = 24.6 eV) from the carrier gas and serves as an internal energy reference. At higher kinetic energies (165–171 eV), a broad and intense feature is observed, originating from valence ionization of 1-butanethiol induced directly by the FEL pulse. This band corresponds to photoemission from the outer-valence orbitals of the molecule.

Fig. 7.14 illustrates the sulfur energy-level diagram, showing the L_2 and $M_{1,23}$ subshells and the corresponding LMM AM decay pathways responsible for the observed features.

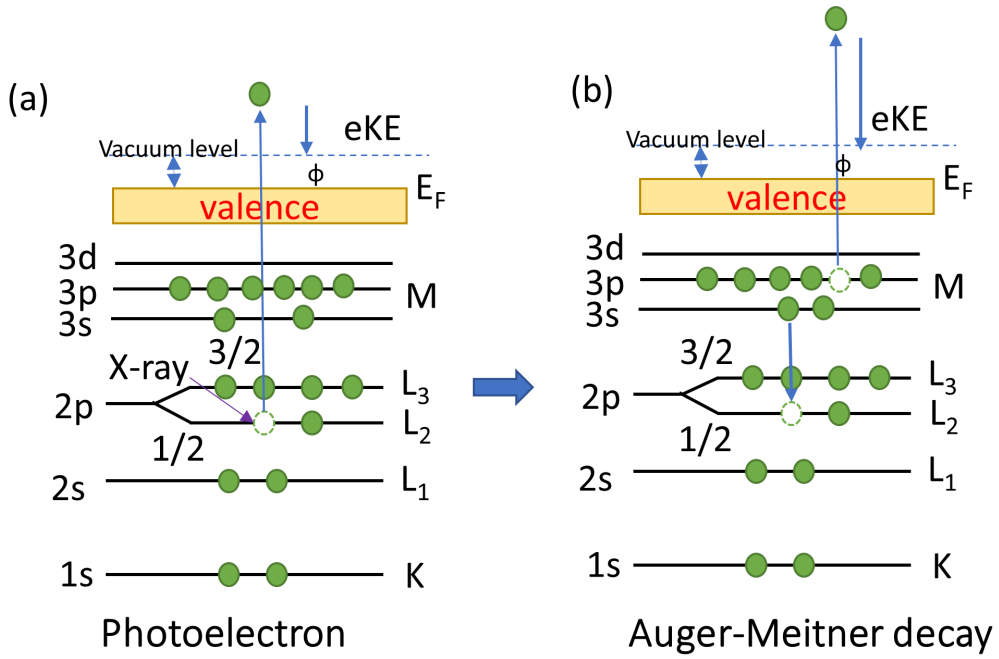

Figure 7.14: (a) Photoionization of the sulfur 2p (L_2) subshell by a 179 eV photon, creating a core vacancy and emitting a photoelectron. (b) Relaxation of the L_2 vacancy via LMM AM decay, illustrating the L_2 and $M_{1,23}$ subshells and the corresponding decay channels. The three dominant transitions, $L_2M_1M_1$, $L_2M_1M_{23}$, and $L_2M_{23}M_{23}$, correspond to kinetic energies near 125, 138, and 148 eV, respectively.

Time-Resolved X-ray Photoelectron Spectroscopy (TR-XPS)

The TR-XPS data are shown in Fig. 7.15 as a two-dimensional differential heat map, plotted versus pump–probe delay on the x-axis and photoelectron kinetic energy on the y-axis. The differential signal is defined as

$$\Delta S(E,t) = S(E,t) - S_{\text{late}}(E), \tag{7.3}$$

where $S(E,t)$ is the measured intensity at pump-probe delay (t) and $S_{\text{late}}(E)$ is the UV-late reference spectrum.

At t_0, the TR-XPS map shows a clear depletion of the S (2p) line at 11.5 eV (negative signal), accompanied by a positive feature in the 5–10 eV region associated with dissociation photoproducts.

To quantify the delay dependence, the kinetic-energy window indicated by the dashed line in Fig. 7.15 was integrated at each delay, yielding the delay-dependent S (2p) photoelectron intensity. The resulting one-dimensional traces shown in Fig. 7.16 were then analyzed using time-resolved fits to extract the decay of the parent S (2p) signal and the rise of photoproduct features.

$$I(t) = \int_{E_{\text{min}}}^{E_{\text{max}}} S(E,t)\,\mathrm{d}E, \tag{7.4}$$

where $S(E,t)$ denotes the electron spectrum as a function of the kinetic energy E and the pump–probe delay (t). The bounds E_{min} and E_{max} define the lower and upper limits of the kinetic-energy window associated with the spectral feature of interest (e.g., a selected photoelectron or AM line).

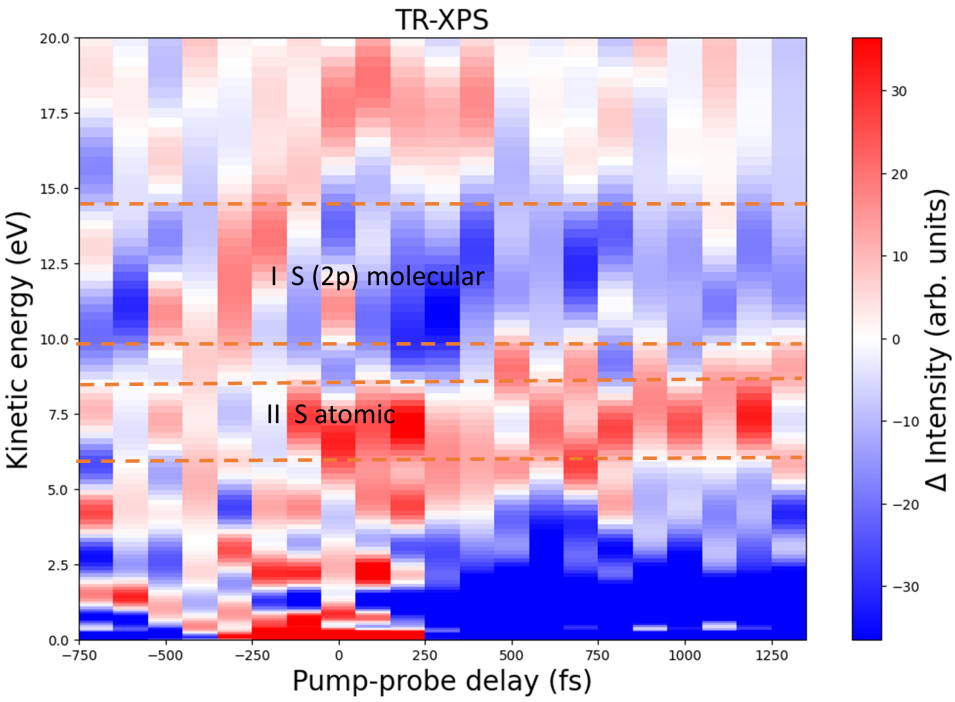

Figure 7.15: Differential TR-XPS spectra of 1-butanethiol are shown as a two-dimensional differential heat map. Positive (red) signals indicate increased photoelectron intensity after UV excitation, while negative (blue) signals represent depletion relative to the ground state.

Fig. 7.16(a,b) shows the integrated S (2p) signal and the sulfur photoproduct signal as a function of pump–probe delay, together with the corresponding fits. The depletion region,

shown as the black curve in Fig. 7.16(a), was modeled as an excited-state contribution combined with a negative error function to account for the loss of the ground-state 1-butanethiol signal, broadened by the finite temporal resolution. The extracted excited-state lifetime is approximately 29 fs with a huge error due to very noisy pump–probe electron data.

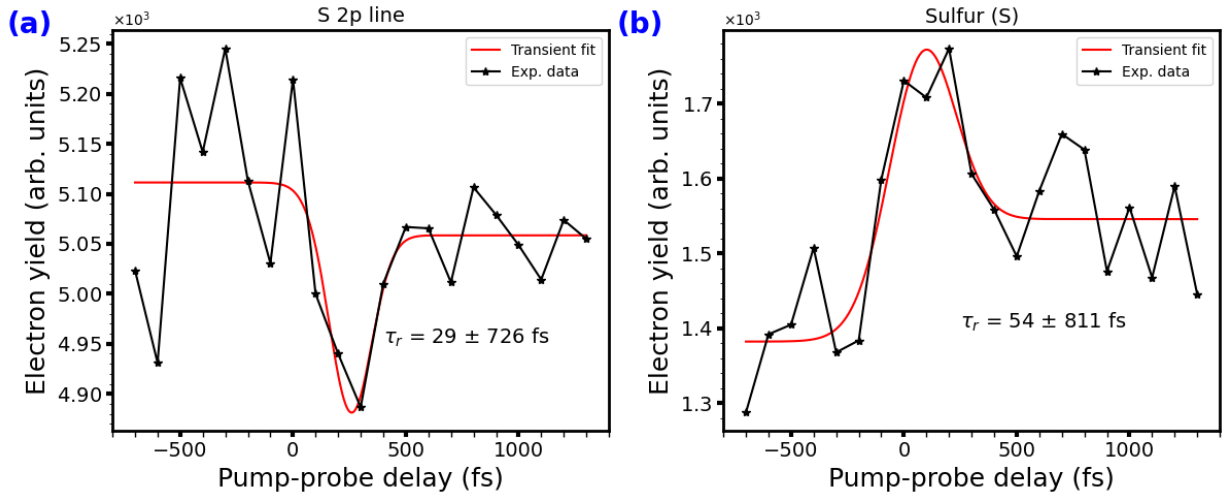

Figure 7.16: Intensity integrated over the photoelectron kinetic energy 10-12 eV (Left) and 5-8 eV (Right) in black color and associated fit in red solid line.

For the sulfur photoproduct region, shown in Fig. 7.16(a), the lowest-energy photoelectron signal—dominated by contributions from sulfur-containing fragments—exhibits a characteristic rise time of roughly 54 fs. Lifetimes for individual fragment channels cannot be uniquely assigned within the available temporal resolution.

Time-Resolved Auger–Meitner Spectroscopy

Fig. 7.17 shows the differential 2D TR-AMS map, which contains three distinct kinetic-energy regions. The helium line at 155 eV provides a strong, time-dependent reference signal for calibrating the VMI electron spectra and determining t_0. A second feature, arising from FEL-induced valence ionization near 170 eV, follows the dynamics of the bound excited state of 1-butanethiol. The third feature, the AM region (125–145 eV), contains the molecular decay dynamics of interest. Near t_0, an enhancement appears in the 140–148 eV range together with depletion between 137–140 eV, indicating a transient blue shift of the AM features in the excited state relative to the ground state.

To analyze the time-resolved behavior in the AM region, the electron yield was integrated over the kinetic-energy windows indicated by the dashed lines in Fig. 7.17, producing the 1D electron-yield traces shown below. Fig. 7.18(a) shows the integrated helium signal as a function of pump–probe delay, which is used to determine t_0 and to extract the cross-correlation time. Fig. 7.18(b) displays the high–kinetic–energy electrons generated by FEL-driven valence ionization of 1-butanethiol. A short-delay enhancement is observed in the 160–170 eV window, associated with population of a bound electronically excited state.

The integrated helium and valence-ionization signals were fitted with a Gaussian-convolved exponential decay to extract temporal parameters. The fit yields a cross-correlation (instrument response) time of approximately 200 fs, consistent with the UV-FEL timing jitter, and an excited-state decay constant of about 50 fs, characterizing relaxation of the bound excited state prior to dissociation.

Fig. 7.19(a) and (b) show the energy-integrated AM-region signals. Near t_0, a clear enhancement appears in the 142–150 eV range, accompanied by a partial depletion at

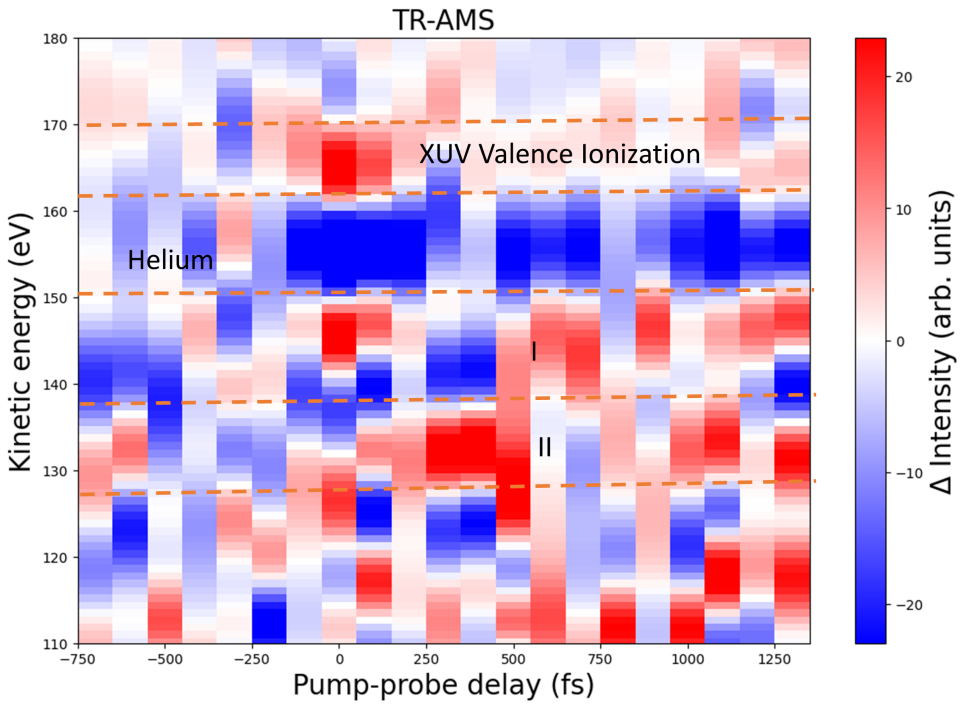

Figure 7.17: Differential 2D TR-AMS spectra of 1-butanethiol. Several regions are highlighted with orange dotted lines. Regions (I) and (II) originate from AM decay, while two additional regions arise from helium ionization and valence ionization of the molecule induced by the XUV pulse.

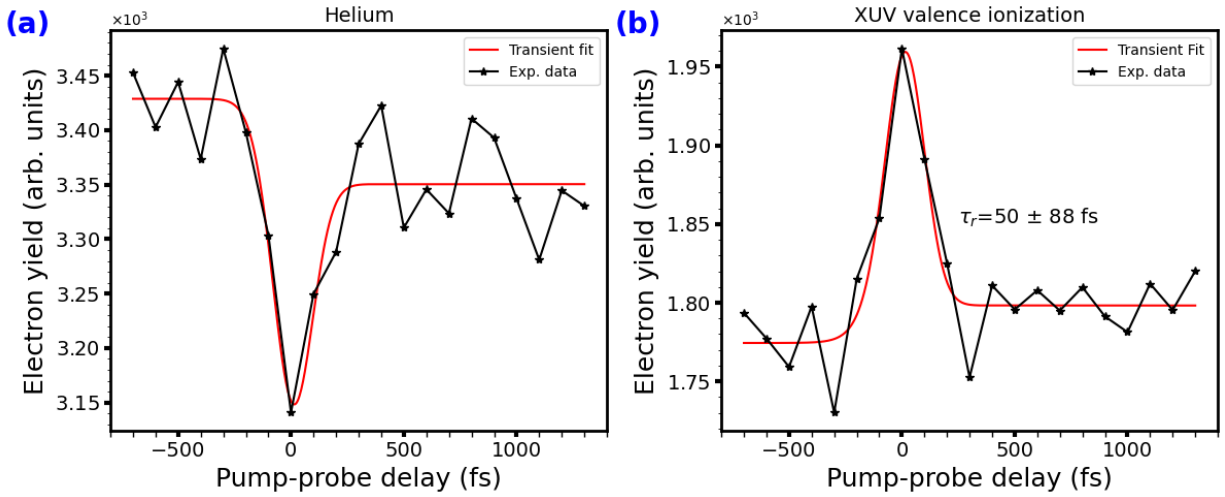

Figure 7.18: Integrated intensity as a function of pump–probe delay for (a) the helium region (electron kinetic energy (eKE) = 155–160 eV) and (b) valence ionization in the XUV region (eKE = 165–170 eV).

slightly lower energies. These overlapping features indicate a transient blue shift in the AM spectrum upon excitation.

In contrast, the lower kinetic-energy window (130–136 eV) exhibits a delayed rise that begins around 300 fs. This delayed growth may reflect population transfer through a conical intersection, leading to the appearance of AM features at lower kinetic energy, or it may originate from fragments formed after molecular dissociation. Overall, the observed AM kinetic-energy shifts to higher energies near t_0 confirm the presence of excited-state dynamics prior to fragmentation.

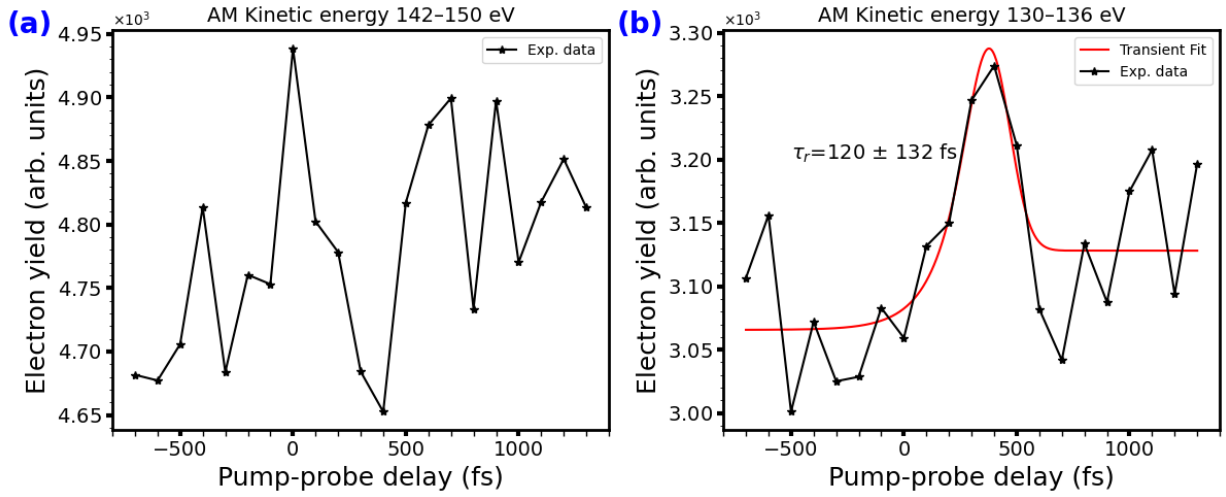

Figure 7.19: Intensity integrated over the AM kinetic energy 142-150 eV (Left) and 130-136 eV (Right) in black color and associated fit in red solid line.

7.4 Summary

The UV-induced dissociation dynamics of 1-butanethiol were investigated using femtosecond time-resolved inner-shell photoionization at the sulfur (S 2p) edge. XUV pulses at 179 eV from FLASH1, combined with VMI of ions and electrons, enabled detailed probing of the photoinduced processes triggered by UV pulses. Under these experimental conditions, the UV excitation primarily led to direct ionization of the molecule, which subsequently initiated dissociative ionization pathways.

Time-resolved TOF-MS ion yield analysis as a function of pump–probe delay reveals charge transfer from the sulfur site to the alkyl chain following UV-induced fragmentation, occurring on a timescale of approximately 300 and 500 fs, for S^{2+} and S^{3+}, respectively. The mass spectra also indicate the formation of several notable fragments, including H_3^+, SH_2^+, and SH_3^+. These fragmentation channels are consistent with hydrogen migration processes along the carbon chain, involving intramolecular hydrogen transfer between distinct molecular regions – observed previously in similar molecules ionized by IR pulses.

Time-resolved photoelectron- and AM- spectroscopy provides complementary, site-specific insights into the evolution of the electronic structure. Both techniques indicate that the excited-state lifetime is on the order of hundred femtoseconds, with dissociation and C–S bond cleavage occurring within approximately 200 fs. Transient shifts in the photoelectron and AM spectra reflect changes in the local chemical environment, such as C-S bond breaking, charge redistribution, and the formation of other dissociation products. Although electron spectra regions show overlapping contributions that limit the complete separation of individual decay pathways, the overall findings consistently support a model of ultrafast excited-state relaxation followed by molecular fragmentation.

Ion VMI images were acquired at only two delay conditions, corresponding to early and late arrival of the UV pulse relative to the FEL pulse. Ion images were not gated for higher sulfur charge states, and no additional measurements were performed to complement these data. Ion VMI images of sulfur and the sulfur-loss channel are nevertheless presented and support the current analysis (see Appendix, Section C.2). Furthermore, using a CCD camera instead of a Timepix detector prevented simultaneous acquisition of ion and electron images, limiting the dataset to discrete delay conditions rather than to a fully resolved pump–probe measurement of ion momenta.

Several limitations affected the experimental data. The measurements exhibited low

statistical quality, and the electron VMI spectrometer's specific setup provided limited energy resolution. The FLASH1 beamline was operated in SASE mode, which resulted in rather large bandwidth and reduced spectral stability.

Chapter 8

Summary and Outlook

This thesis comprises two sets of experiments that combine instrumentation development with time-resolved investigations of atomic and molecular dynamics at the FLASH facility. One of the major goals of this thesis was to improve the temporal resolution in pump-probe measurements, particularly at the FL26 REMI endstation, and to use this improved resolution to study systems ranging from atoms to small molecules. The second set of experiments extends to time-resolved ion and electron spectroscopy for larger molecular systems using a double-sided VMI at the CAMP endstation. Together, these studies establish new capabilities, highlight current limitations of ultrafast experiments at FLASH, and outline a trajectory for future development.

A major achievement of this thesis is the first experimental implementation of the LAM at the FL26 beamline (FLASH2). A detailed technical description and performance evaluation of the LAM are presented in Chapter 4. In a benchmark two-color XUV-NIR pump-probe experiment, the LAM setup enabled long-term drift correction and shot-to-shot timing characterization, resulting in an effective temporal resolution of 46 ± 5 fs (FWHM). This shows a substantial improvement over the previously typical resolution of 100-300 fs. Beyond the gain in temporal resolution, active feedback stabilization provided by the LAM system reduces uncertainties in the temporal overlap between the FEL and NIR pulses and minimizes the need for extensive post-processing. This significantly improves the data yield during the beamtime, which is essential for long acquisition campaigns at the REMI endstation.

Exploiting the enhanced temporal resolution at the REMI endstation, xenon (Xe) photionization and subsequent AM decay were investigated using XUV pulses at 90 eV and 160 eV, corresponding to excitation near the giant $4d$ resonance and Cooper minimum, respectively. At 90 eV, ionization is dominated by $4d$ single ionization followed by AM decay; the intensity dependence of the Xe^{4+} ion yield shows evidence of a two-photon process. At 160 eV, both the $4p$ and $4d$ energy levels overlap and exhibit single- and double-ionization. The intensity dependence of the Xe^{5+} and Xe^{6+} ion yields indicates two-photon-induced ionization channels under strong XUV excitation.

The NIR pulse probes transient intermediate excited states prior to their decay, promoting them to energetically higher states and providing insight into the relaxation steps that lead to different final charge states. The measured Xe^{5+} lifetime of 49 ± 3 fs is approximately a factor of two shorter than previously reported values [123], demonstrating the impact of improved temporal resolution. The detailed results of these xenon measurements are presented in Chapter 5.

These results demonstrate that intense XUV radiation enables site-specific creation of core-hole states and, when combined with synchronized NIR probing, provides time-domain access to ultrafast decay dynamics in atomic systems. Future time-resolved electron-ion coincidence measurements will be important for disentangling overlapping AM decay channels

state-selectively and for achieving a more detailed understanding of the underlying relaxation mechanisms. Further improvements in temporal resolution will be essential for resolving the faster AM transitions.

Building on the xenon experiments, the methodology is extended to small molecular systems through time-resolved CEI of CO_2 and CS_2, as detailed in Chapter 6. In both molecules, two-body and three-body fragmentation channels are resolved, and analysis of the delay-dependent ion yields reveals intermediate-state lifetimes of approximately 60 fs for $CO_2{}^{+*}$ and $CS_2{}^{+*}$. These measurements enable a clear distinction between concerted and sequential dissociation mechanisms. In CS_2, the observation of multiple two-body coincidence channels indicates the presence of distinct dissociation pathways associated with different intermediate electronic states. Collectively, these results demonstrate how ultrafast electronic excitation governs subsequent nuclear motion and highlight the importance of precise temporal control for disentangling competing reaction pathways.

Time-resolved CEI experiments demand long-term stability of both the FEL and the pump-probe laser parameters that is greater than that required for comparable atomic measurements. Under these conditions, the effective long-term temporal resolution was approximately 80 fs. Although this resolution is sufficient to identify the dominant fragmentation channels and intermediate lifetimes, it limits sensitivity to faster dynamical processes and highlights the need for further improvements in synchronization stability.

More recently, electron–ion coincidence experiments were performed on sulfur-containing molecules such as OCS using the same experimental setup at the REMI endstation. Site-selective ionization of the sulfur 2p shell provides a well-defined initial excitation for tracking ultrafast charge redistribution and dissociation [204]. Energy-dependent scans across off-resonant, resonant, and above-resonance excitation [205], combined with time-resolved coincidence detection, would directly correlate electronic emission with fragmentation pathways [206]. Such experiments would address limitations encountered in the non-coincident 1-butanethiol study and provide a benchmark for site-specific ultrafast dynamics in molecular systems.

So far, REMI experiments focus on measurements of atomic and small-molecular systems; the second experimental set explores complementary spectroscopic techniques in a larger polyatomic molecule. UV-induced fragmentation dynamics of 1-butanethiol are investigated at the CAMP endstation using a double-sided VMI see Chapter 7. In this approach, ion and electron images are recorded to obtain both fragment distributions and photoelectron spectra. The measurements reveal rapid fragmentation of the hydrogen-transfer channels and charge transfer involving the sulfur site. Time-resolved photoelectron and AM spectra indicate excited-state lifetimes on the order of several hundred femtoseconds, with C–S bond cleavage occurring on a 200 fs timescale.

These results provide a consistent picture of excited-state relaxation followed by dissociation. However, the experiments are not performed in full electron–ion coincidence mode, and overlapping spectral contributions limit the ability to unambiguously assign specific electronic transitions to individual fragmentation channels. This limitation highlights a key challenge in extending ultrafast spectroscopy to complex molecules: resolving correlated electronic and nuclear dynamics requires detection schemes capable of event-by-event coincidence analysis.

The experimental findings of this thesis, therefore, motivate several directions for future development, beginning with continued improvements in pump–probe laser infrastructure [207]. Achieving temporal resolution in the sub-30 fs regime over long acquisition periods is essential for resolving faster atomic and molecular transient states while operating at high repetition rates. The ongoing transition toward high-repetition-rate Yb-based 1030 nm laser systems within the FLASH2020+ upgrade partially addresses this requirement

by providing higher average power and improved stability [120]. Although Yb:YAG pulses are intrinsically relatively long, spectral broadening in a multi-pass cell (MPC) followed by post-compression enables the generation of sub-20 fs pulses with high efficiency [208–210]. Delivering uncompressed pulses to the experimental stations for local compression and diagnostics provides a flexible architecture that supports diverse experimental needs. High-repetition-rate operation will be particularly beneficial for statistically demanding coincidence experiments or experiments with a very low signal-to-noise ratio.

In parallel with laser upgrades, the anticipated implementation of seeded FEL operation will significantly enhance the coherence and stability of the XUV source [211, 212]. In contrast to the SASE process, the seeded operation produces pulses with narrow spectral bandwidth, improved temporal coherence, and enhanced shot-to-shot reproducibility [213]. These properties are directly relevant to time-resolved photoelectron spectroscopy, where improved energy resolution and timing precision are essential for resolving subtle electronic features. For molecular systems such as 1-butanethiol, seeded tunable FEL pulses would enable more selective excitation and more precise tracking of excited-state evolution.

Detector technology represents another critical area for advancement. The CCD-based VMI detectors used in the present experiments integrate signals over exposure times and lack event-resolved timing information, limiting their compatibility with high-repetition-rate sources and coincidence measurements. Time-stamping detectors such as Pixel imaging mass spectrometry (PImMS) [214] and Timepix [215, 216] provide event-by-event spatial and temporal resolution and can operate at repetition rates of up to 1 MHz. Although the Timepix camera can be readily integrated into the CAMP setup, it was not utilized during these experiments. Its operation at the CAMP endstation would enable electron–ion covariance analysis, thereby allowing direct correlation between emitted electrons and the corresponding ionic fragments [216].

The complementary strengths of REMI and double-sided VMI suggest that future experimental architectures will increasingly adopt hybrid strategies optimized for specific scientific objectives. REMI offers complete kinematic information for coincidence measurements but operates at relatively low count rates and requires ultra-high vacuum conditions. VMI provides higher throughput and simpler operation, and when combined with advanced time-stamping detectors, may approach coincidence capability while maintaining high efficiency [217]. Bridging these approaches will expand the range of accessible experiments.

These instrumentation developments occur in the broader context of rapid progress in FEL technology. The emergence of phase-stable few-femtosecond to attosecond X-ray sources [213] enables direct observation of electronic motion on its natural timescale. Increasing repetition rates to the tens or hundreds of kHz supports statistically demanding coincidence and imaging experiments, although practical constraints on ion time-of-flight spectrometers impose trade-offs between repetition rate and time-of-flight window. An operation in the 100–200 kHz repetition-rate range may be an effective compromise, as many coincidence measurements require a time-of-flight window of approximately 10–5 μs.

In summary, this thesis work represents a significant step forward in high–temporal–resolution ultrafast spectroscopy experiments at FLASH, achieved through enhanced synchronization and the development of molecular imaging methods. The results demonstrate both the current capabilities and the remaining challenges in achieving simultaneous high temporal resolution, high statistics, and coincidence or covariance detection. Continued progress in laser stability, seeded FEL operation, detector technology, and experimental architecture will enable increasingly detailed investigations of coupled electronic and nuclear dynamics. As these developments converge, ultrafast spectroscopy at XUV and X-ray FELs will extend to more complex systems and approach the fundamental limits of electronic motion.

Appendix A

Laser Pulse Characterization

To calculate the peak power of the NIR laser or FEL, the laser pulse was approximated as a Gaussian in both time and space, described by the following equation.

$$I(x, y, t) = I_0 \exp\left(-\frac{(x^2 + y^2)}{2\sigma_{spatial}^2}\right) \exp\left(-\frac{t^2}{2\sigma_{temporal}^2}\right) \tag{A.1}$$

Where $I(x, y, t)$ denotes the intensity at time t, at position x, y in a plane perpendicular to the direction of propagation, $\sigma_{temporal}$ is the temporal width, $\sigma_{spatial}$ is the radial width of the pulse, and I_0 is the peak intensity of the pulse.

Pulse energy can be found by integrating this intensity over the entire (x, y) space and over time (t).

$$E_{pulse} = \int_{-\infty}^{\infty}\int_{-\infty}^{\infty}\int_{-\infty}^{\infty} I(x, y, t)\, dx\, dy\, dt \tag{A.2}$$

Substituting the expression for $I(x, y, t)$ into the integral:

$$E_{pulse} = \int_{-\infty}^{\infty}\int_{-\infty}^{\infty}\int_{-\infty}^{\infty} I_0 \exp\left(-\frac{x^2 + y^2}{2\sigma_{spatial}^2}\right) \exp\left(-\frac{t^2}{2\sigma_{temporal}^2}\right) dx\, dy\, dt \tag{A.3}$$

The solution leads to the integral, which yields the total energy E:

$$E_{pulse} = I_0 \cdot (2\pi)^{3/2} \cdot \sigma_{spatial}^2 \cdot \sigma_{temporal} \tag{A.4}$$

The relationship between the full width at half maximum (FWHM) and the standard deviation σ was used for both the spatial and temporal dimensions of the Gaussian pulse. This relationship is given by

$$\text{FWHM} = 2\sqrt{2\ln(2)}\,\sigma \tag{A.5}$$

Substituting these values into the above equation and rearranging.

$$I_0 = 8 \cdot \left(\frac{ln(2)}{\pi}\right)^{3/2} \cdot \frac{E_{pulse}}{FWHM_{temporal} \cdot FWHM_{spatial}^2} \tag{A.6}$$

The NIR laser pulse energy was measured using a calibrated power meter positioned upstream of the in-coupling windows of the REMI. A photodiode was calibrated to enable shot-to-shot measurements of the laser pulse energy. The focal spot size of the NIR pulse was estimated using a virtual focus camera that accurately reproduces the beam profile at the interaction point. This was achieved by recording beam-profile images at the focus at a repetition rate of 10 Hz and by converting the pixel coordinates to real space after per-pixel

camera calibration. The resulting beam-profile data were fitted with a Gaussian function, which gives the pulse focal dimensions.

During the 2021 beamtime, the temporal profile of the laser pulse was characterized upstream of the REMI in-coupling windows using single-shot Frequency-Resolved Optical Gating (FROG) with a commercial Femto Easy device. The measured pulse duration was approximately sub-20 fs. Pulse properties are shown in Fig. A.1.

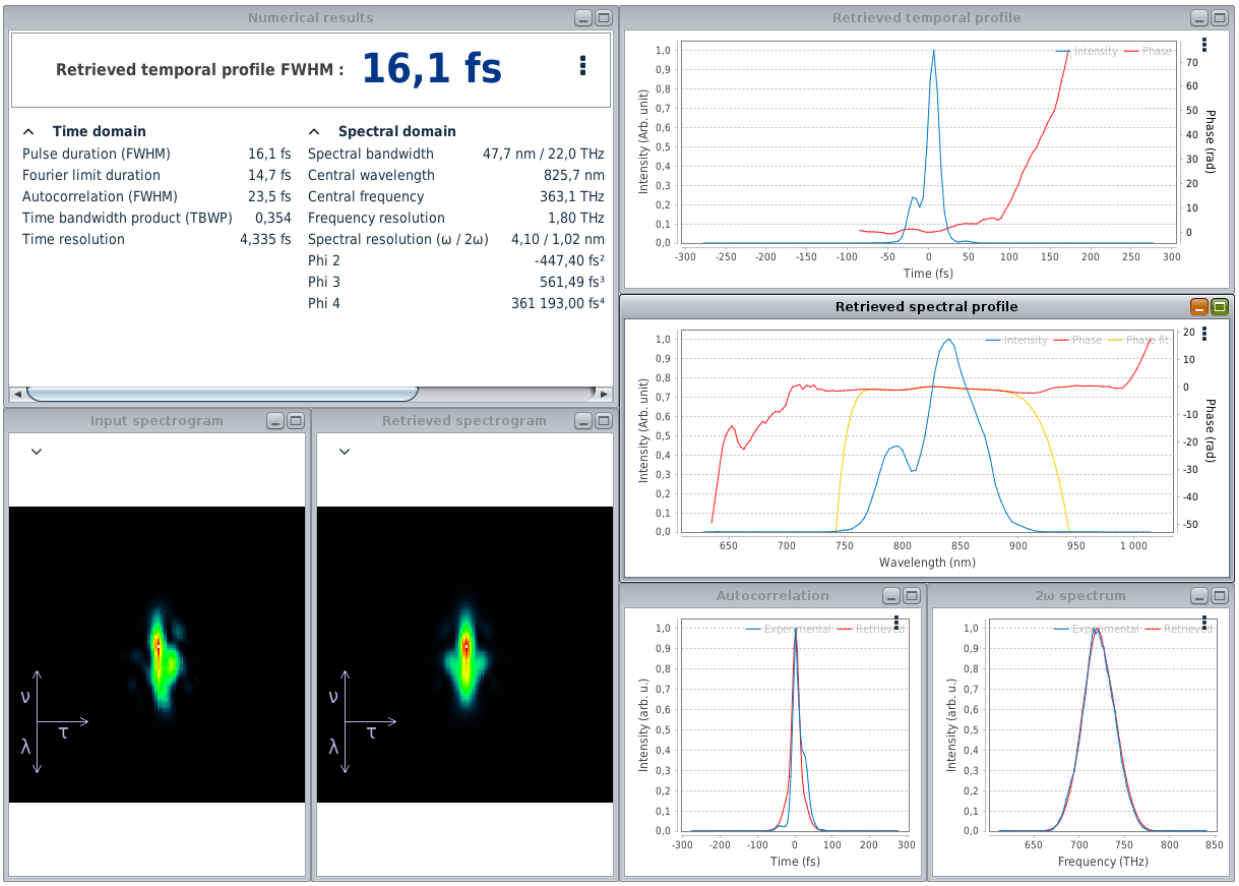

Figure A.1: Single-shot FROG measurement of the NIR laser pulse during the 2021 beamtime.

However, during the 2023 beamtime (11015327), a commercial single-shot autocorrelator from Avesta was employed to characterize the laser pulse, yielding a pulse duration on the order of sub-20 fs, comparable to that measured in 2021. This measurement is shown in Fig. A.2. The NIR laser experimental parameters for the 2021 and 2023 beam times, along with the corresponding calculations, are summarized in Table A.1.

Beamtime	FWHM Temporal (fs)	FWHM σ_x, σ_y (µm)	E_{pulse} (µJ)	I_0 (W/cm^2)
2021	< 20	20 and 50	20	8.29×10^{13}
2023	< 20	20 and 60	68	1.88×10^{14}

Table A.1: Pump-probe laser beam parameters.

The energy of each FEL pulse and the beam's position are determined for every shot using a GMD [66]. Additionally, the focal spot size—with a diameter $d \approx 20$–$30\,\mu\text{m}$—and the pulse duration, $\tau_{\text{FEL}} \approx 20\,\text{fs}$, are obtained from THz streaking measurements [116]. The FEL experimental parameters and the corresponding peak intensity, calculated using Eq. (A.6), are listed in Table A.2.

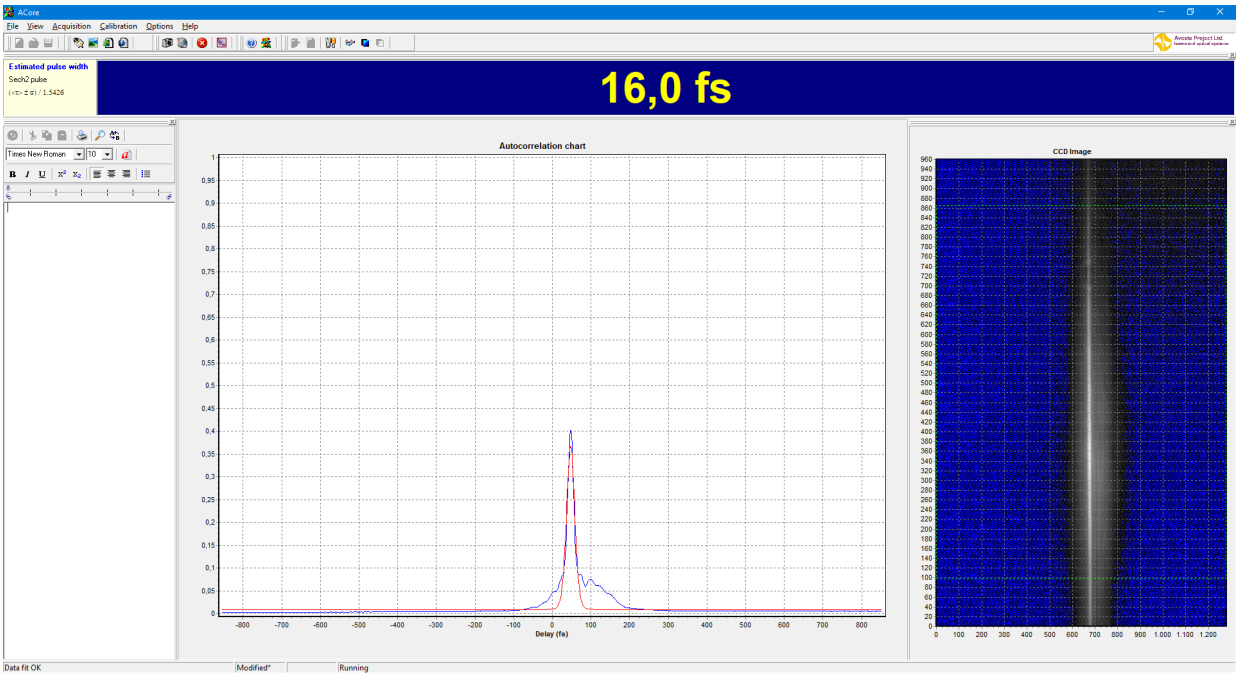

Figure A.2: Single-shot autocorrelation measurement of the NIR laser pulse during the 2023 beamtime.

Beam Time ID	FWHM Temporal (fs)	FWHM Spatial (µm)	E_{pulse} (µJ)	I_0 (W/cm^2)
2021 (F-11010412)	< 20	20–30	1.5	$0.6–1.5 \times 10^{13}$
2023 (F-11015327)	< 20	20–30	3	$1.3–3 \times 10^{13}$

Table A.2: Summary of FEL beam parameters.

A.1 Estimation of NIR Intensity

At the REMI endstation, measuring the exact pulse energy and pulse duration at the target is challenging. Although several pulse characterization diagnostics are available, they are all located upstream of the coupling windows of the REMI, introducing additional uncertainties due to transmission losses. Therefore, a direct determination of the peak intensity of the NIR laser at the interaction region is not feasible.

The laser intensity can be determined using the charge-state ratio of argon ions (Ar^{2+}/Ar^{+}), obtained from the measured mass spectrum shown in Fig. A.3 and another from ADK-theory to fit the momentum distribution of Ar^{+} [218].

The yields of Ar^{+} and Ar^{2+} were extracted by integrating their respective peaks in the TOF-MS at different NIR intensity.

Table A.3 summarizes the laser intensity calculated from the measured pulse energy, pulse duration, and focal spot size, estimated using a virtual focus upstream of the in-coupling window of the REMI spectrometer. The argon mass spectrum was used to determine the relative ion yields. The Keldysh parameter (γ) values listed in Table A.3 indicate that ionization occurs predominantly in the tunneling regime ($\gamma < 1$), supporting the use of tunneling-based models, such as the ADK model, for intensity estimation.

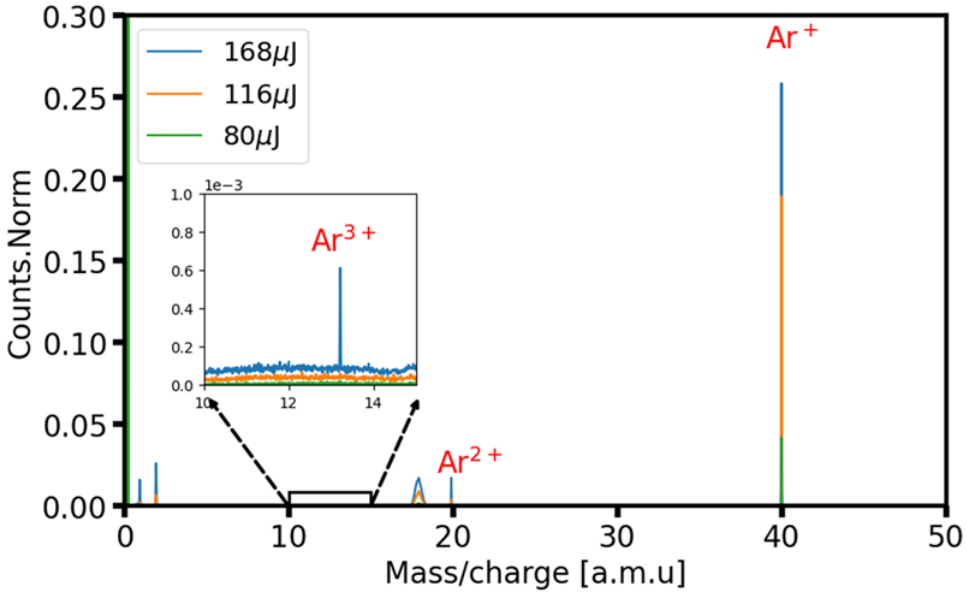

Figure A.3: Argon time-of-flight mass spectra recorded at three pulse energies. Charge states up to Ar^{3+} are observed only at the highest pulse energy of 168 μJ using a NIR laser.

Table A.3: Laser peak intensity from measured pulse parameter before in-coupling to REMI spectrometer

Pulse Energy (μJ)	**Peak Intensity** (W/cm^2)	**Ratio** (Ar^{2+}/Ar^{+})	**Keldysh Parameter**
168	4.64×10^{14}	0.1023	0.53
116	3.21×10^{14}	0.0601	0.64
80	2.21×10^{14}	0.0370	0.77
68	1.88×10^{14}	—	0.83

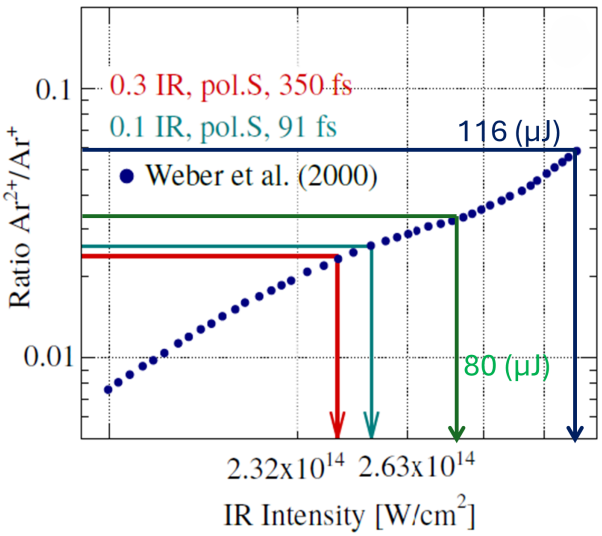

Figure A.4: The theoretical values are in good agreement with the experimental results. The blue and green lines correspond to laser intensities of 3.21×10^{14} W/cm^2 and 2.21×10^{14} W/cm^2, respectively, while the red and cyan lines are taken from the experiment by Georg Schmid at REMI endstation at FLASH2 [219]. The blue dotted line represents the theoretical ratio from Weber et al. [218].

Appendix B

Pump-probe Laser Drift Measurement

B.1 Two-Color Balanced Cross-Correlator

The FLASH2 pump–probe laser oscillator is synchronized to the MLO reference clock using feedback from a two-color BCC, following the scheme described in Ref. [100]. The schematic of the BCC setup is shown in Fig. B.1.

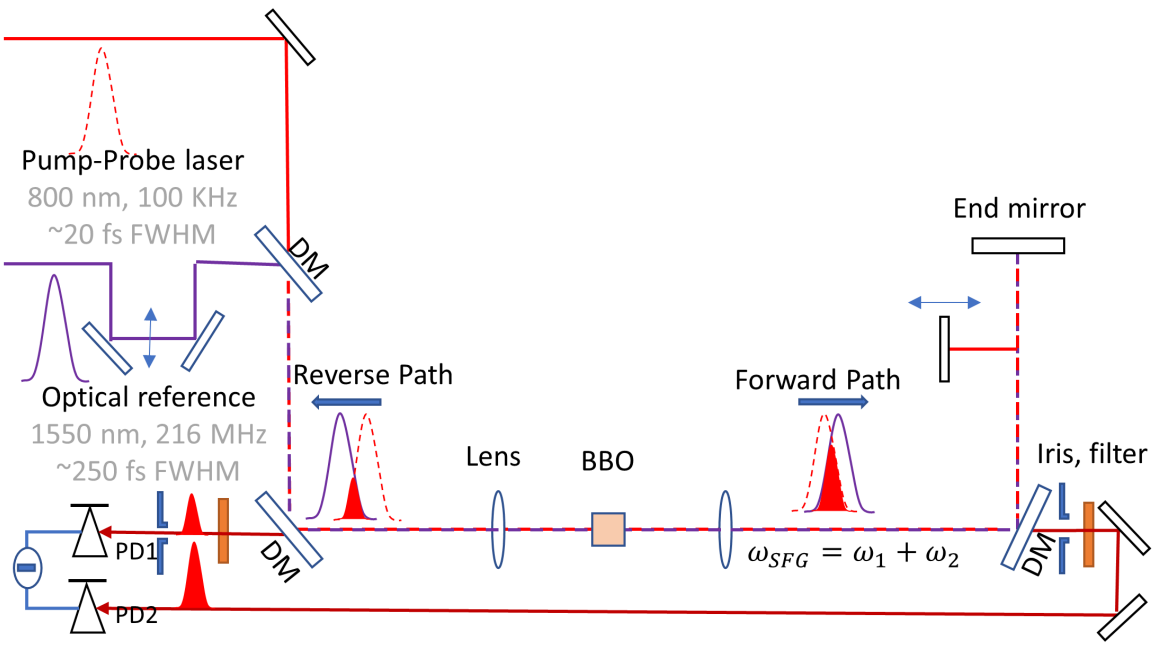

Figure B.1: Schematic of the two-colour BCC. Pulses from the MLO reference and pump–probe laser oscillator are combined with a dichroic mirror (DM) and focused into a BBO crystal to generate a SFG signal. After passing through a retro-reflector, the pulses generate a second SFG signal in the crystal. The two signals are detected and used to determine the relative timing between the pulses.

Pulse trains from the MLO reference signal at 1550 nm and the pump–probe laser oscillator at 800 nm are spatially and temporally overlapped using a dichroic mirror. The collinearly propagating pulses are focused into a type-I phase-matched BBO crystal, where a signal is generated via SFG. The intensity of the generated SFG light depends sensitively on the temporal overlap of the two pulses as well as on their individual intensities. The sum-frequency light is separated from the fundamental beams using a second dichroic mirror and detected with balanced photodetectors (PD1 and PD2).

To remove the ambiguity arising from the symmetric delay dependence of the SFG signal, a second cross-correlation measurement is performed. The pulses are then refocused into the crystal to generate a second SFG signal, producing a differential timing signal. The resulting S-curve calibration of the BCC signal is shown in Fig. B.2.

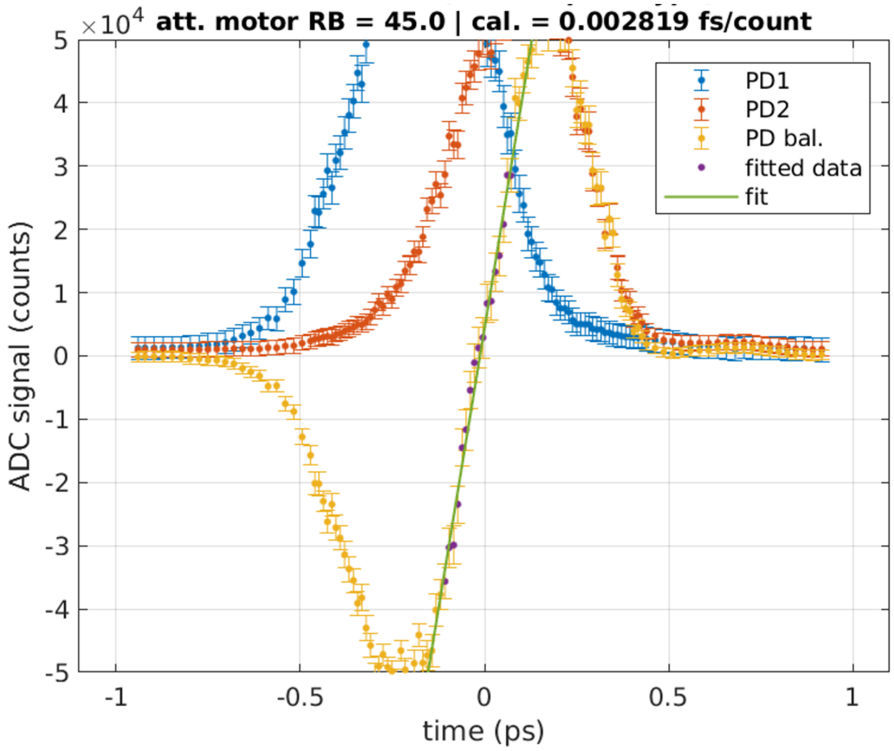

Figure B.2: Calibration of the BCC S-curve. The differential signal obtained from the balanced photodetectors (PD1–PD2), originating from the two cross-correlation stages, is plotted as a function of the relative delay between the optical reference and pump–probe laser pulses. Around the zero-crossing, the response is approximately linear and defines the operating point for timing stabilization.

Near the zero-crossing of this curve, the response is approximately linear, and the detector output becomes directly proportional to the timing offset. This linear region defines the operating point for the feedback loop. By locking the system to this point, the BCC provides a stable error signal for active synchronization, enabling few-femtosecond timing precision between the pump–probe laser and the optical reference.

B.2 Interferometer Measurement Data at the REMI Endstation

A commercial interferometer (SIOS Messtechnik GmbH) was used to measure the optical path length between the MOD2.6 and REMI. The path-length change is converted to femtoseconds to show the corresponding optical path delay. The measured distance signal is shown in Fig. B.4.

Environmental parameters such as air pressure, temperature, and humidity are monitored simultaneously during the measurement. These parameters are used to estimate their influence on the optical path length over approximately 4 m between the MOD2.6 output and the REMI in-coupling window. Variations in these environmental conditions affect the

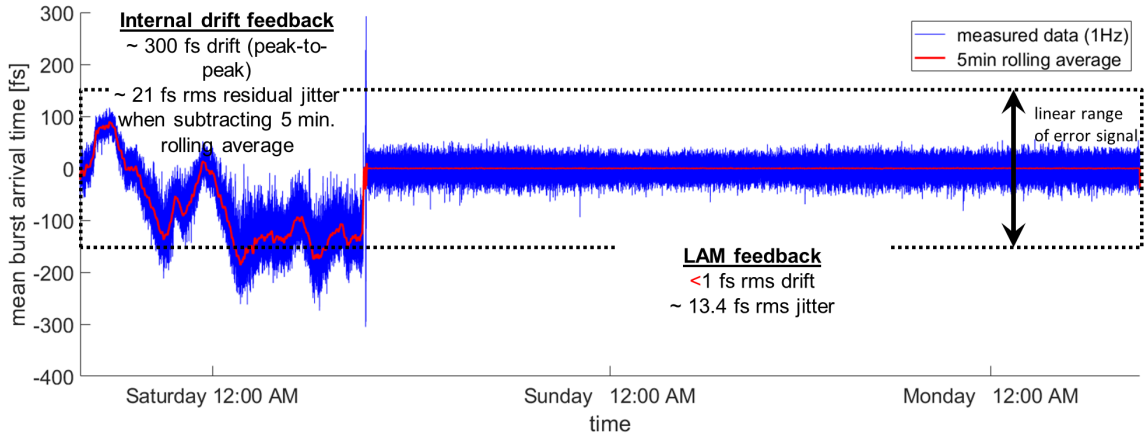

Figure B.3: Long-term timing drift measured over three days of continuous operation during the 2021 beamtime campaign. After activating the LAM feedback system, the drift is reduced from approximately 300 fs to about 1 fs.

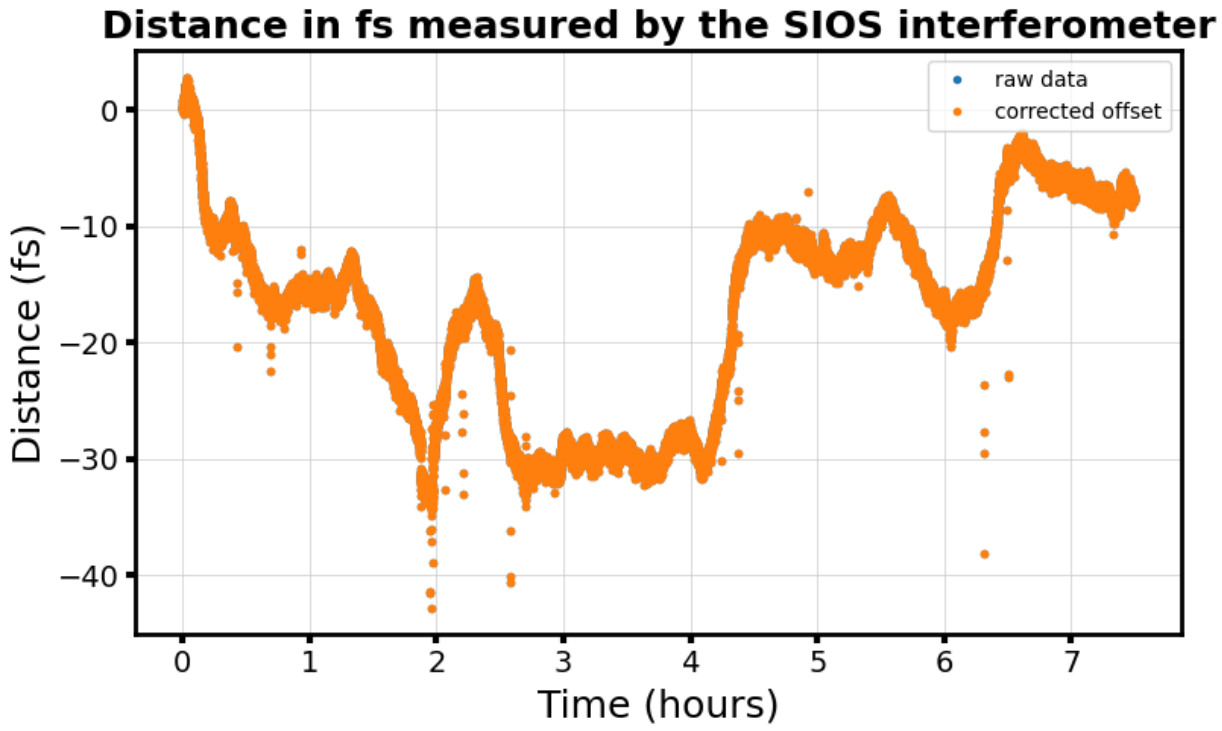

Figure B.4: Distance measured by the SIOS interferometer. The distance is converted into femtoseconds to represent the corresponding optical path delay.

refractive index of air and therefore introduce additional drift in the measured optical path length.

The recorded environmental parameters are shown in Fig. B.5. Based on these measurements, the expected drift contributions to the optical path delay can be calculated.

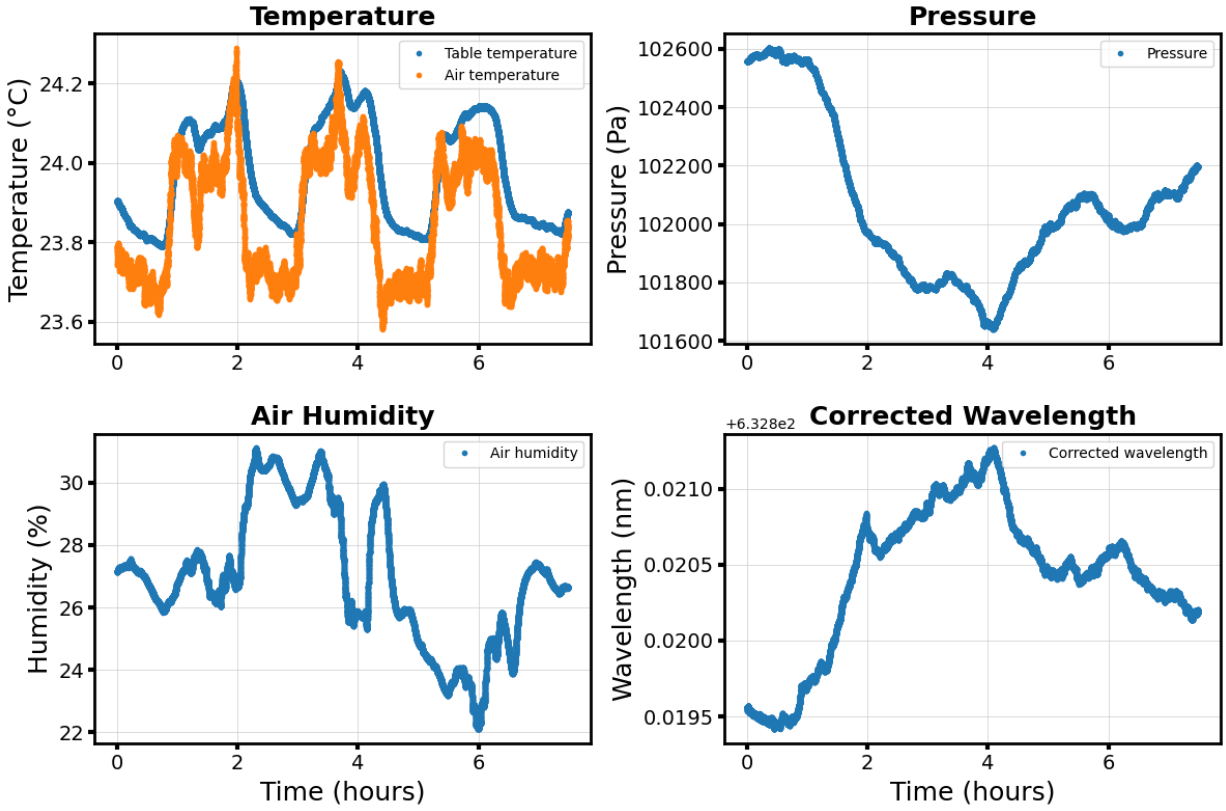

Figure B.5: Environmental parameters recorded during the interferometer measurement, including table and air temperature, air pressure, humidity, and corrected laser wavelength.

Fig. B.6 shows the measured interferometer signal together with the estimated contributions from environmental effects. The calculated drift contributions primarily arise from variations in air pressure and from changes in the effective laser wavelength induced by environmental conditions. After subtracting the estimated environmental influence, the residual represents the uncompensated optical path-length fluctuations of the system.

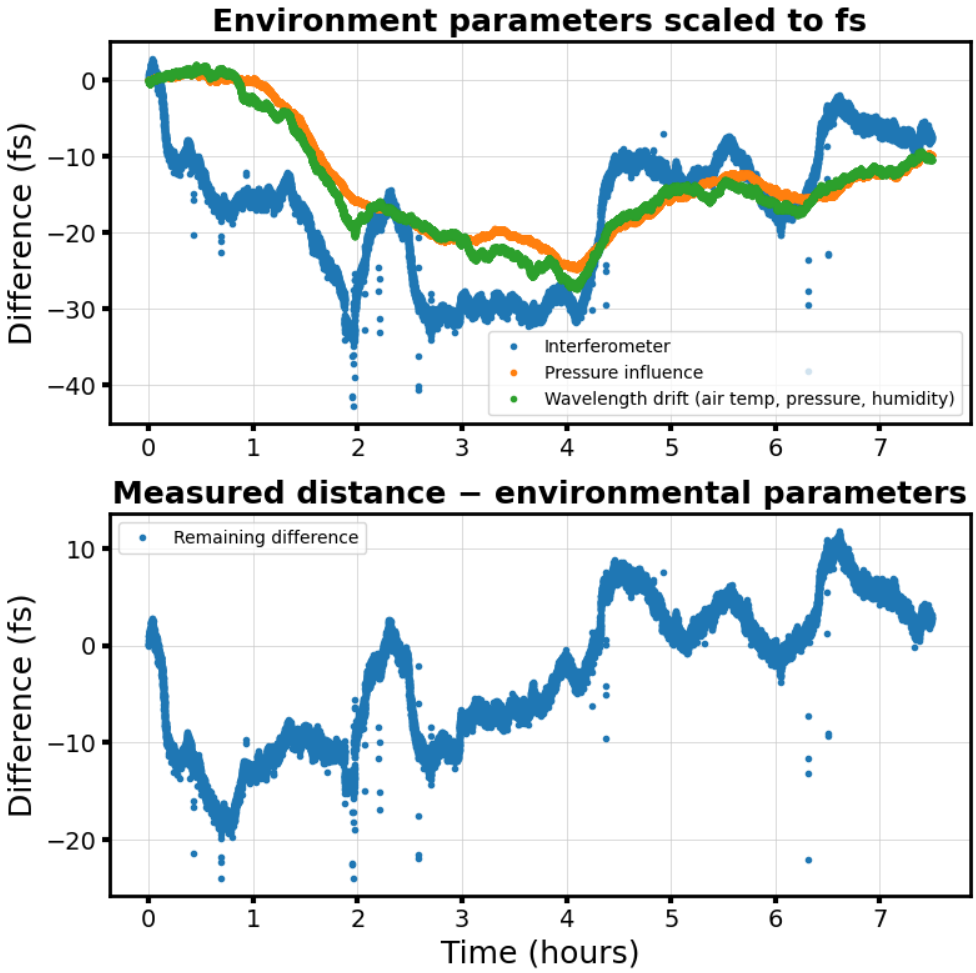

Figure B.6: Measured interferometer signal together with the estimated environmental contributions to the optical path delay and the remaining residual after correction.

Appendix C

Supplementary Material: UV-Induced Dynamics of 1-Butanethiol

C.1 Mass Spectrum

Fig. C.1 shows the measured mass spectra of 1-butanethiol at different UV intensities. At higher intensities, enhanced fragmentation leads to a broader distribution of ionic species. This behavior reflects the increasing contribution of multiphoton ionization, leading to higher total ionization of the molecule and fragmentation into smaller fragments.

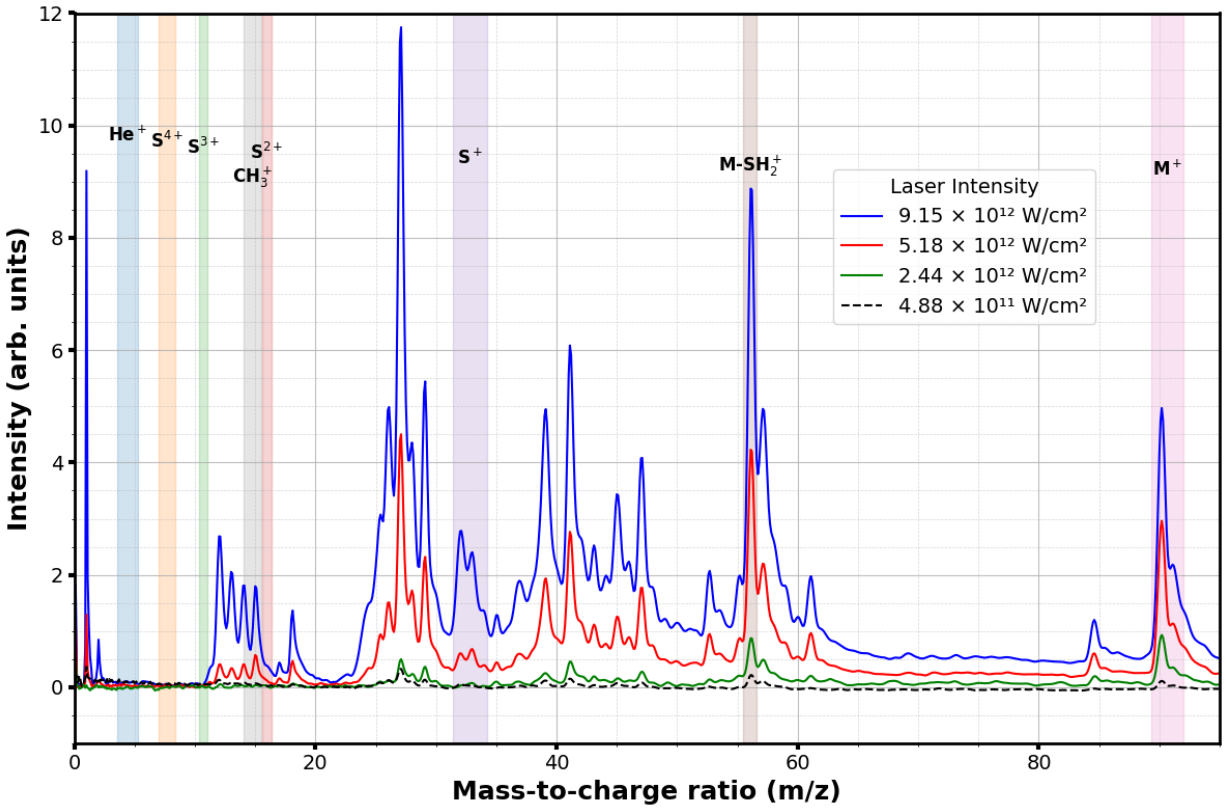

Figure C.1: Mass spectra of 1-butanethiol recorded at different UV laser intensities, showing the evolution of fragmentation patterns with increasing intensity.

Fig.C.2 shows the high-resolution mass spectrum of 1-butanethiol acquired under UV and FEL combined (integrated over all pump-probe delays). The spectrum was recorded in so-called spatial imaging mode rather than in the spectrometer's VMI mode, thereby improving mass resolution. This higher resolution helps us to better identify the closed ionic

fragments in the mass spectrum. Key fragment peaks are identified and assigned based on their mass-to-charge ratios.

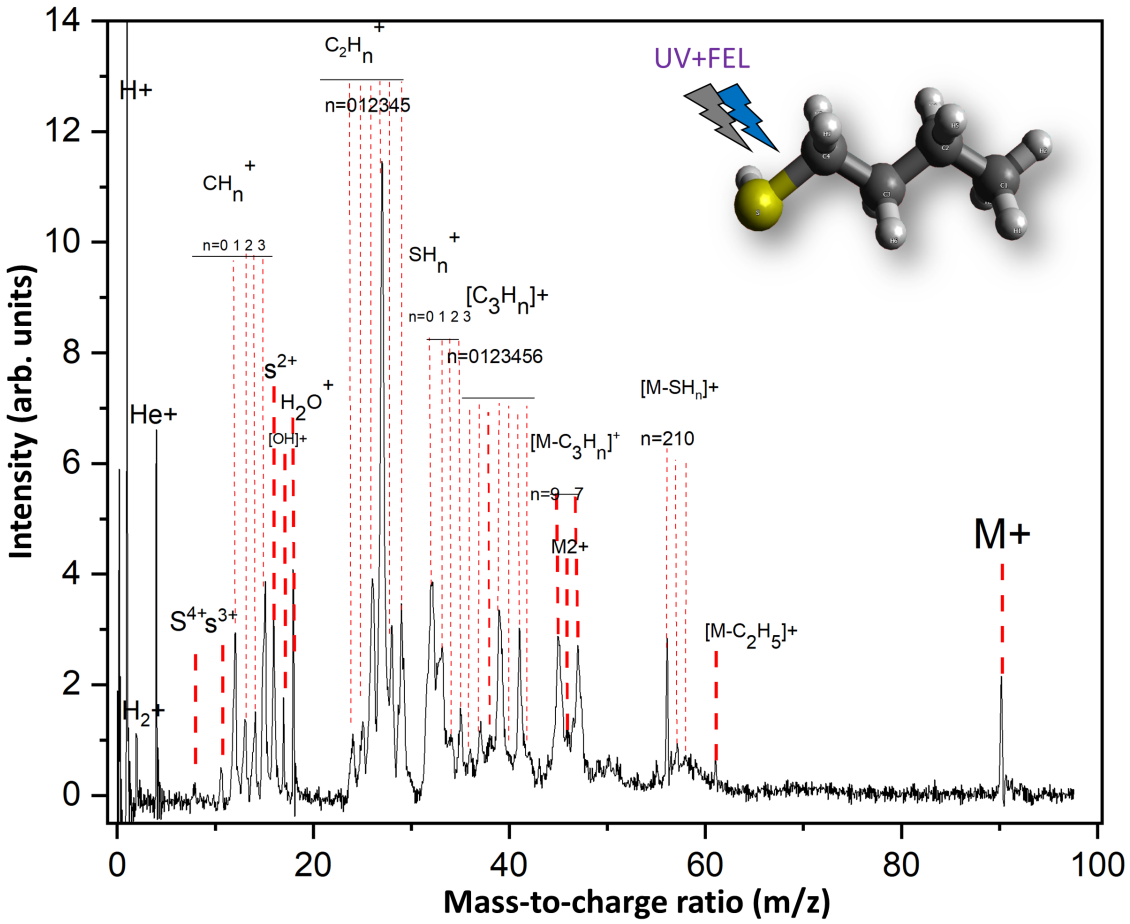

Figure C.2: High-resolution mass spectrum of 1-butanethiol with UV and XUV pulse recorded in spatial imaging mode.

C.2 Ion VMI

The ion VMI data were recorded by selecting specific TOF regions corresponding to different fragment ions. This TOF gating enables the isolation of particular ionic species and the reconstruction of their momentum distributions.

Fig. C.3(a) shows the VMI images of sulfur-containing fragments with hydrogen, SH_n^+ ($n = 0, 1, 2, 3$), along with the corresponding radial intensity distributions obtained by integrating the images over angle. The results show that when the UV pulse arrives later, the sulfur-fragment yield increases, as evidenced by the enhanced signal in the corresponding radial distributions. In contrast, Fig. C.3(c) and (d), which correspond to $[M{-}SH_n]^+$ fragments (formed by the loss of SH_n from the parent molecule), show a depletion in signal when the UV pulse is delayed.

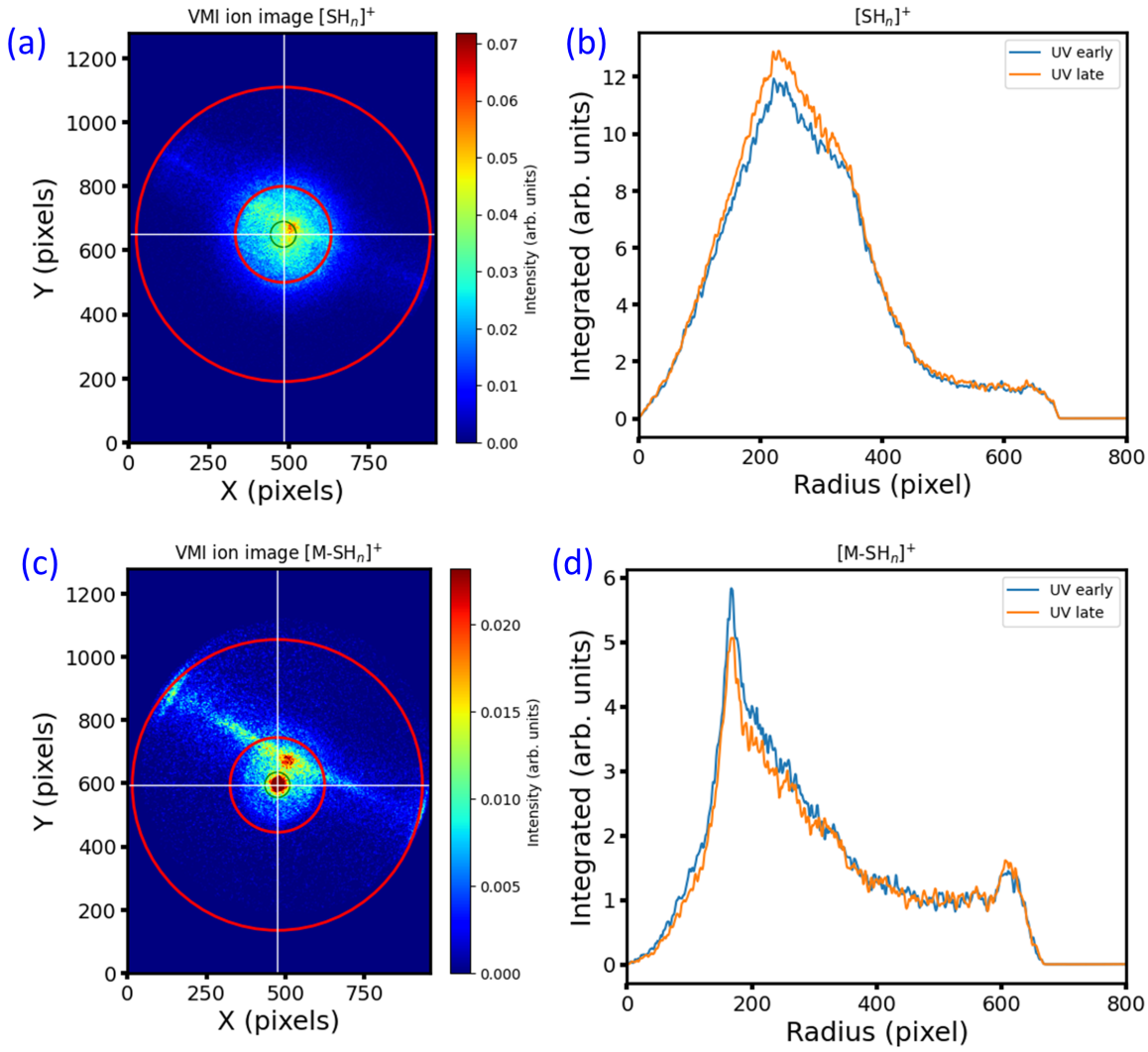

Figure C.3: VMI ion images of 1-butanethiol. Panels (a,b) show SH_n^+ ($n = 0$–3) with corresponding radial distributions, while (c,d) show $[M{-}SH_n]^+$. Both images have contributions from the background.

C.3 Electron VMI: Helium and Krypton

Helium is used as a carrier gas and to calibrate the electron spectrometer, whereas krypton is used solely for calibration because it produces multiple peaks upon ionization at a photon energy of 179 eV, with contributions from multiphoton processes at high FEL intensities. The corresponding raw and Abel-inverted VMI images for helium and krypton are shown in Fig. C.4 and Fig. C.5, respectively. The Abel-inversion procedure described in Section 3.4.6.

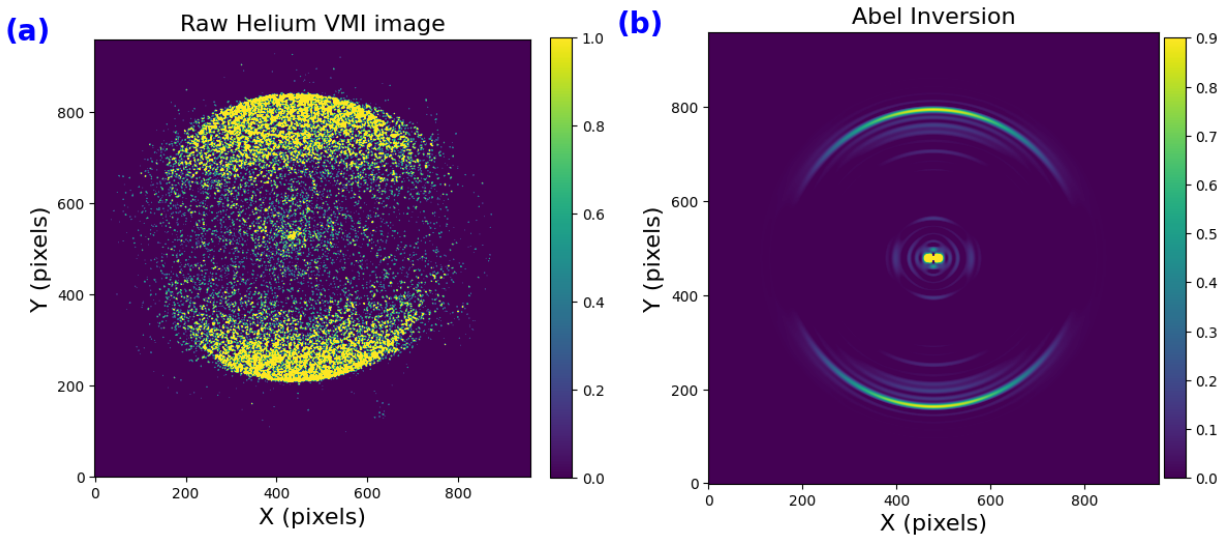

Figure C.4: Raw and Abel-inverted electron VMI images of helium, used for spectrometer calibration.

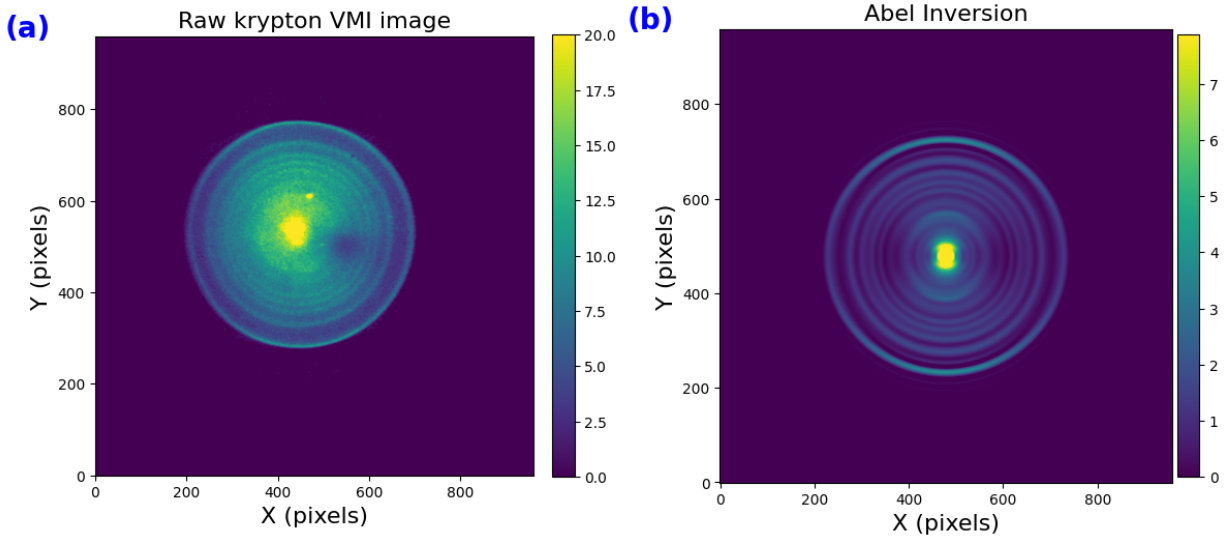

Figure C.5: Raw and Abel-inverted electron VMI images of krypton, also used for spectrometer calibration. The Abel-inverted image shows multiple rings, originating from multiphoton ionization by the FEL pulse.

C.4 Simulation of XPS Spectra

Binding energies of photoelectrons were calculated using GAMESS [220, 221] with DFT (B3LYP/cc-pCVQZ). Binding energies were obtained via the Δ self-consistent field (SCF) method as the energy difference between neutral fragments and fragments containing a sulfur $2p$ core hole.

Geometries were optimized at the Hartree–Fock/6-31G* level prior to the calculations. The SCF convergence of core-hole states was improved by using modified SCF settings. The calculated binding energies were compared with reported values for similar sulfur-containing molecules, where the S (2p) core-level binding energy is approximately 168 eV [196].

Molecule	SCF [a.u.]	SCF (S $2p^{-1}$) [a.u.]	ΔSCF [a.u.]	ΔSCF [eV]	Chemical shift (eV)
R-SH (literature)				$\sim$168	
Butanethiol	-556.5783	-550.3613	-6.2170	-169.16	0
C_2H_4SH	-477.3046	-471.0859	-6.2187	-169.21	0.05
CH_2SH	-437.9654	-431.7222	-6.2432	-176.88	0.71
SH	-398.7221	-392.4301	-6.2920	-171.21	-2.04
S	-398.0233	-391.6532	-6.3701	-173.33	-4.16
Butanethiol$^+$	-556.2484	-549.7148	-6.5336	-177.78	-8.62
$C_2H_4SH^+$	-477.0641	-470.5297	-6.5344	-177.80	-8.64
CH_2SH^+	-437.5662	-430.9779	-6.5813	-179.08	-9.92
SH^+	-398.2762	-391.5252	-6.7510	-183.69	-14.53
S^+	-397.6192	-390.7691	-6.8501	-186.39	-17.23

Table C.1: SCF energies, core-ionized energies, and chemical shifts for sulfur-containing species relative to butanethiol.

Bibliography

[1]L. Young, K. Ueda, M. Gühr, P. H. Bucksbaum, M. Simon, S. Mukamel, N. Rohringer, K. C. Prince, C. Masciovecchio, M. Meyer, A. Rudenko, D. Rolles, C. Bostedt, M. Fuchs, D. A. Reis, R. Santra, H. Kapteyn, M. Murnane, H. Ibrahim, F. Légaré, M. Vrakking, M. Isinger, D. Kroon, M. Gisselbrecht, A. L'Huillier, H. J. Wörner, and S. R. Leone, "Roadmap of ultrafast x-ray atomic and molecular physics", Journal of Physics B: Atomic, Molecular and Optical Physics **51**, 032003 (2018).

[2]T. Heinz, O. Shpyrko, D. Basov, N. Berrah, P. Bucksbaum, T. Devereaux, D. Fritz, K. Gaffney, O. Gessner, V. Gopalan, Z. Hasan, A. Lanzara, T. Martinez, A. Millis, S. Mukamel, M. Murnane, K. Nelson, R. Prasankumar, D. Reis, K. Schafer, G. Scholes, Z.-X. Shen, A. Stolow, H. Wen, M. Wolf, D. Xiao, L. Young, B. Garrett, L. Horton, H. Kerch, J. Krause, T. Settersten, L. Wilson, K. Runkles, T. Anderson, G. Chui, and E. Rutherford, *Basic energy sciences roundtable: opportunities for basic research at the frontiers of XFEL ultrafast science*, None, 1616251 (Oct. 25, 2017), None, 1616251.

[3]J. Cao, H. Ihee, and A. H. Zewail, "Ultrafast electron diffraction and direct observation of transient structures in a chemical reaction", Proceedings of the National Academy of Sciences **96**, 338–342 (1999).

[4]D. Schwickert, A. Przystawik, D. Diaman, D. Kip, J. P. Marangos, and T. Laarmann, "Coupled electron–nuclear dynamics induced and monitored with femtosecond soft x-ray pulses in the amino acid glycine", The Journal of Physical Chemistry A **128**, 989–995 (2024).

[5]P. Cong, G. Roberts, J. L. Herek, A. Mohktari, and A. H. Zewail, "Femtosecond real-time probing of reactions. 18. experimental and theoretical mapping of trajectories and potentials in the NaI dissociation reaction", The Journal of Physical Chemistry **100**, 7832–7848 (1996).

[6]S. X. Hu and L. A. Collins, "Attosecond pump probe: exploring ultrafast electron motion inside an atom", Physical Review Letters **96**, 073004 (2006).

[7]C. Nicolas and C. Miron, "Lifetime broadening of core-excited and -ionized states", Journal of Electron Spectroscopy and Related Phenomena, Special Issue in honor of Prof. T. Darrah Thomas: High-Resolution Spectroscopy of Isolated Species **185**, 267–272 (2012).

[8]S. Heinäsmäki, H. Aksela, J. Nikkinen, E. Kukk, A. Kivimäki, S. Aksela, and S. Fritzsche, "Lifetime and auger decay of strongly correlated 4p hole states of xenon", Journal of Electron Spectroscopy and Related Phenomena, ICESS-9 Proceedings of the 9th International Conference on Electronic Spectroscopy and Structure **137-140**, 281–285 (2004).

[9]A. H. Zewail, "Femtochemistry: atomic-scale dynamics of the chemical bond", The Journal of Physical Chemistry A **104**, 5660–5694 (2000).

[10]W. C. Röntgen, "Ueber eine neue art von strahlen", Annalen der Physik **300**, _eprint: https://onlinelibrary.wiley.com/doi/pdf/10.1002/andp.18983000103, 12–17 (1898).

[11]R. F. Mould, "The early history of x-ray diagnosis with emphasis on the contributions of physics 1895-1915", Physics in Medicine & Biology **40**, 1741 (1995).

[12]W. Friedrich, P. Knipping, and M. Laue, "Interferenzerscheinungen bei röntgenstrahlen", Annalen der Physik **346**, _eprint: https://onlinelibrary.wiley.com/doi/pdf/10.1002/andp.19133461004, 971–988 (1913).

[13]J. D. Watson and F. H. C. Crick, "Molecular structure of nucleic acids: a structure for deoxyribose nucleic acid", Nature **171**, 737–738 (1953).

[14]K. Siegbahn, "Electron spectroscopy for atoms, molecules, and condensed matter", Reviews of Modern Physics **54**, 709–728 (1982).

[15]W. Mehlhorn, "Atomic auger spectroscopy: historical perspective and recent highlights", in (2000), pp. 33–56.

[16]F. R. Elder, A. M. Gurewitsch, R. V. Langmuir, and H. C. Pollock, "Radiation from electrons in a synchrotron", Physical Review **71**, 829–830 (1947).

[17]W. Guo, B. Yang, C.-x. Wang, K. Harkay, and M. Borland, "Generating picosecond x-ray pulses in synchrotron light sources using dipole kickers", Physical Review Special Topics - Accelerators and Beams **10**, 020701 (2007).

[18]C. Bostedt, H. N. Chapman, J. T. Costello, J. R. Crespo López-Urrutia, S. Düsterer, S. W. Epp, J. Feldhaus, A. Föhlisch, M. Meyer, T. Möller, R. Moshammer, M. Richter, K. Sokolowski-Tinten, A. Sorokin, K. Tiedtke, J. Ullrich, and W. Wurth, "Experiments at FLASH", Nuclear Instruments and Methods in Physics Research Section A: Accelerators, Spectrometers, Detectors and Associated Equipment, Special issue in honour of Prof. Kai Siegbahn **601**, 108–122 (2009).

[19]S. Ackermann, "Experimental and numerical investigations on seeding options for the multi-beam line free-electron laser facility FLASH", Accepted: 2020-10-19T13:16:37Z Journal Abbreviation: Experimentelle und numerische Untersuchungen von Seeding Optionen für die Mehrfach-Elektronenstrahl Freie-Elektronen Laseranlage FLASH, doctoralThesis (Staats- und Universitätsbibliothek Hamburg Carl von Ossietzky, 2016).

[20]J. M. J. Madey, "Stimulated emission of bremsstrahlung in a periodic magnetic field", Journal of Applied Physics **42**, 1906–1913 (1971).

[21]N. Berrah, J. Bozek, J. Costello, S. Düsterer, L. Fang, J. Feldhaus, H. Fukuzawa, M. Hoener, Y. Jiang, P. Johnsson, E. Kennedy, M. Meyer, R. Moshammer, P. Radcliffe, M. Richter, A. Rouzée, A. Rudenko, A. Sorokin, K. Tiedtke, K. Ueda, J. Ullrich, and M. Vrakking, "Non-linear processes in the interaction of atoms and molecules with intense EUV and x-ray fields from SASE free electron lasers (FELs)", Journal of Modern Optics **57**, _eprint: https://doi.org/10.1080/09500340.2010.487946, 1015–1040 (2010).

[22]H. N. Chapman, A. Barty, M. J. Bogan, S. Boutet, M. Frank, S. P. Hau-Riege, S. Marchesini, B. W. Woods, S. Bajt, W. H. Benner, R. A. London, E. Plönjes, M. Kuhlmann, R. Treusch, S. Düsterer, T. Tschentscher, J. R. Schneider, E. Spiller, T. Möller, C. Bostedt, M. Hoener, D. A. Shapiro, K. O. Hodgson, D. van der Spoel, F. Burmeister, M. Bergh, C. Caleman, G. Huldt, M. M. Seibert, F. R. N. C. Maia, R. W. Lee, A. Szöke, N. Timneanu, and J. Hajdu, "Femtosecond diffractive imaging with a soft-x-ray free-electron laser", Nature Physics **2**, 839–843 (2006).

[23]C.-G. Wahlström, J. Larsson, A. Persson, T. Starczewski, S. Svanberg, P. Salières, P. Balcou, and A. L'Huillier, "High-order harmonic generation in rare gases with an intense short-pulse laser", Physical Review A **48**, 4709–4720 (1993).

[24]K. S. Zinchenko, F. Ardana-Lamas, V. U. Lanfaloni, T. T. Luu, Y. Pertot, M. Huppert, and H. J. Wörner, "Apparatus for attosecond transient-absorption spectroscopy in the water-window soft-x-ray region", Scientific Reports **13**, 3059 (2023).

[25]J. Li, X. Ren, Y. Yin, K. Zhao, A. Chew, Y. Cheng, E. Cunningham, Y. Wang, S. Hu, Y. Wu, M. Chini, and Z. Chang, "53-attosecond x-ray pulses reach the carbon k-edge", Nature Communications **8**, 186 (2017).

[26]M. Protopapas, C. H. Keitel, and P. L. Knight, "Atomic physics with super-high intensity lasers", Reports on Progress in Physics **60**, 389 (1997).

[27]A. Rudenko, V. Makhija, A. Vajdi, T. Ergler, M. Schürholz, R. K. Kushawaha, J. Ullrich, R. Moshammer, and V. Kumarappan, "Strong-field-induced wave packet dynamics in carbon dioxide molecule", Faraday Discussions **194**, 463–478 (2016).

[28]C. Burger, A. Atia-Tul-Noor, T. Schnappinger, H. Xu, P. Rosenberger, N. Haram, S. Beaulieu, F. Légaré, A. S. Alnaser, R. Moshammer, R. T. Sang, B. Bergues, M. S. Schuurman, R. de Vivie-Riedle, I. V. Litvinyuk, and M. F. Kling, "Time-resolved nuclear dynamics in bound and dissociating acetylene", Structural Dynamics **5**, 044302 (2018).

[29]T. Moon, K. Bartschat, and N. Douguet, "Strong-field ionization phenomena revealed by quantum trajectories", Physical Review Letters **133**, 073201 (2024).

[30]I. Bersons, "WKB theory of multiphoton processes in atoms", JOSA B **7**, 617–621 (1990).

[31]D. Mathur and F. A. Rajgara, "Nonadiabatic response of molecules to strong fields of picosecond, femtosecond, and subfemtosecond duration: an experimental study of the methane dication", The Journal of Chemical Physics **124**, 194308 (2006).

[32]P. Agostini, F. Fabre, G. Mainfray, G. Petite, and N. K. Rahman, "Free-free transitions following six-photon ionization of xenon atoms", Physical Review Letters **42**, 1127–1130 (1979).

[33]D. Garg, P. Chopra, J. W. L. Lee, D. S. Tikhonov, S. Kumar, O. Akcaalan, F. Allum, R. Boll, A. A. Butler, B. Erk, E. Gougoula, S. P. Gruet, L. He, D. Heathcote, E. Jones, M. M. Kazemi, J. Lahl, A. K. Lemmens, Z. Liu, D. Loru, S. Maclot, R. Mason, J. Merrick, E. Müller, T. Mullins, C. C. Papadopoulou, C. Passow, J. Peschel, M. Plach, D. Ramm, P. Robertson, D. Rompotis, A. Simao, A. L. Steber, A. Tajalli, A. Tul-Noor, N. Vadassery, I. S. Vinklárek, S. Techert, J. Küpper, A. M. Rijs, D. Rolles, M. Brouard, S. Bari, P. Eng-Johnsson, C. Vallance, M. Burt, B. Manschwetus, and M. Schnell, "Ultrafast dynamics of fluorene initiated by highly intense laser fields", Physical Chemistry Chemical Physics **26**, 20261–20272 (2024).

[34]M. V. Ammosov and V. P. Krainov, "Tunnel ionization of complex atoms and of atomic ions in an alternating electromagnetic field",

[35]L. V. Keldysh, "Ionization in the field of a strong electromagnetic wave", in M. V. Sadovskii, *Selected papers of leonid v keldysh* (WORLD SCIENTIFIC, Nov. 2023), pp. 56–63.

[36]P. B. Corkum, "Plasma perspective on strong field multiphoton ionization", Physical Review Letters **71**, 1994–1997 (1993).

[37]M. Lewenstein, P. Balcou, M. Y. Ivanov, A. L'Huillier, and P. B. Corkum, "Theory of high-harmonic generation by low-frequency laser fields", Physical Review A **49**, 2117–2132 (1994).

[38]I. V. Litvinyuk, K. F. Lee, P. W. Dooley, D. M. Rayner, D. M. Villeneuve, and P. B. Corkum, "Alignment-dependent strong field ionization of molecules", Physical Review Letters **90**, 233003 (2003).

[39]J. Svensmark, "Tunneling ionization of diatomic molecules", PhD thesis (Aarhus University, Aarhus, Denmark, Sept. 2016).

[40]X. M. Tong, Z. X. Zhao, and C. D. Lin, "Theory of molecular tunneling ionization", Physical Review A **66**, 033402 (2002).

[41]S. Schippers, A. L. D. Kilcoyne, R. A. Phaneuf, and A. Müller, "Photoionisation of ions with synchrotron radiation: from ions in space to atoms in cages", Contemporary Physics **57**, _eprint: https://doi.org/10.1080/00107514.2015.1109771, 215–229 (2016).

[42]Z. Jurek, S.-K. Son, B. Ziaja, and R. Santra, "XMDYN and XATOM: versatile simulation tools for quantitative modeling of x-ray free-electron laser induced dynamics of matter", Journal of Applied Crystallography **49**, 1048–1056 (2016).

[43]Y. H. Jiang, "Ultrafast extreme ultraviolet induced isomerization of acetylene cations", Physical Review Letters **105**, 10.1103/PhysRevLett.105.263002 (2010).

[44]A. Hishikawa, A. Matsuda, M. Fushitani, and E. J. Takahashi, "Visualizing recurrently migrating hydrogen in acetylene dication by intense ultrashort laser pulses", Physical Review Letters **99**, 258302 (2007).

[45]P. Atkins, J. D. Paula, and J. Keeler, *Atkins' physical chemistry*, 12th ed. (Oxford University Press, Dec. 5, 2022).

[46]S. P. A. H. ZEWAIL, "Femtosecond real time probing of reactions XXII kinetic description of probe absorption fluorescence depletion and mass spectrometry", Molecular Physics **89**, _eprint: https://doi.org/10.1080/002689796173291, 1455–1502 (1996).

[47]D. S. Tikhonov, D. Garg, and M. Schnell, "Inverse problems in pump–probe spectroscopy", Photochem **4**, 57–110 (2024).

[48]D. A. G. Deacon, L. R. Elias, J. M. J. Madey, G. J. Ramian, H. A. Schwettman, and T. I. Smith, "First operation of a free-electron laser", Physical Review Letters **38**, 892–894 (1977).

[49]P. Schmüser, M. Dohlus, J. Rossbach, and C. Behrens, "Low-gain FEL theory", in *Free-electron lasers in the ultraviolet and x-ray regime: physical principles, experimental results, technical realization*, edited by P. Schmüser, M. Dohlus, J. Rossbach, and C. Behrens (Springer International Publishing, Cham, 2014), pp. 25–38.

[50]C. Pellegrini, "X-ray free-electron lasers: from dreams to reality", Physica Scripta **2016**, 014004 (2017).

[51]W. Ackermann, G. Asova, V. Ayvazyan, A. Azima, N. Baboi, J. Bähr, V. Balandin, B. Beutner, A. Brandt, A. Bolzmann, R. Brinkmann, O. I. Brovko, M. Castellano, P. Castro, L. Catani, E. Chiadroni, S. Choroba, A. Cianchi, J. T. Costello, D. Cubaynes, J. Dardis, W. Decking, H. Delsim-Hashemi, A. Delserieys, G. Di Pirro, M. Dohlus, S. Düsterer, A. Eckhardt, H. T. Edwards, B. Faatz, J. Feldhaus, K. Flöttmann, J. Frisch, L. Fröhlich, T. Garvey, U. Gensch, C. Gerth, M. Görler, N. Golubeva, H.-J. Grabosch, M. Grecki, O. Grimm, K. Hacker, U. Hahn, J. H. Han, K. Honkavaara, T. Hott, M. Hüning, Y. Ivanisenko, E. Jaeschke, W. Jalmuzna, T. Jezynski, R. Kammering, V. Katalev, K. Kavanagh, E. T. Kennedy, S. Khodyachykh, K. Klose, V. Kocharyan, M. Körfer, M. Kollewe, W. Koprek, S. Korepanov, D. Kostin, M. Krassilnikov, G. Kube, M. Kuhlmann, C. L. S. Lewis, L. Lilje, T. Limberg, D. Lipka, F. Löhl, H. Luna, M. Luong, M. Martins, M. Meyer, P. Michelato, V. Miltchev, W. D. Möller, L. Monaco, W. F. O. Müller, O. Napieralski, O. Napoly, P. Nicolosi, D. Nölle, T. Nuñez, A. Oppelt, C. Pagani, R. Paparella, N. Pchalek, J. Pedregosa-Gutierrez, B. Petersen, B. Petrosyan, G. Petrosyan, L. Petrosyan, J. Pflüger, E. Plönjes, L. Poletto, K. Pozniak, E. Prat, D. Proch, P. Pucyk, P. Radcliffe, H. Redlin, K. Rehlich, M. Richter, M. Roehrs, J. Roensch, R. Romaniuk, M. Ross, J. Rossbach,

V. Rybnikov, M. Sachwitz, E. L. Saldin, W. Sandner, H. Schlarb, B. Schmidt, M. Schmitz, P. Schmüser, J. R. Schneider, E. A. Schneidmiller, S. Schnepp, S. Schreiber, M. Seidel, D. Sertore, A. V. Shabunov, C. Simon, S. Simrock, E. Sombrowski, A. A. Sorokin, P. Spanknebel, R. Spesyvtsev, L. Staykov, B. Steffen, F. Stephan, F. Stulle, H. Thom, K. Tiedtke, M. Tischer, S. Toleikis, R. Treusch, D. Trines, I. Tsakov, E. Vogel, T. Weiland, H. Weise, M. Wellhöfer, M. Wendt, I. Will, A. Winter, K. Wittenburg, W. Wurth, P. Yeates, M. V. Yurkov, I. Zagorodnov, and K. Zapfe, "Operation of a free-electron laser from the extreme ultraviolet to the water window", Nature Photonics **1**, 336–342 (2007).

[52]P. Schmüser, M. Dohlus, J. Rossbach, and C. Behrens, "Self-amplified spontaneous emission and FEL seeding", in *Free-electron lasers in the ultraviolet and x-ray regime: physical principles, experimental results, technical realization*, edited by P. Schmüser, M. Dohlus, J. Rossbach, and C. Behrens (Springer International Publishing, Cham, 2014), pp. 107–131.

[53]K. Wille, "Synchrotron radiation sources", Reports on Progress in Physics **54**, 1005 (1991).

[54]A. G. Stepanov and C. P. Hauri, "Short x-ray pulses from third-generation light sources", Journal of Synchrotron Radiation **23**, 141–151 (2016).

[55]J. Ullrich, A. Rudenko, and R. Moshammer, "Free-electron lasers: new avenues in molecular physics and photochemistry", Annual Review of Physical Chemistry **63**, 635–660 (2012).

[56]A. Barty, S. Boutet, M. J. Bogan, S. Hau-Riege, S. Marchesini, K. Sokolowski-Tinten, N. Stojanovic, R. Tobey, H. Ehrke, A. Cavalleri, S. Düsterer, M. Frank, S. Bajt, B. W. Woods, M. M. Seibert, J. Hajdu, R. Treusch, and H. N. Chapman, "Ultrafast single-shot diffraction imaging of nanoscale dynamics", Nature Photonics **2**, 415–419 (2008).

[57]R. Neutze, "Opportunities and challenges for time-resolved studies of protein structural dynamics at x-ray free-electron lasers", Philosophical Transactions of the Royal Society B: Biological Sciences **369**, 20130318 (2014).

[58]D. Kraus, J. Rips, M. Schörner, M. G. Stevenson, J. Vorberger, D. Ranjan, J. Lütgert, B. Heuser, J. H. Eggert, H.-P. Liermann, I. I. Oleynik, S. Pandolfi, R. Redmer, A. Sollier, C. Strohm, T. J. Volz, B. Albertazzi, S. J. Ali, L. Antonelli, C. Bähtz, O. B. Ball, S. Banerjee, A. B. Belonoshko, C. A. Bolme, V. Bouffetier, R. Briggs, K. Buakor, T. Butcher, V. Cerantola, J. Chantel, A. L. Coleman, J. Collier, G. W. Collins, A. J. Comley, T. E. Cowan, G. Cristoforetti, H. Cynn, A. Descamps, A. Di Cicco, S. Di Dio Cafiso, F. Dorchies, M. J. Duff, A. Dwivedi, C. Edwards, D. Errandonea, S. Galitskiy, E. Galtier, H. Ginestet, L. Gizzi, A. Gleason, S. Göde, J. M. Gonzalez, M. G. Gorman, M. Harmand, N. J. Hartley, P. G. Heighway, C. Hernandez-Gomez, A. Higginbotham, H. Höppner, R. J. Husband, T. M. Hutchinson, H. Hwang, D. A. Keen, J. Kim, P. Koester, Z. Konôpková, A. Krygier, L. Labate, A. Laso Garcia, A. E. Lazicki, Y. Lee, P. Mason, M. Masruri, B. Massani, E. E. McBride, J. D. McHardy, D. McGonegle, C. McGuire, R. S. McWilliams, S. Merkel, G. Morard, B. Nagler, M. Nakatsutsumi, K. Nguyen-Cong, A.-M. Norton, N. Ozaki, C. Otzen, D. J. Peake, A. Pelka, K. A. Pereira, J. P. Phillips, C. Prescher, T. R. Preston, L. Randolph, A. Ravasio, D. Santamaria-Perez, D. J. Savage, M. Schölmerich, J.-P. Schwinkendorf, S. Singh, J. Smith, R. F. Smith, J. Spear, C. Spindloe, T.-A. Suer, M. Tang, M. Toncian, T. Toncian, S. J. Tracy, A. Trapananti, C. E. Vennari, T. Vinci, M. Tyldesley, S. C. Vogel, J. P. S. Walsh, J. S. Wark, J. T. Willman, L. Wollenweber, U. Zastrau, E. Brambrink, K. Appel, and M. I. McMahon, "The structure of liquid carbon elucidated by in situ x-ray diffraction", Nature **642**, 351–355 (2025).

[59]C. Pellegrini and J. Stöhr, "X-ray free-electron lasers—principles, properties and applications", Nuclear Instruments and Methods in Physics Research Section A: Accelerators, Spectrometers, Detectors and Associated Equipment, NIMA Vol 500 **500**, 33–40 (2003).

[60]V. Ayvazyan, N. Baboi, J. Bähr, V. Balandin, B. Beutner, A. Brandt, I. Bohnet, A. Bolzmann, R. Brinkmann, O. I. Brovko, J. P. Carneiro, S. Casalbuoni, M. Castellano, P. Castro, L. Catani, E. Chiadroni, S. Choroba, A. Cianchi, H. Delsim-Hashemi, G. Di Pirro, M. Dohlus, S. Düsterer, H. T. Edwards, B. Faatz, A. A. Fateev, J. Feldhaus, K. Flöttmann, J. Frisch, L. Fröhlich, T. Garvey, U. Gensch, N. Golubeva, H.-J. Grabosch, B. Grigoryan, O. Grimm, U. Hahn, J. H. Han, M. V. Hartrott, K. Honkavaara, M. Hüning, R. Ischebeck, E. Jaeschke, M. Jablonka, R. Kammering, V. Katalev, B. Keitel, S. Khodyachykh, Y. Kim, V. Kocharyan, M. Körfer, M. Kollewe, D. Kostin, D. Krämer, M. Krassilnikov, G. Kube, L. Lilje, T. Limberg, D. Lipka, F. Löhl, M. Luong, C. Magne, J. Menzel, P. Michelato, V. Miltchev, M. Minty, W. D. Möller, L. Monaco, W. Müller, M. Nagl, O. Napoly, P. Nicolosi, D. Nölle, T. Nuñez, A. Oppelt, C. Pagani, R. Paparella, B. Petersen, B. Petrosyan, J. Pflüger, P. Piot, E. Plönjes, L. Poletto, D. Proch, D. Pugachov, K. Rehlich, D. Richter, S. Riemann, M. Ross, J. Rossbach, M. Sachwitz, E. L. Saldin, W. Sandner, H. Schlarb, B. Schmidt, M. Schmitz, P. Schmüser, J. R. Schneider, E. A. Schneidmiller, H.-J. Schreiber, S. Schreiber, A. V. Shabunov, D. Sertore, S. Setzer, S. Simrock, E. Sombrowski, L. Staykov, B. Steffen, F. Stephan, F. Stulle, K. P. Sytchev, H. Thom, K. Tiedtke, M. Tischer, R. Treusch, D. Trines, I. Tsakov, A. Vardanyan, R. Wanzenberg, T. Weiland, H. Weise, M. Wendt, I. Will, A. Winter, K. Wittenburg, M. V. Yurkov, I. Zagorodnov, P. Zambolin, and K. Zapfe, "First operation of a free-electron laser generating GW power radiation at 32 nm wavelength", The European Physical Journal D - Atomic, Molecular, Optical and Plasma Physics **37**, 297–303 (2006).

[61]M. Beye, M. Gühr, I. Hartl, E. Plönjes, L. Schaper, S. Schreiber, K. Tiedtke, and R. Treusch, "FLASH and the FLASH2020+ project—current status and upgrades for the free-electron laser in hamburg at DESY", The European Physical Journal Plus **138**, 193 (2023).

[62]P. Schmüser, M. Dohlus, J. Rossbach, and C. Behrens, "One-dimensional theory of the high-gain FEL", in *Free-electron lasers in the ultraviolet and x-ray regime: physical principles, experimental results, technical realization*, edited by P. Schmüser, M. Dohlus, J. Rossbach, and C. Behrens (Springer International Publishing, Cham, 2014), pp. 39–61.

[63]B. W. J. McNeil and N. R. Thompson, "X-ray free-electron lasers", Nature Photonics **4**, 814–821 (2010).

[64]P. Schmüser, M. Dohlus, J. Rossbach, and C. Behrens, "Appendices", in *Free-electron lasers in the ultraviolet and x-ray regime: physical principles, experimental results, technical realization*, edited by P. Schmüser, M. Dohlus, J. Rossbach, and C. Behrens (Springer International Publishing, Cham, 2014), pp. 183–228.

[65]A. A. Sorokin, Y. Bican, S. Bonfigt, M. Brachmanski, M. Braune, U. F. Jastrow, A. Gottwald, H. Kaser, M. Richter, and K. Tiedtke, "An x-ray gas monitor for free-electron lasers", Journal of Synchrotron Radiation **26**, 1092–1100 (2019).

[66]K. Tiedtke, J. Feldhaus, U. Hahn, U. Jastrow, T. Nunez, T. Tschentscher, S. V. Bobashev, A. A. Sorokin, J. B. Hastings, S. Möller, L. Cibik, A. Gottwald, A. Hoehl, U. Kroth, M. Krumrey, H. Schöppe, G. Ulm, and M. Richter, "Gas detectors for x-ray lasers", Journal of Applied Physics **103**, 094511 (2008).

[67]K. Tiedtke, A. Azima, N. von Bargen, L. Bittner, S. Bonfigt, S. Düsterer, B. Faatz, U. Frühling, M. Gensch, C. Gerth, N. Guerassimova, U. Hahn, T. Hans, M. Hesse, K. Honkavaar, U. Jastrow, P. Juranic, S. Kapitzki, B. Keitel, T. Kracht, M. Kuhlmann, W. B. Li, M. Martins, T. Núñez, E. Plönjes, H. Redlin, E. L. Saldin, E. A. Schneidmiller, J. R. Schneider, S. Schreiber, N. Stojanovic, F. Tavella, S. Toleikis, R. Treusch, H. Weigelt, M. Wellhöfer, H. Wabnitz, M. V. Yurkov, and J. Feldhaus, "The soft x-ray free-electron laser FLASH at DESY: beamlines, diagnostics and end-stations", New Journal of Physics **11**, 023029 (2009).

[68]R. Moshammer, M. Unverzagt, W. Schmitt, J. Ullrich, and H. Schmidt-Böcking, "A 4 recoil-ion electron momentum analyzer: a high-resolution "microscope" for the investigation of the dynamics of atomic, molecular and nuclear reactions", Nuclear Instruments and Methods in Physics Research Section B: Beam Interactions with Materials and Atoms **108**, 425–445 (1996).

[69]J. Ullrich, R. Moshammer, A. Dorn, R. Dörner, L. P. H. Schmidt, and H. Schmidt-Böcking, "Recoil-ion and electron momentum spectroscopy: reaction-microscopes", Reports on Progress in Physics **66**, 1463 (2003).

[70]M. Kurka, A. Rudenko, L. Foucar, K. U. Kühnel, Y. H. Jiang, T. Ergler, T. Havermeier, M. Smolarski, S. Schössler, K. Cole, M. Schöffler, R. Dörner, M. Gensch, S. Düsterer, R. Treusch, S. Fritzsche, A. N. Grum-Grzhimailo, E. V. Gryzlova, N. M. Kabachnik, C. D. Schröter, R. Moshammer, and J. Ullrich, "Two-photon double ionization of ne by free-electron laser radiation: a kinematically complete experiment", Journal of Physics B: Atomic, Molecular and Optical Physics **42**, 141002 (2009).

[71]G. Schmid, K. Schnorr, S. Augustin, S. Meister, H. Lindenblatt, F. Trost, Y. Liu, M. Braune, R. Treusch, C. D. Schröter, T. Pfeifer, and R. Moshammer, "Reaction microscope endstation at FLASH2", Journal of Synchrotron Radiation **26**, 854–867 (2019).

[72]C. Benvenuti, J. M. Cazeneuve, P. Chiggiato, F. Cicoira, A. Escudeiro Santana, V. Johanek, V. Ruzinov, and J. Fraxedas, "A novel route to extreme vacua: the non-evaporable getter thin film coatings", Vacuum **53**, 219–225 (1999).

[73]G. Schmid, "Two-color pump-probe experiments on small quantum systems at the free-electron laser in hamburg",

[74]A. Senftleben, "Kinematically complete study on electron impact ionisation of aligned hydrogen molecules", 10.11588/HEIDOK.00010015 (2009).

[75]J. Adamczewski-Musch, M. Al-Turany, S. Augustin, D. Bertini, H. G. Essel, and S. Linev, "The go4 analysis framework",

[76]R. Brun and F. Rademakers, "ROOT — an object oriented data analysis framework", Nuclear Instruments and Methods in Physics Research Section A: Accelerators, Spectrometers, Detectors and Associated Equipment, New Computing Techniques in Physics Research V **389**, 81–86 (1997).

[77]K. Schnorr, "XUV pump-probe experiments on electron rearrangement and interatomic coulombic decay in diatomic molecules", 10.11588/HEIDOK.00016294 (2014).

[78]F. Trost, "Time-resolved fragmentation of diiodomethane studied in an XUV pump-probe experiment", 10.11588/HEIDOK.00033303 (2023).

[79]R. Kuprieiev, skshetry, P. Rowlands (), D. Petrov, P. Redzyński, C. d. Costa-Luis, D. d. l. I. Castro, A. Schepanovski, I. Shcheklein, Gao, B. Taskaya, J. Orpinel, D. Berenbaum, F. Santos, Daniele, R. Lamy, A. Sharma, Z. Kaimuldenov, D. Hodovic, N. Kodenko, A. Grigorev, Earl, N. Dash, G. Vyshnya, maykulkarni, M. Hora, Vera, and S. Mangal, *DVC: data version control - git for data & models*, Sept. 7, 2023.

[80]P. Virtanen, R. Gommers, T. E. Oliphant, M. Haberland, T. Reddy, D. Cournapeau, E. Burovski, P. Peterson, W. Weckesser, J. Bright, S. J. van der Walt, M. Brett, J. Wilson, K. J. Millman, N. Mayorov, A. R. J. Nelson, E. Jones, R. Kern, E. Larson, C. J. Carey, İ. Polat, Y. Feng, E. W. Moore, J. VanderPlas, D. Laxalde, J. Perktold, R. Cimrman, I. Henriksen, E. A. Quintero, C. R. Harris, A. M. Archibald, A. H. Ribeiro, F. Pedregosa, and P. van Mulbregt, "SciPy 1.0: fundamental algorithms for scientific computing in python", Nature Methods **17**, 261–272 (2020).

[81]J. D. Hunter, "Matplotlib: a 2d graphics environment", Computing in Science & Engineering **9**, 90–95 (2007).

[82]C. R. Harris, K. J. Millman, S. J. van der Walt, R. Gommers, P. Virtanen, D. Cournapeau, E. Wieser, J. Taylor, S. Berg, N. J. Smith, R. Kern, M. Picus, S. Hoyer, M. H. van Kerkwijk, M. Brett, A. Haldane, J. F. del Río, M. Wiebe, P. Peterson, P. Gérard-Marchant, K. Sheppard, T. Reddy, W. Weckesser, H. Abbasi, C. Gohlke, and T. E. Oliphant, "Array programming with NumPy", Nature **585**, 357–362 (2020).

[83]T. p. d. team, *Pandas-dev/pandas: pandas*, June 28, 2023.

[84]S. Hoyer and J. Hamman, "Xarray: n-d labeled arrays and datasets in python", Journal of Open Research Software **5**, 10.5334/jors.148 (2017).

[85]J. Pivarski, I. Osborne, I. Ifrim, H. Schreiner, A. Hollands, A. Biswas, P. Das, S. Roy Choudhury, N. Smith, and M. Goyal, *Awkward array*, Aug. 17, 2023.

[86]J. Pivarski, H. Schreiner, A. Hollands, P. Das, K. Kothari, A. Roy, J. Ling, N. Smith, C. Burr, and G. Stark, *Uproot*, Aug. 11, 2023.

[87]M. Rocklin, "Dask: parallel computation with blocked algorithms and task scheduling", in (2015), pp. 126–132.

[88]B. Erk, J. P. Müller, C. Bomme, R. Boll, G. Brenner, H. N. Chapman, J. Correa, S. Düsterer, S. Dziarzhytski, S. Eisebitt, H. Graafsma, S. Grunewald, L. Gumprecht, R. Hartmann, G. Hauser, B. Keitel, C. von Korff Schmising, M. Kuhlmann, B. Manschwetus, L. Mercadier, E. Müller, C. Passow, E. Plönjes, D. Ramm, D. Rompotis, A. Rudenko, D. Rupp, M. Sauppe, F. Siewert, D. Schlosser, L. Strüder, A. Swiderski, S. Techert, K. Tiedtke, T. Tilp, R. Treusch, I. Schlichting, J. Ullrich, R. Moshammer, T. Möller, and D. Rolles, "CAMP@FLASH: an end-station for imaging, electron- and ion-spectroscopy, and pump–probe experiments at the FLASH free-electron laser", Journal of Synchrotron Radiation **25**, 1529–1540 (2018).

[89]L. Strüder, S. Epp, D. Rolles, R. Hartmann, P. Holl, G. Lutz, H. Soltau, R. Eckart, C. Reich, K. Heinzinger, C. Thamm, A. Rudenko, F. Krasniqi, K.-U. Kühnel, C. Bauer, C.-D. Schröter, R. Moshammer, S. Techert, D. Miessner, M. Porro, O. Hälker, N. Meidinger, N. Kimmel, R. Andritschke, F. Schopper, G. Weidenspointner, A. Ziegler, D. Pietschner, S. Herrmann, U. Pietsch, A. Walenta, W. Leitenberger, C. Bostedt, T. Möller, D. Rupp, M. Adolph, H. Graafsma, H. Hirsemann, K. Gärtner, R. Richter, L. Foucar, R. L. Shoeman, I. Schlichting, and J. Ullrich, "Large-format, high-speed, x-ray pnCCDs combined with electron and ion imaging spectrometers in a multipurpose chamber for experiments at 4th generation light sources", Nuclear Instruments and Methods in Physics Research Section A: Accelerators, Spectrometers, Detectors and Associated Equipment **614**, 483–496 (2010).

[90]D. Rolles, "Time-resolved experiments on gas-phase atoms and molecules with XUV and x-ray free-electron lasers", Advances in Physics: X **8**, _eprint: https://doi.org/10.1080/23746149.2022.2132182, 2132182 (2023).

[91]M. Vogt, S. Schreiber, and J. Zemella, "FLASH: status and upgrade", edited by H.-H. Braun, J. Chrin, R. Ganter, N. Hiller, and V. R. Schaa, Artwork Size: 6 pages, 0.335 MB ISBN: 9783954502240 Medium: application/pdf, 6 pages, 0.335 MB (2023).

[92]M. Sauppe, D. Rompotis, B. Erk, S. Bari, T. Bischoff, R. Boll, C. Bomme, C. Bostedt, S. Dörner, S. Düsterer, T. Feigl, L. Flückiger, T. Gorkhover, K. Kolatzki, B. Langbehn, N. Monserud, E. Müller, M. J.p, C. Passow, D. Ramm, D. Rolles, K. Schubert, L. Schwob, B. Senfftleben, R. Treusch, A. Ulmer, H. Weigelt, J. Zimbalski, J. Zimmermann, M. T, and D. Rupp, "XUV double-pulses with femtosecond to 650 ps separation from a multilayer-mirror-based split-and-delay unit at FLASH", Journal of Synchrotron Radiation **25**, 1517–1528 (2018).

[93]D. W. Chandler and P. L. Houston, "Two-dimensional imaging of state-selected photodissociation products detected by multiphoton ionization", The Journal of Chemical Physics **87**, 1445–1447 (1987).

[94]D. H. Parker and A. T. J. B. Eppink, "Photoelectron and photofragment velocity map imaging of state-selected molecular oxygen dissociation/ionization dynamics", The Journal of Chemical Physics **107**, 2357–2362 (1997).

[95]D. D. Hickstein, S. T. Gibson, R. Yurchak, D. D. Das, and M. Ryazanov, "A direct comparison of high-speed methods for the numerical abel transform", Review of Scientific Instruments **90**, 065115 (2019).

[96]C. Sparling and J. Onvlee, "Revisiting the inverse abel integral for reconstructing velocity-map images", Physical Chemistry Chemical Physics **27**, 18694–18709 (2025).

[97]G. A. Garcia, L. Nahon, and I. Powis, "Two-dimensional charged particle image inversion using a polar basis function expansion", Review of Scientific Instruments **75**, 4989–4996 (2004).

[98]Atia-tul-noor, S. Kumar, N. Schirmel, B. Erk, B. Manschwetus, S. Alisaukas, M. Braune, G. Cirmi, M. K. Czwalinna, U. Frühling, U. Grosse-Wortmann, N. Kschuev, F. Kuschewski, T. Lang, H. Lindenblatt, I. Litvinyuk, S. Meister, R. Moshammer, C. C. Papadopoulou, C. Passow, J. Roensch-Schulenburg, F. Trost, I. Hartl, S. Düsterer, and S. Schulz, "Sub-50 fs temporal resolution in an FEL-optical laser pump-probe experiment at FLASH2", Opt. Express **32**, 6597–6608 (2024).

[99]M. Rebholz, T. Ding, V. Despré, L. Aufleger, M. Hartmann, K. Meyer, V. Stooß, A. Magunia, D. Wachs, P. Birk, Y. Mi, G. D. Borisova, C. d. C. Castanheira, P. Rupprecht, G. Schmid, K. Schnorr, C. D. Schröter, R. Moshammer, Z.-H. Loh, A. R. Attar, S. R. Leone, T. Gaumnitz, H. J. Wörner, S. Roling, M. Butz, H. Zacharias, S. Düsterer, R. Treusch, G. Brenner, J. Vester, A. I. Kuleff, C. Ott, and T. Pfeifer, "All-XUV pump-probe transient absorption spectroscopy of the structural molecular dynamics of di-iodomethane", Physical Review X **11**, 031001 (2021).

[100]S. Schulz, I. Grguraš, C. Behrens, H. Bromberger, J. T. Costello, M. K. Czwalinna, M. Felber, M. C. Hoffmann, M. Ilchen, H. Y. Liu, T. Mazza, M. Meyer, S. Pfeiffer, P. Predki, S. Schefer, C. Schmidt, U. Wegner, H. Schlarb, and A. L. Cavalieri, "Femtosecond all-optical synchronization of an x-ray free-electron laser", Nature Communications **6**, 5938 (2015).

[101]D. E. Rivas, S. Serkez, T. M. Baumann, R. Boll, M. K. Czwalinna, S. Dold, A. d. Fanis, N. Gerasimova, P. Grychtol, B. Lautenschlager, M. Lederer, T. Jezynksi, D. Kane, T. Mazza, J. Meier, J. Müller, F. Pallas, D. Rompotis, P. Schmidt, S. Schulz, S. Usenko, S. Venkatesan, J. Wang, and M. Meyer, "High-temporal-resolution x-ray spectroscopy with free-electron and optical lasers", Optica **9**, 429–430 (2022).

[102]K. Mecseki, H. Höppner, M. Büscher, V. Tkachenko, N. Medvedev, J. J. Bekx, V. Lipp, P. Piekarz, M. Windeler, J. W. G. Tisch, D. J. Walke, M. Nakatsutsumi, M. J. Prandolini, J. M. Glownia, T. Sato, M. Sikorski, M. Chollet, U. Teubner, J. Robinson, S. Toleikis, B. Ziaja, and F. Tavella, "Hard x-ray induced fast secondary electron cascading processes in solids", Applied Physics Letters **113**, 114102 (2018).

[103]E. Biasin, Z. W. Fox, A. Andersen, K. Ledbetter, K. S. Kjær, R. Alonso-Mori, J. M. Carlstad, M. Chollet, J. D. Gaynor, J. M. Glownia, K. Hong, T. Kroll, J. H. Lee, C. Liekhus-Schmaltz, M. Reinhard, D. Sokaras, Y. Zhang, G. Doumy, A. M. March, S. H. Southworth, S. Mukamel, K. J. Gaffney, R. W. Schoenlein, N. Govind, A. A. Cordones, and M. Khalil, "Direct observation of coherent femtosecond solvent reorganization coupled to intramolecular electron transfer", Nature Chemistry **13**, 343–349 (2021).

[104]E. Allaria, D. Castronovo, P. Cinquegrana, M. B. Danailov, A. Demidovich, G. De Ninno, S. Di Mitri, B. Diviacco, E. Ferrari, L. Froehlich, D. Gauthier, L. Giannessi, B. Mahieu, G. Penco, P. Sigalotti, S. Spampinati, C. Spezzani, C. Svetina, M. Zangrando, D. Zangrando, et al., "Two-stage seeded soft-x-ray free-electron laser", Nature Photonics **7**, 913–918 (2013).

[105]P. Finetti, H. Höppner, E. Allaria, C. Callegari, F. Capotondi, P. Cinquegrana, M. Coreno, R. Cucini, M. B. Danailov, A. Demidovich, G. De Ninno, M. Di Fraia, R. Feifel, E. Ferrari, L. Fröhlich, D. Gauthier, T. Golz, C. Grazioli, Y. Kai, G. Kurdi, N. Mahne, M. Manfredda, N. Medvedev, I. P. Nikolov, E. Pedersoli, G. Penco, O. Plekan, M. J. Prandolini, K. C. Prince, L. Raimondi, P. Rebernik, R. Riedel, E. Roussel, P. Sigalotti, R. Squibb, N. Stojanovic, S. Stranges, C. Svetina, T. Tanikawa, U. Teubner, V. Tkachenko, S. Toleikis, M. Zangrando, B. Ziaja, F. Tavella, and L. Giannessi, "Pulse duration of seeded free-electron lasers", Physical Review X **7**, 021043 (2017).

[106]J. LaRue, B. Liu, G. L. S. Rodrigues, C. Liu, J. A. Garrido Torres, S. Schreck, E. Diesen, M. Weston, H. Ogasawara, F. Perakis, M. Dell'Angela, F. Capotondi, D. Ball, C. Carnahan, G. Zeri, L. Giannessi, E. Pedersoli, D. Naumenko, P. Amann, I. Nikolov, L. Raimondi, C. Spezzani, M. Beye, J. Voss, H.-Y. Wang, F. Cavalca, J. Gladh, S. Koroidov, F. Abild-Pedersen, M. Kolb, P. S. Miedema, R. Costantini, T. F. Heinz, A. C. Luntz, L. G. M. Pettersson, and A. Nilsson, "Symmetry-resolved CO desorption and oxidation dynamics on o/ru(0001) probed at the C K-edge by ultrafast x-ray spectroscopy", The Journal of Chemical Physics **157**, 164705 (2022).

[107]D. Faccialà, "Time-resolved chiral x-ray photoelectron spectroscopy with transiently enhanced atomic site selectivity: a free-electron laser investigation of electronically excited fenchone enantiomers", Physical Review X **13**, 10.1103/PhysRevX.13.011044 (2023).

[108]D. Mayer, F. Lever, and M. Gühr, "Data analysis procedures for time-resolved x-ray photoelectron spectroscopy at a SASE free-electron-laser", Journal of Physics B: Atomic, Molecular and Optical Physics **55**, 054002 (2022).

[109]D. Mayer, F. Lever, D. Picconi, J. Metje, S. Alisauskas, F. Calegari, S. Düsterer, C. Ehlert, R. Feifel, M. Niebuhr, B. Manschwetus, M. Kuhlmann, T. Mazza, M. S. Robinson, R. J. Squibb, A. Trabattoni, M. Wallner, P. Saalfrank, T. J. A. Wolf, and M. Gühr, "Following excited-state chemical shifts in molecular ultrafast x-ray photoelectron spectroscopy", Nature Communications **13**, 198 (2022).

[110]X. Wang, R. Y. Engel, I. Vaskivskyi, D. Turenne, V. Shokeen, A. Yaroslavtsev, O. Grånäs, R. Knut, J. O. Schunck, S. Dziarzhytski, G. Brenner, R.-P. Wang, M. Kuhlmann, F. Kuschewski, W. Bronsch, C. Schüßler-Langeheine, A. Styervoyedov, S. S. P. Parkin, F. Parmigiani, O. Eriksson, M. Beye, and H. A. Dürr, "Ultrafast manipulation of the NiO

antiferromagnetic order via sub-gap optical excitation", Faraday Discussions **237**, 300–316 (2022).

[111]E. Savelyev, R. Boll, C. Bomme, N. Schirmel, H. Redlin, B. Erk, S. Düsterer, E. Müller, H. Höppner, S. Toleikis, J. Müller, M. Kristin Czwalinna, R. Treusch, T. Kierspel, T. Mullins, S. Trippel, J. Wiese, J. Küpper, F. Braue, F. Krecinic, A. Rouzée, P. Rudawski, P. Johnsson, K. Amini, A. Lauer, M. Burt, M. Brouard, L. Christensen, J. Thøgersen, H. Stapelfeldt, N. Berrah, M. Müller, A. Ulmer, S. Techert, A. Rudenko, and D. Rolles, "Jitter-correction for IR/UV–XUV pump-probe experiments at the FLASH free-electron laser", New Journal of Physics **19**, 043009 (2017).

[112]S. Meister, H. Lindenblatt, F. Trost, K. Schnorr, S. Augustin, M. Braune, R. Treusch, T. Pfeifer, and R. Moshammer, "Atomic, molecular and cluster science with the reaction microscope endstation at FLASH2", Applied Sciences **10**, Number: 8, 2953 (2020).

[113]R. Ivanov, I. J. Bermúdez Macias, J. Liu, G. Brenner, J. Roensch-Schulenburg, G. Kurdi, U. Frühling, K. Wenig, S. Walther, A. Dimitriou, M. Drescher, I. P. Sazhina, A. K. Kazansky, N. M. Kabachnik, and S. Düsterer, "Single-shot temporal characterization of XUV pulses with duration from 10 fs to 350 fs at FLASH", Journal of Physics B: Atomic, Molecular and Optical Physics **53**, 184004 (2020).

[114]E. Plönjes, B. Faatz, M. Kuhlmann, and R. Treusch, "FLASH2: operation, beamlines, and photon diagnostics", in (2016), p. 020008.

[115]C. Behrens, "Constraints on photon pulse duration from longitudinal electron beam diagnostics at a soft x-ray free-electron laser", Physical Review Special Topics - Accelerators and Beams **15**, 10.1103/PhysRevSTAB.15.030707 (2012).

[116]S. Düsterer, "Development of experimental techniques for the characterization of ultrashort photon pulses of extreme ultraviolet free-electron lasers", Physical Review Special Topics - Accelerators and Beams **17**, 10.1103/PhysRevSTAB.17.120702 (2014).

[117]E. L. Saldin, E. A. Schneidmiller, and M. V. Yurkov, "Statistical properties of radiation from VUV and x-ray free-electron lasers", Optics Communications **148**, 383–403 (1998).

[118]B. Faatz, E. Plönjes, S. Ackermann, A. Agababyan, V. Asgekar, V. Ayvazyan, S. Baark, N. Baboi, V. Balandin, N. v. Bargen, Y. Bican, O. Bilani, J. Bödewadt, M. Böhnert, R. Böspflug, S. Bonfigt, H. Bolz, F. Borges, O. Borkenhagen, M. Brachmanski, M. Braune, A. Brinkmann, O. Brovko, T. Bruns, P. Castro, J. Chen, M. K. Czwalinna, H. Damker, W. Decking, M. Degenhardt, A. Delfs, T. Delfs, H. Deng, M. Dressel, H.-T. Duhme, S. Düsterer, H. Eckoldt, A. Eislage, M. Felber, J. Feldhaus, P. Gessler, M. Gibau, N. Golubeva, T. Golz, J. Gonschior, A. Grebentsov, M. Grecki, C. Grün, S. Grunewald, K. Hacker, L. Hänisch, A. Hage, T. Hans, E. Hass, A. Hauberg, O. Hensler, M. Hesse, K. Heuck, A. Hidvegi, M. Holz, K. Honkavaara, H. Höppner, A. Ignatenko, J. Jäger, U. Jastrow, R. Kammering, S. Karstensen, A. Kaukher, H. Kay, B. Keil, K. Klose, V. Kocharyan, M. Köpke, M. Körfer, W. Kook, B. Krause, O. Krebs, S. Kreis, F. Krivan, J. Kuhlmann, M. Kuhlmann, G. Kube, T. Laarmann, C. Lechner, S. Lederer, A. Leuschner, D. Liebertz, J. Liebing, A. Liedtke, L. Lilje, T. Limberg, D. Lipka, B. Liu, B. Lorbeer, K. Ludwig, H. Mahn, G. Marinkovic, C. Martens, F. Marutzky, M. Maslocv, D. Meissner, N. Mildner, V. Miltchev, S. Molnar, D. Mross, F. Müller, R. Neumann, P. Neumann, D. Nölle, F. Obier, M. Pelzer, H.-B. Peters, K. Petersen, A. Petrosyan, G. Petrosyan, L. Petrosyan, V. Petrosyan, A. Petrov, S. Pfeiffer, A. Piotrowski, Z. Pisarov, T. Plath, P. Pototzki, M. J. Prandolini, J. Prenting, G. Priebe, B. Racky, T. Ramm, K. Rehlich, R. Riedel, M. Roggli, M. Röhling, J. Rönsch-Schulenburg, J. Rossbach, V. Rybnikov, J. Schäfer, J. Schaffran, H. Schlarb, G. Schlesselmann, M. Schlösser, P. Schmid, C. Schmidt, F. Schmidt-Föhre, M. Schmitz, E. Schneidmiller, A. Schöps, M. Scholz, S. Schreiber, K. Schütt, U. Schütz,

H. Schulte-Schrepping, M. Schulz, A. Shabunov, P. Smirnov, E. Sombrowski, A. Sorokin, B. Sparr, J. Spengler, M. Staack, M. Stadler, C. Stechmann, B. Steffen, N. Stojanovic, V. Sychev, E. Syresin, T. Tanikawa, F. Tavella, N. Tesch, K. Tiedtke, M. Tischer, R. Treusch, S. Tripathi, P. Vagin, P. Vetrov, S. Vilcins, M. Vogt, A. d. Z. Wagner, T. Wamsat, H. Weddig, G. Weichert, H. Weigelt, N. Wentowski, C. Wiebers, T. Wilksen, A. Willner, K. Wittenburg, T. Wohlenberg, J. Wortmann, W. Wurth, M. Yurkov, I. Zagorodnov, and J. Zemella, "Simultaneous operation of two soft x-ray free-electron lasers driven by one linear accelerator", New Journal of Physics **18**, 062002 (2016).

[119]T. Lang, S. Alisauskas, U. Große-Wortmann, T. Hülsenbusch, B. Manschwetus, C. Mohr, J. Müller, F. Peters, N. Schirmel, S. Schulz, A. Swiderski, J. Zheng, and I. Hartl, "Versatile OPCPA pump-probe laser system for the FLASH2 XUV FEL beamline at DESY", in 2019 conference on lasers and electro-optics europe & european quantum electronics conference (CLEO/europe-EQEC) (June 2019), pp. 1–1.

[120]A.-L. Viotti, S. Alisauskas, A. Bin Wahid, P. Balla, N. Schirmel, B. Manschwetus, I. Hartl, and C. M. Heyl, "60 fs, 1030 nm FEL pump–probe laser based on a multi-pass post-compressed yb:YAG source", Journal of Synchrotron Radiation **28**, 36–43 (2021).

[121]M. Czwalinna, R. Boll, H. Kirkwood, J. Koliyadu, J. Kral, B. Lautenschlager, R. Letrun, J. Liu, J. Müller, F. Pallas, D. Rivas, T. Sato, H. Schlarb, S. Schulz, and B. Steffen, "Beam arrival stability at the european XFEL", Proceedings of the 12th International Particle Accelerator Conference **IPAC2021**, in collab. with L. Liu (Ed.), B. M. (Ed.) John, R. Neuenschwander (Ed.), P. Renan (Ed.), and S. W. (Ed.) Volker R., Artwork Size: 6 pages, 0.921 MB ISBN: 9783954502141 Medium: PDF, 6 pages, 0.921 MB (2021).

[122]A. Angelovski, "Evaluation of the cone-shaped pickup performance for low-charge sub-10 fs arrival-time measurements at free-electron laser facilities", Physical Review Special Topics - Accelerators and Beams **18**, 10.1103/PhysRevSTAB.18.012801 (2015).

[123]M. Krikunova, T. Maltezopoulos, A. Azima, M. Schlie, U. Frühling, H. Redlin, R. Kalms, S. Cunovic, N. M. Kabachnik, M. Wieland, and M. Drescher, "Time-resolved ion spectrometry on xenon with the jitter-compensated soft x-ray pulses of a free-electron laser", New Journal of Physics **11**, 123019 (2009).

[124]V. Jonauskas, L. Partanen, S. Kučas, R. Karazija, M. Huttula, S. Aksela, and H. Aksela, "Auger cascade satellites following $3d$ ionization in xenon", Journal of Physics B: Atomic, Molecular and Optical Physics **36**, 4403 (2003).

[125]M. Uiberacker, T. Uphues, M. Schultze, A. J. Verhoef, V. Yakovlev, M. F. Kling, J. Rauschenberger, N. M. Kabachnik, H. Schröder, M. Lezius, K. L. Kompa, H.-G. Muller, M. J. J. Vrakking, S. Hendel, U. Kleineberg, U. Heinzmann, M. Drescher, and F. Krausz, "Attosecond real-time observation of electron tunnelling in atoms", Nature **446**, 627–632 (2007).

[126]D. Rolles, R. Boll, B. Erk, D. Rompotis, and B. Manschwetus, "An experimental protocol for femtosecond NIR/UV - XUV pump-probe experiments with free-electron lasers", Journal of Visualized Experiments (JoVE), e57055 (2018).

[127]I. J. B. Macias, S. Düsterer, R. Ivanov, J. Liu, G. Brenner, J. Rönsch-Schulenburg, M. K. Czwalinna, and M. V. Yurkov, "Study of temporal, spectral, arrival time and energy fluctuations of SASE FEL pulses", Optics Express **29**, 10491–10508 (2021).

[128]A. Ludwig, E. Liberatore, J. Herrmann, L. Kasmi, P. López-Tarifa, L. Gallmann, U. Rothlisberger, U. Keller, and M. Lucchini, "Ultrafast relaxation dynamics of the ethylene cation c2h4+", The Journal of Physical Chemistry Letters **7**, 1901–1906 (2016).

[129]S. Kumar, S. Düsterer, U. Frühling, S. Alisauskas, G. Cirmi, M. Kristin Czwalinna, U. Große-Wortmann, N. Kschuev, F. Kuschewski, T. Lang, H. Lindenblatt, B. Manschwetus, S. Meister, C. C. Papadopoulou, C. Passow, J. Rönsch-Schulenburg, N. Schirmel, S. Schulz, F. Trost, H. Xu, I. Litvinyuk, R. Moshammer, N. M. Kabachnik, B. Erk, and A. Tul-Noor, "Xenon photoionization in the vicinity of 4*d* giant resonance and cooper minimum using an XUV-NIR pump-probe experiment", Physical Review A **110**, 063104 (2024).

[130]W. Mehlhorn, "70 years of auger spectroscopy, a historical perspective", Journal of Electron Spectroscopy and Related Phenomena **93**, 1–15 (1998).

[131]Y. Hikosaka, "Multi-electron–ion coincidence spectrometer with a high-efficiency microchannel plate detector", Journal of Electron Spectroscopy and Related Phenomena **255**, 147158 (2022).

[132]Y. Hikosaka, "Single, double, and triple auger decay of the Xe 4*p* core-hole states", Physical Review A **76**, 10.1103/PhysRevA.76.032708 (2007).

[133]P. Zhang, "Time-resolved multielectron coincidence spectroscopy of double auger-meitner decay following xe 4*d* ionization", Physical Review Letters **132**, 10.1103/PhysRevLett.132.083201 (2024).

[134]N. Saito and I. H. Suzuki, "Multiple photoionization in Ne, Ar, Kr, and Xe from 44 to 1300 ev", International Journal of Mass Spectrometry and Ion Processes **115**, 157–172 (1992).

[135]T. Hayaishi, T. Matsui, H. Yoshii, A. Higurashi, E. Murakami, A. Yagishita, T. Aoto, T. Onuma, and Y. Morioka, "Post-collision interaction effects following 4p-shell ionization of xe", Journal of Physics B: Atomic, Molecular and Optical Physics **35**, 141 (2001).

[136]T. Hayaishi, A. Yagishita, E. Shigemasa, E. Murakami, and Y. Morioka, "Coincidence spectra of threshold electrons and ions around the kr 3*d* and xe 4*d* delayed onset regions", Physica Scripta **41**, 35 (1990).

[137]D. M. P. Holland, K. Codling, G. V. Marr, and J. B. West, "Multiple photoionisation in the rare gases from threshold to 280 eV", Journal of Physics B: Atomic and Molecular Physics **12**, 2465 (1979).

[138]T. Hayaishi, Y. Morioka, Y. Kageyama, M. Watanabe, I. H. Suzuki, A. Mikuni, G. Isoyama, S. Asaoka, and M. Nakamura, "Multiple photoionisation of the rare gases in the XUV region", Journal of Physics B: Atomic and Molecular Physics **17**, 3511 (1984).

[139]G. Wendin and M. Ohno, "Strong dynamical effects of many-electron interactions in photoelectron spectra from 4*s* and 4*p* core levels", Physica Scripta **14**, 148 (1976).

[140]Y. Hikosaka and S. Fritzsche, "Coster–kronig and super coster–kronig transitions from the xe 4s core-hole state", Physical Chemistry Chemical Physics **24**, 17535–17541 (2022).

[141]Y. Hikosaka, "Double photoionization into double core-hole states in xe", Physical Review Letters **98**, 10.1103/PhysRevLett.98.183002 (2007).

[142]M. Fushitani, "Multielectron-ion coincidence spectroscopy of xe in extreme ultraviolet laser fields: nonlinear multiple ionization via double core-hole states", Physical Review Letters **124**, 10.1103/PhysRevLett.124.193201 (2020).

[143]U. Becker, "Subshell photoionization of xe between 40 and 1000 eV", Physical Review A **39**, 3902–3911 (1989).

[144]D. W. Lindle, "Photoemission from Xe in the vicinity of the 4*d* cooper minimum", Physical Review A **37**, 3808–3812 (1988).

[145]A. A. Sorokin, "Photoelectric effect at ultrahigh intensities", Physical Review Letters **99**, 10.1103/PhysRevLett.99.213002 (2007).

[146]M. Richter, "Extreme ultraviolet laser excites atomic giant resonance", Physical Review Letters **102**, 10.1103/PhysRevLett.102.163002 (2009).

[147]F. Penent, J. Palaudoux, P. Lablanquie, L. Andric, R. Feifel, and J. H. D. Eland, "Multielectron spectroscopy: the xenon $4d$ hole double auger decay", Physical Review Letters **95**, 083002 (2005).

[148]T. Luhmann, C. Gerth, M. Groen, M. Martins, B. Obst, M. Richter, and P. Zimmermann, "Final ion-charge resolving electron spectroscopy for the investigation of atomic photoionization processes: xe in the region of the $4d \rightarrow \epsilon f$ resonance", Physical Review A **57**, 282–291 (1998).

[149]L. Partanen, R. Sankari, S. Osmekhin, Z. F. Hu, E. Kukk, and H. Aksela, "Multiple ionization of Xe—comparison of de-excitation pathways following $3d_{5/2}$ ionization and $3d_{5/2} \rightarrow 6p$ resonance excitation", Journal of Physics B: Atomic, Molecular and Optical Physics **38**, 1881 (2005).

[150]S. Svensson, B. Eriksson, N. Mårtensson, G. Wendin, and U. Gelius, "Electron shake-up and correlation satellites and continuum shake-off distributions in x-ray photoelectron spectra of the rare gas atoms", Journal of Electron Spectroscopy and Related Phenomena **47**, 327–384 (1988).

[151]J. W. Cooper, "Photoionization from outer atomic subshells. a model study", Physical Review **128**, 681–693 (1962).

[152]Z. Liu, Q. Liu, Y. Ma, F. Zhou, and Y. Qu, "Multiple auger decay following Xe^+ $(4p_{3/2}^{-1})$ ionization", Chinese Physics Letters **38**, 023201 (2021).

[153]S. Fritzsche, A. N. Grum-Grzhimailo, E. V. Gryzlova, and N. M. Kabachnik, "Sequential two-photon double ionization of the $4d$ shell in xenon", Journal of Physics B: Atomic, Molecular and Optical Physics **44**, 175602 (2011).

[154]S. Falcinelli, F. Pirani, M. Alagia, L. Schio, R. Richter, S. Stranges, N. Balucani, and F. Vecchiocattivi, "Molecular dications in planetary atmospheric escape", Atmosphere **7**, 112 (2016).

[155]R. Dong, A. Chen, J. Feng, S. Zhang, W. Jiang, X. Hu, Y. Wu, J. Wang, X. Wang, and Y. Jiang, "Isomerization in highly excited states of triply charged carbon dioxide ions produced by intense laser fields", Physical Review A **110**, 053110 (2024).

[156]O. Witasse, O. Dutuit, J. Lilensten, R. Thissen, J. Zabka, C. Alcaraz, P.-L. Blelly, S. W. Bougher, S. Engel, L. H. Andersen, and K. Seiersen, "Prediction of a CO_2^{2+} layer in the atmosphere of mars", Geophysical Research Letters **29**, _eprint: https://agupubs.onlinelibrary.wiley.com/doi/pdf/10.1029/2002GL014781, 104–1–104–4 (2002).

[157]G. Gronoff, J. Lilensten, C. Simon, O. Witasse, R. Thissen, O. Dutuit, and C. Alcaraz, "Modelling dications in the diurnal ionosphere of venus", Astronomy & Astrophysics **465**, 641–645 (2007).

[158]F. Légaré, K. F. Lee, I. V. Litvinyuk, P. W. Dooley, A. D. Bandrauk, D. M. Villeneuve, and P. B. Corkum, "Imaging the time-dependent structure of a molecule as it undergoes dynamics", Physical Review A **72**, 052717 (2005).

[159]M. R. Jana, P. N. Ghosh, B. Bapat, R. K. Kushawaha, K. Saha, I. A. Prajapati, and C. P. Safvan, "Ion-induced triple fragmentation of CO_2^{3+} into $C^+ + O^+ + O^+$", Physical Review A **84**, 062715 (2011).

[160]R. K. Singh, G. S. Lodha, V. Sharma, I. A. Prajapati, K. P. Subramanian, and B. Bapat, "Triply charged carbon dioxide molecular ion: formation and fragmentation", Physical Review A **74**, 022708 (2006).

[161]N. Neumann, D. Hant, L. P. H. Schmidt, J. Titze, T. Jahnke, A. Czasch, M. S. Schöffler, K. Kreidi, O. Jagutzki, H. Schmidt-Böcking, and R. Dörner, "Fragmentation dynamics of CO_2^{3+} investigated by multiple electron capture in collisions with slow highly charged ions", Physical Review Letters **104**, 103201 (2010).

[162]A. E. Slattery, T. A. Field, M. Ahmad, R. I. Hall, J. Lambourne, F. Penent, P. Lablanquie, and J. H. D. Eland, "Spectroscopy and metastability of CO_2^{2+} molecular ions", The Journal of Chemical Physics **122**, 084317 (2005).

[163]T. A. Field and J. H. D. Eland, "The fragmentation dynamics of CS_2^{2+}", Chemical Physics Letters **303**, 144–150 (1999).

[164]W. Zuo, H. Lv, L. Zhao, Q. Zhang, and H. Xu, "Ionization and dissociation of linear triatomic molecules in strong laser fields", International Journal of Mass Spectrometry **392**, 80–85 (2015).

[165]C. Wu, C. Wu, D. Song, H. Su, Y. Yang, Z. Wu, X. Liu, H. Liu, M. Li, Y. Deng, Y. Liu, L.-Y. Peng, H. Jiang, and Q. Gong, "Nonsequential and sequential fragmentation of CO_2^{3+} in intense laser fields", Physical Review Letters **110**, 103601 (2013).

[166]*The go4 home page*, GSI, (May 12, 2015) https://www.gsi.de//en/work/research/experiment_electronics/data_processing/data_analysis/the_go4_home_page (visited on 12/05/2025).

[167]R. Dalitz, "CXII. on the analysis of τ-meson data and the nature of the τ-meson", The London, Edinburgh, and Dublin Philosophical Magazine and Journal of Science **44**, _eprint: https://doi.org/10.1080/14786441008520365, 1068–1080 (1953).

[168]E. Wang, M. Gong, Z. Shen, X. Shan, X. Ren, A. Dorn, and X. Chen, "Fragmentation dynamics of CS_2 in collisions with 1.0 kev electrons", The Journal of Chemical Physics **149**, 204301 (2018).

[169]E. Wang, X. Shan, Z. Shen, M. Gong, Y. Tang, Y. Pan, K.-C. Lau, and X. Chen, "Pathways for nonsequential and sequential fragmentation of CO_2^{3+} investigated by electron collision", Physical Review A **91**, 052711 (2015).

[170]A. Khan, L. C. Tribedi, and D. Misra, "Observation of a sequential process in charge-asymmetric dissociation of CO_2^{q+} $(q = 4, 5)$ upon the impact of highly charged ions", Physical Review A **92**, 030701 (2015).

[171]F. A. Rajgara, M. Krishnamurthy, D. Mathur, T. Nishide, T. Kitamura, H. Shiromaru, Y. Achiba, and N. Kobayashi, "Fragmentation dynamics of CS_2^{q+} $(q = 3 - -10)$ molecular ions", Physical Review A **64**, 032712 (2001).

[172]C. V. Brodowsky, T. Sukhodolov, G. Chiodo, V. Aquila, S. Bekki, S. S. Dhomse, M. Höpfner, A. Laakso, G. W. Mann, U. Niemeier, G. Pitari, I. Quaglia, E. Rozanov, A. Schmidt, T. Sekiya, S. Tilmes, C. Timmreck, S. Vattioni, D. Visioni, P. Yu, Y. Zhu, and T. Peter, "Analysis of the global atmospheric background sulfur budget in a multi-model framework", Atmospheric Chemistry and Physics **24**, 5513–5548 (2024).

[173]R. J. Charlson, J. E. Lovelock, M. O. Andreae, and S. G. Warren, "Oceanic phytoplankton, atmospheric sulphur, cloud albedo and climate", Nature **326**, 655–661 (1987).

[174]C. Wohl, J. Villamayor, M. Galí, A. S. Mahajan, R. P. Fernández, C. A. Cuevas, A. Bossolasco, Q. Li, A. J. Kettle, T. Williams, R. Sarda-Esteve, V. Gros, R. Simó, and A. Saiz-Lopez, "Marine emissions of methanethiol increase aerosol cooling in the southern ocean", Science Advances **10**, eadq2465 (2024).

[175]J. D. Cope, K. H. Bates, L. N. Tran, K. A. Abellar, and T. B. Nguyen, "Sulfur radical formation from the tropospheric irradiation of aqueous sulfate aerosols", Proceedings of the National Academy of Sciences **119**, e2202857119 (2022).

[176]A. Levy, E. L. Merryman, and W. T. Reid, "Mechanisms of formation of sulfur oxides in combustion", Environmental Science & Technology **4**, 653–662 (1970).

[177]I. Gabalski, F. Allum, I. Seidu, M. Britton, G. Brenner, H. Bromberger, M. Brouard, P. H. Bucksbaum, M. Burt, J. P. Cryan, T. Driver, N. Ekanayake, B. Erk, D. Garg, E. Gougoula, D. Heathcote, P. Hockett, D. M. P. Holland, A. J. Howard, S. Kumar, J. W. L. Lee, S. Li, J. McManus, J. Mikosch, D. Milesevic, R. S. Minns, S. Neville, Atia-Tul-Noor, C. C. Papadopoulou, C. Passow, W. O. Razmus, A. Röder, A. Rouzée, A. Simao, J. Unwin, C. Vallance, T. Walmsley, J. Wang, D. Rolles, A. Stolow, M. S. Schuurman, and R. Forbes, "Time-resolved x-ray photoelectron spectroscopy: ultrafast dynamics in CS_2 probed at the S $2p$ edge", The Journal of Physical Chemistry Letters **14**, 7126–7133 (2023).

[178]M. Ochmann, I. von Ahnen, A. A. Cordones, A. Hussain, J. H. Lee, K. Hong, K. Adamczyk, O. Vendrell, T. K. Kim, R. W. Schoenlein, and N. Huse, "Light-induced radical formation and isomerization of an aromatic thiol in solution followed by time-resolved x-ray absorption spectroscopy at the sulfur k-edge", Journal of the American Chemical Society **139**, 4797–4804 (2017).

[179]F. Lever, D. Mayer, J. Metje, S. Alisauskas, F. Calegari, S. Düsterer, R. Feifel, M. Niebuhr, B. Manschwetus, M. Kuhlmann, T. Mazza, M. S. Robinson, R. J. Squibb, A. Trabattoni, M. Wallner, T. J. A. Wolf, and M. Gühr, "Core-level spectroscopy of 2-thiouracil at the sulfur L_1- and $L_{2,3}$-edges utilizing a SASE free-electron laser", Molecules **26**, 6469 (2021).

[180]F. Lever, D. Mayer, D. Picconi, J. Metje, S. Alisauskas, F. Calegari, S. Düsterer, C. Ehlert, R. Feifel, M. Niebuhr, B. Manschwetus, M. Kuhlmann, T. Mazza, M. S. Robinson, R. J. Squibb, A. Trabattoni, M. Wallner, P. Saalfrank, T. J. A. Wolf, and M. Gühr, "Ultrafast dynamics of 2-thiouracil investigated by time-resolved auger spectroscopy", Journal of Physics B: Atomic, Molecular and Optical Physics **54**, 014002 (2020).

[181]F. Roth, M. Borgwardt, L. Wenthaus, J. Mahl, S. Palutke, G. Brenner, G. Mercurio, S. Molodtsov, W. Wurth, O. Gessner, and W. Eberhardt, "Direct observation of charge separation in an organic light harvesting system by femtosecond time-resolved XPS", Nature Communications **12**, 1196 (2021).

[182]S. Pathak, L. M. Ibele, R. Boll, C. Callegari, A. Demidovich, B. Erk, R. Feifel, R. Forbes, M. Di Fraia, L. Giannessi, C. S. Hansen, D. M. P. Holland, R. A. Ingle, R. Mason, O. Plekan, K. C. Prince, A. Rouzée, R. J. Squibb, J. Tross, M. N. R. Ashfold, B. F. E. Curchod, and D. Rolles, "Tracking the ultraviolet-induced photochemistry of thiophenone during and after ultrafast ring opening", Nature Chemistry **12**, 795–800 (2020).

[183]H. J. Thompson, O. Plekan, M. Bonanomi, N. Pal, F. Allum, A. D. Brynes, M. Coreno, S. Coriani, M. B. Danailov, P. Decleva, A. Demidovich, M. Devetta, D. Faccialà, R. Feifel, R. Forbes, C. Grazioli, D. M. P. Holland, P. Piseri, K. C. Prince, D. Rolles, M. S. Schuurman, A. Simoncig, R. J. Squibb, B. N. C. Tenorio, C. Vozzi, M. Zangrando, C. Callegari, R. S. Minns, and M. Di Fraia, "Time-resolved auger–meitner spectroscopy of the photodissociation dynamics of CS_2", Journal of Physics B: Atomic, Molecular and Optical Physics **57**, 215602 (2024).

[184]F. Neese, "Software update: the ORCA program system—version 6.0", WIREs Computational Molecular Science **15**, _eprint: https://wires.onlinelibrary.wiley.com/doi/pdf/10.1002/wcms.70019, e70019 (2025).

[185]J. Feldhaus, "FLASH—the first soft x-ray free electron laser (FEL) user facility", Journal of Physics B: Atomic, Molecular and Optical Physics **43**, 194002 (2010).

[186]S. Denifl, M. Stano, A. Stamatovic, P. Scheier, and T. D. Märk, "Electron-impact ionization of helium clusters close to the threshold: appearance energies", The Journal of Chemical Physics **124**, 054320 (2006).

[187]T. Hatsui, H. Setoyama, N. Kosugi, B. Wassermann, I. L. Bradeanu, and E. Rühl, "Photoionization of small krypton clusters in the kr $3d$ regime: evidence for site-specific photoemission", The Journal of Chemical Physics **123**, 154304 (2005).

[188]P. L. Ross and M. V. Johnston, "Unimolecular photochemistry of alkanethiols studied by photodissociation-photoionization mass spectrometry", The Journal of Physical Chemistry **97**, 10725–10731 (1993).

[189]E. Soh, P. M. Mayer, and T. Baer, "The unimolecular chemistry of ionized 1- and 2-butanethiol", International Journal of Mass Spectrometry and Ion Processes, In Honour of Fred McLafferty **160**, 63–71 (1997).

[190]W. Bleakney, "The ionization potential of molecular hydrogen", Physical Review **40**, 496–501 (1932).

[191]R. F. Fink, A. Eschner, M. Magnuson, O. Björneholm, I. Hjelte, C. Miron, M. Bassler, S. Svensson, M. N. Piancastelli, and S. L. Sorensen, "Specific production of very long-lived core-excited sulfur atoms by $2p^{-1}\sigma^*$ excitation of the OCS molecule followed by ultrafast dissociation", Journal of Physics B: Atomic, Molecular and Optical Physics **39**, L269 (2006).

[192]E. Livshits, I. Luzon, K. Gope, R. Baer, and D. Strasser, "Time-resolving the ultrafast h2 roaming chemistry and h3+ formation using extreme-ultraviolet pulses", Communications Chemistry **3**, 49 (2020).

[193]A. R. Abid, S. Bhattacharyya, A. S. Venkatachalam, S. Pathak, K. Chen, H. V. S. Lam, K. Borne, D. Mishra, R. C. Bilodeau, I. Dumitriu, N. Berrah, M. Patanen, and D. Rolles, "Hydrogen migration in inner-shell ionized halogenated cyclic hydrocarbons", Scientific Reports **13**, 2107 (2023).

[194]N. Ekanayake, T. Severt, M. Nairat, N. P. Weingartz, B. M. Farris, B. Kaderiya, P. Feizollah, B. Jochim, F. Ziaee, K. Borne, K. Raju P., K. D. Carnes, D. Rolles, A. Rudenko, B. G. Levine, J. E. Jackson, I. Ben-Itzhak, and M. Dantus, "H_2 roaming chemistry and the formation of H_3^+ from organic molecules in strong laser fields", Nature Communications **9**, 5186 (2018).

[195]D. Mishra, A. C. LaForge, L. M. Gorman, S. Díaz-Tendero, F. Martín, and N. Berrah, "Direct tracking of H_2 roaming reaction in real-time", Nature Communications **15**, 6656 (2024).

[196]R. B. Bernini, L. B. G. da Silva, F. N. Rodrigues, L. H. Coutinho, A. B. Rocha, and G. G. B. de Souza, "Core level (s 2p) excitation and fragmentation of the dimethyl sulfide and dimethyldisulfide molecules", The Journal of Chemical Physics **136**, 144307 (2012).

[197]N. Ekanayake, M. Nairat, N. P. Weingartz, M. J. Michie, B. G. Levine, and M. Dantus, "Substituent effects on H_3^+ formation via H_2 roaming mechanisms from organic molecules under strong-field photodissociation", The Journal of Chemical Physics **149**, 244310 (2018).

[198]T. Oka, "Interstellar h3+", Chemical Reviews **113**, 8738–8761 (2013).

[199]J. W. L. Lee, D. S. Tikhonov, P. Chopra, S. Maclot, A. L. Steber, S. Gruet, F. Allum, R. Boll, X. Cheng, S. Düsterer, B. Erk, D. Garg, L. He, D. Heathcote, M. Johny, M. M. Kazemi, H. Köckert, J. Lahl, A. K. Lemmens, D. Loru, R. Mason, E. Müller, T. Mullins, P. Olshin, C. Passow, J. Peschel, D. Ramm, D. Rompotis, N. Schirmel, S. Trippel, J. Wiese, F. Ziaee, S. Bari, M. Burt, J. Küpper, A. M. Rijs, D. Rolles, S. Techert, P. Eng-Johnsson, M. Brouard, C. Vallance, B. Manschwetus, and M. Schnell, "Time-resolved relaxation and fragmentation of polycyclic aromatic hydrocarbons investigated in the ultrafast XUV-IR regime", Nature Communications **12**, 6107 (2021).

[200]D. Jadoun and M. Kowalewski, "Time-resolved photoelectron spectroscopy of conical intersections with attosecond pulse trains", The Journal of Physical Chemistry Letters **12**, 8103–8108 (2021).

[201]M. O. Krause, "Atomic radiative and radiationless yields for k and l shells", Journal of Physical and Chemical Reference Data **8**, 307–327 (1979).

[202]B. K. McFarland, J. P. Farrell, S. Miyabe, F. Tarantelli, A. Aguilar, N. Berrah, C. Bostedt, J. D. Bozek, P. H. Bucksbaum, J. C. Castagna, R. N. Coffee, J. P. Cryan, L. Fang, R. Feifel, K. J. Gaffney, J. M. Glownia, T. J. Martinez, M. Mucke, B. Murphy, A. Natan, T. Osipov, V. S. Petrović, S. Schorb, T. Schultz, L. S. Spector, M. Swiggers, I. Tenney, S. Wang, J. L. White, W. White, and M. Gühr, "Ultrafast x-ray auger probing of photoexcited molecular dynamics", Nature Communications **5**, 4235 (2014).

[203]R. N. S. Sodhi and R. G. Cavell, "KLL auger and core-level (1s and 2p) photoelectron shifts in a series of gaseous sulfur compounds", Journal of Electron Spectroscopy and Related Phenomena **41**, 1–24 (1986).

[204]Y. Hikosaka, "Metastability and fragmentation of the OCS^{3+} states produced by S $2p$ double auger decay", The Journal of Chemical Physics **158**, 214306 (2023).

[205]R. Feng, G. Cooper, Y. Sakai, and C. E. Brion, "Dipole (e,e+ ion) coincidence studies of the ionic photofragmentation and photoionization of carbonyl sulfide in the valence shell and S $2p$, $2s$ and C $1s$ inner-shell regions (10–300 ev)", Chemical Physics **255**, 353–368 (2000).

[206]X. Zhao, T. Xu, X. Yu, D. Ren, X. Zhang, X. Li, P. Ma, C. Wang, D. Zhang, Q. Wang, X. Hu, S. Luo, Y. Wu, J. Wang, and D. Ding, "Tracking the nuclear movement of the carbonyl sulfide cation after strong-field ionization by time-resolved coulomb-explosion imaging", Physical Review A **103**, 053103 (2021).

[207]A.-L. Viotti, S. Alisauskas, M. Seidel, A. Tajalli, B. Manschwetus, H. Cankaya, K. Jurkus, V. Sinkus, and I. Hartl, "FLASH free electron laser pump-probe laser concept based on spectral broadening of high-power ytterbium picosecond systems in multi-pass cells", Review of Scientific Instruments **94**, 023002 (2023).

[208]P. Balla, A. B. Wahid, I. Sytcevich, C. Guo, A.-L. Viotti, L. Silletti, A. Cartella, S. Alisauskas, H. Tavakol, U. Grosse-Wortmann, A. Schönberg, M. Seidel, A. Trabattoni, B. Manschwetus, T. Lang, F. Calegari, A. Couairon, A. L'Huillier, C. L. Arnold, I. Hartl, and C. M. Heyl, "Postcompression of picosecond pulses into the few-cycle regime", Optics Letters **45**, 2572–2575 (2020).

[209]A.-L. Viotti, M. Seidel, E. Escoto, S. Rajhans, W. P. Leemans, I. Hartl, and C. M. Heyl, "Multi-pass cells for post-compression of ultrashort laser pulses", Optica **9**, 197–216 (2022).

[210]L. Silletti, A. b. Wahid, E. Escoto, P. Balla, S. Rajhans, K. Horn, L. Winkelmann, V. Wanie, A. Trabattoni, C. M. Heyl, and F. Calegari, "Dispersion-engineered multi-pass cell for single-stage post-compression of an ytterbium laser", Optics Letters **48**, 1842–1845 (2023).

[211]S. Ackermann, A. Azima, S. Bajt, J. Bödewadt, F. Curbis, H. Dachraoui, H. Delsim-Hashemi, M. Drescher, S. Düsterer, B. Faatz, M. Felber, J. Feldhaus, E. Hass, U. Hipp, K. Honkavaara, R. Ischebeck, S. Khan, T. Laarmann, C. Lechner, T. Maltezopoulos, V. Miltchev, M. Mittenzwey, M. Rehders, J. Rönsch-Schulenburg, J. Rossbach, H. Schlarb, S. Schreiber, L. Schroedter, M. Schulz, S. Schulz, R. Tarkeshian, M. Tischer, V. Wacker, and M. Wieland, "Generation of coherent 19- and 38-nm radiation at a free-electron laser directly seeded at 38 nm", Physical Review Letters **111**, 114801 (2013).

[212]C. Lechner, R. Aßmann, A. Azima, J. Bödewadt, M. Dohlus, M. Drescher, N. Ekanayake, G. Feng, I. Hartl, S. Khan, T. Laarmann, T. Lang, T. Maltezopoulos, T. Plath, J. Roßbach, L. Winkelmann, W. Wurth, and I. Zagorodnov, "Concept for a seeded FEL at FLASH2", Proceedings of the 38th Int. Free Electron Laser Conf. **FEL2017**, edited by B. Kip (Ed.), C. Bruce (Ed.), and S. RW (Ed.) Volker, Artwork Size: 4 pages, 0.362 MB ISBN: 9783954501793 Medium: PDF, 4 pages, 0.362 MB (2018).

[213]E. Allaria, R. Appio, L. Badano, W. A. Barletta, S. Bassanese, S. G. Biedron, A. Borga, E. Busetto, D. Castronovo, P. Cinquegrana, S. Cleva, D. Cocco, M. Cornacchia, P. Craievich, I. Cudin, G. D'Auria, M. Dal Forno, M. B. Danailov, R. De Monte, G. De Ninno, P. Delgiusto, A. Demidovich, S. Di Mitri, B. Diviacco, A. Fabris, R. Fabris, W. Fawley, M. Ferianis, E. Ferrari, S. Ferry, L. Froehlich, P. Furlan, G. Gaio, F. Gelmetti, L. Giannessi, M. Giannini, R. Gobessi, R. Ivanov, E. Karantzoulis, M. Lonza, A. Lutman, B. Mahieu, M. Milloch, S. V. Milton, M. Musardo, I. Nikolov, S. Noe, F. Parmigiani, G. Penco, M. Petronio, L. Pivetta, M. Predonzani, F. Rossi, L. Rumiz, A. Salom, C. Scafuri, C. Serpico, P. Sigalotti, S. Spampinati, C. Spezzani, M. Svandrlik, C. Svetina, S. Tazzari, M. Trovo, R. Umer, A. Vascotto, M. Veronese, R. Visintini, M. Zaccaria, D. Zangrando, and M. Zangrando, "Highly coherent and stable pulses from the FERMI seeded free-electron laser in the extreme ultraviolet", Nature Photonics **6**, 699–704 (2012).

[214]J. J. John, M. Brouard, A. Clark, J. Crooks, E. Halford, L. Hill, J. W. L. Lee, A. Nomerotski, R. Pisarczyk, I. Sedgwick, C. S. Slater, R. Turchetta, C. Vallance, E. Wilman, B. Winter, and W. H. Yuen, "PImMS, a fast event-triggered monolithic pixel detector with storage of multiple timestamps", Journal of Instrumentation **7**, C08001 (2012).

[215]H. Bromberger, D. Pennicard, R. Ballabriga, S. Trippel, and J. Küpper, "Timepix3: single-pixel multi-hit energy-measurement behaviour", Journal of Instrumentation **19**, P11008 (2024).

[216]H. Bromberger, C. Passow, D. Pennicard, R. Boll, J. Correa, L. He, M. Johny, C. C. Papadopoulou, A. Tul-Noor, J. Wiese, S. Trippel, B. Erk, and J. Küpper, "Shot-by-shot 250 kHz 3d ion and MHz photoelectron imaging using timepix3", Journal of Physics B: Atomic, Molecular and Optical Physics **55**, 144001 (2022).

[217]F. Allum, C.-s. Lam, B. Erk, H. Bromberger, P. H. Bucksbaum, M. Britton, M. Burt, N. Ekanayake, I. Gabalski, D. Garg, E. Gougoula, D. Heathcote, A. J. Howard, P. Hockett, D. M. P. Holland, S. Kumar, J. W. L. Lee, J. McManus, J. Mikosch, D. Milešević, R. S. Minns, C. C. Papadopoulou, C. Passow, W. O. Razmus, A. Röder, D. Rolles, A. Rouzée, M. S. Schuurman, A. Simao, A. Stolow, A.-T. Noor, J. Unwin, C. Vallance, T. Walmsley, M. Brouard, and R. Forbes, "Fragmentation dynamics of CS_2 dications and trications following S $2p$ ionization", The Journal of Chemical Physics **164**, 024304 (2026).

[218]T. Weber, M. Weckenbrock, A. Staudte, L. Spielberger, O. Jagutzki, V. Mergel, F. Afaneh, G. Urbasch, M. Vollmer, H. Giessen, and R. Dörner, "Sequential and nonsequential contributions to double ionization in strong laser fields", Journal of Physics B: Atomic, Molecular and Optical Physics **33**, L127–L133 (2000).

[219]G. Schmid, "Two-color pump-probe experiments on small quantum systems at the free-electron laser in hamburg", 10.11588/HEIDOK.00024786 (2018).

[220]M. J. Perri and S. H. Weber, "Web-based job submission interface for the GAMESS computational chemistry program", Journal of Chemical Education **91**, 2206–2208 (2014).

[221]G. M. J. Barca, C. Bertoni, L. Carrington, D. Datta, N. De Silva, J. E. Deustua, D. G. Fedorov, J. R. Gour, A. O. Gunina, E. Guidez, T. Harville, S. Irle, J. Ivanic, K. Kowalski, S. S. Leang, H. Li, W. Li, J. J. Lutz, I. Magoulas, J. Mato, V. Mironov, H. Nakata, B. Q. Pham, P. Piecuch, D. Poole, S. R. Pruitt, A. P. Rendell, L. B. Roskop, K. Ruedenberg, T. Sattasathuchana, M. W. Schmidt, J. Shen, L. Slipchenko, M. Sosonkina, V. Sundriyal, A. Tiwari, J. L. Galvez Vallejo, B. Westheimer, M. Włoch, P. Xu, F. Zahariev, and M. S. Gordon, "Recent developments in the general atomic and molecular electronic structure system", The Journal of Chemical Physics **152**, 154102 (2020).

List of Publications

Parts of this work have been published in the following peer-reviewed journal articles:

1. A. Tul-Noor[1], **S. Kumar**[1],, N. Schirmel, B. Erk, B. Manschwetus, S. Alisauskas, M. Braune, G. Cirmi, M. K. Czwalinna, U. Frühling, U. Große-Wortmann, N. Kschuev, F. Kuschewski, T. Lang, H. Lindenblatt, I. Litvinyuk, S. Meister, R. Moshammer, C. C. Papadopoulou, C. Passow, J. Rönsch-Schulenburg, F. Trost, I. Hartl, S. Düsterer, and S. Schulz, "Sub-50 fs temporal resolution in an FEL–optical laser pump–probe experiment at FLASH2," *Optics Express*, vol. 32, pp. 6597–6608, 2024.

2. **S. Kumar**, S. Düsterer, U. Frühling, S. Alisauskas, G. Cirmi, M. K. Czwalinna, U. Große-Wortmann, N. Kschuev, F. Kuschewski, T. Lang, H. Lindenblatt, B. Manschwetus, S. Meister, C. C. Papadopoulou, C. Passow, J. Rönsch-Schulenburg, N. Schirmel, S. Schulz, F. Trost, H. Xu, I. Litvinyuk, R. Moshammer, N. M. Kabachnik, B. Erk, and A. Tul-Noor, "Xenon photoionization in the vicinity of the $4d$ giant resonance and Cooper minimum using an XUV–NIR pump–probe experiment," *Physical Review A*, vol. 110, no. 6, p. 063104, 2024.

Further publications with own contribution

3. F. Allum, C.-S. Lam, B. Erk, H. Bromberger, P. H. Bucksbaum, M. Britton, M. Burt, N. Ekanayake, I. Gabalski, D. Garg, E. Gougoula, D. Heathcote, A. J. Howard, P. Hockett, D. M. P. Holland, **S. Kumar**, J. W. L. Lee, J. McManus, J. Mikosch, D. Milešević, R. S. Minns, C. C. Papadopoulou, C. Passow, W. O. Razmus, A. Röder, D. Rolles, A. Rouzée, M. S. Schuurman, A. Simao, A. Stolow, A. Tul-Noor, J. Unwin, C. Vallance, T. Walmsley, M. Brouard, and R. Forbes, "Fragmentation dynamics of CS_2^{2+} and CS_2^{3+} following S $2p$ ionization," *The Journal of Chemical Physics*, vol. 164, no. 2, 2026.

4. D. Garg, P. Chopra, J. W. L. Lee, D. S. Tikhonov, **S. Kumar**, Ö. Akcaalan, F. Allum, R. Boll, A. A. Butler, B. Erk, E. Gougoula, S. P. Gruet, L. He, D. Heathcote, E. Jones, M. M. Kazemi, J. Lahl, A. K. Lemmens, Z. Liu, D. Loru, S. Maclot, R. Mason, J. Merrick, E. Müller, T. Mullins, C. C. Papadopoulou, C. Passow, J. Peschel, M. Plach, D. Ramm, P. Robertson, D. Rompotis, A. Simao, A. L. Steber, A. Tajalli, A. Tul-Noor, N. Vadassery, I. S. Vinklárek, S. Techert, J. Küpper, A. M. Rijs, D. Rolles, M. Brouard, S. Bari, P. Eng-Johnsson, C. Vallance, M. Burt, B. Manschwetus, and M. Schnell, "Ultrafast dynamics of fluorene initiated by highly intense laser fields," *Physical Chemistry Chemical Physics*, vol. 26, no. 30, pp. 20261–20272, 2024.

5. J. Unwin, F. Allum, M. Britton, I. Gabalski, H. Bromberger, M. Brouard, P. H. Bucksbaum, T. Driver, N. Ekanayake, D. Garg, E. Gougoula, D. Heathcote, A. J. Howard,

P. Hockett, D. M. P. Holland, **S. Kumar**, C.-S. Lam, J. W. L. Lee, J. McManus, J. Mikosch, D. Milesevic, R. S. Minns, C. C. Papadopoulou, C. Passow, W. O. Razmus, A. Röder, A. Rouzée, M. Schuurman, A. Simao, A. Stolow, A. Tul-Noor, C. Vallance, T. Walmsley, D. Rolles, B. Erk, M. Burt, and R. Forbes, "X-ray induced Coulomb explosion imaging of transient excited-state structural rearrangements in CS_2," *Communications Physics*, vol. 6, Article 309, 2023.

6. I. Gabalski, F. Allum, I. Seidu, M. Britton, G. Brenner, H. Bromberger, M. Brouard, P. H. Bucksbaum, M. Burt, J. P. Cryan, T. Driver, N. Ekanayake, B. Erk, D. Garg, E. Gougoula, D. Heathcote, P. Hockett, D. M. P. Holland, A. J. Howard, **S. Kumar**, J. W. L. Lee, S. Li, J. McManus, J. Mikosch, D. Milesevic, R. S. Minns, S. Neville, A. Tul-Noor, C. C. Papadopoulou, C. Passow, W. O. Razmus, A. Röder, A. Rouzée, A. Simao, J. Unwin, C. Vallance, T. Walmsley, J. Wang, D. Rolles, A. Stolow, M. S. Schuurman, and R. Forbes, "Time-resolved X-ray photoelectron spectroscopy: Ultrafast dynamics in CS_2 probed at the S $2p$ edge," *The Journal of Physical Chemistry Letters*, vol. 14, no. 31, pp. 7126–7133, 2023.

7. J. Wang, T. Driver, F. Allum, C. C. Papadopoulou, C. Passow, G. Brenner, S. Li, S. Düsterer, A. Tul Noor, **S. Kumar**, P. H. Bucksbaum, B. Erk, R. Forbes, and J. P. Cryan, "Photon energy-resolved velocity map imaging from spectral domain ghost imaging," *New Journal of Physics*, vol. 25, p. 033017, 2023.

8. A. Schönberg, H. S. Salman, A. Tajalli, **S. Kumar**, I. Hartl, and C. M. Heyl, "Below-threshold harmonic generation in gas-jets for Th-229 nuclear spectroscopy," *Optics Express*, vol. 31, pp. 12880–12893, 2023.

[1]These authors contributed equally to this work.

Declaration on oath

I hereby declare and affirm that this doctoral dissertation is my own work and that I have not used any aids and sources other than those indicated.

If electronic resources based on generative artificial intelligence (gAI) were used in the course of writing this dissertation, I confirm that my own work was the main and value-adding contribution and that complete documentation of all resources used is available in accordance with good scientific practice. I am responsible for any erroneous or distorted content, incorrect references, violations of data protection and copyright law or plagiarism that may have been generated by the gAI.

26-03-2026

Date

Signature of doctoral candidate

Acknowledgment

My PhD journey began in the FS-LA laser group at the beginning of the COVID-19 pandemic. During this challenging period, I was exceptionally fortunate to have Dr. Bastian Manschwetus as my mentor, whose guidance enabled me to quickly familiarize myself with the FLASH facility and its ongoing projects. His support was crucial in easing my transition into the research environment. I am equally grateful to Ingmar Hartl for the opportunity to pursue my doctoral studies in his group.

Starting out in Hamburg and at DESY was made much easier thanks to Pranny Balla, Dominic Lammer, Frederik Kuschewski, and Nora Schirmel, who guided me through the technical details of the FLASH2 pump–probe laser system. I would also like to thank the other members of the FS-LA group, Tino Lang, Skirmantas Alisauskas, Giovanni Cirmi, and others, for their laser support during in-house beamtimes at FLASH. I also thank Sebastian Schulz and the MSK DESY group for their help in understanding the principles of the laser arrival monitor.

Two years into my PhD, when Bastian Manschwetus moved into industry, Melanie Schnell and Benjamin Erk kindly welcomed me into the FS-SMP and FS-FLASH groups. Melanie became an inspiring role model, and her encouragement carried me through many challenging moments. At the same time, Atia-Tul-Noor and Benjamin generously shared their expertise, teaching me everything I needed to know about the REMI and CAMP end-station skills, which became the foundation of my experimental work.

This journey was not without its challenges. FLASH data analysis initially felt like a steep mountain to climb, especially for someone with a non-programming background. Christopher and Denis Tikhonov played a crucial role at this stage, guiding me in writing analysis scripts and helping me design algorithms to handle complex datasets. Processing REMI data was a truly collaborative effort, and it would not have been possible without the support of Hannes Lindenblatt, Christopher Passow, Stefan Düsterer, and Ulrike Frühling in developing the data pipeline. The butanethiol project involved analyzing large VMI datasets, and I am grateful to Bastian, Christopher, Denis, and Benjamin, along with many others, for their contributions to developing the tools required for VMI data processing and Abel inversion. Their efforts were essential to the successful handling and interpretation of the data. Throughout this entire journey, Denis Tikhonov remained a constant source of theoretical insight and support. I also thank Wenhao Sun for performing the TD-DFT calculation for the butanethiol molecule at the last moment.

I would also like to extend a heartfelt thank-you to all past and present members of the FS-SMP group. In particular, I am grateful to former members—Denis Tikhonov, Jason Lee, Alcides Simao, Pragya Chopra, Diksha Garg, Gayatri Batra, Fan Xie, Eva Gougoula, Pablo Pinacho, Himanshi Singh, as well as current members Wenhao Sun, Donatella Loru, Swantje Caliebe, Maureen Ayon Alfaro, Christina Tonauer, Jiayi Li, Ningjing Jiang, Freya Berggötz, and my wonderful officemate, Liuting Wang. The many insightful discussions we shared allowed me to learn something new every day, not only in science but also about food and cultures.

Beyond the scientific challenges, the most difficult part of this journey was personal.

Losing my father while completing this thesis made everything feel overwhelming. I owe an immeasurable debt to my parents, whose sacrifices created opportunities that once felt out of reach for someone from my background. Being the first in my family to attend university is something I carry with great pride. This achievement belongs not only to me, but also to my grandfather, grandmother, my parents, and my sister, who never stopped believing in me.

A very special thank you to Gayatri Batra and Krishna Kumar, who stood by me in ways I could never have imagined during some of the most difficult moments of this journey. Your support means more to me than words can express. I would also like to thank Angha for always listening to me and for the emotional support that helped me through difficult times.

I would also like to thank the DESY International Office for their assistance with immigration matters, the DESY library for their invaluable resources, and the IT and technical staff who keep everything running smoothly. Finally, to all my friends and family, thank you for your unwavering support throughout this process. This has been a long and transformative journey, and I am truly grateful to have shared it with you.